N d'ordre :
N attribué par la bibliothèque :

ÉCOLE NORMALE SUPÉRIEURE DE LYON

Laboratoire de Physique

Mémoire rédigé en vue de l'obtention du diplôme
d'Habilitation à Diriger des Recherches

auteur :

Romain Volk

Transport de particules en écoulement turbulent

Après avis de : Alain Cartellier, Rapporteur
Beat Lüthi, Rapporteur
Luminita Danaila, Rapportrice

Devant la Commission d'examen formée de :

Alain Cartellier, Rapporteur
Luminita Danaila, Rapportrice
Michel Lance, Président
Beat Lüthi, Rapporteur
Alain Pumir
Jean-François Pinton

Table des matières

I.Introduction générale et présentation du mémoire

Les écoulements turbulents sont très répandus et influencent un grand nombre d'aspects de notre vie quotidienne. En particulier, et même si l'on n'en a pas ou plus conscience, elle peut à la fois être un désavantage lorsqu'elle détermine en partie la consommation de nos voitures, ou un avantage lorsqu'elle améliore l'efficacité du mélange du sucre dans le café ou permet une meilleure dispersion des polluants dans les villes les jours de vent. Elle a aussi un impact majeur sur la génération du champ magnétique au coeur des planètes et des étoiles par effet dynamo.

C'est à cette influence de la turbulence sur le transport (de champ magnétique, de particules, de masse ou de chaleur) que j'ai consacré mon activité de recherche. Tout d'abord en étudiant l'amplification du champ magnétique au cours d'une thèse (2002-2005) qui m'a amené à travailler dans des écoulements de gallium et de sodium liquide à Lyon ou au CEA Cadarache dans le cadre de la collaboration VKS [B1-B4, B7]. Il a donc été relativement naturel de continuer des recherches au sein de la collaboration VKS après la fin de ma thèse. Elles ont été particulièrement centrées, non plus sur les effets d'induction, mais sur l'effet dynamo lui-même à l'aide de deux dispositifs : la dynamo synthétique Bullard-von Kármán construite à Lyon [B5,B12], ainsi que l'expérience VKS qui a permis d'observer une grande variété de régimes dynamiques du champ magnétique (stationnaires, intermittents, chaotiques, bistables, ...) [B6,B8-B11], dont certains présentent une analogie troublante avec les renversements du champ magnétique terrestre.

Parallèlement j'ai débuté une activité en turbulence lagrangienne en 2006 à laquelle j'ai consacré de plus en plus de temps. Lorsque celle-ci a commencé à arriver à maturité en 2008, j'ai décidé de m'y consacrer pleinement en quittant la collaboration VKS (alors au faîte de son activité). C'est au prix de ce choix que j'ai pu trouver le temps, non seulement de développer mes activités personnelles centrées sur le transport turbulent de particules [A1-A11], mais aussi de collaborer avec le monde industriel sans pour autant négliger mon rôle d'enseignant. Ce mémoire regroupe l'ensemble de ces nouvelles activités, dont je dresserai un bilan au chapitre III, et qui forment aujourd'hui, selon moi, un tout cohérent. Le chapitre IV abordera mes activités industrielles dans le cadre de la collaboration FUI-PATVAX, tandis que le chapitre V décrira mes nouvelles activités plus récentes. Cette dernière partie constitue les grands axes de recherche sur lesquels je souhaite porter mon effort dans les prochaines années.

II.Bilan des activités de recherche

Depuis 2006 une grande part de mon activité de recherche est centrée sur l'étude de la turbulence hydrodynamique et en particulier l'étude du transport de particules par les écoulements turbulents.

Ce chapitre aborde de façon synthétique les différents angles sous lesquels j'ai été amené à aborder ce problème. La première section expose le cadre général du transport de particules par un écoulement turbulent et les techniques expérimentales de suivi lagrangien de particules. Dans la seconde section, je présente la technique de vélocimétrie Doppler que j'ai développée au laboratoire, tout d'abord en tant qu'agrégé préparateur, puis ensuite en tant que maître de conférences. Les résultats sur la dynamique des particules inertielles que j'ai obtenus en l'utilisant seront présentés dans la troisième section. La quatrième section sera consacrée à l'étude du transport de particules matérielles, dont la taille est plus grande que l'échelle de Kolmogorov, ainsi qu'aux travaux de modélisation numérique effectués en collaboration avec Enrico Calzavarini et Emmanuel Lévêque. Les cinquième et sixième sections aborderont le travail de thèse de Robert Zimmermann, que j'ai co-encadré avec Jean-François Pinton, qui explore la dynamique d'une particule de taille intégrale librement advectée par un écoulement turbulent et la possibilité de mesures lagrangiennes d'accélération utilisant des particules instrumentées.

II.1 Introduction

II.1.1 Transport de particules par un écoulement turbulent

Les écoulements turbulents chargés de particules sont très courants, que ce soit dans la nature (formation des nuages, transport de polluants dans l'atmosphère, ...) ou encore dans l'industrie où leur champ d'application couvre un spectre très large allant des sprays de carburant dans les moteurs aux écoulements à bulles dans des réacteurs chimiques. La compréhension du transport de ces particules est importante car ce dernier joue un grand rôle dans des actions aussi commune que la dissolution d'un morceau de sucre dans une tasse de café, phénomène dont il est assez difficile de prédire à l'avance la cinétique même lorsque l'on connaît bien les conditions d'agitation. Le transport des particules est complexe car la turbulence elle-même l'est : un écoulement turbulent fluctue fortement en temps et en espace et possède de l'énergie sur une large gamme d'échelles spatiales s'étendant depuis l'échelle intégrale L jusqu'à l'échelle de dissipation η (figure II.1, gauche).

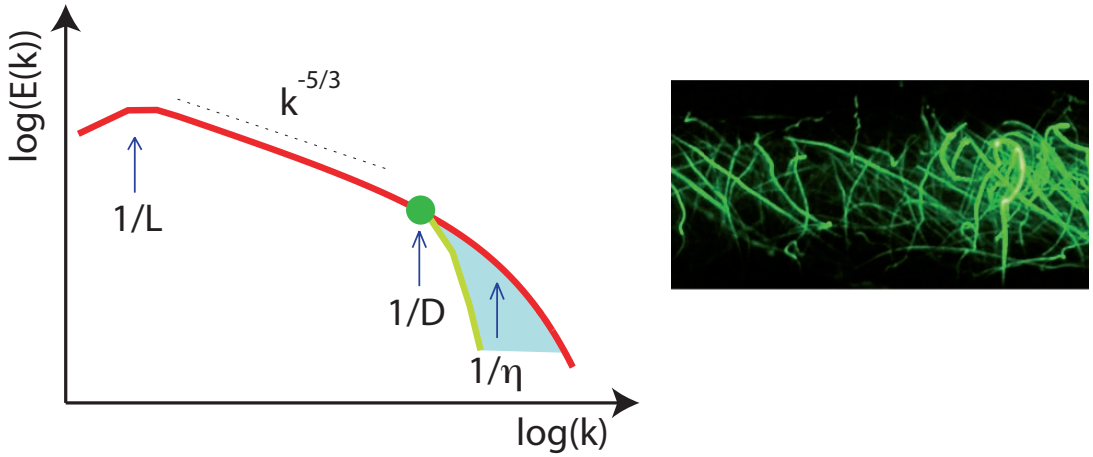

Fig. II.1: Gauche : spectre d'énergie cinétique $E(k)$ d'un écoulement turbulent en fonction du nombre d'onde k. L est l'échelle intégrale de l'écoulement, η l'échelle de dissipation et D le diamètre de la particule considérée. Droite : trajectoires de bulles de diamètre moyen $\langle D \rangle \sim 20\eta$ en mouvement au centre d'un écoulement de von Kármán. La photographie a été prise par G. Verhille lors de son stage de M2.

Ainsi, observant la trajectoire d'un objet de taille D en mouvement dans un écoulement, celle-ci va apparaître fortement aléatoire et tourmentée (figure II.1, droite) puisqu'elle est influencée par une vaste gamme de tourbillons de tailles et de durées de vie variées. Naturellement, le mouvement des particules dépend à la fois des caractéristiques physiques de celles-ci (densité ρ_p, diamètre D), de celles du fluide (viscosité ν, densité ρ_f), mais aussi de celles de l'écoulement. On conçoit intuitivement qu'une particule isodensité ($\rho_p/\rho_f \sim 1$) de taille $D \leq \eta$ pourra suivre parfaitement les fluctuations de l'écoulement : l'étude de leurs trajectoires renseignera alors sur la turbulence elle-même.
Mais dès lors que les particules auront une densité différente de celle du fluide (telles des bulles de gaz dans l'eau), ou une taille D plus grande que η, leur inertie et leur taille vont jouer un rôle fondamental. Les particules lourdes auront alors tendance à être éjectées des structures tourbillonnaires alors que les particules légères s'y accumuleront. De même, les particules de taille $D \geq \eta$ (figure II.1) seront incapables de répondre aux échelles les plus petites. Dans cette dernière situation, pour laquelle l'interaction particule écoulement est non linéaire, la force exercée par l'écoulement sur la particule est d'ailleurs largement inconnue : aucun développement théorique n'est parvenu à écrire l'équation du mouvement d'une particule dans un écoulement turbulent lorsque son diamètre n'est pas de dimension négligeable devant l'échelle de dissipation.

La problématique est pourtant simple à énoncer : **Quelle est la statistique de force qu'exerce un écoulement pleinement turbulent sur une particule de taille et de densité données ?** C'est à cette question que je me suis consacré depuis la fin de ma thèse. J'ai abordé cette question à la fois de manière expérimentale en développant des techniques de suivi de particules, mais aussi en collaboration avec des spécialistes de la simulation numérique directe (DNS) dans le but de confronter et d'améliorer les modèles de transport existant.

II.1.2 Mesures lagrangiennes en turbulence

L'étude de la force exercée par un écoulement turbulent sur une particule librement advectée est assez simple dans son principe puisqu'il *suffit* de suivre les particules le long de leur trajectoire en mesurant l'évolution de leur vitesse lagrangienne $\mathbf{v}_p(t)$ et de leur vecteur rotation $\mathbf{\Omega}_p(t)$. Connaissant leur masse m_p et leur moment d'inertie I_p, on a alors en principe accès à la force $\mathbf{F}$ et au couple $\mathbf{\Gamma}$ exercés par l'écoulement au travers des relations :

$$m_p \frac{\mathrm{d}\mathbf{v}_p}{\mathrm{d}t} = \mathbf{F} \qquad I_p \frac{\mathrm{d}\mathbf{\Omega}_p}{\mathrm{d}t} = \mathbf{\Gamma} \tag{II.1}$$

A partir d'une collection de trajectoires lagrangiennes, on peut donc caractériser la statistique de la force $\mathbf{F}$ au travers de la densité de probabilité de l'accélération PDF(a) et de sa fonction d'autocorrélation $C_{aa}(\tau)$ par exemple. Si elles sont simples dans leur principe, les mesures lagrangiennes se heurtent toutefois à plusieurs difficultés expérimentales assez sévères du fait du spectre très large des échelles spatio-temporelles des écoulements turbulents. Dans un écoulement pleinement turbulent tels que les écoulements de von Kármaán avec lesquels j'ai eu l'occasion de travailler ($Re_\lambda \in [130 - 900]$), et pour lesquels la puissance massique injectée ϵ est assez grande ($\epsilon \sim 10$ W.kg^{-1}), l'échelle de dissipation est $\eta = (\nu^3/\epsilon)^{1/4} \sim 20$ μm dans l'eau pour une échelle intégrale de l'ordre de $L = 3$ cm. Dans le cas d'un traceur de diamètre $D \sim \eta$, il s'agit de suivre un objet minuscule une distance de l'ordre de L avec une fréquence d'acquisition nettement plus grande que $1/\tau_\eta = \sqrt{\nu/\epsilon} \sim 3$ kHz qui représente les mouvements les plus rapides que l'on peut observer.

• **Les techniques Doppler** sont basées sur la modulation de fréquence que subit une onde lorsqu'elle est diffusée par une particule en mouvement. Qu'elles utilisent une onde acoustique [32, 23, 42] ou un faisceau LASER [49], le principe est identique et permet de mesurer directement l'évolution de la vitesse d'une particule le long de sa trajectoire en mesurant le décalage de fréquence instantané entre le signal reçu et le signal émit (figure II.2, gauche). Ces techniques temps-fréquences, qui n'utilisent qu'un détecteur (Photomultiplicateur ou transducteur acoustique) sont très efficaces : si elles ne permettent pas de remonter (avec un seul détecteur) à la position de la particule, elles permettent d'obtenir une grande résolution temporelle pour la mesure de la vitesse, ce qui est nécessaire pour mesurer avec précision l'accélération de particules de taille voisine de η. Les techniques Doppler permettent donc d'avoir une caractérisation lagrangienne de l'écoulement avec une grande précision à un coût modeste (en euros et en volume d'informations à traiter)

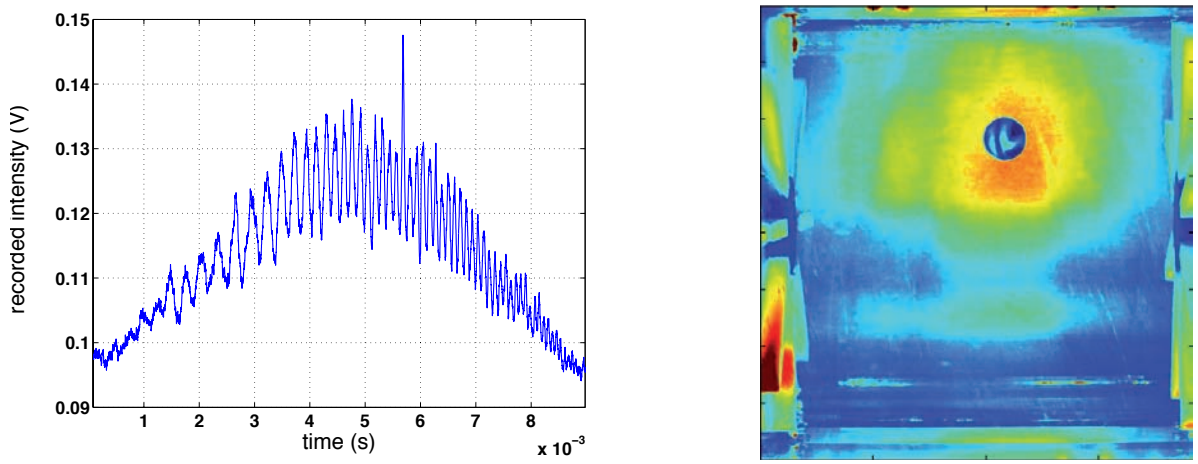

Fig. II.2: Gauche : signal enregistré par une photodiode lors du passage d'une bulle dans un réseau de franges d'interférences. On distingue la forme gaussienne du faisceau LASER et une fréquence instantanée qui augmente car la bulle accélère. Droite : image obtenue (en fausses couleurs) en filmant le mouvement d'une sphère peinte en mouvement dans un écoulement de von Kármán. L'utilisation de 2 caméras permet d'obtenir la position 3D de la sphère tandis que le motif peint permet de connaître l'orientation absolue de la sphère.

en comparaison des techniques d'imagerie rapide plus classiques. Toute technique ayant ses qualités et défauts, si les techniques Doppler sont parfaitement adaptées au problème du mouvement d'une particule, elles ne permettent pas d'aborder les problèmes multiparticules et ne peuvent apporter d'informations sur le mouvement de rotation de la particule dont on mesure la vitesse.

• **La technique de suivi direct (PTV pour Particle Tracking Velocimetry)** utilise quant à elle plusieurs caméras ultrarapides (Phantom V.12 dans notre cas) qui permettent un suivi lagrangien de la position 3D $(\vec{X}_i(t))_{[1,N]}$ d'une assemblée de petites particules avec une cadence d'échantillonnage élevée [1]. Initialement limitée à de petits volumes de mesures [27, 50], cette technique a connu de nombreux développements ces dernières années et permet de résoudre complètement la dynamique des traceurs à haut nombre de Reynolds ($Re_\lambda \sim 900$) lorsque la taille de l'expérience est grande et la puissance massique faible ($\epsilon \sim 0.15\text{W.kg}^{-1}$, $\eta \sim 50$ μm dans l'eau). Le caractère multiparticules permet alors d'obtenir une bonne convergence statistique (au prix de la manipulation d'un grand volume de données à transférer), et a permis d'étudier des problèmes tels que les effets d'anisotropie dans les écoulements de type von Kármán [37], ou encore la dispersion de paires de traceurs à haut nombre de Reynolds [8]. Lorsque l'on s'intéresse non pas à de petites particules, mais à un objet de plus grande taille telle une sphère peinte (figure II.2, droite), l'imagerie directe permet de remonter à l'orientation absolue de l'objet, ce qui permet de faire un suivi dans

1. D'autres techniques, telle l'holographie en ligne [13], ne nécessitent qu'une seule caméra pour la reconstruction 3D des trajectoires.

l'espace position-orientation [57] et ainsi d'avoir accès au couple exercé par l'écoulement sur la particule. C'est au développement de cette seconde version de la PTV que j'ai apporté ma contribution pour l'étude du couplage rotation-translation d'une sphère isodensité en mouvement dans un écoulement de von Kármán.

II.2 Vélocimétrie Laser Doppler Etendue

Comme mentionné précédemment, le suivi lagrangien de particules est difficile à réaliser à haut nombre de Reynolds car il demande, pour résoudre les échelles les plus rapides, de pouvoir suivre des particules plus petites que l'échelle de Kolmogorov avec une grande fréquence d'échantillonnage. Pour aborder cette thématique, j'ai développé un montage original de Vélocimétrie Laser Doppler Etendue (ELDV).

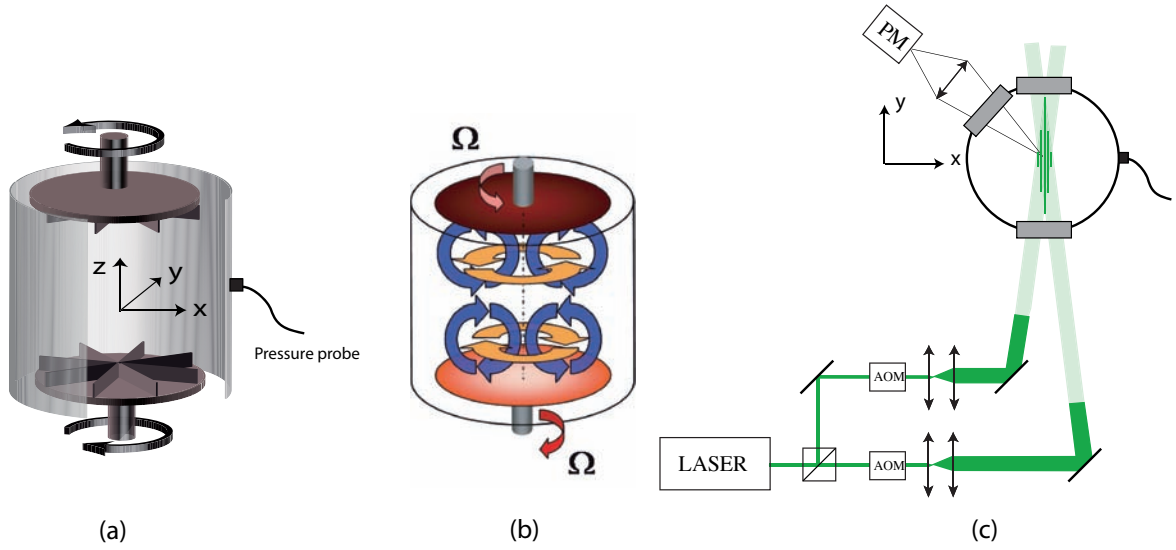

Fig. II.3: Dispositif expérimental. (a) : géométrie de la cuve. (b) : représentation de l'écoulement de von Kármán contrarotatif. (c) : principe de la vélocimétrie laser Doppler étendue (ELDV) – vue de dessus de l'expérience. PM : position du photomultiplicateur qui détecte les modulations d'intensité de la lumière diffusée lorsqu'une particule traverse les franges d'interférence à l'intersection des faisceaux laser. Les figures sont tirées de la référence [47].

La technique ELDV est adaptée de la vélocimétrie ultrasonore développée pour le suivi lagrangien de particules en turbulence [36] ; le gain en longueur d'onde étant de l'ordre de 1000, la technique optique permet de suivre des particules dont la taille est de l'ordre de 10 microns, beaucoup plus petites que les tailles accessibles ($D \geq 100$ μm) par la technique acoustique dans l'eau. Le montage optique peut aussi être vu comme une extension de la vélocimétrie laser Doppler (figure II.2(c)) : un faisceau laser est séparé en deux faisceaux

qui sont élargis à l'aide de télescopes, décalés en fréquence à l'aide de deux modulateurs acousto optiques, puis recombinés au centre d'un écoulement de von Kármán. L'ensemble créé un réseau de franges d'interférences, dans un volume de l'ordre de 1 cm^3, qui défile à vitesse constante $v_f = e\delta f$ avec e l'interfrange et δf le décalage de fréquence des deux bras de l'interféromètre.
Lorsqu'une particule traverse les franges, la lumière est alors modulée à une fréquence instantanée $\delta f + f(t)$ avec $f(t)$ le décalage Doppler proportionnel à la composante de vitesse perpendiculaire aux franges (figure II.2, gauche). Utilisant une carte d'acquisition rapide, on peut alors démoduler les variations d'intensité [36] de chaque trajectoire avec une résolution temporelle suffisante pour résoudre les petites échelles du mouvement des billes dans la gamme $Re_\lambda \in [450, 850]$. La mesure consiste alors en une collection d'environ 15000 trajectoires $(u^n(t))_n$ de durée moyenne 20 temps (τ_η) dont on tire l'accélération $(a^n(t))_n$ par différentiation. Contrairement à la technique LDV eulérienne, le montage utilise une grande valeur de l'interfrange ($e \sim 40$ μm), ce qui permet de suivre, soit des particules fluorescentes de 30 microns (traceurs de l'écoulement), soit d'autres particules (bulles ou particules matérielles) dont on souhaite étudier le mouvement.

J'ai utilisé la technique ELDV pour étudier la dynamique de particules de diamètres proches de l'échelle de Kolmogorov dans un écoulement de von Kármán dans le régime de turbulence pleinement développé (figure II.2(a,b)). Dans le cas de traceurs, dont la variance d'accélération augmente comme $a^2 \sim (\eta/\tau_\eta^2)^2 = \epsilon^{3/2}\nu^{-1/2}$, j'ai comparé les résultats obtenus aux résultats de l'expérience de l'Université de Cornell utilisant des Silicon Strip Detectors [50]. Utilisant la normalisation de Heisenberg-Yaglom, on retrouve que l'évolution de $a_0 \equiv a_{rms}^2 \nu^{1/2}\epsilon^{-3/2}$ augmente avec la vitesse de rotation Ω pour atteindre une valeur de l'ordre de 5 à haut nombre de Reynolds, l'accélération approchant l'isotropie pour les vitesses de rotation les plus élevées (figure II.4(a)). On retrouve par ailleurs que les PDF d'accélération sont extrêmement intermittentes, avec des ailes en exponentielles étirées qui se superposent très bien avec les données de référence publiée dans [33] (figure II.4(b,c)). Malgré un volume de mesure réduit (de l'ordre de 1 cm^3), la durée moyenne permet de calculer les corrélations d'accélération $C_{aa}(\tau) = \langle a(t)a(t+\tau)\rangle / a_{rms}^2$ sans biais de mesure. Ces courbes se superposent très bien lorsqu'elles sont tracées en fonction de τ/τ_η (figure II.4(d)), ce qui montre que la résolution temporelle du dispositif est suffisante pour que l'incrément $\delta_\tau v/\tau$ converge bien vers l'accélération aux nombres de Reynolds les plus élevés. Concernant l'étude des statistiques lagrangiennes à une particule, cette technique expérimentale permet donc d'obtenir toutes les quantités d'intérêt, à un coût modeste en regard du prix des caméras rapides (Phantom V.12), avec une résolution temporelle supérieure à toute autres technique lagrangienne actuellement disponible.

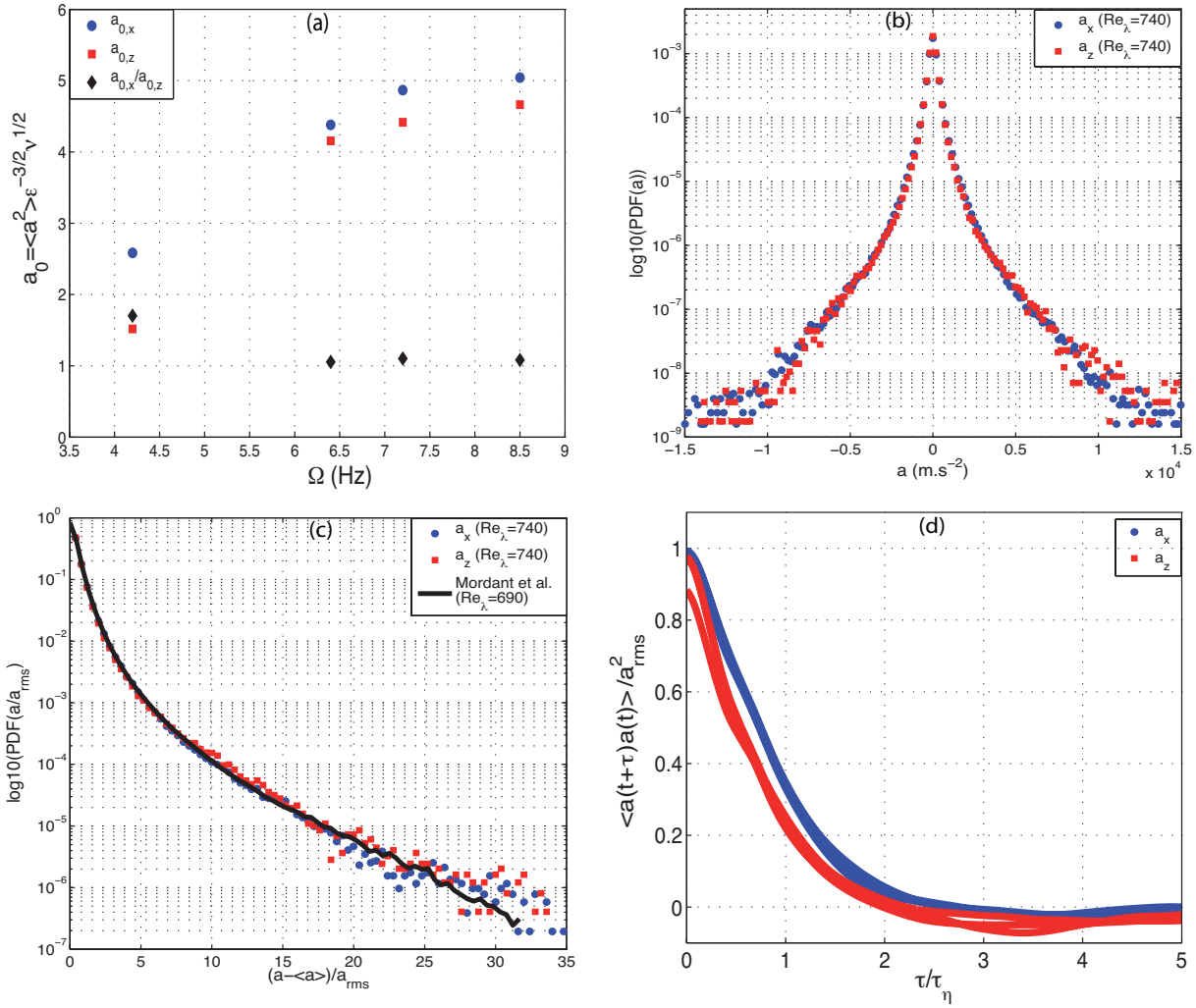

Fig. II.4: (a) : évolution de la variance réduite $a_0 = a_{rms}^2 \nu^{1/2} \epsilon^{-3/2}$ de a_x (ronds bleus) et de a_z (carrés rouges), et du rapport $a_{0,x}/a_{0,z}$ (losanges noirs) en fonction de la vitesse de rotation Ω. (b) : PDFs d'accélération de a_x et a_z à $Re_\lambda = 740$. (b) : PDFs d'accélération centrées et réduites de a_x et a_z à $Re_\lambda = 740$ superposées à la PDF d'accélération de Mordant et al. [34]. (d) : Fonctions d'autocorrélation de a_x et a_z obtenues pour les différents nombres de Reynolds, tracées en fonction du temps sans dimension τ/τ_η. Les figures sont tirées de la référence [46].

II.3 Dynamique des particules inertielles

Si lorsque l'on suit de petites particules de même densité que celle du fluide, on obtient des informations sur la turbulence elle-même, il est intéressant d'étudier la dynamique de particules inertielles dans l'écoulement pour obtenir non seulement des informations sur la turbulence mais aussi sur les propriétés de transport des écoulements multiphasiques. Beaucoup de modèles déterministes (ou non) permettent de décrire la dynamique de telles particules, l'approche la plus commune consistant à utiliser l'équation de Maxey-Riley-Gatignol [29, 22] qui décrit l'évolution de la vitesse $\mathbf{v}$ d'une particule de rayon r_p dans un écoulement connu. Cette équation est obtenue dans la limite des tailles suffisamment petites pour que le nombre de Reynolds de la particule Re_p tende vers 0. Négligeant les effets de gravité, l'équation s'écrit :

$$m_p \frac{\mathrm{d}\mathbf{v}}{\mathrm{d}t} = m_f \frac{D\mathbf{u}}{Dt} + 6\pi\mu r_p (\mathbf{u}-\mathbf{v}) + \frac{1}{2} m_f \frac{\mathrm{d}(\mathbf{u}-\mathbf{v})}{\mathrm{d}t} \tag{II.2}$$

$$+ 6r_p^2 \int_0^t \left(\frac{\pi\mu\rho_f}{(t-\tau)} \right)^{\frac{1}{2}} \frac{\mathrm{d}}{\mathrm{d}\tau} (\mathbf{u}-\mathbf{v}) \, \mathrm{d}\tau, \tag{II.3}$$

avec $\mathbf{u}$ la vitesse du fluide à la position de la particule, $m_p = \frac{4}{3}\pi r_p^3 \rho_p$ sa masse, $m_f = \frac{4}{3}\pi r_p^3 \rho_f$ la masse de fluide de même volume et $\mu = \rho_f \nu$ la viscosité dynamique du fluide. Cette équation fait apparaître successivement différents termes au second membre : l'accélération du fluide à la position de la particule, la traînée de Stokes, la masse ajoutée qui est non nulle lorsque le fluide (ou la particule) accélère, et la force d'histoire qui provient de la diffusion de la quantité de mouvement dans le sillage de la particule. Ce dernier terme, non local en temps, est en général négligé car non seulement il demande un coût de calcul prohibitif mais la forme réelle du noyau de convolution (ici diffusif) n'est pas connue pour un écoulement turbulent. L'équation se simplifie alors pour sous la forme plus simple :

$$\frac{\mathrm{d}\mathbf{v}}{\mathrm{d}t} = \beta \frac{D\mathbf{u}}{Dt} + \frac{1}{\tau_p} (\mathbf{u}-\mathbf{v}) \, . \tag{II.4}$$

Ce modèle, appelé β-Stokes, ne dépend que de deux paramètres, $\beta = 3\rho_f/(\rho_f + 2\rho_p)$ qui rend compte des effets de masse ajoutée, et le nombre de Stokes $St = \tau_p/\tau_\eta$ (avec $\tau_p = r_p^2/(3\beta\nu)$) qui quantifie les effets de la force de traînée. Les implications de ces deux termes sont qualitativement clairs : ignorant les effets de ségrégation, la dynamique d'une bulle de gaz $\beta = 3$ sera dominée par les effets de masse ajoutée, lui donnant un caractère fortement intermittent, tandis que la dynamique des particules lourdes ($\beta \sim 0$) doit être dominée par un effet de filtrage temporel tendant à lisser ce caractère intermittent.

J'ai abordé cette problématique sous l'angle expérimental en utilisant la technique ELDV pour étudier la dynamique de particules plus lourdes que le fluide (PMMA, densité 1.4), ou plus légères (bulles d'air de taille diamètre $D \sim 10\eta$) dans le même écoulement de von Kármán, au même nombre de Reynolds $Re_\lambda = 850$. Cette étude, qui constitue la première mesure de l'accélération lagrangienne de bulles à haut nombre de Reynolds, a mis

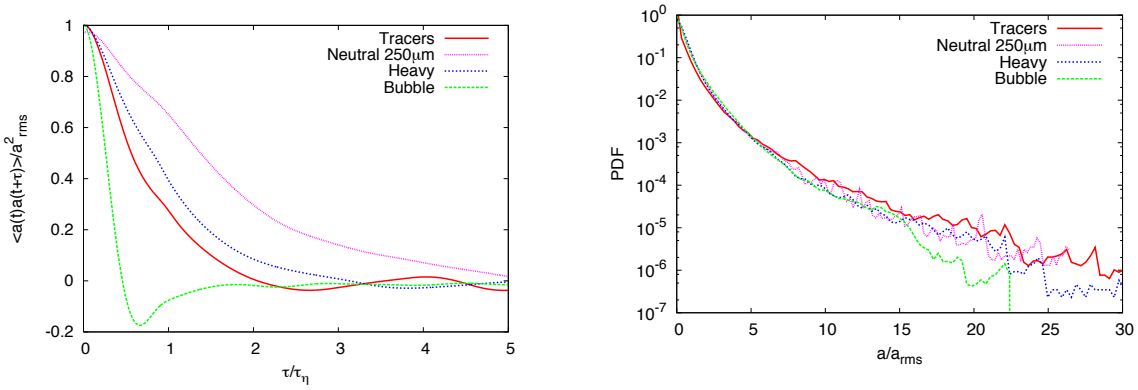

Fig. II.5: Gauche : Fonctions d'autocorrélation de l'accélération obtenues pour des traceurs (rouge), des particules de PMMA (bleu), des bulles (vert) et des particules matérielles (magenta). Droite : PDF d'accélération obtenues pour des traceurs (rouge), des particules de PMMA (bleu), des bulles (vert) et des particules matérielles (magenta). Les courbes sont issues de la référence [48].

en lumière quelques caractéristiques génériques du transport des particules inertielles par un écoulement turbulent. Alors que les statistiques à grande échelle (v_{rms}, PDF(v/v_{rms})) dépendent peu de la nature de la particule, la statistique d'accélération dépend de manière cruciale de la densité des particules. Ainsi les particules lourdes ont une accélération typique $\langle a_p^2 \rangle$ plus faible que les traceurs alors que les bulles ont une variance d'accélération beaucoup plus grande (environ 4 fois) que celle du fluide. Cette observation va dans le même sens que l'évolution des temps d'autocorrélation de l'accélération des particules (figure II.5(a)), les particules lourdes ayant un temps de corrélation τ_{corr} plus grand que celui des traceurs alors que les bulles ont un temps de corrélation beaucoup plus petit que τ_η. C'est d'ailleurs cette dernière observation qui explique pourquoi le suivi lagrangien des bulles est si difficile puisqu'il nécessite une fréquence d'échantillonnage que peu de techniques peuvent offrir.

Toutefois, si certaines quantités statistiques de l'accélération changent de manière cruciale en fonction de la densité des particules, on observe que les PDF d'accélération, une fois réduites à variance unité, sont peu différentes quel que soit le type de particules dont on peut effectuer le suivi (figure II.5(b)). Cette observation expérimentale étonnante, jamais reproduite dans les simulations numériques, a par ailleurs été faite indépendamment [42, 41] dans une turbulence de grille pour une grande variété de particules ayant des densités et des tailles différentes.

J'ai ensuite été amené à comparer mes résultats expérimentaux avec les simulations numérique de E. Calzavarini & F. Toschi qui effectuaient, au même moment, l'étude de l'influence de la taille et de la densité pour des particules ponctuelles transportées dans une

turbulence homogène et isotrope, et dont le mouvement est décrit par le modèle β-Stokes (équation [10]). Cette comparaison a permis d'observer que le modèle ponctuel, lorsqu'il prend en compte les effets de masse ajoutée, permet de reproduire qualitativement (mais pas quantitativement) l'influence de la densité sur les fonctions d'autocorrélation de l'accélération lagrangienne [48]. Cependant, nous avons également observé à cette occasion que le modèle n'était pas capable de décrire l'influence de la taille des particules dans le régime $D/\eta \geq 1$ puisqu'il prévoit que les particules isodensité se comportent toujours comme des traceurs alors que l'expérience montre que le temps de corrélation des particules isodensité augmente avec leur taille (figure II.5, gauche).

Cette comparaison modèle-expérience, initiée à cette occasion et continuée depuis lors, est caractéristique de ma démarche de recherche de collaborations avec des numériciens-théoriciens de la turbulence. Cette volonté de collaboration s'est concrétisée en particulier lors de la venue en Post-Doc de E. Calzavarini à l'ENS de Lyon, avec qui Emmanuel Lévêque et moi avons travaillé durant deux ans sur le problème de la prise en compte des effets de taille sur le transport des particules.

II.4 Transport de particules de taille finie

Dès les premières études de la turbulence lagrangienne à très haut nombre de Reynolds, le choix des particules à utiliser comme traceurs du mouvement du fluide s'est avéré crucial [32, 50]. Il a alors été remarqué qu'une particule de diamètre $D \gg \eta$ montrait une accélération bien plus faible que celle des traceurs, prouvant que ces particules ne suivent pas le mouvement du fluide [50]. La question s'est donc naturellement posée de comprendre comment une particule de taille finie, pour laquelle l'interaction avec l'écoulement est non linéaire, répond aux différentes échelles spatio-temporelles de l'écoulement et comment se comparent leurs statistiques lagrangiennes avec celles des traceurs.

J'ai abordé ce problème à la fois sous l'angle expérimental et sous l'angle de la modélisation et de la simulation numérique :
• J'ai utilisé la technique ELDV pour étudier la dynamique des particules de taille finie pour une large gamme de tailles et de nombres de Reynolds. Cette étude a permis d'une part, de compléter les études [42, 9] qui s'était concentrées sur l'évolution de la variance de l'accélération des particules, mais aussi de quantifier la réduction de l'intermittence de l'accélération lorsque l'on augmente la taille des particules.
• En collaboration avec E. Calzavarini et E. Lévêque, nous avons incorporé les corrections de Faxen dans l'équation de transport des particules ponctuelles (équation de Maxey-Riley-Gatignol). Nous avons observé que contrairement aux particules inertielles, il faut tenir compte de l'extension spatiale des particules pour simuler une dynamique reproduisant (au moins qualitativement) les données expérimentales.

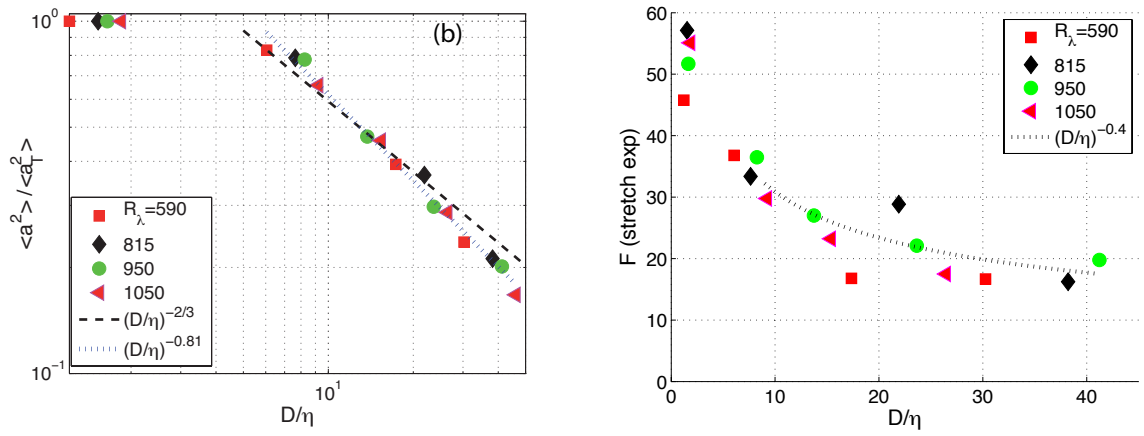

Fig. II.6: Gauche : Evolution de la variance de l'accélération des particules matérielles en fonction du rapport D/η. Droite : Evolution de la flatness de l'accélération des particules matérielles en fonction du rapport D/η. Les figures sont tirées de la référence [47].

II.4.1 Etude expérimentale de l'Intermittence des particules matérielles

Plusieurs groupes se sont concentrés sur le transport des particules de taille finie, que ce soit dans une turbulence de grille ou dans des écoulements de von Kármán. Qureshi et al. ont montré, pour des particules de diamètre D correspondant au régime inertiel et un nombre de Reynolds $Re_\lambda = 160$, que les particules ont une variance d'accélération $\langle a_D^2 \rangle$ qui décroit selon une loi de puissance en $D^{-2/3}$ [42]. Cette loi de puissance se comprend si en l'on admet que l'accélération de la particule est donnée par le gradient de pression $\delta_D P/D$ calculé à l'échelle de la particule. La variance de l'accélération suit alors la fonction de structure d'ordre 2 de la pression, et évolue selon une loi de puissance $\langle a_D^2 \rangle \propto \langle (\delta_D P/D)^2 \rangle \propto D^{4/3-2}$ suivant la prédiction de Kolmogorov en l'absence d'intermittence. Ce lien entre fonction de structure de la pression et accélération des particules matérielles a été confirmé par Brown et al. qui ont montré que l'évolution de la variance d'accélération suit l'évolution de la fonction de structure d'ordre 2 de la pression [51].

Dans le cas des mesures effectuées à l'aide de la technique ELDV, nous obtenons des résultats cohérents avec ces deux études précédentes pour une grande gamme de diamètres et de nombres de Reynolds $Re_\lambda \in [450, 800]$. En normalisant la variance de l'accélération des particules par celle des traceurs, ce qui élimine l'effet du nombre de Reynolds, la variance de accélération évolue selon une loi de puissance $\langle a_D^2 \rangle / \langle a_T^2 \rangle \propto (D/\eta)^{-0.8}$ (figure II.6, gauche). Cette valeur, si elle est différente de la prédiction K41, est toutefois cohérente avec les mesures des fonctions de structure de la pression effectuées par Pearson et Antonia [38].

Supposant que le lien entre accélération incréments de pression est vrai pour les différents moments des PDF, le comportement intermittent observé pour la variance m'a incité à rechercher un changement de forme des PDF d'accélération avec la taille des particules.

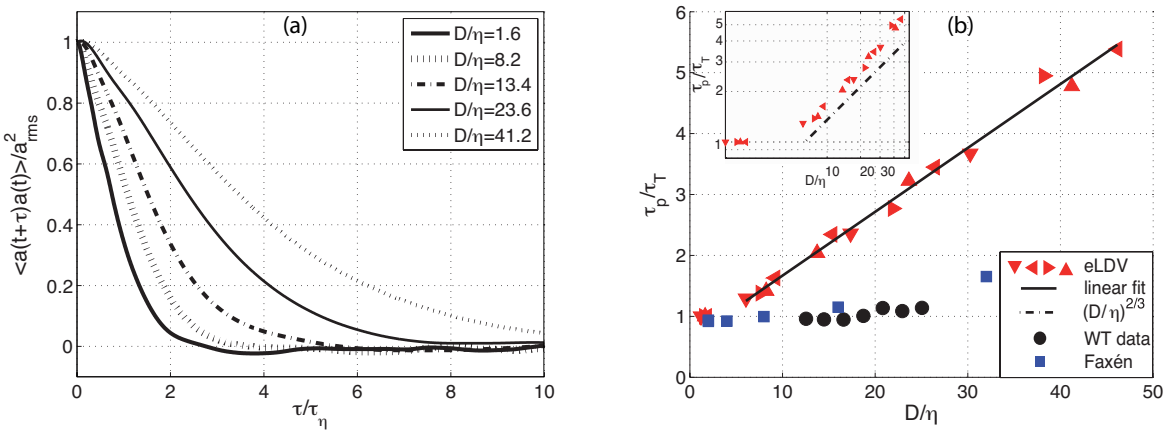

Fig. II.7: Gauche : Fonction d'autocorrélation de l'accélération des particules matérielles en fonction du temps adimentionné τ/τ_η. Droite : Evolution du temps de corrélation des particules τ_p/τ_T en fonction du rapport D/η. Les figures sont tirées de la référence [47].

J'ai donc cherché à mettre en évidence les variations de la flatness $F(D) = \langle a_D^4\rangle/\langle a_D^2\rangle^2$ avec la taille des particules. Cette mesure étant relativement difficile à converger pour de grands nombres de Reynolds, j'ai estimé $F(D)$ en ajustant les PDF mesurées avec deux formes (dont l'exponentielle étirée) qui permettent d'approcher raisonnablement les PDF d'accélération à haut Re_λ. Pour chacun des estimateurs utilisés, les résultats sont qualitativement semblables avec une décroissance de la flatness de l'accélération lorsque l'on augmente la taille des particules (figure II.6, droite). De manière analogue au cas des particules lourdes, pour lesquelles les ailes de la PDF d'accélération se réduisent lorsque l'on augmente l'inertie (ou la taille) des particules, on observe aussi une réduction de l'intermittence de l'accélération des grosses particules par rapport au cas des traceurs.
A partir de la fonction d'auto-corrélation de l'accélération $C_{aa}(\tau) = \langle a(t)a(t+\tau)\rangle/\langle a^2\rangle$, qui tombe à zéro en un temps de l'ordre de quelques τ_η (figure II.7, gauche), il est possible de définir un temps caractéristique de la dynamique des particules (noté τ_p) comme l'intégrale de la partie positive de la courbe. Comme mentionné dans la section précédente, ce temps augmente avec le diamètre D tout en restant de l'ordre du temps dissipatif τ_η. Une fois normalisé par la valeur mesurée pour des traceurs $\tau_T \simeq \tau_\eta$, on constate que le rapport τ_p/τ_T décrit une courbe croissante en fonction du rapport D/η (figure II.7, droite). Le rapport des temps, dont il est difficile de dire s'il croît linéairement avec D/η ou en suivant une loi de puissance $(D/\eta)^{2/3}$ (prédiction dimensionnelle), n'est donc pas proportionnel au nombre de stokes de la particule $St = (D/\eta)^2/12$. Ce dernier paramètre, qui suffit à décrire la dynamique des particules lourdes, n'est donc pas le bon paramètre pour décrire la dynamique des particules matérielles isodenses.

Pour étudier l'intermittence de la dynamique des particules, on peut tracer l'évolution de la flatness des incréments de vitesse $\delta_\tau v = v(t+\tau) - v(t)$ en fonction du log de l'incrément

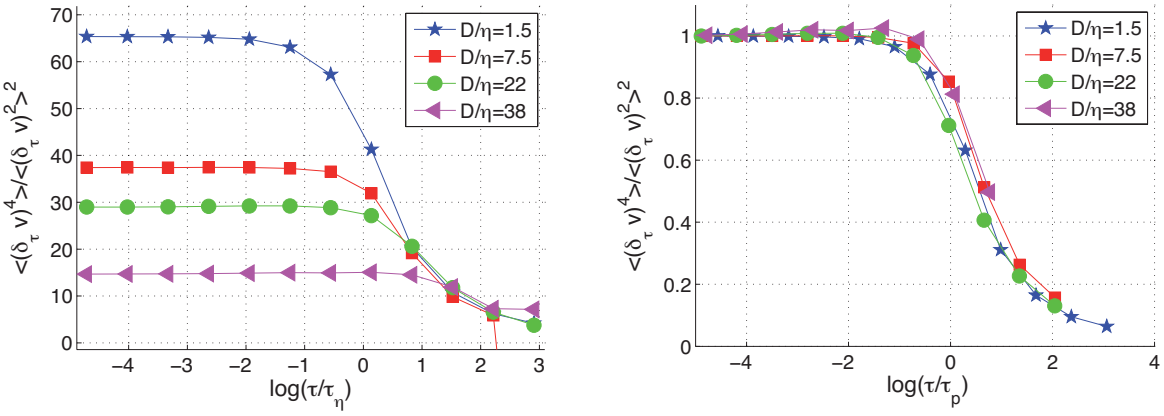

Fig. II.8: Gauche : Flatness des incréments de vitesse $\delta_\tau v$ de quatre types de particules matérielles en fonction de τ/τ_η. Gauche : Flatness des incréments de vitesse $\delta_\tau v$ (normalisées à 1) de quatre types de particules matérielles en fonction de τ/τ_p. Toutes les courbes obtenues (toutes particules isodenses, tous nombres de Reynolds) tombent sur une courbe unique (figures non publiées à ce jour).

temporel τ (figure II.8, gauche). Dans le cas des traceurs, et comme l'on montré Mordant et al. [35], on observe une transition dans le régime dissipatif ($\tau \sim \tau_\eta$) pour laquelle la flatness $F(\delta_\tau v)$ chute brusquement depuis une valeur très élevée (pour l'accélération, $F(a) > 50$) jusqu'à une valeur beaucoup plus faible $F < 10$. Comme l'a montré l'utilisation du formalisme multifractal [15], le temps τ_η est donc le temps qui pilote l'intermittence de la dynamique lagrangienne. Nous retrouvons un résultat analogue dans le cas des particules matérielles (figure II.8, gauche) avec une transition depuis une valeur égale à la flatness de l'accélération $F(a)$ (qui décroît lorsque la taille augmente) jusqu'à une valeur plus faible en un temps de l'ordre de τ_η. Pour analyser plus finement quel est le temps qui gouverne la transition, on peut normaliser les courbes par la flatness de l'accélération. Il apparaît alors que l'on peut superposer l'ensemble des courbes sur une courbe maîtresse lorsque l'on utilise un incrément adimensionné par τ_p (figure II.8, droite). Ce résultat reste vrai dans tout le régime pleinement turbulent, et il est aussi possible de superposer les courbes obtenues soit en changeant la taille des particules, soit en changeant le nombre de Reynolds Re_λ.

Du point de vue de la dynamique des particules, le temps τ_p joue donc un rôle analogue à celui joué par τ_η pour les traceurs. Il doit donc être possible d'adapter la description multifractale de la dynamique des traceurs [15] au cas des statistiques lagrangiennes des particules matérielles.

II.4.2 Modélisation numérique du mouvement des particules matérielles : le modèle de Faxen

Bien que le modèle des particules ponctuelles tienne compte de la taille des particules au travers du temps de réponse $\tau_p = r_p^2/(3\beta\nu)$, la comparaison avec les données expérimentales a permis de montrer que celui-ci était incapable de rendre compte de l'influence de l'extension spatiale des particules sur leur dynamique. Ceci provient de la nature même de l'équation du mouvement des particules

$$\frac{\mathrm{d}\mathbf{v}}{\mathrm{d}t} = \beta\frac{D\mathbf{u}}{Dt} + \frac{1}{\tau_p}(\mathbf{u}-\mathbf{v}) \tag{II.5}$$

pour laquelle les forces de masse ajoutée et de traînée sont calculées uniquement en tenant compte de l'accélération $\frac{D\mathbf{u}}{Dt}$ et la vitesse $\mathbf{u}$ au centre de masse de la particule. Ainsi, bien qu'une particule puisse avoir un diamètre $D = 2r_p$ plus grand que η, elle peut répondre aux fluctuations de la vitesse et de l'accélération du fluide à toutes les échelles. Pour tenir compte de l'extension spatiale des particules, nous avons donc incorporé les corrections de faxen, qui permettent de tenir compte de la non uniformité de l'écoulement à l'échelle de la particule, et dont Gatignol a montré [22] que la force de traînée s'obtient par moyenne sur la surface $\mathcal{S} = 4\pi r_p^2$ de la particule, tandis que le terme de masse ajouté doit être moyenné sur le volume $\mathcal{V} = 4\pi r_p^3/3$ de la sphère. L'équation du mouvement s'écrit alors :

$$\frac{\mathrm{d}\mathbf{v}}{\mathrm{d}t} = \beta\left\langle\frac{D\mathbf{u}}{Dt}\right\rangle_{\mathcal{V}} + \frac{1}{\tau_p}(\langle\mathbf{u}\rangle_{\mathcal{S}} - \mathbf{v}) \tag{II.6}$$

Pour des raisons d'efficacité numérique, et puisque les DNS de turbulence homogène et isotrope utilisent des codes pseudo-spectraux, nous avons choisi d'implémenter les moyennes en utilisant un noyau gaussien d'extension σ qui s'écrit dans l'espace de Fourier $\tilde{G}_\sigma = \exp(-\sigma\mathbf{k}^2/2)$, ce qui correspond à une particule de taille $\sigma = r_p/\sqrt{5}$. E. Calzavarini et E. Lévêque ont alors modifié leurs codes de DNS simulant la dynamique des particules ponctuelles [11], ma contribution (en dehors de l'analyse des données) étant centrée principalement sur l'écriture d'un code matlab simulant le modèle de Faxen dans des cas laminaires, ce qui aura permis de faire un benchmark et un déboggage rapide et efficace des nombreuses modifications des deux codes DNS.

Les deux séries de données obtenues pour une turbulence homogène et isotrope à $Re_\lambda = 75$ et $Re_\lambda = 180$ pour des tailles $D/\eta \in [2, 30]$ ont été comparées aux données expérimentales de Voth et al. ([50], $Re_\lambda = 970$) et Qureshi et al. [42], $Re_\lambda = 160$) concernant la variance de l'accélération. Nous avons observé que la prise en compte de l'extension spatiale de la particule permet de simuler de manière beaucoup plus réaliste la dynamique des particules matérielles. En particulier, on observe bien la décroissance de la variance de l'accélération (figure II.9(a)), l'accord devenant même relativement bon lorsque l'on normalise la variance par la valeur mesurée pour des traceurs (en inset). Par ailleurs, lorsque l'on augmente le rapport D/η, on observe une augmentation du temps de corrélation proche des mesures en soufflerie (figure II.9(b)), valeurs qui sont beaucoup plus faibles que celles

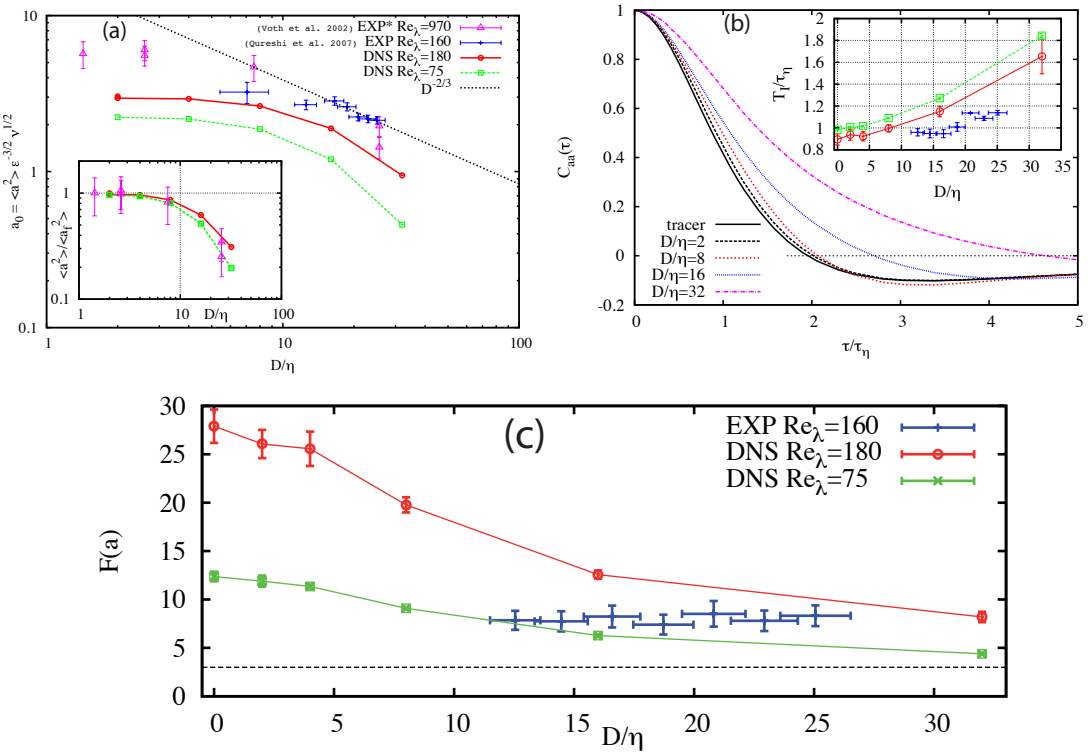

Fig. II.9: (a) Variance de l'accélération normalisée par $\epsilon^{3/2}\nu^{-1/2}$ en fonction de D/η pour le modèle de Faxen et les données des expériences de Qureshi al. et Voth et al.. (b) Fonction d'autocorrélation de l'accélération pour différentes tailles de particules utilisant le modèle de faxen. Inset : temps de corrélation pour des particules Faxen et les données de Qureshi et al.. (c) Evolution de la flatness de l'accélération des particules Faxen et les données de Qureshi et al.. Les courbes sont issues de la référence [11].

observées dans l'écoulement de von Kármán [47]. Concernant l'intermittence, les flatness d'accélération observées sont du même ordre de grandeur que celles observée par Qureshi et al. dans la même gamme de paramètres (D/η, Re_λ), toutefois le modèle de Faxen prévoit une diminution de l'intermittence lorsqu'on augmente le rapport D/η, ce qui n'est pas observé pour les données de soufflerie dans la gamme $D/\eta \in [10,\ 25]$ (figure II.9(c)). Les valeurs de flatness obtenues en soufflerie étant un peu faible en comparaison de ce qui est attendu pour des traceurs à $Re_\lambda = 160$, nous devons suspecter que les mesures ont été faites au delà de la transition pour la flatness.

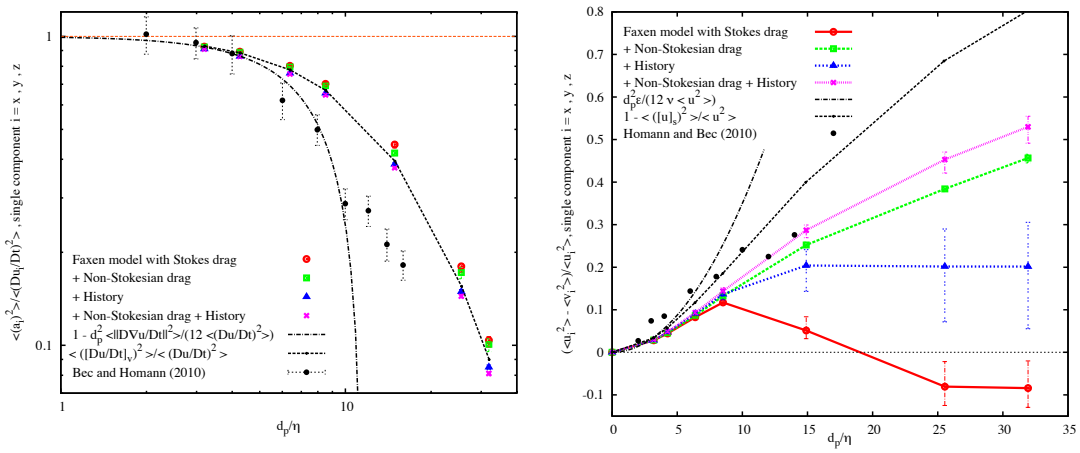

Fig. II.10: Gauche : Variance de l'accélération normalisée en fonction de D/η pour le modèle de Faxen modifié et les simulations directes de [26]. Droite : Défaut d'énergie cinétique des particules en fonction de D/η pour le modèle de Faxen modifié et les simulations directes de [26]. Les figures sont tirées de la référence [12].

Amélioration du modèle de Faxen : Dès lors que la taille des particules devient supérieure à quelques fois η, le terme de traînée dans le modèle de Faxen devient négligeable en comparaison du terme de masse ajoutée. Ce modèle prévoit donc que toute particule assez grosse possède une accélération $\mathbf{a} \sim \beta \langle D\mathbf{u}/Dt \rangle_{\mathcal{V}}$, ceci bien que le nombre de Reynolds à l'échelle de la particule $Re_p = |\langle \mathbf{u} \rangle_{\mathcal{S}} - \mathbf{v}| D/\nu$ puisse devenir arbitrairement grand. Pour résoudre ce problème, nous avons modifié le modèle de Faxen pour inclure les corrections non linéaires à la traînée de Stokes [12]. Nous avons alors effectué une simulation à très bas nombre de Reynolds ($Re_\lambda = 32$) afin de comparer les résultats obtenus avec la simulation directe de Homann et Bec qui ont étudié la dynamique des particules matérielles en utilisant la méthode de pénalisation [26]. Comme le montre la figure II.10(gauche), l'ajout de termes supplémentaires dans l'équation du mouvement (traînée non linéaire ou force d'histoire) change peu la courbe donnant la variance de l'accélération en fonction de D/η. En revanche, les quantités "grande échelle" comme la valeur rms des composantes de la vitesse (figure II.10(b)) est beaucoup plus sensible aux modifications de l'équation du mouvement. Ceci montre que les effets de traînée ont un effet cumulatif important sur les statistiques

de la vitesse, et sont importants pour simuler avec précision des phénomènes tels que la dispersion des particules. Ceci suggère aussi que pour tester des modèles de transport lagrangien, la comparaison à des données d'accélération n'est pas suffisante mais nécessite plutôt soit des trajectoires longues permettant l'accès aux corrélations de vitesse, soit des données de dispersion de paires de particules.

II.5 Mouvement d'une particule de taille intégrale

Comme nous l'avons vu au travers des sections précédentes, la dynamique des particules matérielles isodenses reste fortement intermittente, leur PDF d'accélération n'approchant pas une forme gaussienne même pour des diamètres $D \gg \eta$. Pour des tailles voisines de l'échelle de dissipation, pour lesquelles les degrés de liberté de rotation et de translation se découplent, la dynamique des particules est dominée par les forces de masse ajoutée et de traînée. Lorsque la taille augmente, l'interaction entre les particules et l'écoulement devient non linéaire et il peut apparaître une force supplémentaire dans une direction perpendiculaire à la vitesse de glissement $\mathbf{v}_{rel} = \mathbf{u} - \mathbf{v}$. Un candidat naturel pour cette nouvelle force peut être une généralisation de force de Magnus $\mathbf{F}_{lift} = C_{lift}\mathbf{v}_{rel} \times \mathbf{\Omega}_p$, qui fait intervenir le vecteur rotation de la particule dans l'écoulement $\mathbf{\Omega}_p$ et a été mise en évidence expérimentalement dans des cas laminaires [16].
Pour étudier le couplage entre la rotation et la translation des particules à haut nombre de Reynolds, il faut effectuer un suivi en 6 dimensions et mesurer à la fois le vecteur rotation de la particule ainsi que sa vitesse (qui permet de calculer son accélération). Si le suivi en translation d'une particule peut être effectué à l'aide de caméras rapides en utilisant les algorithmes de PTV standards, le suivi en orientation demande des développements spécifiques en terme de traitement d'images. La suite de cette section décrit la méthode et les résultats que nous avons obtenus durant la thèse de Robert Zimmermann qui a développé les algorithmes de suivi en orientation pour étudier la dynamique des particules de taille intégrale dans un écoulements de von Kármán à haut nombre de Reynolds.

Suivi en translation et orientation :
Le dispositif expérimental est décrit sur la figure II.11 : il consiste en un montage de PTV utilisant deux caméras rapides (phantom V.12) disposées à 90° l'une de l'autre. A l'aide d'un éclairage utilisant un ensemble de LED, il permet de suivre une particule sphérique de diamètre 18mm dans tout le volume $[20\text{cm}]^3$ d'un écoulement de von Kármán contrarotatif, ce qui permet d'obtenir des trajectoires très longues (plusieurs temps intégraux). La sphère étant en polyamide (de densité 1.14), la densité du fluide est ajustée à celle de la particule en ajoutant du glycérol dans l'eau. Le mélange est donc beaucoup plus visqueux ($\nu_f \sim 8\nu_{eau}$) que pour les mesures ELDV, et le nombre de Reynolds beaucoup moins élevé, de l'ordre de $Re_\lambda = 130$ pour une fréquence de rotation $\Omega = 3\text{Hz}$. Le montage permet donc d'étudier la dynamique d'une particule de ratio $D/\eta \sim 130$ et $D/L \sim 0.6$ dans un régime très turbulent avec une fréquence d'échantillonage $F_s \sim 1.3/\tau_\eta$, nettement suffisante pour résoudre l'accélération de la particule, tout en ayant des images de suffisamment haute

résolution pour pouvoir observer des motifs préalablement peints sur la particule.

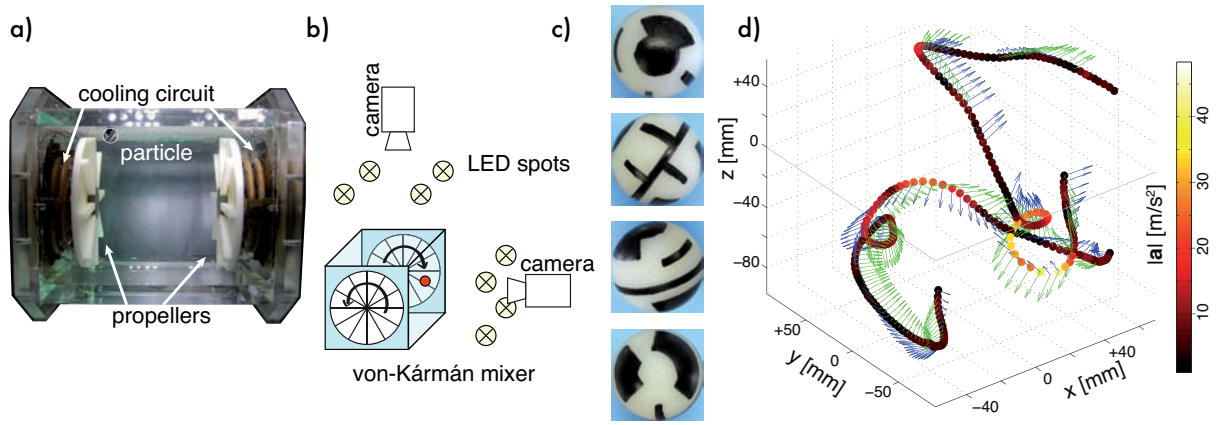

Fig. II.11: (a) Ecoulement de von Kármán. (b) Arrangement des caméras rapides. (c) Vues d'une même particule peintes. (d) Reconstruction d'une trajectoire dans l'espace, la couleur codant l'accélération de la particule et la flèche marquant l'orientation de celle-ci. Figures extraites de la référence [56].

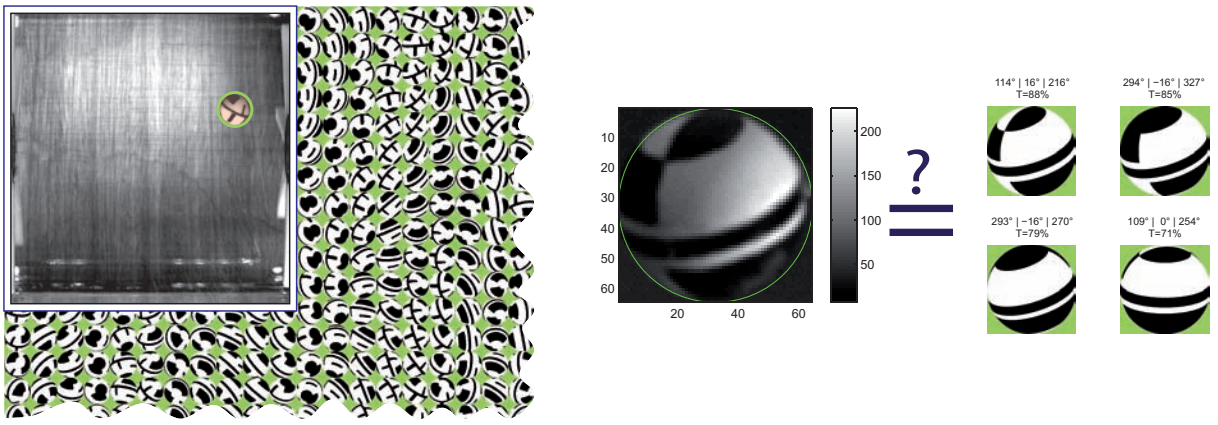

Fig. II.12: Gauche : ensemble des images synthétiques comparées à l'image de la particule. Droite : candidats suffisamment proches pour être retenus comme candidats possibles. Figures extraites de [57].

Le suivi en position utilise une procédure de PTV stéréoscopique standard [50], tandis que l'orientation absolue de la particule est mesurée en peignant une texture à sa surface (figure II.11(c)) et en comparant le motif observé par chaque caméra à des images de synthèse [57]. La mesure de l'orientation se fait en plusieurs étapes : une fois son diamètre mesuré avec précision, l'image de la particule est comparée à un ensemble d'images de synthétiques (figure II.12(a)). La procédure permet d'identifier un ensemble de candidats qui donnent un résultat acceptable (figure II.12(b)). L'ensemble de la série temporelle des trois

angles d'Euler (définissant l'orientation de la sphère) est extraite a posteriori par minimisation globale le long de chaque trajectoire. De cette manière, l'histoire passée et future de la particule est utilisée pour identifier l'évolution la plus probable des angles en cherchant une évolution la plus lisse possible [57]. La figure II.13(a) montre que la série temporelle observée est effectivement relativement lisse, les deux orientations indépendantes obtenues à l'aide des deux caméras pouvant être combinées pour réduire l'erreur sur la mesure.

Dynamique de translation et dynamique de rotation :
La méthode permet d'obtenir un ensemble de trajectoires longues en 6 dimensions donnant la position de la particule et les trois angles d'Euler définissant son orientation. De manière assez surprenante, on observe que la dynamique d'un objet de taille intégrale montre toujours une forte intermittence, comme c'est le cas pour les "petites" particules matérielles :
• Alors que la statistique de vitesse PDF($\mathbf{v}$) est gaussienne, la statistique d'accélération PDF($\mathbf{a}$) reste non gaussienne avec une flatness proche de $F = 7$ (figure II.13(b)). Si la valeur rms de la vitesse de la particule est du même ordre de grandeur que celle du fluide (mesurée dans le même écoulement par ELDV), son accélération $a_{rms} \sim 6\text{m.s}^{-2}$ est en revanche largement plus faible que la valeur $a_f = \sqrt{a_0}\epsilon^{3/4}\nu^{-1/4} \sim 27$ m.s^{-2} calculée pour des traceurs au même nombre de Reynolds ($a_0 \sim 1$ à $Re_\lambda = 130$).

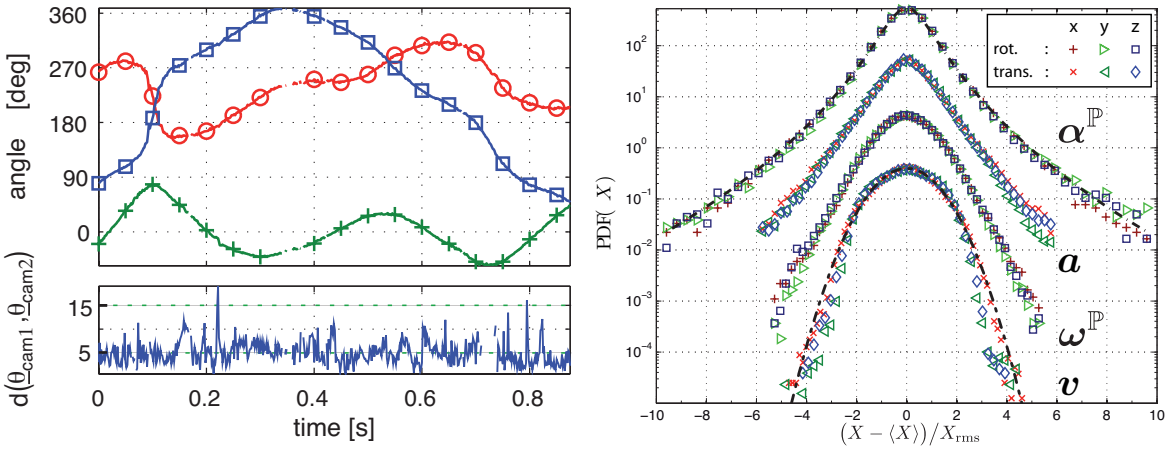

Fig. II.13: Gauche : Evolution des angles d'Euler en fonction du temps et erreur associée entre les mesures des deux caméras. Figure extraite de [57]. Droite : PDF de vitesse, de vitesse angulaire, d'accélération et d'accélération angulaire de la particule. Figure extraite de [56].

• La vitesse et l'accélération de rotation de la particule sont aussi des quantités qui fluctuent autour d'une moyenne nulle, sans montrer de direction privilégiée dans le repère du laboratoire. De manière analogue avec les statistiques du mouvement de translation, nous avons pu observer que la dynamique de rotation est, elle-aussi, intermittente. La PDF des taux de rotation est légèrement non gaussienne ($F \sim 4$) avec une PDF d'accélération angulaire nettement plus plate (figure II.13(b)). Ce résultat surprenant met en défaut la vision

naïve qui suppose que le couple exercé par l'écoulement sur la particule provient de petits tourbillons dont les contributions incohérentes se somment pour donner des fluctuations gaussiennes. Il faudra sans doute s'intéresser à l'écoulement autour de la particule pour avoir des informations concernant l'influence des structures cohérentes sur la dynamique de la particule.

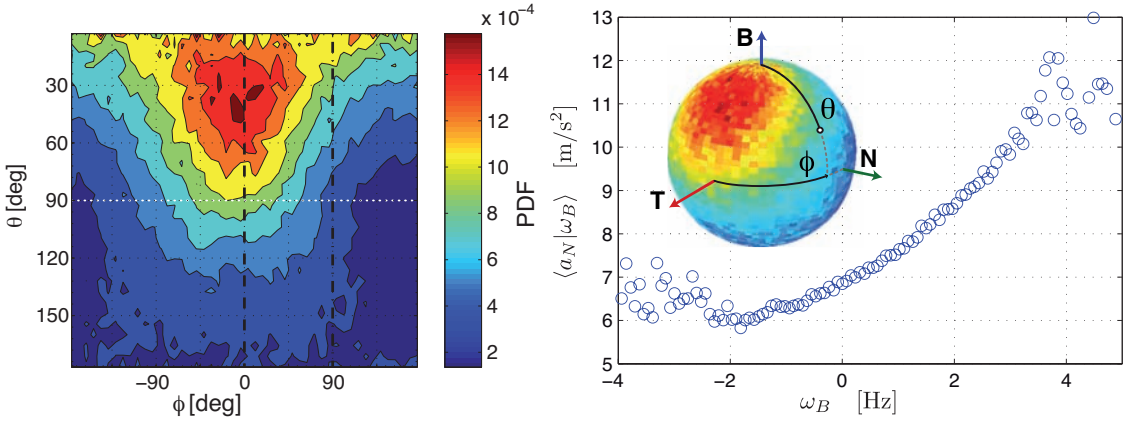

Fig. II.14: Gauche : alignement de la vitesse angulaire Ω_p dans le repère de Frenet. Droite : accélération normale conditionnée à la valeur de ω_B. Figures extraites de [56].

Couplage Rotation-Translation :
Pour étudier le couplage entre rotation et translation, nous avons projeté le vecteur $\mathbf{\Omega}_p$ dans le trièdre de Frenet $(\mathbf{T}, \mathbf{N}, \mathbf{B})$ que l'on définit à partir de la vitesse et de l'accélération de translation de la particule. Nous avons alors observé que, contrairement aux observations dans le référentiel du laboratoire, le vecteur rotation $\mathbf{\Omega}_p$ s'aligne préférentiellement avec dans le plan $(\mathbf{T}, \mathbf{B})$ avec une probabilité maximale à 45° du vecteur $\mathbf{B}$ (figure II.14). Cet alignement est remarquable puisqu'il est compatible avec une force de lift $\mathbf{F}_{lift} \propto \mathbf{v}_p \times \mathbf{\Omega}_p$ donnant une contribution selon le vecteur $\mathbf{N}$. Nous avons pu confirmer la présence de cette force de lift en montrant que l'accélération normale $a_N = \mathbf{a} \cdot \mathbf{N}$ décrit une courbe en fonction de $\omega_B = \mathbf{\Omega}_P \cdot \mathbf{B}$ lorsqu'elle est conditionnée à la valeur de ω_B (figure II.14, droite). Se pose la question de l'origine de cette force de couplage qui pourrait être due à la présence d'un cisaillement à grande échelle dans l'écoulement de von Kármán, et son évolution avec le diamètre des particules et le nombre de Reynolds. Pour répondre à cette question, R. Zimmermann a effectué des mesures de rotation pour différents diamètres et différents nombres de Reynolds. Ces mesures sont en cours d'analyse.

II.6 Mesures d'accélération lagrangienne par une particule instrumentée

Lorsque l'on fait une mesure lagrangienne dans un écoulement, la durée des trajectoire est limitée par la taille nécessairement finie du volume de mesure. Par ailleurs lorsque l'on utilise des techniques telles que la PTV ou les techniques Doppler, on ne peut mesurer que des quantités cinématiques (vitesse, accélération, vorticité, ...) alors que des quantités scalaires telles que la salinité ou la température peuvent être intéressantes pour des problèmes reliés au mélange. Pour obtenir des trajectoires longues, on peut alors imaginer utiliser des particules instrumentées qui vont mesurer des grandeurs locales liées à l'écoulement (ou au fluide) pour les transmettre en temps réel par radio-fréquence à un opérateur pour stockage et traitement des données. De telles particules ont tout d'abord été développées pour mesurer la température vue par une particule de diamètre 18 mm en mouvement dans une cellule de convection de Rayleigh-Bénard [21, 44]. Combinée à un suivi de la particule par PTV, cette technique a notamment permis l'étude du flux local de chaleur $\langle v'T' \rangle$ (v' et T' sont les fluctuations lagrangiennes de vitesse et de température) ou encore de l'influence des plumes thermiques dans le transport de chaleur. Plus récemment, le concept a été étendu aux mesures d'accélération lagrangienne, tout d'abord par Yoann Gasteuil [20], puis par la société smartINST [2] avec notamment pour but le développement d'instruments de mesure permettant une caractérisation *in situ* des mélangeurs industriels. Ce sont ces nouvelles particules mesurant l'accélération que nous avons testées dans le cadre de la thèse de Robert Zimmermann. Cette activité est naturellement fortement liée avec mes activités industrielles dans le cadre du projet PATVAX (chapitre suivant).

Fig. II.15: Gauche : particule instrumentée de diamètre 24mm fabriquée par smartINST qui contient le capteur, une carte d'acquisition et un système d'émission RF. Droite : smartCENTER décodant les signaux émis par la particules.

Description la mesure d'accélération embarquée :
La technique est relativement simple dans son principe, la particule est une coquille sphé-

2. La société smartINST est une startup issue du laboratoire de physique, développant des mesures lagrangiennes par particules instrumentées, qui actuellement hébergée à l'ENS Lyon.

rique de diamètre 24 mm qui embarque un circuit autonome d'accélération 3-axes, une pile bouton, un digitaliseur 12 bits, et un système de transmission Radio-Fréquence (figure II.15). Ce dernier multiplexe les mesures digitalisées et les transmet à une centrale d'acquisition (le smartCENTER) qui décode et stocke les signaux d'accélération pendant que la particule est librement advectée par l'écoulement. La particule, dont la densité est ajustable dans la gamme $[0.8 - 1.4]$ g/cm^3, peut donc être utilisée dans les milieux acqueux et donne accès aux signaux d'accélération mesurés dans une gamme ± 3 g avec une fréquence d'échantillonnage $f_s = 316$ Hz. Les durées de trajectoires sont typiquement de l'ordre de quelques heures, et dépendent de la puissance d'émission du transmetteur RF.

Mesures dans un référentiel en rotation :
Comme nous l'avons vu dans la section précédente, des sphères en mouvement à haut nombre de Reynolds ont non seulement une dynamique de translation compliquée, mais aussi une dynamique de rotation intermittente avec un vecteur de rotation $\mathbf{\Omega}_p$ dont l'amplitude est d'environ 10% de la fréquence de rotation Ω des disques. La rotation de la particule pose deux types de problèmes :
• La particule tourne donc sur elle-même projetant ainsi aléatoirement le vecteur gravité $\mathbf{g}$ sur les trois axes de l'accéléromètre. Notant $\mathbf{a}_{\text{trans}} = \mathrm{d}^{\mathbf{2}}\mathbf{X}/\mathrm{d}\mathbf{t}^{\mathbf{2}}$ l'accélération de translation de la sphère (que l'on veut mesurer), et $\underline{\underline{\mathbf{R}}}(t)$ la matrice de rotation décrivant l'orientation instantanée de la particule par rapport au repère du laboratoire, le signal instantané $\mathbf{a}_{\text{SP}}(\mathbf{t})$ observé par la particule est $\mathbf{a}_{\text{SP}}(\mathbf{t}) = \underline{\underline{\mathbf{R}}}(\mathbf{t})(\mathbf{a}_{\text{trans}}(\mathbf{t}) + \mathbf{g})$. Pour exploiter les signaux, il faut donc un moyen pour séparer les contributions de la gravité, de la rotation, et de la translation.
• Si de plus le capteur est décentré d'un vecteur $\mathbf{r}$ par rapport au centre de masse de la particule, il se rajoute en plus une contribution centrifuge $\mathbf{a}_{\text{c}} = \mathbf{\Omega}_p \times (\mathbf{\Omega}_p \times \mathbf{r}) + \mathbf{r} \times \mathrm{d}\mathbf{\Omega}_p/\mathrm{d}t$ à l'accélération.

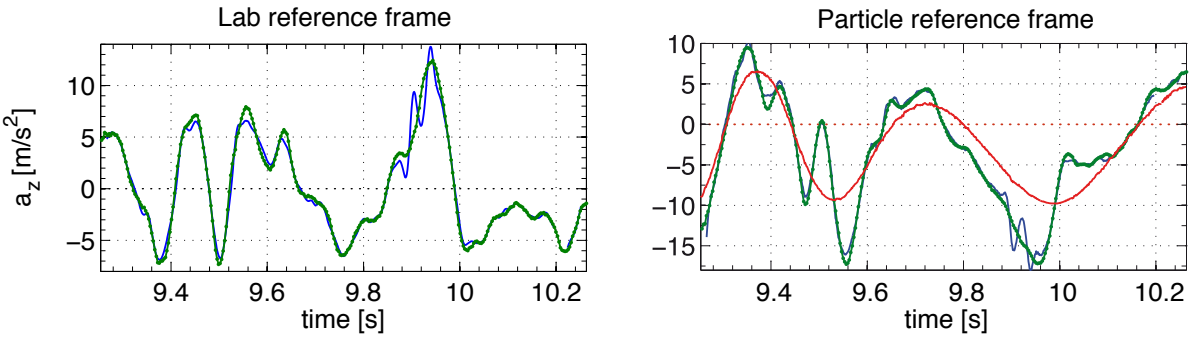

Fig. II.16: Gauche : accélération a_z mesurée dans le repère du laboratoire à partir des caméras rapides ($-$, bleu) et de la particule instrumentée ($\bullet$, vert). Les orientations absolues de la particule (et du capteur 3-axes) ont été utilisées pour exprimer la mesure dans le repère du laboratoire, et la contribution de gravité soustraite. Droite : même mesure dans le repère de la particule. La courbe rouge marque la contribution dominante de la gravité obtenue à partir de l'orientation instantanée de la particule. Figures extraites de [53].

Du fait de la combinaison des effets de rotation et de translation, les signaux bruts délivrés par la particule sont très complexes. Pour valider la technique nous avons donc mis en oeuvre un suivi en orientation-translation de la particule instrumentée préalablement calibrée et peinte, puis filmé la particule pendant l'acquisition des signaux à l'aide du smartCENTER [53]. Les caméras donnant accès à $\mathbf{a}_{\text{trans}}$ et à l'orientation de la particule (dont on déduit $\mathbf{\Omega}_p$), on peut alors projeter le vecteur $\mathbf{a}_{\text{trans}} + \mathbf{g} + \mathbf{a}_{\text{c}}$ dans le repère du capteur pour une comparaison directe avec $\mathbf{a}_{\text{SP}}(\mathbf{t})$ (figure II.16). Cette comparaison a permis d'observer le très bon accord entre les signaux reconstruits et le signal directement mesuré par la particule (figure II.16, gauche). Elle a aussi permis d'observer que du fait des échelles mises en jeu (le décentrage est faible), on peut négliger la contribution centrifuge $\mathbf{a}_{\text{c}}$ pour calculer les statistiques d'accélération [53]. En revanche, l'ordre de grandeur de l'accélération a_{trans} n'étant pas très grand devant l'accélération de la pesanteur g, les signaux instantanés sont fortement influencés par la gravité lorsque mesurés dans le référentiel de la particule (figure II.16, droite).

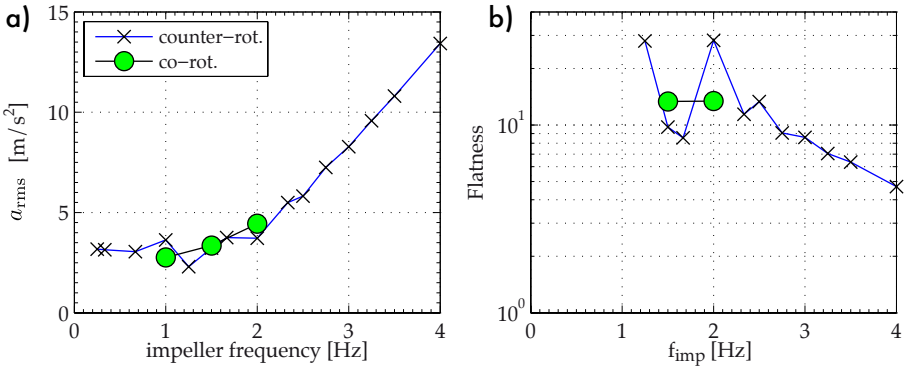

Fig. II.17: Gauche : variance de l'accélération en fonction de la fréquence de rotation des disques. Droite : flatness de l'accélération en fonction de la vitesse de rotation des disques. La courbe décroît du fait de la saturation du capteur. Figures extraites de [55].

Mesure des moments de $\mathbf{a_{trans}}$:
Pour extraire les informations relatives à $\mathbf{a}_{\text{trans}} = \mathrm{d}^{\mathbf{2}}\mathbf{X}/\mathrm{d}\mathbf{t}^{\mathbf{2}}$, il faut donc s'affranchir des effets de la gravité. Ceci peut être fait si l'on suppose que les moments impaires $\mathbf{a}_{\text{trans}}$ sont nuls, résultat connu pour des particules matérielles. Les moments pairs de l'accélération, qui ne dépendent pas de l'orientation de la particule, prennent alors une forme simple et l'on a : $\langle \mathbf{a}_{\text{SP}}^{\mathbf{2}} \rangle \simeq \mathbf{g}^{\mathbf{2}} + \langle \mathbf{a}_{\text{trans}}^{\mathbf{2}} \rangle$ pour la variance d'accélération et $\langle \|\mathbf{a}_{\text{SP}}\|^{\mathbf{4}} \rangle \simeq \mathbf{g}^{\mathbf{4}} + \langle \|\mathbf{a}_{\text{trans}}\|^{\mathbf{2}} \rangle + \mathbf{10g}^{\mathbf{2}} \langle \mathbf{a}_{\text{trans}}^{\mathbf{2}} \rangle / \mathbf{3}$ pour le moment d'ordre 4 [55].
On peut donc obtenir les deux moments les plus importants de la PDF d'accélération à partir des signaux de la particule instrumentée sans avoir besoin de la filmer pour connaître son orientation. On retrouve alors que la variance de l'accélération est proportionnelle au carré de la fréquence de rotation des disques avec une Flatness proche de 10 (figure II.17). Cette mesure permet d'ailleurs d'observer un résultat étrange concernant la dynamique des particules de taille intégrale : la variance et la flatness de l'accélération sont quasiment identiques que ce soit pour un écoulement contra-rotatif et un écoulement co-rotatif. Ce résultat, qui serait totalement différent pour des traceurs, est cohérent avec une dynamique des grands objets influencée en majorité par les grandes échelles de l'écoulement, les grandes structures de l'écoulement obtenu en co-rotation ou contra-rotation possédant les mêmes ingrédients (rotation et recirculation).

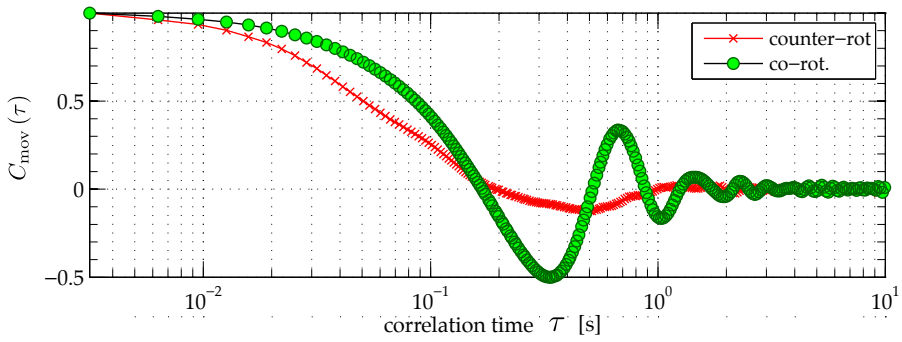

Fig. II.18: Fonction d'autocorrélation de $\|\mathbf{a}_{SP}(\mathbf{t})^2\| - \langle\|\mathbf{a}_{SP}(\mathbf{t})^2\|\rangle$ en fonction de τ (en secondes). On distingue une oscillation dans le cas co-rotatif. Figure extraite de [55].

Corrélations de $\mathbf{a}_{trans}$:
De la même manière que les moments de l'accélération $\mathbf{a}_{trans}$ renseignent sur l'amplitude des fluctuations dans le mélangeur, les corrélations de la l'accélération $C_{aa} = \langle \mathbf{a}_{trans}(\mathbf{t}) \cdot \mathbf{a}_{trans}(\mathbf{t}+\tau)\rangle$ peuvent apporter des informations sur la persistance des structures. Comme il est impossible de calculer directement cette quantité, nous avons recherché une définition des corrélations ne dépendant pas de la rotation de la particule. La corrélation du module de l'accélération possède cette propriété et s'écrit :

$$\begin{aligned}&\langle\|\mathbf{a}_{SP}(\mathbf{t})\|^2\|\mathbf{a}_{SP}(\mathbf{t}+\tau)\|^2\rangle \\ &\simeq \langle\|\mathbf{a}_{trans}(\mathbf{t})\|^2\|\mathbf{a}_{trans}(\mathbf{t}+\tau)\|^2\rangle + \mathbf{g^4} + \mathbf{2g^2}\langle\mathbf{a}_{trans}^2\rangle + \mathbf{4g^2}\langle\mathbf{a_z}(\mathbf{t})\mathbf{a_z}(\mathbf{t}+\tau)\rangle\end{aligned} \tag{II.7}$$

Que l'on calcule en pratique sous la forme de la corrélation de la partie fluctuante de $\|\mathbf{a}_{SP}\|^2$ pour obtenir les courbes de la figure II.18. Lorsqu'on utilise cet estimateur des corrélation de l'accélération, on observe alors bien une différence de comportement de la bille en fonction du mode de forçage, la configuration de co-rotation des disques montrant des oscillations et une cohérence plus grande.

Suite des travaux :
Nous avons montré la faisabilité de la mesure d'accélération grâce à la particule instrumentée, et défini des estimateurs des moments de l'accélération et de ses corrélations qui sont insensibles à la rotation de la particule sur elle-même. Ce travail trouvera naturellement son aboutissement dans l'utilisation de ces particules dans les mélangeurs industriels (partie suivante). D'un point de vue plus fondamental, une partie de la thèse de N. Machicoane est consacrée à la dynamique lente des particules de taille intégrale dans les mélangeurs avec à l'esprit deux questions d'importance :
- ces particules visitent-elles l'écoulement de manière homogène ?
- quel est l'impact de leur densité sur leur dynamique ?

III.Activités Industrielles

Depuis 2010 environ 30% de mon activité de recherche est consacrée à une collaboration industrielle financée par le ministère de l'industrie au travers du Fond Unitaire Interministériel (FUI). Le projet PATVAX est un projet collaboratif à but industriel entre les partenaires académiques LP-ENS Lyon et CEA LETI, les sociétés d'instrumentation Cyberstar et smartINST, ainsi que les deux industriels de la pharmacie Sanofi-Pasteur et Merial. L'objectif de cette collaboration est le développement de systèmes de mesure permettant de suivre en ligne et en temps réel le procédé d'adjuvantation des vaccins dans des cuves de formulation.
Il s'agit d'un projet aval de 3 ans suivant assez strictement un calendrier préalablement établi dans un document de suivi contractuel décrivant le partage des tâches des différents partenaires. L'ensemble des partenaires se réunit fréquemment (une fois par mois) pour des points d'avancement du projet soit sous la forme de réunions scientifiques, soit sous la forme d'un comité de pilotage (dont je suis membre) chargé d'arbitrer les réorientations du projet et/ou de gérer les éventuels litiges entre partenaires. Ce projet fait par ailleurs l'objet d'une revue annuelle par le ministère (scientifique et financière), ce qui m'a conduit à m'impliquer en profondeur dans ses aspects administratifs en plus de ses aspects scientifiques. Il s'agit donc d'une activité de recherche dans un cadre un peu plus rigide qu'habituellement, mais qui trouve une compensation de taille dans les moyens financiers importants (390 k€pour mes seules activités) qui donnent une grande souplesse pour réaliser le projet.

III.1 Enjeux du projet PATVAX

L'adjuvantation est l'étape finale de formulation d'un vaccin qui combine les antigènes avec les excipients et adjuvants requis lorsque les protéines et/ou virus ont été cultivés et purifiés. Une vision schématique de ce procédé consiste en l'adsorption, dans une cuve agitée, d'un ensemble de protéines sur une suspension de microparticules d'alumine dans une solution ionique complexe comprenant divers sels, acides, et bases. L'adsorption met en jeu des interactions électrostatiques qui sont modulées par la composition du mélange solvatant les particules. Les paramètres clefs sont donc la composition des particules, leur granulométrie, la température, le pH et la force ionique de la solution. L'agitation de la cuve est par ailleurs un paramètre critique puisqu'il faut assurer une bonne dispersion et homogénéité de la suspension (plus dense que l'eau) tout en évitant de changer la

granulométrie du gel avec un cisaillement trop fort [1].

Dans ce contexte, le projet PATVAX est une application du concept PAT (Process Analytical Technology) initié par les autorités de santé américaine (FDA) et européenne (EMEA) qui a pour objectif de développer le concept de qualité de conception par opposition au concept de qualité par le contrôle actuellement en vigueur. En effet dans les procédés actuellement mis en oeuvre, les vaccins sont fabriqués suivant un protocole défini avec un contrôle limité durant la fabrication, puisque seuls quelques paramètres (température, pH, vitesse d'agitation) sont consignés par un opérateur dans un document de suivi. Après les différentes étapes de formulation, dont la durée totale peut atteindre plusieurs jours, les vaccins sont conditionnés puis stockés dans l'attente de tests in vivo libératoires, préalable obligatoire à leur mise sur le marché. L'approche PAT est donc un changement de paradigme puisqu'elle vise à s'assurer que le procédé est resté conforme au procédé de référence durant toutes les étapes de la fabrication. Si cette approche est plus complexe à mettre en oeuvre, elle revêt de multiples intérêts puisqu'elle doit permettre à la fois d'assurer un meilleur contrôle qualité tout en assurant un gain de temps par une détection en amont des lots potentiellement défectueux.

Pour effectuer un suivi en temps réel de l'adjuvantation, l'ensemble des partenaires s'est fixé comme objectif de réaliser deux particules instrumentées, fabriquées par la société smartINST [2], qui sont librement advectées dans le mélangeur et transmettent par radiofréquence des informations soit sur l'adsorption des protéines sur le gel d'alumine, soit sur l'environnement ionique de celui-ci (homogénéité, conductivité, force ionique ...).

III.2 Suivi d'adsorption de protéines par spectroscopie d'impédance

La façon la plus commune de modéliser la fabrication d'un vaccin est d'étudier l'adsorption de la protéine BSA (Bovine Serum Albumin) sur des particules d'alumine (de la boehmite, AlOOH) en suspension dans un électrolyte avec une concentration $c_{Al} \sim 1\text{g.L}^{-1}$. En fonction de la composition de l'électrolyte, qui contient à la fois du sel en concentration $C \sim 10$ g.L^{-1} et un tampon à base de la molécule TRIS [3] ou d'ions phosphates PO_4^{3-}, on module la capacité de la protéine BSA à se fixer sur les particules de boehmite. En particulier dans le cas d'un tampon TRIS, il est possible d'adsorber une grande quantité de BSA (environ 2g de BSA pour un gramme d'alumine) alors que l'adsorption est totalement

1. Les cuves utilisées, cylindres de volume $V \sim 200$ litres, sont faiblement agitées à l'aide d'une petite hélice de fond de cuve. L'écoulement est donc faiblement turbulent et dominé par la rotation, la vitesse de "juste agitation" étant ajustée (en fonction de la hauteur du liquide) de façon a éviter la formation d'un vortex à la surface libre de l'écoulement.

2. La société smartINST est une startup issue du laboratoire de physique, développant des mesures lagrangiennes par particules instrumentées, actuellement hébergée à l'ENS Lyon.

3. Tris(hydroxymethyl)aminomethane, Sigma Aldrich

inhibée en présence d'une forte concentration d'ions phosphates. Bien que ce système soit relativement simple, il est très difficile de mesurer la quantité de protéine adsorbée sur le gel de manière directe, et la technique standard consiste en un dosage de la quantité de protéine restée libre en solution. Pour ce dosage, il faut :
- laisser la suspension d'alumine sédimenter pour prélever un échantillon de liquide surnageant.
- Utiliser un kit de dosage colorimétrique en retour [4] qui permet de déterminer la quantité de protéine présente.

Plutôt que d'utiliser une réaction chimique pour détecter la présence des protéines, j'ai étudié la possibilité de mesurer les changements fins de constante diélectrique de la suspension lorsque des protéines sont adsorbées sur les particules ou non. Pour ce faire j'ai utilisé la spectroscopie diélectrique qui permet de mesurer la permittivité diélectrique ϵ_r d'un échantillon placé entre deux électrodes qui imposent une différence de potentiel sinusoïdal $V(t) = V_0 \cos(2\pi f t)$ à l'échantillon. Utilisant une sonde de conductimétrie commerciale plongée dans la solution, branchée sur un analyseur d'impédance [5]), on obtient l'impédance complexe $Z(f)$ de la cellule qui dépend à la fois des caractéristiques géométriques de celle-ci, mais aussi des propriétés diélectriques de l'échantillon. Dans une vision simple, l'impédance lorsqu'elle est représentée sous la forme d'un circuit RC série : $Z(f) = R + 1/(jC2\pi f)$ permet d'obtenir la conductivité de la solution (σ) par la relation $R = K/\sigma$ (K est la constante de cellule) tandis que la permittivité relative ϵ_r est proportionnelle à C. Dans une vision plus réaliste qui est celle prévalant pour les électrolytes, R et C ne dépendent pas seulement des caractéristiques de la solution, mais aussi de la répartition des ions au voisinage des électrodes. Ce phénomène de polarisation d'électrodes est dominant aux basses fréquences, et l'on mesure en fait l'écrantage des électrodes dû à la présence d'espèces chargées au voisinage de celles-ci. C'est en imaginant possible de mesurer l'interaction entre les particules d'alumine et les électrodes nous avons mis en oeuvre cette technique.

Adsorption en tampons Tris et Phosphate : La spectroscopie diélectrique a été utilisée pour étudier l'adsorption de la protéine BSA sur différents lots de gel mis à disposition par Sanofi-Pasteur que nous avons dilués soit dans un tampon Tris, soit dans un tampon Phosphate. Différentes proportions gel/BSA ont été testées depuis un échantillon de gel pur dilué dans le tampon (noté T0 pour Tris et P0 pour Phosphate), jusqu'à des échantillons pour lesquels le rapport des concentrations massiques est $C_{BSA}/C_{Al} = 0.75$ (noté T750 et P750 respectivement). Le résultat de ces mesures est montré sur la figure III.1, qui permet d'apprécier les variations de capacité de la cellule, non seulement lorsque l'on change la fréquence de l'excitation, mais aussi lorsque l'on ajoute la protéine BSA dans une solution contenant le gel. Ces études ont permis d'observer un résultat inattendu : dans le cas

4. QuantiPrO BCA Assay Kit, Sigma Aldrich

5. Alpha Dielectric Analyser, Novocontrol. L'auteur remercie M. Peyrard et L. Bellon pour le prêt longue durée de cet appareil.

du tampon Tris pour lequel la protéine BSA s'adsorbe sur le gel, le changement dans les courbes de capacité $C(f)$ est inférieur à 1% (figure III.1(a)). En revanche, dans le cas de l'ajout de protéine BSA en tampon phosphate, pour laquelle la protéine reste en solution, le changement relatif de capacité est de l'ordre de 25%, ce qui est extrêmement important (figure III.1 (b)).

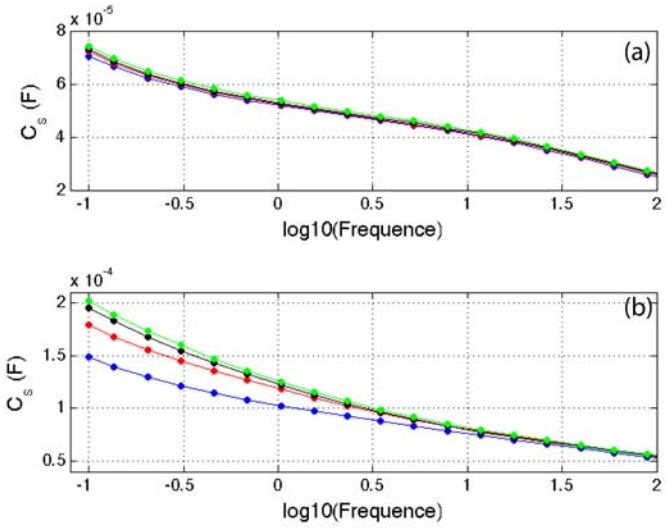

Fig. III.1: Evolution de capacité de la cellule $C(f)$, en fonction de la fréquence dans la gamme $[0.1, 100]$ Hz dans les cas : (a) d'une adsorption totale sur une suspension en tampon Tris, (b) d'une adsorption inhibée sur une suspension en tampon phosphate. Bleu (absence de BSA, aucune protéine), rouge (0.1g de BSA pour 1g d'alumine), noir (0.25g de BSA pour 1g d'alumine), vert (0.5g de BSA pour 1g d'alumine)

Pour comprendre l'origine de ces différences, et pour savoir si les variations observées sont caractéristiques de la présence de protéine libre en solution, nous avons étudié la réponse diélectrique lors de l'ajout de protéine BSA dans différents tampons en l'absence de l'alumine. Partant d'une solution contenant initialement une quantité donnée de BSA dissoute dans le tampon, nous avons ajouté à l'échantillon une quantité donnée du même tampon pour diluer la concentration en protéine BSA sans pour autant diluer le tampon. Cette étude a permis d'observer que c'est bien l'ajout de protéine libre en solution qui provoque la variation de capacité observée. Pour déterminer si ce comportement était générique, nous avons répété ces expériences non seulement dans le tampon Phosphate, mais

aussi dans des solutions salines de différentes salinités.

L'ensemble de ces études ont confirmé ce résultat : quel que soit l'environnement ionique envisagé, on détecte la présence de protéines non adsorbées au travers de cette variation de capacité. Cependant la mesure possède le défaut majeur d'être extrêmement lente puisqu'une mesure précise à fréquence 0.1 Hz demande entre 10 et 100 secondes par point de mesure. Dans l'optique de développer un système de mesure, si cela ne pose pas de problème pour un appareil servant à des mesures statiques (telles que celles présentées), ce défaut est rédhibitoire lorsqu'on veut suivre la dynamique du procédé. Sur la base des résultats obtenus, qui montrent par ailleurs que l'impédance de la cellule n'est pas sensible à la présence de protéines au delà d'une fréquence $f \sim 100$ Hz, nous avons décidé de développer une particule instrumentée effectuant des mesures de conductimétrie rapide pour apporter à la fois des renseignements sur le mélange et sur l'environnement ionique du gel d'alumine.

III.3 Mesures de conductimétrie rapide

La façon la plus simple de réaliser un conductimètre consiste à utiliser deux électrodes conductrices plongeant dans la solution étudiée pour mesurer sa résistance à une fréquence donnée, qui est inversement proportionnelle à la conductivité de la solution selon la relation $R = d/\sigma S$ avec d la distance entre les électrodes et S leur surface en contact avec la solution. Cette mesure ne pose donc pas de problème conceptuel et de nombreuses publication rapportent la réalisation de micro-électrodes pour des mesures de mélange scalaire en écoulement turbulent utilisant des ponts de mesure classiques [24]. Toutefois la réalisation d'une électrode de mesure embarquable dans une particule autonome répond à un ensemble de contraintes techniques que l'on ne peut ignorer : la sonde doit être petite pour avoir un temps de réponse suffisamment faible pour effectuer des mesures dans un milieu en mouvement, et doit avoir une impédance facilement mesurable dans la gamme de salinité $c_{\mathrm{NaCl}} \sim [1 - 20]$ g.L^{-1}, qui est la gamme ciblée dans le cahier des charges établi préalablement. Nous avons donc choisi de réaliser des électrodes dont l'impédance est de l'ordre de $Z \sim 1$ kΩ et choisi de réaliser des circuits électroniques avec des composants consommant le moins d'énergie possible afin d'augmenter la "durée de vie" des particules, essentiellement celle de leur batterie.

La réalisation de l'ensemble est le fruit d'un travail en collaboration avec le CEA-LETI et la société smartINST qui s'est concrétisé par la fabrication des puces par gravure d'électrodes de platine sur un wafer de silicium (figure III.2(a,b)). Pris par des contraintes de temps, et ne sachant pas à l'avance quelle allait être la constante de cellule réelle $K = d/S$ des puces, nous avons choisi de réaliser trois types de puces et imaginé 5 circuits électroniques différents permettant de mesurer le module de l'impédance $|Z|$ des puces à 10 kHz et 100kHz.

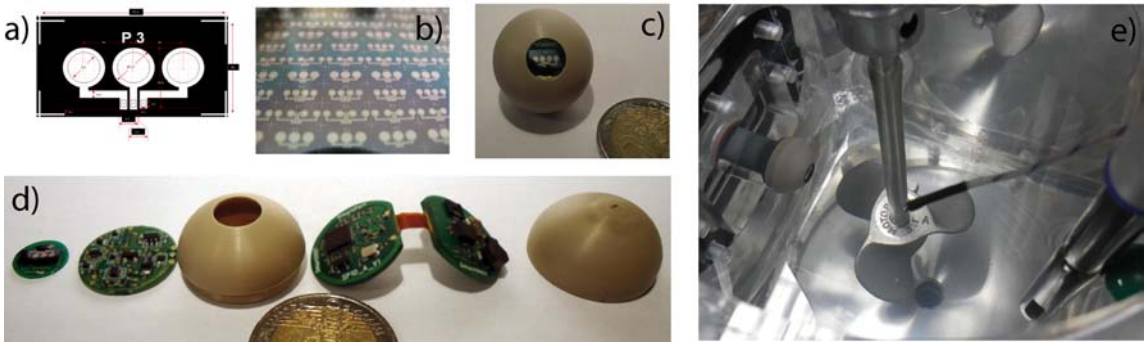

Fig. III.2: a) Design type de l'électrode de conductimétrie. b) électrodes de platine gravées sur wafer de silicium (cliché CEA LETI). c) particule instrumentée réalisée par la société smartINST. d) contenu de la particule avec de gauche à droite (puce de conductimétrie, circuit de mesure d'impédance, capsule supérieure, circuit radio-fréquence, capsule inférieure). e) Sonde fixe (à gauche) et sonde commerciale de conductimétrie (droite) placées dans un mélangeur type de l'industrie pharmaceutique.

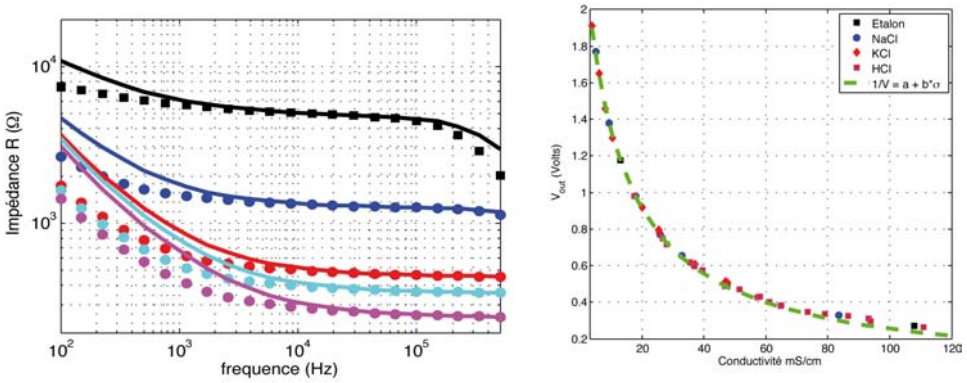

(a) (b)

Fig. III.3: (a) : évolution en fréquence de la résistance R (symboles) et du module de l'impédance $|Z|$ (traits pleins) d'une des puces de conductimétrie pour différentes solutions salines. De haut en bas $c = [2.5,\ 5,\ 10,\ 20,\ 30]$ g.L^{-1}. (b) : tension de sortie du circuit de mesure pour diverses solutions (HCl, NaCl, NaOH, NaCl) de différentes conductivités σ. (symboles) : mesures, (–) ajustement linéaire $V^{-1} = a + b\sigma$.

Choix du couple puce-circuit : une grande partie de mon temps a par la suite été consacré à étudier le comportement des puces et la fiabilité des circuits pour sélectionner le couple le plus performant en vue de l'intégration dans une particule. Comme le montre la figure III.3(a), si la résistance de la cellule varie beaucoup avec la fréquence, elle présente un plateau dans la bande de fréquence $[30 - 100]$ kHz pour laquelle la sonde est purement résistive. La mesure la plus simple de R consiste alors à constituer un pont diviseur de tension avec une résistance R_0 et à mesurer la valeur rms de la tension aux bornes la sonde

lorsque le pont est alimenté par un générateur sinusoïdal $e = e_0 \cos(2\pi f t)$ [6] [7]. La figure III.3(b) montre l'évolution de la tension mesurée en sortie du circuit électronique choisi, dont la tension de sortie s'écrit $V_{rms} = \frac{e_0}{\sqrt{2}} \frac{R}{R + R_0}$, lorsqu'on fait la mesure dans différentes solutions de conductivité variées. Pour chaque solution, la conductivité est mesurée à l'aide d'un conductimètre commercial préalablement calibré à l'aide de solutions étalon de conductivité. Pour toute la gamme de mesure ciblée $\sigma \in [2.5,\ 30]$ mS/cm, la réponse ne dépend pas du type d'ions, mais seulement de la conductivité. Parmi les trois sondes réalisées, notre choix s'est porté sur celle montrant la meilleure linéarité entre $1/V_{rms}$ et la conductivité σ. Pour la sonde de la figure III.2(a) (meilleur choix) la linéarité est de l'ordre de 2% ce qui en fera une sonde de mesure particulièrement aisée à calibrer par un technicien.

Réponse dynamique des sondes : Une fois sélectionné le couple puce-circuit, j'ai cherché à caractériser la performance des sondes en régime dynamique. La détermination d'une fréquence de coupure des sondes n'est pas un problème simple car elle est liée au fait que la sonde n'est pas ponctuelle. Elle est en effet constituée de deux électrodes disques de 1.7 mm de diamètre distants de 2 mm et va donner une mesure de conductivité moyennée sur un volume δV de quelques millimètres de côté. Lors du mélange des constituants, qui se caractérise par des variations spatio-temporelles rapides, c'est donc le lissage spatial associé à la relation entre les échelles de temps et d'espace qui va fixer le temps de réponse de la sonde.
Pour observer jusqu'à quelle fréquence temporelle la sonde permet d'obtenir du signal, j'ai utilisé le dispositif de la figure III.4(a) qui permet de faire des mesures de fluctuation de concentration en injectant, à débit constant à l'aide d'un pousse seringue, une solution concentrée dans un bécher de 1 litre agité à l'aide d'un agitateur magnétique. Puisque à la fois l'injection et l'écoulement sont fortement inhomogènes, les fluctuations de concentration dépendent beaucoup de la distance relative entre l'aiguille servant d'injecteur et la sonde de mesure. Pour éviter, par un mélange trop efficace, que les fluctuations de concentration soient trop atténuées lorsqu'elle sont advectées devant la sonde, l'aiguille est placée à 3 cm de la sonde et injecte directement dans sa direction. Le signal $C(t)$ observé est alors fortement intermittent (figure III.4(b)), avec des pics de concentration très élevés caractéristiques d'un scalaire dans les premières étapes du mélange, et présente une augmentation globale lente $\langle C \rangle(t)$ correspondant à l'ajout de sel dans un volume fermé. La figure montre par ailleurs que lorsque la vitesse d'agitation augmente, les pics de concentration sont atténués, signe d'un mélange plus efficace dans le bécher.
Pour étudier les fluctuations de concentration, les signaux sont stationnarisés en soustrayant l'évolution lente, ce qui permet d'obtenir les densité de probabilité (figure III.4(c))

6. Si cette méthode est moins précise que d'autres ponts de mesures, elle possède comme qualité de pouvoir être réalisée à l'aide de composants actifs consommant très peu. Les microcircuits de détection synchrone consomment malheureusement trop pour être intégrés dans une particule autonome.

7. Deux des circuits intégrés testés, effectivement équivalents à des ponts diviseurs de tension, sont toutefois un peu plus complexes. Ils contiennent entre autre un générateur sinusoïdal régulé en amplitude et fréquence, le pont de mesure, des amplificateurs ainsi que des composants permettant la mesure de la valeur rms d'un signal quelconque.

et les spectres de puissance (figure III.4(d)) des fluctuations $C'(t) = C(t) - \langle C \rangle(t)$ pour les quatre vitesses d'agitation étudiées. Ces figures montrent des caractéristiques typiques de dispersion turbulente à partir d'une source localisée : les PDF sont très asymétriques avec des ailes exponentielles pour les grandes déviations [40, 17] qui se réduisent lorsque la vitesse d'agitation augmente [17]. Parallèlement, les spectres de puissance ne montrent aucune échelle temporelle caractéristique, avec une fréquence de coupure f_c presque proportionnelle à la fréquence de rotation Ω de l'agitateur.
Dans l'optique d'une mesure en environnement de développement ou industriel, pour lesquels les fréquences de rotation dépassent rarement 180 rpm, les mesures montrent que la sonde de mesure développée est capable de capturer correctement les fluctuations de concentration lors du mélange. Contrairement à l'utilisation d'un appareil commercial, qui donne rarement plus d'un point par seconde, la sonde développée permettra d'obtenir des informations non seulement sur l'environnement ionique dans le mélangeur, mais aussi de quantifier l'homogénéité du mélange.
Mesure embarquée : la particule instrumentée a été testée par comparaison aux mesures obtenues par la sonde fixe déjà utilisée d'une part, et à celles obtenues avec un conductimètre commercial délivrant une mesure par seconde. La particule permet de mesurer les trois composantes de l'accélération à l'aide d'un capteur 3-axes (voir section II.6) ainsi que la conductivité de la solution. Contrairement au circuit fixe, qui mesure en permanence la conductivité, la particule n'alimente la puce que lors de la mesure (elle effectue 10 mesures par seconde), enregistre temporairement le résultat dans une mémoire flash et émet un paquet radiofréquence vers le récepteur chaque seconde. Cette procédure permet d'augmenter la durée de fonctionnement de la particule qui peut être utilisée pendant environ 48h de durée de mesure cumulée [8]. Le montage utilisé pour les tests est celui de la figure III.4(e), qui possède les différentes caractéristiques des mélangeurs de sanofi-Pasteur et Merial. Il est régulé en température à l'aide d'une circulation dans le fond de cuve et agité à l'aide d'une hélice située au bout d'un arbre plongeur (figure III.4(e)) mise en mouvement par un moteur asynchrone régulé en vitesse. Le volume totale est d'environ 6 litres, contient des parois métalliques et son moteur rayonne en tournant ce qui permet de tester la robustesse de la mesure dans un environnement bruité. Contrairement aux mesures en bécher, effectuées pour une injection continue, les tests ont été faits lors d'ajouts rapides d'un petit volume de solution concentrée (créneaux de concentration). Pour l'ensemble des mesures, la particule n'est pas rendue iso-dense mais flotte à la surface du mélangeur, électrode vers le bas plongeant dans le liquide. Comme le montre la figure III.4(f), les sondes donnent une information semblable, bien que placées à des endroits très différents de l'écoulement, puisque la sonde fixe plonge au milieu du mélangeur. L'écart entre les mesures (évalué à partir des plateaux) est au maximum de 4%, ce qui correspond à l'ajout des erreurs de linéarité lors de la calibration des différentes sondes. Ces mesures ont révélé une propriété étonnante des mesures embarquées : leur immunité au bruit. Alors que la sonde fixe et le

8. Le programme de pilotage de la particule permet par ailleurs de la mettre soit en sommeil léger entre les expériences pour ne la réveiller que lors des acquisitions. Après fermeture, on peut donc utiliser la particule pendant plusieurs semaines sans avoir à changer la batterie ou changer le joint assurant l'étanchéité de l'ensemble.

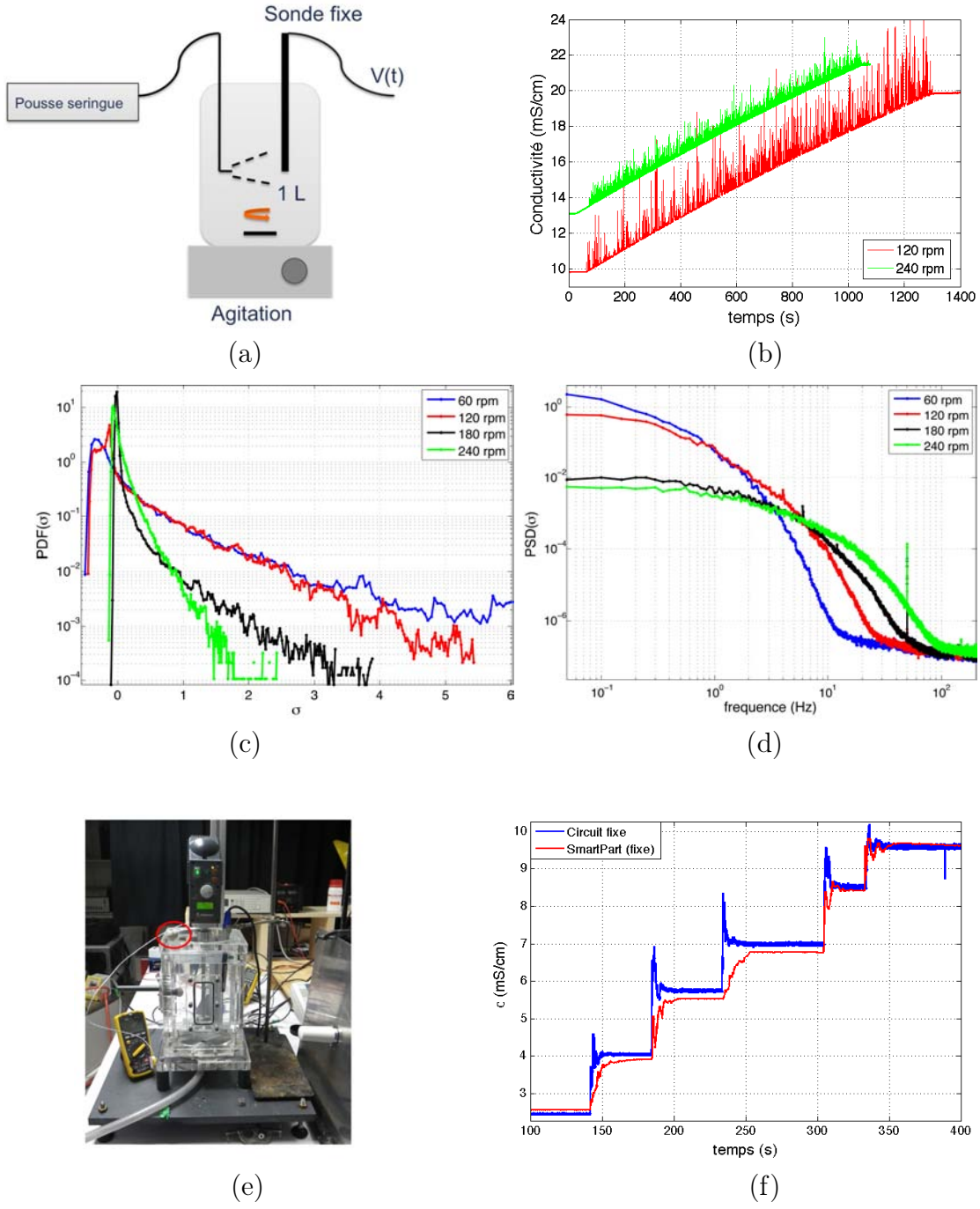

Fig. III.4: (a) Montage utilisé pour l'injection continue d'une solution saline $c_{\mathrm{NaCl}} = 30$ g.L ^{1} dans une solution de plus faible concentration initiale. Les couleurs bleue, rouge, noire et verte correspondent respectivement à = 60 120 180 240 rpm. (b) Evolution temporelle de la conductivité mesurée par la sonde fixe pour = 120 rpm et = 240 rpm. (c) PDF des fluctuations de concentration $C\,(t) = C(t)$ $C\rangle\!\!\rangle(t)$. (d) Spectres de puissance des fluctuations de concentration $C\,(t)$. (e) Montage utilisé pour tester les différentes sondes avant implantation en environnement industriel. (f) Evolution temporelle de la conductivité mesurée par la sonde fixe et la sonde mobile lors d'ajouts rapides d'une solution concentrée.

conductimètre commercial sont facilement perturbés par un mauvais blindage de la carcasse du moteur (il y a un contact partiel entre le moteur et les sondes car la solution est faiblement conductrice), la particule instrumentée est totalement flottante du point de vue électrique puisqu'à la fois l'électronique de mesure, mais aussi son digitaliseur sont alimentés sur batterie. Cette propriété sera d'une grande utilité pour une utilisation en milieu industriel.

Suite du projet PATVAX : Les tests précédemment décrits ont été poursuivis en présence des particules d'alumine et de protéines pour prévenir d'éventuels problèmes liés soit à la présence de l'alumine, soit liés à l'adsorption de protéines sur les électrodes. L'ensemble de ces tests n'ont pas mis en évidence de problèmes de mesure. Le système de mesure est actuellement utilisée par sanofi-Pasteur lors de procédés d'adjuvantation dans une cuve pilote de développement (volume de 6L, mais dans des conditions électromagnétiques industrielles). Mon rôle dans cette partie consiste en une aide pour l'analyse des signaux obtenus.
Parallèlement à cette utilisation en laboratoire R&D, de nouveaux tests concernant la robustesse (mécanique) et le vieillissement des sondes de mesure sont actuellement pratiqués. En effet lorsque la particule possède une densité voisine de celle du fluide, elle explore une large part de l'écoulement et est susceptible d'être heurtée par les pales de l'agitateur, ce qui peut l'endommager.
Après validation de ces tests en environnement de développement, les particules seront utilisées par Merial pour validation de leur utilisation dans une cuve de formulation (volume de 100L).

Lien avec mes autres activités de recherche : comme l'a montré ce chapitre, le centre de gravité de mon activité de recherche se déplace vers une problématique liée au mélange. Les activités prospectives décrites dans le suite, que ce soit celle du mélange de colloïdes ou encore celle des mesures lagrangiennes de transfert de masse (dissolution ou fonte de particules) intègrent un aspect de mélange turbulent. Les moyens de mesures développés pendant ce projet seront donc naturellement mis à profit dans le développement de ces activités.

IV.Activités prospectives

Ce chapitre regroupe les activités de recherche démarrées récemment, et sur lesquelles je compte porter mes efforts dans les prochaines années. Elles sont en cours de développement dans le cadre de la thèse de N. Machicoane et des post-doctorats de L. Fiabane et C. Mauger. Ils devraient donner lieu à de premières publications dans la prochaine année.

IV.1 Changement de phase d'une particule transportée par un écoulement turbulent

Comme nous l'avons vu, la dynamique des particules transportées par les écoulements est fortement influencée par leur taille et leur densité. Les particules inertielles ou matérielles ne suivent pas le mouvement du fluide et il peut exister une vitesse de glissement $\mathbf{u}_s = \mathbf{u} - \mathbf{v}$ entre la particule et le fluide environnant. Se pose alors la question du transfert de masse ou de chaleur entre une particule sphérique de rayon r_p pouvant fondre ou se dissoudre dans l'eau, ou s'évaporer dans l'air. Ce problème possède naturellement un lien avec celui de la traînée d'une sphère en mouvement dans un écoulement à ceci près que le transfert (par exemple) de chaleur fait intervenir à la fois le nombre de Reynolds à l'échelle de la particule $Re_p = u_s r_p/\nu$ et le nombre de Prandtl $Pr = \nu/\kappa$, où κ est la diffusivité du champ de température [1]. Historiquement, ce problème a donc été abordé de la même manière que pour l'équation de Maxey-Riley-Gatignol [29, 22] : dans une vision perturbative pour laquelle Re_p est petit, on obtient une expression du nombre de Nusselt [2] Nu en fonction des nombres sans dimension Re_p et Pr. Dans ce contexte, et pour un transfert en régime stationnaire, la relation la plus célèbre est sans doute la corrélation de Ranz-Marshall [3] $Nu = 2 + 0.6 Re_p^{1/2} Pr^{1/3}$ [16], valable pour $Pr > 1$, qui a fait l'objet de nombreuses études expérimentales indirectes effectuées en mesurant l'évolution de la conductivité dans un mélangeur pendant la dissolution de très petits cristaux ioniques [28, 7].

Pour répondre à la question de l'influence de la turbulence sur le transfert thermique, des expériences plus modernes ont été menées sur des gouttelettes de composés volatils soit

1. Dans le cas du transfert de masse d'un soluté, l'analogue du nombre de Prandtl est le nombre de Schmidt $Sc = \nu/D$ avec D le coefficient de diffusion de l'espèce dissoute.

2. Si l'on note ΔT la différence de température entre la surface de la particule et le volume du fluide, le nombre de Nusselt Nu est définit comme le rapport du flux surfacique convectif $\phi_c = h(Re, Pr)\Delta T$ adimentionné par le flux surfacique diffusif $\phi_d = \kappa \Delta T / r_p$.

3. Dans le cas d'un transfert de masse, on parle du nombre de Sherwood. La relation est alors la même.

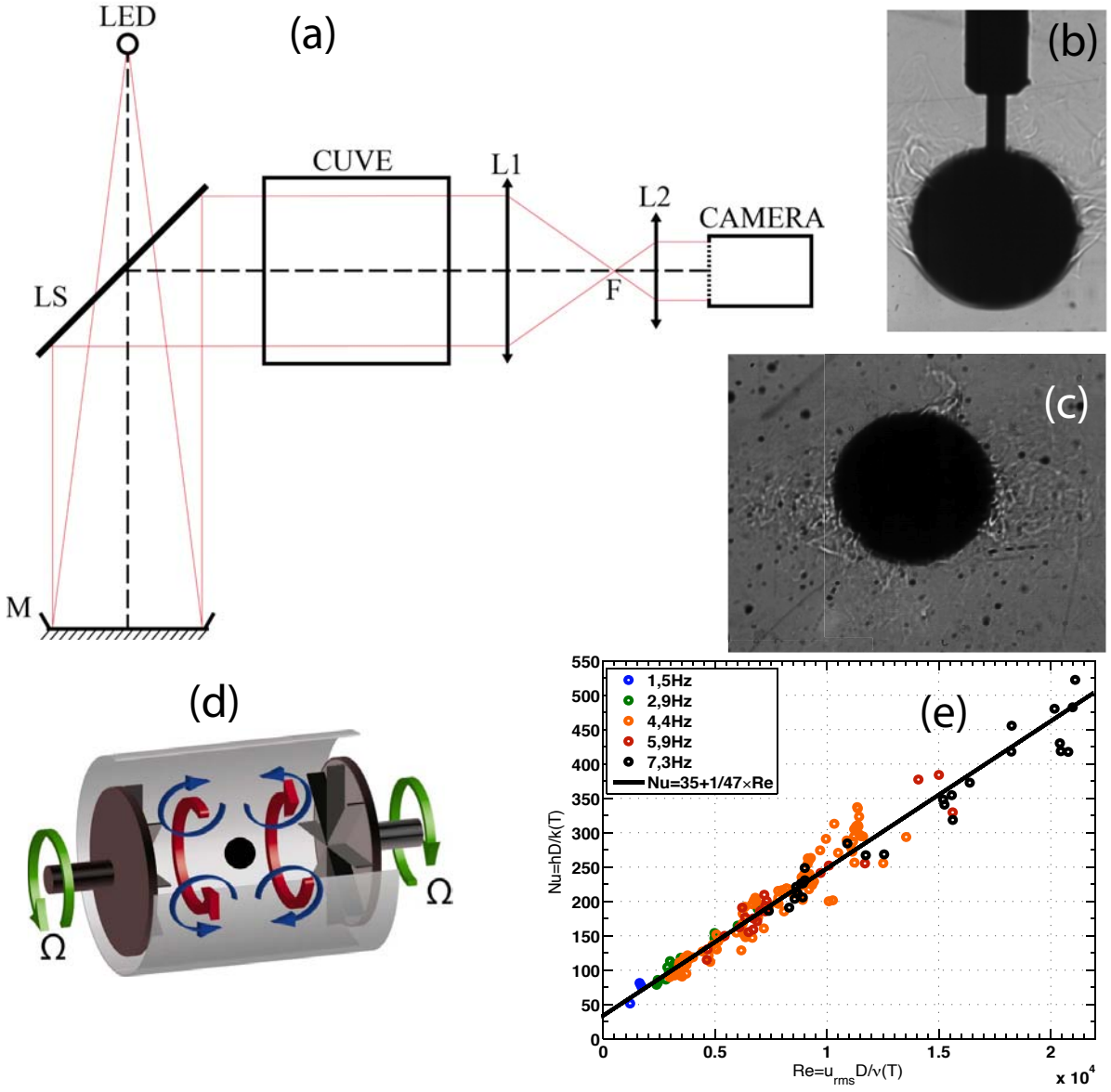

Fig. IV.1: (a) : schéma du dispositif expérimental de suivi de particules par ombroscopie. Le miroir parabolique et la lame semi-réfléchissante permettent d'éclairer la cuve en lumière parallèle avec un champ de vue de 15 cm de diamètre. Les lentilles L1 et L2, montées en télèscope, permettent une projection parallèle directement sur le capteur d'une caméra rapide phantom V.10 (4 Mpx@400Hz). (b) : image obtenue lors de la fonte d'un glaçon suspendu au centre d'un écoulement de von Kármán. (c) : image obtenue dans le cas d'un glaçon librement advecté par l'écoulement. (d) Géométrie de l'écoulement utilisé et position du glaçon maintenu fixe. (e) Evolution (affine) du Nombre de Nusselt (Nu) en fonction du nombre de Reynolds ($Re_p = u_{rms}D$) pour différentes tailles de glaçons. Dans ce régime fortement turbulent, la taille n'a plus influence sur le transfert thermique.

avec des gouttes suspendues [5, 6], soit librement advectées dans une turbulence homogène isotrope [14, 13]. Ces expériences, qui tendent à montrer que la relation de Ranz-Marshall doit être remise en question en présence de turbulence [5], sont très difficiles car le problème de diffusion thermique à l'intérieur de la particule vient retarder l'évaporation de celle-ci lorsqu'elle n'est pas préalablement portée à sa température d'évaporation [14].

Cette thématique du changement de phase des particules dans un écoulement turbulent, est au coeur de la collaboration ANR TEC (Turbulence Evaporation and Condensation, collaboration avec LMFA Lyon, LEGI Grenoble, OCA Nice) et constitue le travail de thèse de N. Machicoane que j'encadre actuellement. Nous avons choisi comme premier cas d'étudier la fonte de glaçons sphériques soit librement advectés dans un écoulement de von Kármán contra-rotatif (figure IV.1(d)), soit fixés au centre de celui-ci, là où l'écoulement moyen est nul. Pour pouvoir mesurer sa taille au cours du temps, nous avons développé une nouvelle technique couplant PTV et ombroscopie (figure IV.1(a)), qui permet non seulement de mesurer la taille d'un objet de phase (impossible à voir en rétro-éclairage) sans biais de distance entre la caméra et la particule, mais aussi de distinguer le sillage thermique de la particule (figure IV.1(b,c)). La fonte des glaçons (initialement portés à leur température de fusion) donne alors directement la mesure du coefficient $h(Re, Pr)$ par le biais de la relation de Stefan [4] $\rho L_f \dot{R} = h\Delta T$ liant la diminution de taille du glaçon au flux de chaleur convectif. Cette technique prometteuse, en cours d'utilisation avec des glaçons de diamètres [10, 14, 18, 24, 30] mm, semble indiquer un résultat surprenant à confirmer : les glaçons librement advectés par l'écoulement ou maintenus au centre fondent à vitesse constante, ce qui indique une relation de proportionnalité entre Nu et u_{rms}. Dans ce regime, la taille du glaçon n'intervient donc plus, ce qui est compatible avec une couche limite pleinement développée à la surface du glaçon.

Dans les prochaines années : Le montage de PTV-ombroscopique permet non seulement de mesurer la taille des particules, mais aussi de pouvoir effectuer un suivi, en milieu dilué, de particules de formes variées avec très peu de lumière (une simple LED par caméra). Il ne nécessite donc pas de laser coûteux. Je souhaite l'utiliser pour étudier la dissolution de bulles de dioxide de carbone dans les écoulements turbulents, ainsi que pour aborder la dynamique lagrangienne d'objets anisotropes (tels des bâtonnets ou des disques) pour lesquels le couplage rotation-translation doit être prépondérant dans la dynamique.

4. Las grandeurs ρ et L_f sont respectivement la densité et la chaleur latente massique de fusion de la glace. Si la température interne du glaçon n'est pas portée à zéro degré, la relation de Stefan fait aussi intervenir le flux diffusif à l'interface, ce qui retarde la fonte.

IV.2 Concentration préférentielle de particules matérielles

Ces recherches sur les effets collectifs des particules de taille finie transportées par un écoulement sont un travail commun avec M. Bourgoin (LEGI, Grenoble) démarré dans le cadre de l'ANR DSPET (2007-2011, collaboration avec LMFA Lyon, LEGI Grenoble, OCA Nice). Elles ont pour but premier de quantifier comment les effets de concentration préférentielle, observés à la fois expérimentalement [25, 18, 30, 31] et numériquement [3, 10] pour des particules inertielles sont modifiés lorsque les particules ont une taille qui excède l'échelle de Kolmogorov. En particulier, nous nous sommes posé la question de savoir si des particules matérielles de même densité que le fluide, qui possèdent certaines propriétés communes avec les particules lourdes (décroissance de la variance et de la flatness de l'accélération, augmentation de leur temps de corrélation, ...) pouvaient, elles aussi, montrer un effet de concentration préférentielle. Ce phénomène risquant d'être sensible à l'anisotropie à grande échelle dans un écoulement de von Kármán, nous avons construit un nouveau mélangeur, le LEM [5] (figure IV.2(a)), qui utilise douze moteurs et est capable de produire une turbulence homogène et isotrope dans une boule d'environ 10 cm de diamètre [54].

Pour étudier la répartition dans l'espace des particules, Lionel Fiabane (actuellement en Post-Doc au laboratoire) a développé le montage optique de la figure IV.2(b) constitué d'une nappe laser obtenue à l'aide d'un laser pulsé (Nd :Yag, 100W) et d'une caméra rapide synchronisée avec les impulsions du laser. La caméra ayant une bonne résolution spatiale, on peut alors directement localiser les particules dans la nappe par seuillage pour obtenir leur position. Les méthodes d'étude des répartitions des populations sont nombreuses (telles les méthodes de box counting [18]), et nous utilisons la tesselation de Voronoï introduite par R. Monchaux qui a montré que cette méthode était très robuste pour estimer les effets de concentration préférentielle [30, 31]. La tessélation est obtenue en pavant le plan d'un ensemble de cellules : chaque cellule ne contient qu'une particule, les limites entre cellules étant définies par les médiatrices des segments formés par chaque paire de particules (figure IV.2(c)). Les avantages principaux de cette méthode est qu'elle n'introduit pas d'échelle caractéristique lors de l'analyse, qu'elle permet de définir la concentration locale en particules (inversement proportionnelle à l'aire de la cellule contenant la particule), et qu'elle est très rapide puisque déjà diponible avec Matlab. Il faut alors collecter un ensemble d'images indépendantes pour calculer la PDF des aires de Voronoï réduites à l'aire moyenne $\mathcal{V} = A/\bar{A}$. L. Fiabane a étudié les effets de concentration préférentielle pour deux types de particules matérielles permettant d'obtenir des nombres de Stokes largement supérieurs à l'unité : des particules sphériques de polystyrène (isodenses à 1% près) de diamètre 750 microns, et des billes de verres de densité $\rho_p/\rho_f = 2.4$ et diamètre 250 microns. Les deux types de populations ont été choisies pour obtenir des nombres de Stokes très

5. Pour Lagrangien Exploration Module. Sa conception et sa construction est le fruit d'une collaboration avec l'équipe de E. Bodenschatz du MPI Göettingen. Un autre exemplaire, subtilement différent, a été construit en Allemagne.

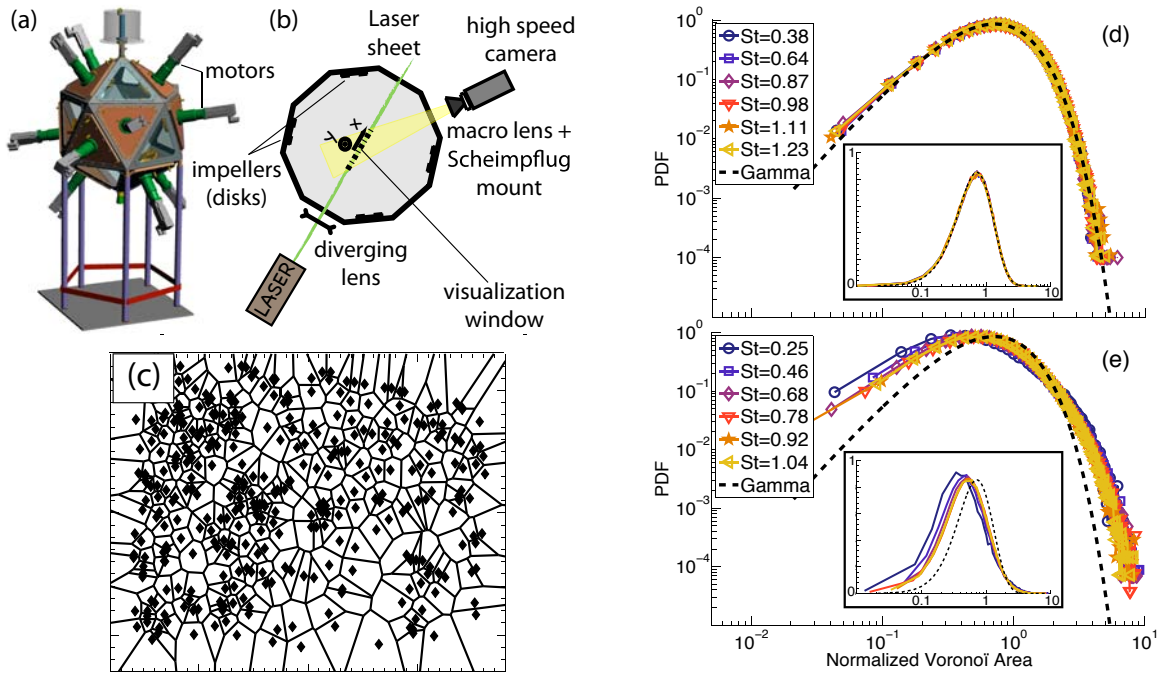

Fig. IV.2: (a) Dessin technique représentant le LEM et ses 12 moteurs. (b) Montage optique utilisé pour les mesures de concentration de particules, il est constitué d'une nappe LASER et d'une caméra rapide haute résolution (Phantom V.10, 4Mpx@400Hz). (c) Image typique de tesselation de Voronoï obtenue à partir de la position des particules. (d) PDF des aires de Voronoï dans le cas des particules isodenses (, PDF d'un processus de Poisson). (e) PDF des aires de Voronoï obtenue dans le cas de particules inertielles.

voisins dans les deux cas. Comparant les PDF des aires de Voronoï à celles obtenues pour un processus de Poisson, nous avons observé que les particules isodenses ne se répartissent pas sous la forme de cluster (figure IV.2(d)), mais se répartissent aléatoirement [19]. Les particules isodenses ne présentent donc pas de caractère inertiel, leur comportement diffère de celui des particules en verre dont les PDF ne se superposent pas à celles du processus de Poisson. Cette conclusion intéressante implique qu'un modèle (tel le modèle multifractal de L. Chevillard) valable pour la description des traceurs doit pouvoir être appliqué pour décrire la dynamique des particules matérielles isodenses. Ce résultat est sans doute connecté à la décroissance de l'intermittence rapportée dans le chapitre III (figure II.8) qui a montré que l'évolution des incréments de vitesse est pilotée par le temps de corrélation de l'accélération τ_p quelle que soit la taille de la particule isodense (traceur ou non).
Dans les prochaines années : Le montage de mesure de concentration préférentielle peut être utilisé en tant que montage de PIV haute cadense. En utilisant des particules fluorescentes comme traceurs et des particules inertielles se répartissant (ou non) sous la forme de clusters, je souhaite étudier la rétroaction exercée par les particules sur l'écoulement. En particulier, je souhaite étudier l'influence de la concentration préférentielle des particules sur le phénomène de "two-way coupling", régime pour lequel les particules sont en nombre suffisant pour influencer l'écoulement sans pour autant interagir entre elles (sous la forme de collisions) [39, 52].

IV.3 Transport turbulent de colloïdes

Lorsque l'on injecte un colorant dans un jet turbulent, le scalaire est transporté le long des trajectoires fluides tout en étant étiré et replié par les gradients de vitesse [17]. En aval du point d'injection, on observe alors des structures très fines ressemblant à des volutes (figure IV.3 (b)) de plus en plus fines à mesure que s'éloigne de la source, jusqu'à ce qu'elles soient suffisamment fines pour que la diffusion moléculaire puisse jouer son rôle et lisse le champ de concentration. Dans la plupart des cas (ions, colloïdes), le coefficient de diffusion des espèces D est tel que le nombre de Schmidt $Sc = \nu/D$ est très grand devant l'unité. L'échelle de dissipation du champ de scalaire (l'échelle de Batchelor) est alors très petite devant l'échelle de Kolmogorov et il n'est pas évident que que le nombre de Schmidt ait encore une influence sur le processus de mélange. Son influence est le plus souvent négligée dans les études bien qu'il y ait des preuves de son influence, notamment lorsqu'on s'intéresse aux fluctuations du champ scalaire [17, 45].
Parallèlement il a été observé dans des dispositifs microfluidiques (canaux en ψ) que l'on peut augmenter le coefficient de diffusion de colloïdes lorsqu'ils sont placés dans un gradient de concentration en sel [1, 2]. Ce phénomène, appelé diffusiophorèse, est particulièrement efficace lorsque l'on injecte des colloïdes (en solution dans l'eau pure) dans un bain d'eau salée, et peut se traduire par une augmentation de la diffusion des particules de plusieurs ordres de grandeur.

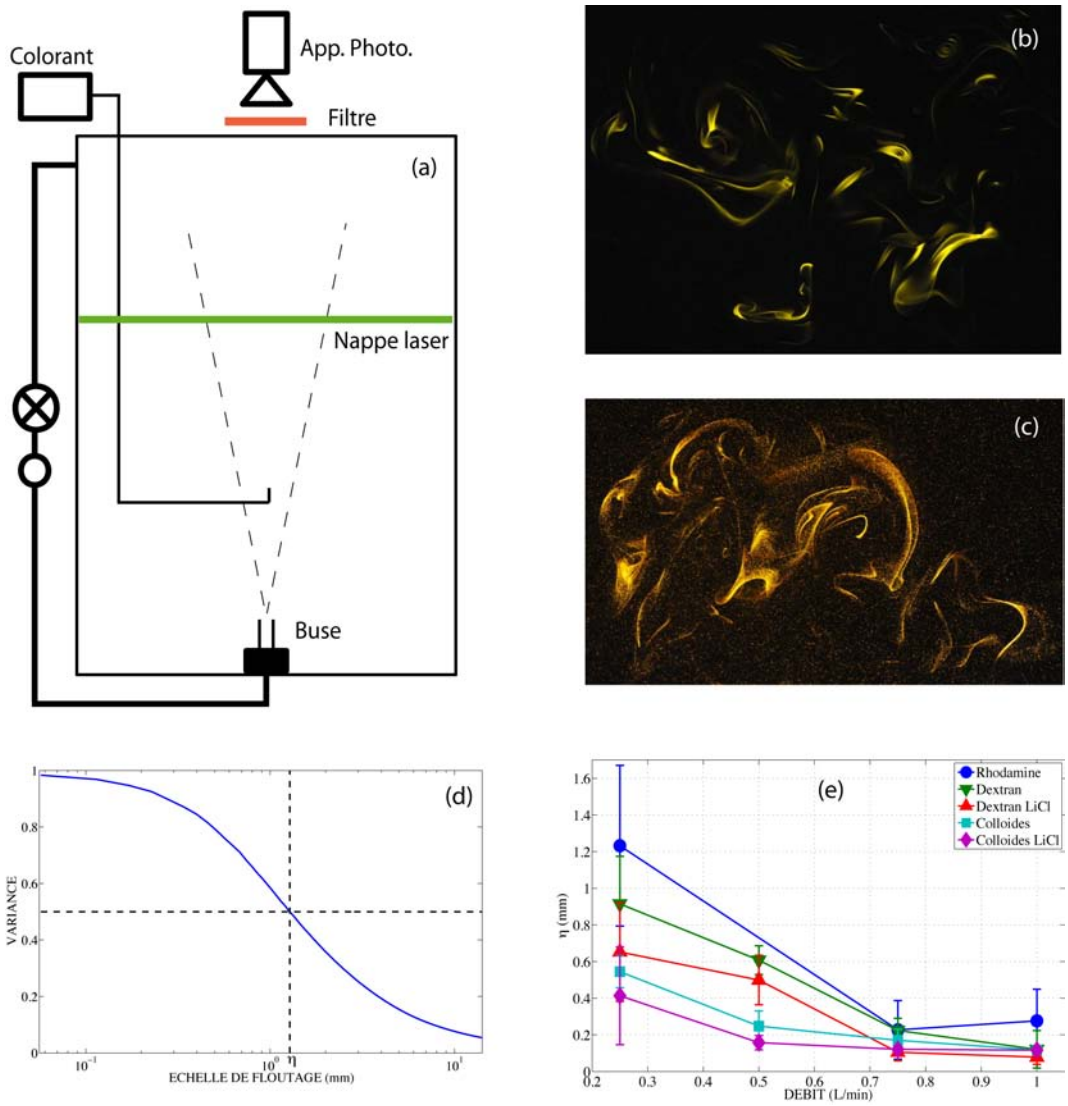

Fig. IV.3: (a) Montage expérimental utilisé pour les mesures de concentration de colorant dans le jet turbulent. La nappe laser est horizontale placée loin en aval de la buse du jet et de l'injecteur de colorant. (b) Image continue obtenue dans le cas d'une injection de rhodamine B dans l'eau. (c) Image granuleuse obtenue dans le cas de l'injection de particules fluorescentes dans l'eau. (d) Evolution de la variance du champ de concentration lors d'un floutage de plus en plus important des images, et définition de l'échelle de floutage η. (e) Evolution, pour différents types de particules, de l'échelle de floutage en fonction du débit du jet. Des expériences test on été pratiquées avec ou sans injection simultanée de sel LiCl.

Le projet MAXIMIX vise à étudier si ce phénomène de diffusiophorèse peut modifier le mélange des colloïdes dans un écoulement macroscopique. Ce projet a été initié sous la forme d'un projet CIBLE (2008-2010) mené en collaboration avec l'équipe microfluidique

du LPMCN (Université Lyon 1), et m'a permis de construire, en collaboration avec M. Bourgoin, une expérience de jet turbulent utilisée par N. Machicoane pendant son stage de M2 pour étudier le phénomène (figure IV.3 (a)). Il s'agit d'une expérience classique de LIF (mais utilisant une nappe laser horizontale) utilisée pour des mesures de champs de concentration de Rhodamine B (figure IV.3 (b)), de Dextran (molécule fluorescente plus grosse), ou de colloïdes (figure IV.3 (c)). Deux configurations ont été testées : l'une pour laquelle on injecte le colorant dans l'eau pure (pas de diffusiophorèse), et une autre pour laquelle le colorant, initialement en solution dans de l'eau salée, est injecté dans de l'eau pure (effet de mélange retardé).
Les tests de l'influence du nombre de Schmidt n'étant pas nombreux, nous avons utilisé le traitement introduit par Villermaux et al. [45] consistant à définir un champ de concentration lissé à une certaine échelle $\langle C \rangle_l$, et à mesurer sa variance en fonction de l (figure IV.3 (d)). Celle-ci décroît alors en fonction de l ce qui permet de définir une échelle de mélange η_f qui décroît avec le nombre de Schmidt selon la loi d'échelle $\eta_f \propto Sc^{-2/5}$. Il s'agit donc d'une mesure détournée de l'échelle des gradients du champ de concentration. En testant cette analyse sur nos données, nous avons pu obtenir de premiers résultats encourageants puisque les courbes obtenue pour des cas de diffusion retardée montrent systématiquement des échelles de mélange plus petites que pour les cas de diffusion simple (figure IV.3 (e)).
Dans les prochaines années : Les résultats préliminaires ont été suffisamment encourageants pour que le Labex IMUST finance une année de Post-Doc (2012-2013) pour un travail collaboratif entre les laboratoires LMFA, LPMCN, et ENS Lyon pour transposer les résultats obtenus par le LPMCN dans des écoulements à plus grande échelle. Cyril Mauger, actuellement en Post-Doc au laboratoire, développe une expérience de mélange par advection chaotique [4, 43] qui sera utilisée pour quantifier les effets de nombre de Schmidt sur le mélange à nombre de Reynolds modéré. Des mesures en jet turbulent seront ensuite reprises sous la forme de mesures combinées LIF-PIV pour une étude approfondie des fluctuations du scalaire et du flux de scalaire turbulent $\langle u'C' \rangle$ à plus haut nombre de Reynolds (u' et C' étant les fluctuations de vitesse et de concentration). Ces deux études devraient permettre de quantifier jusqu'à quel nombre de Reynolds on peut espérer augmenter le mélange des colloïdes par ajout de sel dans l'écoulement.

Bibliographie

[1] B Abécassis, C Cottin-Bizonne, C Ybert, A Ajdari, and L Bocquet. Boosting migration of large particles by solute contrasts. *Nature materials*, 7(10) :785–9, October 2008.

[2] B Abécassis, C Cottin-Bizonne, C Ybert, A Ajdari, and L Bocquet. Osmotic manipulation of particles for microfluidic applications. *New Journal of Physics*, 11(7) :075022, July 2009.

[3] Jeremie Bec, L Biferale, M Cencini, A Lanotte, S Musacchio, and F Toschi. Heavy particle concentration in turbulence at dissipative and inertial scales. *Physical Review Letters*, 98 :84502, 2007.

[4] Aurélien Beuf, Jean-noël Gence, Philippe Carrière, and Florence Raynal. Chaotic mixing efficiency in different geometries of Hele-Shaw cells. *International Journal of Heat and Mass Transfer*, 53(4) :684–693, 2010.

[5] M Birouk, C Chauveau, B Sarh, A Quilgars, and I Gokalp. Turbulence effects on the vaporization of monocomponent single droplets. *Combustion Science and Technology*, 113 :413–428, 1996.

[6] Madjid Birouk and Iskender Gökalp. Current status of droplet evaporation in turbulent flows. *Progress in Energy and Combustion Science*, 32(4) :408–423, 2006.

[7] S Boon-Long, C Laguerie, and J.-P. Couderc. Mass transfer from suspended solids to a liquid in agitated vessels. *Chem. Eng. Science*, 1978.

[8] Mickael Bourgoin, N T Ouellette, H T Xu, J Berg, and E Bodenschatz. The role of pair dispersion in turbulent flow. *Science*, 311(5762) :835–838, 2006.

[9] Rachel D Brown, Z Warhaft, and Greg A Voth. Acceleration statistics of neutrally buoyant spherical particles in intense turbulence. *Physical Review Letters*, 103(19), November 2009.

[10] E. Calzavarini, M. Kerscher, D. Lohse, and F. Toschi. Dimensionality and morphology of particle and bubble clusters in turbulent flow. *Journal of Fluid Mechanics*, 607 :13–24, 2008.

[11] E Calzavarini, Romain Volk, Mickael Bourgoin, E Leveque, J F. Pinton, and F Toschi. Acceleration statistics of finite-sized particles in turbulent flow : the role of Faxen forces. *Journal of Fluid Mechanics*, 630 :179–189, 2009.

[12] Enrico Calzavarini, Romain Volk, Emmanuel Lévêque, Jean-françois Pinton, and Federico Toschi. Impact of trailing wake drag on the statistical properties and dynamics of finite-sized particle in turbulence. *Physica D*, 241(3) :237–244, 2012.

[13] D Chareyron, J L Marié, C Fournier, J Gire, N Grosjean, L Denis, M Lance, and L Méès. Testing an in-line digital holography , inverse method, for the Lagrangian tracking of evaporating droplets in homogeneous nearly isotropic turbulence. *New Journal of Physics*, 14(4) :043039, April 2012.

[14] Delphine Chareyron. *Développement de méthodes instrumentales en vue de l'étude Lagrangienne de l'évaporation dans une turbulence homogène isotrope*. PhD thesis, Ecole Centrale de Lyon, 2010.

[15] Laurent Chevillard, Stéphane G Roux, Émmanuel Lévêque, Nicolas Mordant, Jean-François Pinton, and Alain Arnéodo. Lagrangian velocity statistics in turbulent flows : effects of dissipation. *Physical Review Letters*, 91(21) :214502, 2003.

[16] R Clift, J R Grace, and M E Weber. *Bubbles, drops and particles*. Academic Press, New York, 1978.

[17] J. Duplat. *Mélange turbulent : Sources et loi de composition*. PhD thesis, Université Joseph Fourier, Grenoble, 1999.

[18] Jr Fessler, Jd Kulick, and Jk Eaton. Preferential concentration of heavy-particles in a turbulent channel flow. *Physics of Fluids*, 6(11) :3742–3749, 1994.

[19] L Fiabane, R Zimmermann, R Volk, J.-F Pinton, and M Bourgoin. Clustering of finite-size particles in turbulence. *Physical Review E*, 035301 :1–4, 2012.

[20] Yoann Gasteuil. *Instrumentation Lagrangienne en Turbulence : Mise en oeuvre et Analyse*. PhD thesis, ENS Lyon, 2009.

[21] Yoann Gasteuil, W L Shew, M Gibert, F Chillà, B Castaing, and Jean-François Pinton. Lagrangian temperature, velocity, and local heat flux measurement in Rayleigh-Bénard convection. *Physical Review Letters*, 99(23) :234302, 2007.

[22] Renée Gatignol. The Faxen formulas for a rigid particle in an unsteady non-uniform Stoke flow. *Journal de Mécanique théorique et appliquée*, 2(2) :143–160, 1983.

[23] P Gervais, C Baudet, and Y Gagne. Acoustic Lagrangian velocity measurement in a turbulent air jet. *Experiments in Fluids*, 42(3) :371–384, March 2007.

[24] Gibson and Schwarz. Detection of conductivity fluctuations in a turbulent flow field. *Journal of Fluid Mechanics*, pages 357–364, 1963.

[25] Michele Guala, Alexander Liberzon, Klaus Hoyer, Arkady Tsinober, and Wolfgang Kinzelbach. Experimental study on clustering of large particles in homogeneous turbulent flow. *Journal of Turbulence*, 9(34) :1–20, 2008.

[26] Holger Homann and Jeremie Bec. Finite-size effects in the dynamics of neutrally buoyant particles in turbulent flow. *Journal of Fluid Mechanics*, 651 :81–91, 2010.

[27] A La Porta, G.A. Voth, A.M. Crawford, J. Alexander, and E. Bodenschatz. Fluid particle accelerations in fully developed turbulence. *Nature*, 409 :1017–1019, 2001.

[28] D M Levins and J R Glastonbury. Application of Kolmogorov theory to particle-liquid in agitated vessels mass transfer. *Chem. Eng. Science*, 27(3) :537–543, 1972.

[29] M R Maxey and J J Riley. Equation of motion for a small rigid sphere in a nonuniform flow. *Physics of Fluids*, 26(4) :883, 1983.

[30] R Monchaux, M Bourgoin, and A Cartellier. Preferential concentration of heavy particles : A Voronoi analysis. *Physics of Fluids*, 22(10) :103304, 2010.

[31] Romain Monchaux, Mickael Bourgoin, and Alain Cartellier. Analyzing preferential concentration and clustering of inertial particles in turbulence. *International Journal of Multiphase Flow*, 40 :1–18, April 2012.

[32] N Mordant, P Metz, O Michel, and J.-F. Pinton. Measurement of Lagrangian velocity in fully developed turbulence. *Physical Review Letters*, 87(21) :214501, November 2001.

[33] Nicolas Mordant, Alice M Crawford, and Eberhard Bodenschatz. Experimental Lagrangian acceleration probability density function measurement. *Physica D*, 193 :245–251, 2004.

[34] Nicolas Mordant, Alice M Crawford, and Eberhard Bodenschatz. Three-dimensional structure of the lagrangian acceleration in turbulent flows. *Physical Review Letters*, 93 :214501, 2004.

[35] Nicolas Mordant, Emmanuel Lévêque, and Jean-François Pinton. Experimental and numerical study of the Lagrangian dynamics of high Reynolds turbulence. *New Journal of Physics*, 6 :116, 2004.

[36] Nicolas Mordant, Jean-François Pinton, and Olivier Michel. Time-resolved tracking of a sound scatterer in a complex flow : Nonstationary signal analysis and applications. *Journal of the Acoustical Society of America*, 112(1) :108–118, 2002.

[37] N T Ouellette, H T Xu, Mickael Bourgoin, and E Bodenschatz. Small-scale anisotropy in Lagrangian turbulence. *New Journal of Physics*, 8, 2006.

[38] B. R. Pearson and R. a. Antonia. Reynolds-number dependence of turbulent velocity and pressure increments. *Journal of Fluid Mechanics*, 444 :343–382, September 2001.

[39] C Poelma, J Westerweel, and G Ooms. Particle-fluid interactions in grid-generated turbulence. *Journal of Fluid Mechanics*, 589 :315–351, 2007.

[40] A. Pumir, Shraiman B. I., and E. D. Siggia. Turbulent mixing of a passive scalar. *Physica A*, 263 :95–103, 1999.

[41] N M Qureshi, U Arrieta, C Baudet, A Cartellier, Y Gagne, and Mickael Bourgoin. Acceleration statistics of inertial particles in turbulent flow. *European Physical Journal B*, 66(4) :531–536, 2008.

[42] Nauman M Qureshi, Mickael Bourgoin, Christophe Baudet, Alain Cartellier, and Yves Gagne. Turbulent transport of material particles : an experimental study of finite size effects. *Physical Review Letters*, 99(18), 2007.

[43] Florence Raynal, Aurélien Beuf, Frédéric Plaza, Julian Scott, and Philippe Carrière. Towards better DNA chip hybridization using chaotic advection. *Physics of Fluids*, 19 :1–11, 2007.

[44] Woodrow L Shew, Yoann Gasteuil, Mathieu Gibert, Pascal Metz, and Jean-François Pinton. Instrumented tracer for Lagrangian measurements in Rayleigh-Bénard convection. *Review of Scientific Instruments*, 78(6) :65105, 2007.

[45] E Villermaux and J Duplat. Coarse grained scale of turbulent mixtures. *Physical Review Letters*, 97(14), 2006.

[46] R. Volk, D. Chareyron, and J.-F. Pinton. Mesures d'accélération lagrangienne dans un écoulement anisotrope par vélocimétrie laser Doppler étendue. *Proceeding du 20ième Congrès Français de Mécanique*, pages 1–6, 2011.

[47] Romain Volk, E Calzavarini, E Leveque, and J-F Pinton. Dynamics of inertial particles in a turbulent von Karman flow. *Journal of Fluid Mechanics*, 668 :223–235, 2011.

[48] Romain Volk, E Calzavarini, G Verhille, D Lohse, N Mordant, J F. Pinton, and F Toschi. Acceleration of heavy and light particles in turbulence : Comparison between experiments and direct numerical simulations. *Physica D*, 237(14-17) :2084–2089, 2008.

[49] Romain Volk, Nicolas Mordant, Gaultier Verhille, and Jean-Françoi Pinton. Laser Doppler measurement of inertial particle and bubble accelerations in turbulence. *European Physics Letters*, 81 :34002, 2008.

[50] Greg A Voth, Arthur LaPorta, Alice M Crawford, Jim Alexander, and Eberhard Bodenschatz. Measurement of particle accelerations in fully developed turbulence. *Journal of Fluid Mechanics*, 469 :121–160, 2002.

[51] H. Xu, N.T. Ouellette, D. Vincenzi, and E. Bodenschatz. Acceleration correlations and pressure structure functions in high Reynolds number turbulence. *Physical Review Letters*, 99 :204501, 2007.

[52] T. S. Yang and S. S. Shy. Two-way interaction between solid particles and homogeneous air turbulence : particle settling rate and turbulence modification measurements. *Journal of Fluid Mechanics*, 526 :171–216, March 2005.

[53] R Zimmermann, L Fiabane, Y Gasteuil, and R Volk. Measuring Lagrangian accelerations using an instrumented particle. *arXiv :1206.1617v1, to appear in Proc. Roy. Swed. Soc.*, pages 1–8, 2012.

[54] R Zimmermann, H Xu, Y Gasteuil, M Bourgoin, R Volk, J.-F. Pinton, and E Bodenschatz. The Lagrangian exploration module : an apparatus for the study of homogeneous and isotropic turbulence. *Review of Scientific Instruments*, 81(5), 2010.

[55] Robert Zimmermann, Lionel Fiabane, Yoann Gasteuil, Romain Volk, and Pinton Jean-François. Characterizing flows with an instrumented particle measuring lagrangian accelerations. *arXiv :1208.2809v1, to appear in New Journal of Physics*, pages 1–13, 2012.

[56] Robert Zimmermann, Yoann Gasteuil, Mickael Bourgoin, Romain Volk, Alain Pumir, and Jean-Francois Pinton. Rotational Intermittency and turbulence induced lift experienced by large particles in a turbulent flow. *Physical Review Letters*, 106(15) :154501, 2011.

[57] Robert Zimmermann, Yoann Gasteuil, Mickael Bourgoin, Romain Volk, Alain Pumir, and Jean-François Pinton. Tracking the dynamics of translation and absolute orientation of a sphere in a turbulent flow. *Review of Scientific Instruments*, 82 :033906, 2011.

Annexe

A.Articles présentés

[A 1] R. Volk, N. Mordant, G. Verhille, and J.-F. Pinton. Measurement of particle and bubble accelerations in turbulence. *European Physical Letters*, 81, (2008)
[A 2] R. Volk, E. Calzavarini, G. Verhille, D. Lohse, N. Mordant, J.-F. Pinton, and F. Toschi. Acceleration of heavy and light particles in turbulence : comparison between experiments and direct numerical simulations. *Physica D*, 237 :2084-2089, (2008)
[A 3] E. Calzavarini, R. Volk, M. Bourgoin, E. L'évêque, J.-F. Pinton, F. Toschi. Acceleration statistics of finite-sized particles in turbulent flows : the role of Faxen forces. *J. Fluid Mech.*, 630 , 179–189 (2009).
[A 4] R. Zimmermann, H. Xu, Y. Gasteuil, M. Bourgoin, R. Volk, J.-F. Pinton, E. Bodenschatz. The lagrangian exploration module : an apparatus for the study of homogeneous and isotropic turbulence. *Review Of Scientific Instrument*, 81(5), (2010).
[A 5] R. Volk, E. Calzavarini, E. L'évêque, J.-F. Pinton. Dynamics of inertial particles in a von Karman turbulent flow. *J. Fluid Mech.*, 668 :223-235, (2011).
[A 6] R. Zimmermann, Y. Gasteuil, M. Bourgoin, R. Volk, A. Pumir, J.-F. Pinton. Tracking the dynamics of translation and absolute orientation of a sphere in a turbulent flow. *Review of Scientific Instruments*, 82 :033906, (2011).
[A 7] R. Zimmermann, Y. Gasteuil, M. Bourgoin, R. Volk, A. Pumir, and J.-F. Pinton. Rotational Intermittency and Turbulence Induced Lift Experienced by Large Particles in a Turbulent Flow. *Physical Review Letters*, 106(15) :154501, (2011).
[A 8] E. Calzavarini, R. Volk, E. L'évêque, J.-F. Pinton, Federico Toschi. Impact of trailing wake drag on the statistical properties and dynamics of finite-sized particle in turbulence. *Physica D*, 241(3) :237-241 (2012).
[A 9] L Fiabane, R Zimmermann, R Volk, J.-F Pinton, and M Bourgoin. Clustering of finite-size particles in turbulence. *Physical Review E*, 035301 :1–4, (2012).
[A 10] Robert Zimmermann, Lionel Fiabane, Yoann Gasteuil, and Romain Volk. Characterizing flows with an instrumented particle measuring lagrangian accelerations. *arXiv : 1208.2809v1*, pages 1–13, (2012).
[A 11] R Zimmermann, L Fiabane, Y Gasteuil, and R Volk. Measuring Lagrangian accelerations using an instrumented particle. *arXiv :1206.1617v1*, pages 1–8, (2012).

A.1 Dynamique des particules inertielles

[A 1] R. Volk, N. Mordant, G. Verhille, and J.-F. Pinton. Measurement of particle and bubble accelerations in turbulence. *European Physical Letters*, 81, (2008)

[A 2] R. Volk, E. Calzavarini, G. Verhille, D. Lohse, N. Mordant, J.-F. Pinton, and F. Toschi. Acceleration of heavy and light particles in turbulence : comparison between experiments and direct numerical simulations. *Physica D*, 237 :2084-2089, (2008)

A Letters Journal Exploring the Frontiers of Physics

February 2008

EPL, **81** (2008) 34002
doi: 10.1209/0295-5075/81/34002

www.epljournal.org

Laser Doppler measurement of inertial particle and bubble accelerations in turbulence

R. Volk[1], N. Mordant[2], G. Verhille[1] and J.-F. Pinton[1]

[1] *Laboratoire de Physique de l'École normale supérieure de Lyon, CNRS UMR5672 46 Allée d'Italie, 69007 Lyon, France*
[2] *Laboratoire de Physique Statistique de l'École normale supérieure de Paris, CNRS UMR8550 24 rue Lhomond, 75005 Paris, France*

received 10 October 2007; accepted in final form 26 November 2007
published online 31 December 2007

PACS 47.27.Jv – High-Reynolds-number turbulence
PACS 47.27.Gs – Isotropic turbulence; homogeneous turbulence
PACS 47.80.-v – Instrumentation and measurement methods in fluid dynamics

Abstract – We use an extended laser Doppler technique to track optically the velocity of individual particles in a high Reynolds number turbulent flow. The particle sizes are of the order of the Kolmogorov scale and the time resolution, 30 microseconds, resolves the fastest scales of the fluid motion. Particles are tracked for mean durations of the order of 10 Kolmogorov time scales and their accelerations are measured. For neutrally buoyant particles (fluid tracers), this technique matches the performance of the silicon strip detector technique introduced at Cornell University (Voth G. A. *et al.*, *J. Fluid Mech.*, **469** (2002) 121). This reference dynamics is then compared to that of slightly heavier solid particles (density 1.4) and to air bubbles. We observe that the dynamics of the particles strongly depends on their density. Bubbles have a much faster dynamics and experience much higher accelerations than fluid tracers. Although the particles dynamics are different, we find that the probability distribution functions of accelerations normalized to the variance always remain very close to the one for the fluid tracers.

The Lagrangian approach to fluid dynamics is a natural one when one addresses problems related to mixing and transport [1]. It is widely studied in the context of intermittency in fully developed turbulence, and, in recent years, several experimental techniques have been developed in order to access Lagrangian measurements. The pioneering optical tracking method developed in the Cornell group has revealed that fluid particles experience extremely intense accelerations, with probability density functions (PDFs) having wide stretched exponential tails [2,3]. Initially limited to very short particle tracks, the technique has been extended with the use of ultrafast optical cameras [4], and is currently applied to the study of multiple particle statistics [5]. Individual particles have also been tracked for time duration of the order of the flow integral time scale using an acoustic technique [6]: in an insonified volume, individual particles scatter a sound wave whose Doppler shift carries the tracer velocity. Because of the very fast decrease of any scattering cross-section with scatterer' size, this type of method is limited to particles with size of the order of the wavelength, *i.e.* inertial ranges sizes when using acoustics [7]. However, the principle of the acoustic technique is completely analogous to laser optical Doppler velocimetry (LDV), provided that expanded light beams are used. Interference fringes are created at the intersection of two wide laser beams; a particle that crosses these fringes scatters light with a modulation frequency proportional to its velocity component perpendicular to the direction of the fringes [8]. The advantage, compared to the acoustic method, is that the much smaller wavelength allows a better resolution in space and also the use of smaller tracer particles.

In this letter, we describe the principles of this "extended" Laser Doppler technique (hereafter called "ELDV") and validate it against the known features of Lagrangian acceleration statistics in a fully turbulent von Kármán flow at $R_\lambda \leqslant 850$. We then apply it to track the dynamics of particles whose density differs from that of the fluid. The dynamics of such *inertial* particles is relevant for many engineering applications related to transport, mixing, dispersion, etc. [9]. Significant theoretical and numerical progress in this domain has

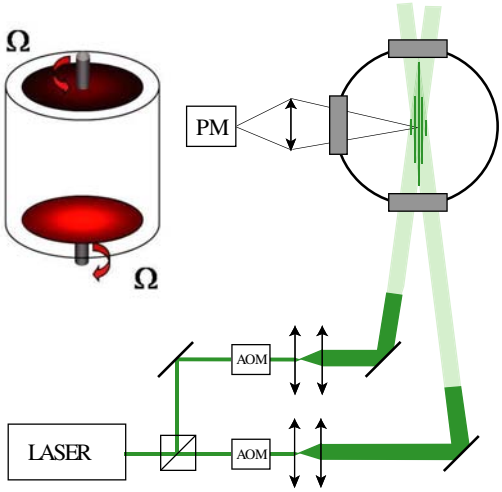

Fig. 1: Experimental setup. Left: schematics of the von Kármán flow in water —side view. Right: principle of the laser Doppler velocimetry using wide beams (ELDV) —top view of the experiment. PM: location of the photomultiplier which detects scattering light modulation as a particle crosses the interference pattern created at the intersection of the laser beams.

been made in the limiting case of infinitely heavy, pointwise particles [10] for which there is a good agreement with experimental data [11,12]. We report here the first experimental measurements of accelerations of particles having a density in the range 10^{-3} (air bubbles) to 1.4 (PMMA) in the same highly turbulent flow. Taking into account the added mass effect for small spherical particles (*i.e.* the displacement of fluid elements during the particle motion), the effective density of the bubbles is only 3 times less than that of the fluid, while the PMMA particles are roughly 1.5 times larger. Because of the mismatch of density, light particles tend to be trapped in high vortical regions: as a result of a lower inertia, the centrifugal force cannot compensate the pressure gradient which drives them into the core of the vortices [13]. On the contrary, for heavy particles the centrifugal force is stronger than the pressure gradient and they tend to be ejected from vortex cores and concentrate in high strain regions [14]. As a result of this distinct spatial sampling of the flow, particles with different buoyancies are thus expected to exhibit different dynamical behavior. We do find that the particles show different dynamical characteristics for quantities such as acceleration variance or correlation time. The PDFs of their (normalized) accelerations remain close for values less than about 10 times the acceleration variance, and differ for higher values.

Our extended laser Doppler technique is adapted from the ultrasound method developed for Lagrangian velocity measurements [6]; the gain is of a factor 1000 in wavelength so that one expects to detect micron-sized particles. Wide laser beams are used in order to follow the particle motion to get information about its dynamics in time. The optical setup is an extension of the well-known laser Doppler velocimetry technique; cf. fig. 1. A laser beam

Table 1: Parameters of the flow. Ω: rotation rate of the disks, ϵ: dissipation rate obtained from the power consumption of the motors (with an accuracy of about 20%). The Taylor-based turbulent Reynolds number is computed as $R_\lambda = \sqrt{15 u_{\rm rms}^4/\epsilon\nu}$, and a_0 is derived from the Heisenberg-Yaglom relationship —eq. (1).

Ω	$u_{\rm rms}$	$a_{\rm rms}$	τ_η	ϵ	R_λ	a_0
Hz	$\mathrm{m\cdot s^{-1}}$	$\mathrm{m\cdot s^{-2}}$	ms	$\mathrm{W\cdot kg^{-1}}$	–	–
4.1	0.5	227	0.57	4	450	4 ± 1.5
6.4	0.8	352	0.36	10	750	4.2 ± 1
8.9	1.1	826	0.24	23	850	6.4 ± 1

is split in two; each beam is then expanded with a telescope to reach a diameter of about 5 mm. They intersect in the flow and create an array of interference fringes in a volume of size of about $5 \times 5 \times 10\,\mathrm{mm}^3$. As a particle moves across the fringes, the scattered light is modulated. The frequency of modulation is directly proportional to the component of the velocity perpendicular to the interference fringes. One then measures one component of the particle velocity. In practice, we use a CW YAG laser with wavelength 532 nm at 1.2 W maximum output power. In order to get the sign of the velocity, the standard method consists in using an acousto-optic modulator (AOM) to shift the frequency of one of the beams so that the fringes are actually traveling at a constant speed. Here we use one AOM for each beam, the two excitation frequencies of the AOM being shifted by 100 kHz. The angle of the two beams is tuned to impose a 60 microns interfringe so that 100 kHz corresponds to 6 m/s. As the beams are not focused, the interfringe remains constant across the measurement volume. This volume is imaged on a photomultiplier whose output is recorded using a National Instrument PXI-NI5621 digitizer.

The flow is a turbulent von Kármán swirling flow as in the acoustics measurements [6]. Water fills a cylindrical container of internal diameter 15 cm, length 20 cm. It is driven by two disks of diameter 10 cm, fitted with blades. The rotation rate is fixed at values up to 10 Hz. For the measurements reported here, the Taylor-based Reynolds number reaches values up to 850 and the dissipation rate ϵ values up to 25 W/kg (table 1). We study three types of particles: neutrally buoyant polystyrene particles of size 31 microns and density 1.06, PMMA particles of size 43 microns and density 1.4 and air bubbles with a size of about 150 microns. The mean size of the bubbles, measured optically by imaging the measurement volume on a CCD, is imposed by the balance between the interfacial surface tension σ and the turbulent fluctuations of pressure. This fragmentation process is known to lead to a well-defined and stationary size distribution with a typical diameter $D = C\,(\sigma/\rho_f)^{3/5}\,\epsilon^{-2/5}$, ρ_f being the density of the fluid and $C \sim 0.1$ [15].

The signal processing step is crucial since both time and frequency —*i.e.* velocity— resolutions rely on its performance. Frequency demodulation is achieved using

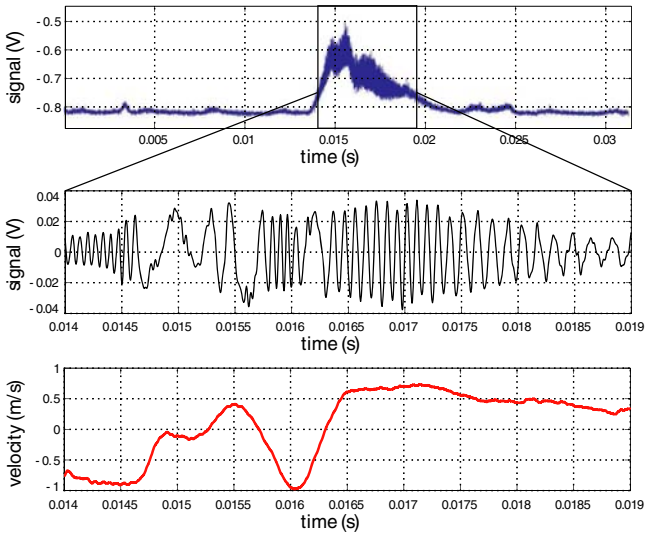

Fig. 2: Signal processing. Top: raw light modulation, as detected by the photodiode when a particle crosses the fringes. Middle: heterodyne detection of the frequency modulation. Bottom: velocity trace extracted using the approximate maximum likelihood (AML) algorithm [16].

the same algorithm as in the acoustic Doppler technique. It is an approximate maximum likelihood (AML) method coupled which a Kalman filter [16]: a parametric estimator assumes that the signal is made of a modulated complex exponential and Gaussian noise. The signal amplitude and the modulation frequencies are assumed to be slowly evolving compared to the duration of the time window used to estimate the instantaneous frequency. Here the time window is about $30\,\mu$s long and sets the time resolution of the algorithm. The outputs of the algorithm are the instantaneous frequency, the amplitude of the modulation and a confidence estimator which can be used to discriminate unreliable detections. An example of the light scattered by a particle is displayed in fig. 2, together with the Doppler frequency modulation, and final velocity signal.

Because of unavoidable noise in the measurement, we first filter out the high frequencies of the velocity signal by convolution of the velocity output with a Gaussian window of width w, and then differentiate the filtered signal to get the acceleration. The acceleration variance is computed using the same procedure as in [3]: it is obtained for several widths of the smoothing kernel used in the differentiation of the velocity signal and then interpolated to zero filter width (fig. 3(a)). As shown in fig. 3(b), since measurements are performed only when a particle moves within the (limited) measurement volume, the data consists in a collection of sequences with variable durations. We have checked that the acceleration variance weakly depends on the duration of the trajectories used for the computation (inset of fig. 3(b)), thus leading to an unbiased estimation of $a_{\rm rms}$.

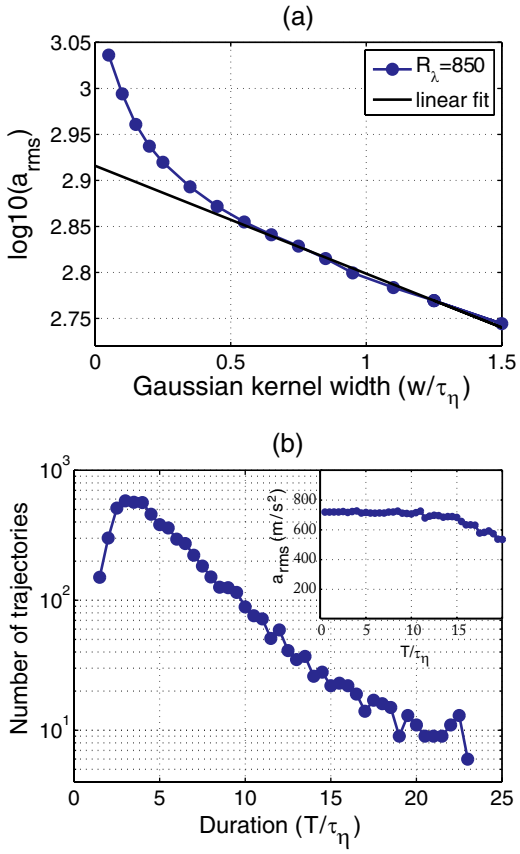

Fig. 3: (a) Evolution of the acceleration variance logarithm with the smoothing kernel width w/τ_η for neutral particles at $R_\lambda = 850$. (b) Number of trajectories of duration T for the same data set (7000 trajectories corresponding to 10^7 data points). The inset shows the evolution of the acceleration variance with T when only trajectories longer than T are used for the computation.

We first compare our data for neutral particles to the Cornell measurement using high-speed imaging [2,3]: their data was obtained using linear cameras with 512 pixels running at speeds up to 70000 frames per seconds. The probability density functions (PDFs) of the acceleration, from our ELDV technique at increasing Reynolds numbers and for the Cornell data at $R_\lambda = 690$ are shown in fig. 4: the distributions are in very good agreement both qualitatively and quantitatively. Note that in order to compare the two experiments, the Heisenberg-Yaglom scaling is used for the normalization of the acceleration variance

$$\langle a^2 \rangle = a_0 \epsilon^{3/2} \nu^{-1/2}, \qquad (1)$$

where ϵ is the dissipation rate per unit mass and $\nu = 1.3 \cdot 10^{-6}\,\mathrm{m}^2 \cdot \mathrm{s}^{-1}$ is the kinematic viscosity of water. We measure $a_0 = 6.4 \pm 1$ at $R_\lambda = 850$ compared to 6.2 ± 0.4 for the Cornell data at $R_\lambda = 690$, both acceleration variances being computed using the same procedure [3]. The acceleration autocorrelation function, shown in fig. 4b, decays in a time of the order of the Kolmogorov time $\tau_\eta = \sqrt{\nu/\epsilon}$, the fastest time scale of the turbulent flow.

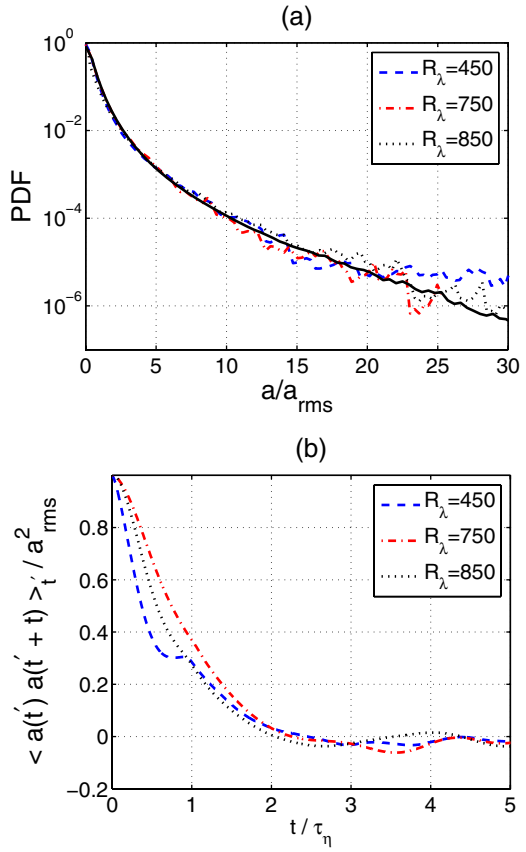

Fig. 4: (a) Probability density functions (PDFs) of the acceleration, normalized by its variance, for neutral particles. Dashed, dotted, dash-dotted lines: ELDV measurements; black solid line: Cornell data at $R_\lambda = 690$. (b) Autocorrelation coefficients of the accelerations for the same cases.

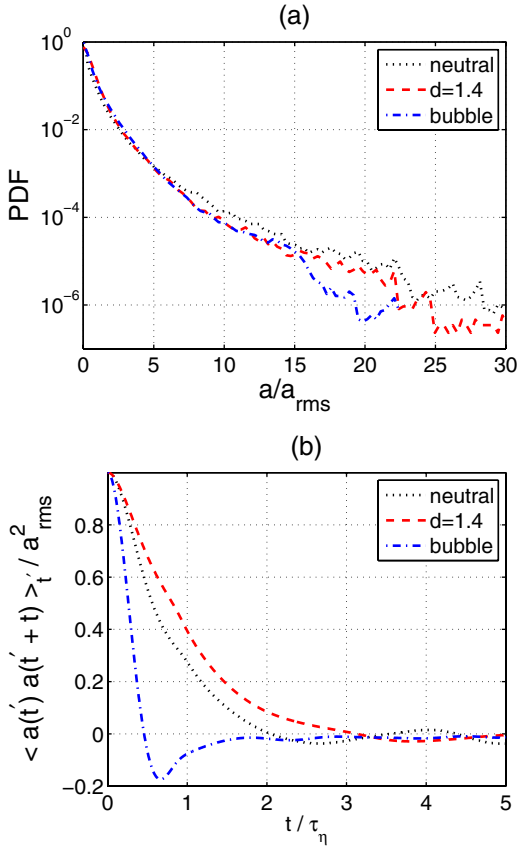

Fig. 5: (a) Probability distribution function of accelerations, normalized to the variance of the data sets. Flow at $R_\lambda = 850$. (b) Normalized autocorrelation coefficient of the acceleration.

These results confirms that our techniques achieves a fast enough time and velocity resolution to get a good estimate of particle acceleration. As they have lower velocities and accelerations at low Reynolds number, it is more difficult to separate the particles acceleration at $R_\lambda = 450$ from the short correlation noise. As previously shown in [2] using the same type of filtering, this is at the origin of the slight difference at small times for the correlation curve at $R_\lambda = 450$ compared to the other cases.

We now apply our technique to compare Lagrangian tracers to the dynamics of heavier and lighter particles. We first compute the velocity root mean square value $u_{\rm rms}$ for all three cases: the values are $1.1, 1.2, 1.0 \pm 0.1\,{\rm m\cdot s^{-1}}$ at $R_\lambda = 850$ for the neutral, heavy (PMMA spheres) and light particles (bubbles). These values are identical within error bars. It indicates that the large-scale dynamics of the particles is unaffected by changes in their density (inertia). The acceleration distribution and autocorrelation are shown in fig. 5. When normalized by the acceleration variance, the acceleration PDFs are quite similar for acceleration values below about $15 a_{\rm rms}$, as also observed in low Reynolds number numerical simulations [17]. The normalized acceleration variance a_0 varies very significantly as shown in table 2: it is reduced to 4.3 ± 1 for heavier particles at $R_\lambda = 850$ while it is increased to 26 ± 5 for bubbles. Note that in dimensional units, the rms acceleration for bubbles is $159\,g$ so that accelerations events a of $15\,a_{\rm rms}$ amplitude (not uncommon as shown in the PDF) corresponds to almost $2400\,g$. The correlation functions also display significant changes with the inertia: the characteristic time of decay is longer for heavy particles and much shorter for bubbles compared to neutral particles. We obtain $\tau_{\rm corr}/\tau_\eta = 0.5, 0.9, 0.25$ respectively, for neutral, heavy and light particles, with the correlation time defined as the half-width at mid-amplitude of the

Table 2: Parameters of the particles at $R_\lambda = 850$ ($\eta = (\nu^3/\epsilon)^{1/4} = 17\,\mu$m and $\tau_\eta = \sqrt{\nu/\epsilon} = 0.26\ 10^{-3}$ s). ρ_p and ρ_f are the densities of the particles and fluid, and $\tau_{\rm corr}$ is defined as the half-width at mid amplitude of the acceleration autocorrelation function.

Particles	radius a	$\beta = \dfrac{3\rho_f}{\rho_f + 2\rho_p}$	$\dfrac{\tau_{\rm corr}}{\tau_\eta}$	a_0
Tracers	$15.5\,\mu$m	0.96	0.5	6.4 ± 1
Heavy	$20.5\,\mu$m	0.79	0.9	4.3 ± 1
Bubbles	$75\,\mu$m	2.99	0.25	26 ± 5

correlation function. We thus observe significant changes in the dynamics, even if the (normalized) distributions of accelerations change weakly with inertia.

We now briefly discuss these results. In order to characterize the dynamics of a solid particle, one must specify two dimensionless numbers: the Stokes number which, in the case of turbulent flows, is the ratio of the response time of the particle to the Kolmogorov time scale, and the density ratio of the particle to that of the fluid. In the asymptotic case of large inertia, only the Stokes number matters [10]. However, in the measurements reported here inertia remains finite, even for the bubble case because of added mass effects. In the limit of small particle sizes compared to the Kolmogorov length scale one generally uses the equation of motion for a solid particle [18,19]:

$$\frac{\mathrm{d}\mathbf{v}_p}{\mathrm{d}t} = \beta \frac{D\mathbf{u}}{Dt} + \mathbf{F}, \tag{2}$$

where $\mathbf{v}_p$ is the particle velocity, $\beta = 3\rho_f/(2\rho_p + \rho_f)$, ρ_f and ρ_p are the fluid and particle specific mass, respectively), $D\mathbf{u}/Dt$ is the acceleration of the fluid particle that would be at the position of the solid particle in the undisturbed flow and $\mathbf{F}$ incorporates other forces such as drag, lift, history and possibly buoyancy. Here, $\beta = 1$, 0.8 and 3 for our neutral, heavy and light particles. Note that bubbles with such a small diameter are usually considered as being rigid because of impurities in the fluid [20], with a boundary condition which may be different from that of a solid particle. Qualitatively, we find that the trend for the measured acceleration variance follows that of β in eq. (2). Quantitatively, for heavy particles it changes roughly as β, but for the bubbles, which may be not considered as pointwise since their radius is $a \sim 5\eta$, the acceleration variance is only about 2 times that of the fluid. This is different from what was reported in [2] where a stronger influence of small change in the particles density was observed.

To conclude, we have reported here an extended laser Doppler velocimetry technique (ELDV) for the tracking of individual particles in fully developed turbulence. Its advantage is that it may be more easily adapted from commercial equipment than ultrafast PIV, and requires less laser power for illumination. The very close agreement between the measurements reported here and the Cornell [3] data is expected because they share the same flow geometry. The fact that it is observed using two very different techniques and signal processing validates both (as the performance of the high-speed imaging method had not been matched previously). Application of the ELDV technique to the study of inertial particles with a finite density shows that quite different dynamics may lead to very similar statistics of (normalized) particle accelerations, an observation that may prove useful for modeling.

* * *

We are indebted to A. Petrosian for his help in setting up the optics of the experiment, and to M. Bourgoin for many fruitful discussions. This work was partially funded by the Region Rhône-Alpes, under Emergence Contract No. 0501551301.

REFERENCES

[1] Fox R. O. and Yeung P. K., *Phys. Fluids*, **15** (2003) 961; Sawford B., *Annu. Rev. Fluid Mech.*, **33** (2001) 289.
[2] Voth G. A., La Porta A., Crawford A. M., Alexander J. and Bodenschatz E., *J. Fluid Mech.*, **469** (2002) 121.
[3] Mordant N., Crawford A. M. and Bodenschatz E., *Physica D*, **193** (2004) 245; *Phys. Rev. Lett.*, **94** (2004) 024501.
[4] Xu H. *et al.*, *Phys. Rev. Lett.*, **96** (2006) 024503.
[5] Lüthi B., Ott S., Berg J. and Mann J., *Phys. Rev. E*, **74** (2006) 016304; Bourgoin M. *et al.*, *Science*, **311** (2006) 835; Xu H., Ouellette N. T., Nobach H. and Bodenschatz E., *ETC11 Proceedings* (Springer) 2007.
[6] Mordant N. *et al.*, *Phys. Rev. Lett.*, **87** (2001) 214501; Mordant N., Metz P., Michel O. and Pinton J.-F., *Rev. Sci. Instrum.*, **76** (2005) 025105.
[7] Mordant N., Lévêque E. and Pinton J.-F., *New J. Phys.*, **6** (2004) 116.
[8] Lehmann B., Nobach H. and Tropea C., *Meas. Sci. Technol.*, **13** (2002) 1367.
[9] Falkovich G., Fouxon A. and Stepanov M., *Nature*, **419** (2002) 151; Shaw R., *Annu. Rev. Fluid Mech.*, **35** (2003) 183.
[10] Bec J., Cencini M. and Hillerbrand R., *Physica D*, **226** (2007) 11; Bec J. *et al.*, *Phys. Rev. Lett.*, **98** (2007) 084502.
[11] Fessler J. R., Kulick J. D. and Eaton J. K., *Phys. Fluids*, **6** (1994) 3742.
[12] Ayyalasomayajula S., Gylfason A., Collins L. R., Bodenschatz E. and Warhaft Z., *Phys. Rev. Lett.*, **97** (2006).
[13] Calzavarini E., Cencini M., Lohse D. and Toschi F., *Advances in Turbulence XI* (Springer) 2007, ISBN: 978-3-540-72603-6, pp. 418–420.
[14] Sundaram S. and Collins L. R., *J. Fluid Mech.*, **379** (1999) 105.
[15] Martinez-Bazá C., Montañés J.-L. and Lasheras J. C., *J. Fluid Mech.*, **401** (1999) 183.
[16] Mordant N., Michel O. and Pinton J.-F., *J. Acoust. Soc. Am.*, **112** (2002) 108.
[17] Mazzitelli I. M. and Lohse D., *New J. Phys.*, **6** (2004) 203.
[18] Maxey M. R. and Riley J., *Phys. Fluids*, **26** (1983) 883.
[19] Howe M. S., *Q. J. Mech. Appl. Math.*, **48** (1995) 401.
[20] Duineveld P. C., *J. Fluid Mech.*, **292** (1995) 325.

Available online at www.sciencedirect.com
ScienceDirect
Physica D 237 (2008) 2084–2089
PHYSICA D
www.elsevier.com/locate/physd

Acceleration of heavy and light particles in turbulence: Comparison between experiments and direct numerical simulations

R. Volk[a,*], E. Calzavarini[b], G. Verhille[a], D. Lohse[b], N. Mordant[c], J.-F. Pinton[a], F. Toschi[d,e]

[a] *Laboratoire de Physique, de l'École normale supérieure de Lyon, CNRS UMR5672, 46 Allée d'Italie, 69007 Lyon, France*
[b] *Faculty of Science, J.M. Burgers Centre for Fluid Dynamics, and Impact-Institute, University of Twente, 7500 AE Enschede, The Netherlands*
[c] *Laboratoire de Physique, Statistique de l'École normale supérieure de Paris, CNRS UMR8550, 24 rue Lhomond, 75005 Paris, France*
[d] *Istituto per le Applicazioni del Calcolo CNR, Viale del Policlinico 137, 00161 Roma, Italy*
[e] *INFN, Sezione di Ferrara, Via G. Saragat 1, I-44100 Ferrara, Italy*

Available online 24 January 2008

Abstract

We compare experimental data and numerical simulations for the dynamics of inertial particles with finite density in turbulence. In the experiment, bubbles and solid particles are optically tracked in a turbulent flow of water using an Extended Laser Doppler Velocimetry technique. The probability density functions (PDF) of particle accelerations and their auto-correlation in time are computed. Numerical results are obtained from a direct numerical simulation in which a suspension of passive pointwise particles is tracked, with the same finite density and the same response time as in the experiment. We observe a good agreement for both the variance of acceleration and the autocorrelation time scale of the dynamics; small discrepancies on the shape of the acceleration PDF are observed. We discuss the effects induced by the finite size of the particles, not taken into account in the present numerical simulations.

PACS: 47.27.Jv; 47.27.Gs; 02.50.-r

Keywords: Inertial particles; Lagrangian acceleration; Lagrangian turbulence

1. Introduction

Understanding the transport of inertial particles with finite density, such as sediments, neutrally buoyant particles or bubbles in turbulent flows of water is of practical interest for both industrial engineering or environmental problems. In a turbulent flow, the mismatch in density between the particles and the fluid causes light particles to be trapped in high vortical regions while heavy particles are ejected form vortex cores and concentrate in high strain regions [1]. As particles with different buoyancy tend to concentrate in different regions of the flow, they are expected to exhibit different dynamic behaviours. In recent years, significant progress has been made in the limit of infinitely heavy, pointwise particles [2,3], and numerical simulations have received experimental support [4,5]. In case of infinitely light particles (*bubbles*): the result of the numerical simulations on particle distributions and on fluid velocity spectra [6–8] agree in various aspects with experimental findings [9–12] although direct comparison between experiments and numerical simulations for the acceleration PDF and correlation of the particles has not been investigated in the past.

Indeed, in spite of the growing resolution of Direct Numerical Simulations (DNS) of the Navier-Stokes equations at high Reynolds numbers, it remains a challenge to resolve the motion of realistic inertial particles: some degree of modelization is necessary. The equation of motion of finite size, finite density particles moving in a turbulent flow, is not precisely known, and a comparison with experimental data can help in refining the models and extending their range of validity.

Several experimental techniques have been developed for measuring the velocity of particles along their trajectories. The optical tracking method developed in the Cornell group

* Corresponding author. Tel.: +33 472728472; fax: +33 472728080.
E-mail address: romain.volk@ens-lyon.fr (R. Volk).

0167-2789/$ - see front matter © 2008 Elsevier B.V. All rights reserved.
doi:10.1016/j.physd.2008.01.016

has revealed that fluid particles experience extremely intense accelerations [13], while individual particles have been tracked for time durations of the order of the flow integral time scale using an acoustic technique [14]. Because of the very fast decrease of the acoustic scattering cross-section with the scatterer's size, this method is limited to particles with diameter of the order of the wavelength, *i.e.* inertial range sizes [15, 23]. The principle of the acoustic technique is completely analogous to laser Doppler velocimetry (LDV), provided that expanded light beams are used (an arrangement we call E-LDV hereafter). The advantage of E-LDV, compared to acoustics, is that the much smaller wavelength of light allows a better resolution in space and also the use of smaller tracer particles. The principle of the measurement technique is reported in [16], where its performance has been compared and validated against silicon-strip tracking [13,17] of neutrally buoyant Lagrangian tracers. We focus here on the dynamics of inertial particles *i.e.* particles whose density differ from that of the fluid. We report the first comparison between experimental measurements of acceleration of particles having a relative density in the range 10^{-3} (air bubbles) to 1.4 (PMMA) in the same highly turbulent flow, and numerical results obtained by tracking pointwise particles with finite density in a direct numerical simulation of isotropic homogeneous turbulence [18,19].

Numerical simulations are performed by means of standard pseudo-spectral methods, where particular care has been used in keeping a good resolution at the dissipative scales. The numerical code for integrating the evolution of the Eulerian field and the Lagrangian tracing of particles is the same as described in [7,8,25]. A thorough validation of the numerical approach, included the Lagrangian evolution of the tracers has recently been performed against experimental measurements [26]. The numerical integration of tracers has, with respect to experiments, the clear advantage of a uniform, well controlled geometry and very large statistics; on the opposite, the resolution can be limited to small Reynolds numbers. For what concerns the treatment of realistic particles, i.e. particles with a density mismatch and a "finite" size, the best modelization to use is not clear and one of the main goals of this manuscript is indeed to compare state-of-the-art Lagrangian data against numerical results from a current modelization.

2. Experimental setup and results

The Laser Doppler technique is based on the same principle as the ultrasound Doppler method which has good tracking performance of individual Lagrangian tracers [14,23]. In order to access dissipative scales, and in particular for acceleration measurements, we adapt the technique from ultrasound to laser light: the gain is of a factor 1000 in wavelength so that one expects to detect micron-sized particles. For a Lagrangian measurement, one has to be able to follow the particle motion to get information about its dynamics in time. For this, wide Laser beams are needed to illuminate the particle on a significant fraction of its path. The optical setup is an extension of the well known laser Doppler velocimetry technique; Fig. 1. A Laser beam is split into two beams; each is then expanded by

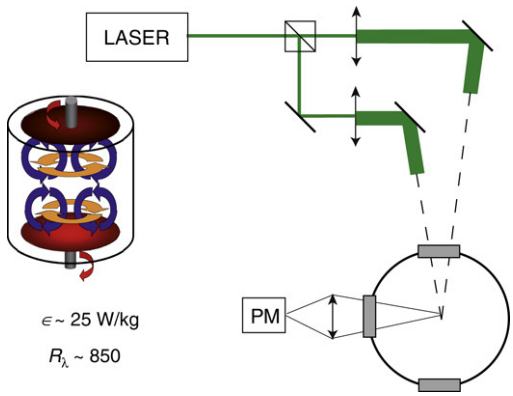

Fig. 1. Experimental setup. (Top left): schematics of the von Kármán flow in water – side view. (Top right): principle of the Laser-Doppler Velocimetry using wide beams (ELDV) – top view of the experiment. PM: location of the photmultipler which detects scattering light modulation as a particle crosses the interference pattern created at the intersection of the laser beams.

a telescope so that their diameter is about 5 mm. Then the two beams intersect in the flow where they create an array of interference fringes. As a particle crosses the fringes, the scattered light is modulated at a frequency directly proportional to the component of the velocity perpendicular to the fringes. It yields a measurement of one component of the particle velocity. In practice, we use a CW YAG laser of wave length 532 nm with 1.2 W maximum output power. In order to get the sign of the velocity we use acousto-optic modulators (AOM) to shift the frequency of the beams so that the fringes are actually travelling at a constant speed. The angle of the two beams is tuned to impose a 60 microns inter-fringe so that the frequency shift between the beams (100 kHz) corresponds to 6 m/s. As the beams are not focused, the inter-fringe remains constant across the measurement volume whose size is about $5 \times 5 \times 10$ mm^3. It is imaged on a photomultiplier whose output is recorded using a National Instrument PXI-NI5621 digitizer at rate 1 MHz.

The flow is of the Von Kármán kind as in several previous experiments using acoustics [14] or optical techniques [13]. Water fills a cylindrical container of internal diameter 15 cm, length 20 cm. It is driven by two disks of diameter 10 cm, fitted with blades in order to increase steering. The rotation rate is fixed at values up to 10 Hz. For the measurements reported here, the Taylor-based Reynolds number reaches up to 850 at a maximum dissipation rate ϵ equal to 25 W/kg. We study three types of particles: neutrally buoyant polystyrene particles with size 31 microns and density 1.06, PMMA particles with size 43 microns and density 1.4 and air bubbles with a size of about 150 microns. The mean size of the bubbles, measured optically by imaging the measurement volume on a CCD, is imposed by the balance between the interfacial surface tension σ and the turbulent fluctuations of pressure. This fragmentation process is known to lead to a well defined and stationary size distribution [20] with a typical diameter $D \propto (\sigma/\rho_f)^{3/5}\epsilon^{-2/5}$, ρ_f being the density of the fluid.

The signal processing step is crucial as both time and frequency – (*i.e.* velocity) – resolutions rely on its performance. Frequency demodulation is achieved using the same algorithm as in the acoustic Doppler technique. It is a approximated

Table 1
(top) Parameters of the particles in the von Kármán flow at $R_\lambda = 850$ ($\eta = (\nu^3/\epsilon)^{1/4} = 17$ μm and $\tau_\eta = \sqrt{\nu/\epsilon} = 0.26\ 10^{-3}$ s)

Experiment					
Particle	Radius a	$\beta = \frac{3\rho_f}{\rho_f+2\rho_p}$	$St = \frac{\tau_p}{\tau_\eta}$	a_0	$a_0/a_{0,T}$
Tracers	15.5 μm	0.96	0.24	6.4 ± 1	1
Neutral	125 μm	0.96	16	2.2 ± 1	0.34
Heavy	20.5 μm	0.79	0.58	4.3 ± 1	0.67
Bubble	75 μm	2.99	1.85	26 ± 5	4.06
Numerics					
Particle	Radius a	$\beta = \frac{3\rho_f}{\rho_f+2\rho_p}$	$St = \frac{\tau_p}{\tau_\eta}$	a_0	$a_0/a_{0,T}$
Tracers	–	1	0.31	2.85 ± 0.07	1
Neutral	–	1	4.1	2.94 ± 0.07	1.03
Heavy	–	0.75	1.03	2.63 ± 0.12	0.92
Bubble	–	3	1.64	25.9 ± 0.46	9.08

ρ_p and ρ_f are the densities of the particles and fluid, and $\tau_p = a^2/(3\beta\nu)$ is the stokes response time of the particles. The Taylor-based turbulent Reynolds number is computed as $R_\lambda = \sqrt{15u_{\rm rms}^4/\epsilon\nu}$ measuring the one-component root-mean-square velocity, $u_{\rm rms}$, with the E-LDV system and ϵ by monitoring the power consumption of the motors. The nondimensional constant a_0 is derived from the Heisenberg–Yaglom relationship. The last column compares the value for the inertial particle to the one obtained for the Lagrangian tracer (which is denoted by the subscript T). (bottom) Same as above: parameters of the particles tracked in the DNS of homogeneous isotropic turbulence at $R_\lambda = 180$. Out of the numerically analysed 64 parameter combinations (β, St), we have picked those which were close to the experimental values for (β, St).

maximum likelihood method coupled with a Kalman filter [21]: a parametric estimator assumes that the signal is made of a modulated complex exponential and Gaussian noise. The amplitude of the recorded signal and the modulation frequencies are assumed to be slowly evolving compared to the duration of the time window used to estimate the instantaneous frequency. Here the time window is about 30 μs long and sets the time resolution of the algorithm. Outputs of the algorithm are the instantaneous frequency, the amplitude of the modulation and a confidence estimate which is used to eliminate unreliable detections. Afterwards, the acceleration of the particle is computed by differentiation of the velocity output. Note that measurements are performed only when a particle moves within the (limited) measurement volume so that after processing, the data consists in a collection of sequences with variable lengths. For all the measurements, the acceleration variance is computed using the same procedure as in [17]: it is obtained for several widths of the smoothing kernel used in the differentiation of the velocity signal and then interpolated to zero filter width.

For small neutrally buoyant particles, *i.e.* Lagrangian tracers, our data is in excellent agreement with the high-speed imaging measurements performed by the Cornell group [13,16,17]. When the variance of the acceleration is normalized by the Heisenberg–Yaglom scaling: $\langle a^2\rangle = a_0\epsilon^{3/2}\nu^{-1/2}$ (ϵ being the energy dissipation rate per unit mass and $\nu = 1.3 \cdot 10^{-6}$ m^2 s^{-1} the kinematic viscosity of the fluid), both experiments yields the same values for the nondimensional constant a_0 ($a_0 = 6.4 \pm 1$ at $R_\lambda = 850$ for the E-LDV compared to 6.2 ± 0.4 for the Cornell data at $R_\lambda = 690$).

We have applied our technique to compare the dynamics of Lagrangian tracers to the one of heavier or lighter particles (see Table 1 for numbers). We first compute the velocity root-mean-square value $u_{\rm rms}$ for the three cases: the values are $\{1.1, 1.2, 1.0\} \pm 0.1$ m.s^{-1} at $R_\lambda = 850$ for the tracers, heavy (PMMA spheres), and light particles (bubbles). Within error bars, the large scale dynamics seems to be unaffected by changes in the particle inertia. The acceleration distribution and autocorrelation in the three cases are shown respectively in Fig. 2 (top) and Fig. 3 (top). The acceleration PDFs are quite similar for moderate acceleration values (below about $10\,a_{\rm rms}$), as also observed in low Reynolds number numerical simulations [22]. However, the probability of very large accelerations seems to be reduced in the case of inertial particles as compared to Lagrangian tracers. The normalized acceleration variance a_0 varies very significantly: it is reduced to 4.3 ± 1 for heavier particles while it is increased to 26 ± 5 for bubbles. The correlation functions also show significant changes with inertia: the characteristic time of decay is longer for heavy particles and shorter for bubbles compared to tracers. We measure $\tau_{\rm corr}/\tau_\eta = \{0.5,\ 0.9,\ 0.25\}$ respectively for tracers, heavy and light particles, with the correlation time defined as the half-width at mid-amplitude of the correlation function. We thus observe important changes in the dynamics, even if the distribution of acceleration weakly changes with inertia.

Note that in our setup the Kolmogorov length is about $\eta = 17$ μm at $R_\lambda = 850$, so that the bubble size is about $10\ \eta$ and therefore may not be considered as a point particle. Thus, one may wonder if the bubble dynamics is not altered by spatial filtering as recently demonstrated for particles with diameters in the inertia range [23]. To check, we have compared the dynamics of large neutrally buoyant particles with diameter 250 μm to the one of Lagrangian tracers. The results is shown in Fig. 2 together with the other particles: the effect of the particle size on the PDF is found to be weak as the curve nicely superimposes with the ones for inertial particles. However, the size effect is clear when comparing either the coefficient a_0 (reduced to 2.2), or the autocorrelation functions. One observes that the correlation time of the large particles is twice that

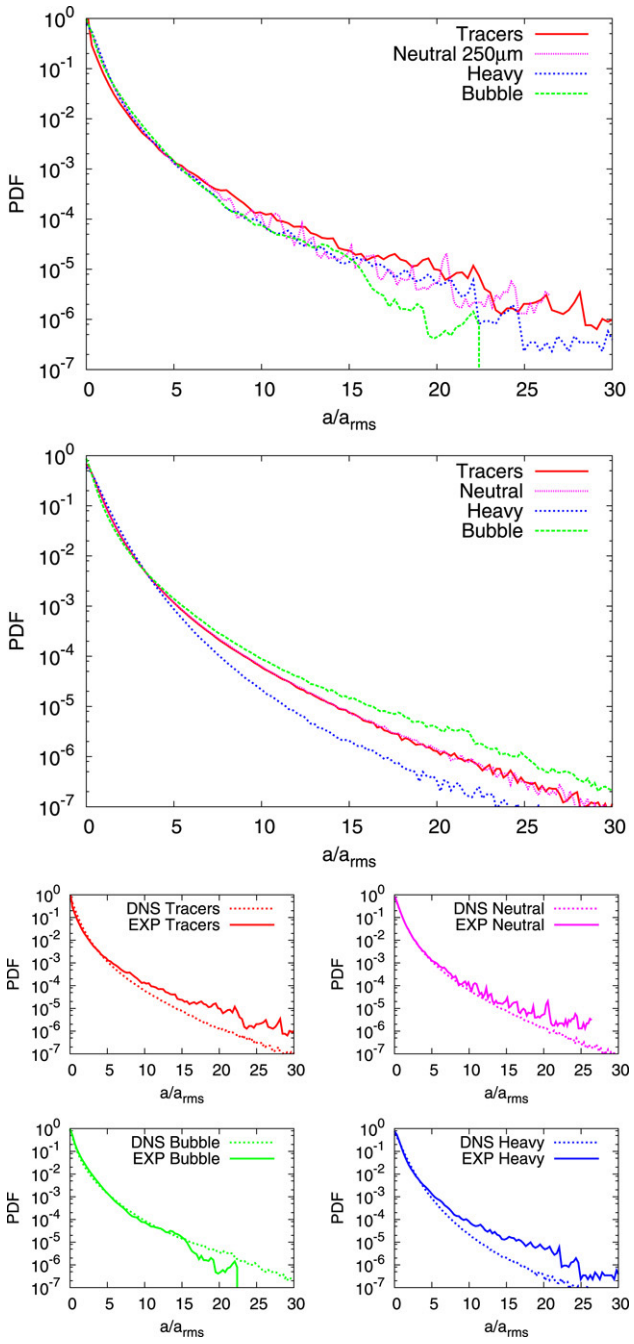

Fig. 2. Probability distribution function of accelerations, normalized to the variance of the data sets. (top) Data from experiment at $R_\lambda = 850$. (middle) DNS of homogeneous isotropic turbulence at $R_\lambda = 180$. (bottom) Comparison of experimental measurements and DNS results.

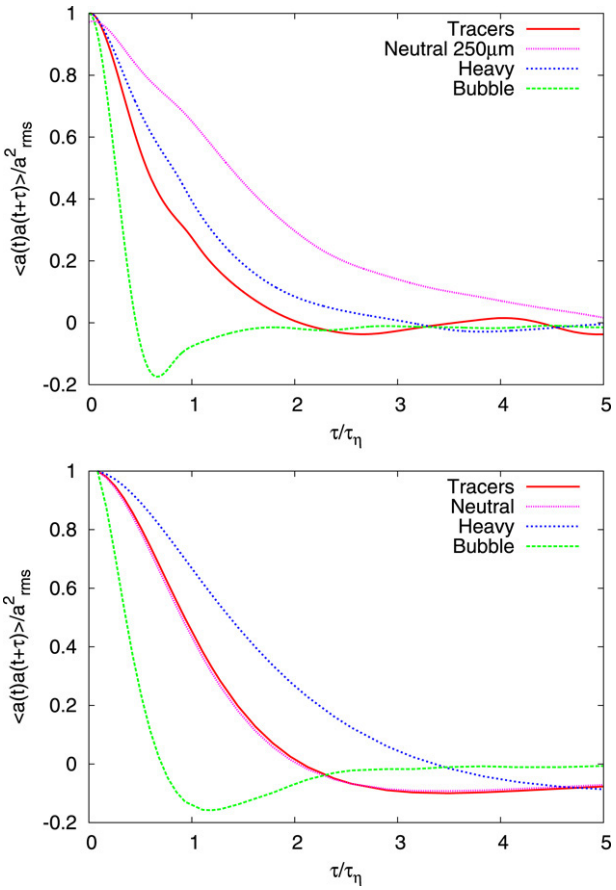

Fig. 3. Autocorrelation coefficients of the accelerations: (top) Data from experiments at $R_\lambda = 850$. (bottom) Data from DNS of homogeneous isotropic turbulence at $R_\lambda = 180$ For the (β, St) values we refer to Table 1.

for the tracers. We conclude that the bubbles size may have a leading effect on the acceleration variance, and that the value of a_0 reported here probably underestimates the one that would be measured for smaller bubbles (with diameters closer to the Kolmogorov scale).

3. Comparison with numerical simulations

We compare the experimental data with the results from a direct numerical simulation [18,19] where a passive suspension of pointwise particles with finite density are tracked in a homogeneous isotropic turbulent flow. The dynamics of the particles is computed in the most simplified form of the equation of motion, *i.e.* assuming that the particles are spherical, nondeformable, smaller than the Kolmogorov length scale of the flow, and that their Reynolds number is small [24]. When we retain only the Stokes drag force and the added mass effect, the equation of motion then reads

$$\frac{\mathrm{d}\mathbf{v}_p}{\mathrm{d}t} = \beta \frac{D\mathbf{u}}{Dt} + \frac{1}{\tau_p}\left(\mathbf{u} - \mathbf{v}_p\right), \tag{1}$$

where $\mathbf{v}_p = \dot{x}(t)$ is the particle velocity, $\mathbf{u}(x(t), t)$ the velocity of the fluid at the location of the particle described by the Navier–Stokes equation, while $\beta = 3\rho_f/(\rho_f + 2\rho_p)$ accounts for the added mass effect and and $\tau_p = a^2/(3\beta\nu)$ is the Stokes response time for a particle of radius a. When made dimensionless by the Kolmogorov dissipative scales $(\tau_\eta, \eta, u_\eta)$ Eq. (1) reads

$$\mathbf{a} \equiv \frac{\mathrm{d}\mathbf{v}_p}{\mathrm{d}t} = \beta \frac{D\mathbf{u}}{Dt} + \frac{1}{St}\left(\mathbf{u} - \mathbf{v}_p\right), \tag{2}$$

with the particle acceleration $\mathbf{a}$ now expressed in the Heisenberg–Yaglom units. Thus, at a given Reynolds number, the particles dynamics only depends on the values of the two dimensionless parameters β and $St = \tau_p/\tau_\eta$ This is generally

different from the case of infinite inertia of the particles ($\beta = 0$) and finite response time τ_p, which has been formerly addressed in several numerical and theoretical studies [2], and for which instead only the Stokes number St matters. It is also different from the pure bubble case ($\beta = 3$) for which the particle indeed has no inertia but only added mass [6–8]. We performed numerical simulation at $Re_\lambda = 180$ (grid resolution 512^3), in which many particles, characterized by different pairs, (β, St) (specifically 64 different sets of $O(10^5)$ particles) were numerically integrated by means of Eq. (1). Particles do not have feedback on the flow field.

In order to compare the numerical results with the experimental data, three types of particles (tracers, heavy and bubbles) with different inertia and Stokes number have been studied. The values for both β and St have been chosen close to the ones of the particles used for the E-LDV (see Table 1). The evolution of the normalized acceleration variance shows the same trend in experiments and numerics: a_0 is reduced from the tracer value 2.85 to 2.63 for heavier particles and increased to 26 for bubbles (Table 1). This seems to be a robust trend in the DNS. To emphasize this, in Fig. 4 we show the behaviour of $\sqrt{a_0}$, i.e. the root-mean-square value of the particle acceleration normalized by the Heisenberg–Yaglom scaling, in a wide range of the (β, St) parameter space from a less turbulent DNS ($Re_\lambda = 75$) which has a very large number of (β, St) pairs. Results from the $Re_\lambda = 180$, not shown here, are qualitatively similar. Note again that no significant Reynolds number dependence of the probability distribution was found in Ref. [16].

The acceleration distribution behavior and its comparison with the experiment is reported in Fig. 2. In the numerics we observe that the probability of very large accelerations is reduced for the heavier particles as compared with tracers, while it is increased for the bubbles. This feature,seems not to be present in the experimental results. Furthermore, we notice that for the three types of particles, the acceleration PDFs, rescaled by the *rms* acceleration, is close to the experiments. Experimental ones have always longer tails, reflecting the more intermittent nature of the turbulent flow, which has a larger Reynolds number ($Re_{\lambda,\mathrm{EXP}} = 850$ vs. $Re_{\lambda,\mathrm{DNS}} = 180$). We also observe a qualitative agreement for the changes in the acceleration autocorrelation functions when changing inertia, Fig. 3. One measures $\tau_{\mathrm{corr}}/\tau_\eta = \{0.95,\ 1.35,\ 0.25\}$ respectively for tracers, heavy and light particles. Just as observed for the experiments, the dynamics is faster for the bubbles while heavier particles decorrelate slower than fluid tracers. The Re_λ difference is more pronounced here than in the PDFs (see Ref. [16]) and prevent a more detailed comparison.

4. Discussion

While solving a simplified version for the equation of motion, the numerics reproduce qualitatively the effect of the particles' inertia on their dynamics. In particular, the dependence of the acceleration autocorrelation on the particle inertia is nicely reproduced, see Fig. 3. However, also some discrepancies become visible, though not yet completely

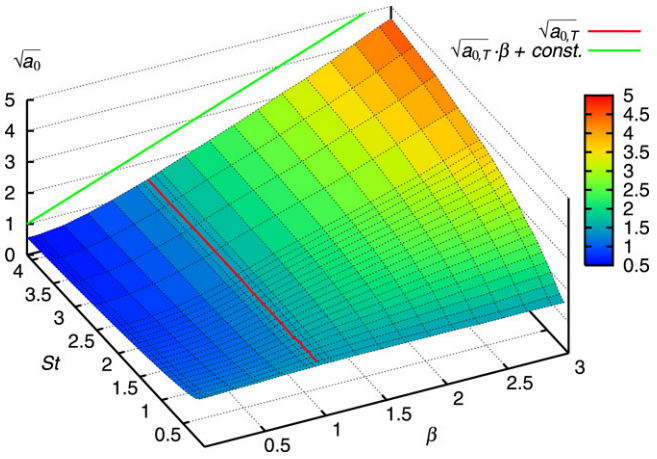

Fig. 4. Behaviour of the normalized *root-mean-square* acceleration $\sqrt{a_0} = (\langle a^2\rangle \epsilon^{-3/2}\nu^{1/2})^{1/2}$ as a function of both St and β for a $Re_\lambda = 75$ DNS. Iso-contour for $\sqrt{a_{0,T}}$ (red) and the line $\sqrt{a_{0,T}}\cdot\beta + const.$ (green) are also reported. Note that a_0 does not depend on St for neutral ($\beta = 1$) particles. While it is always reduced/enhanced for heavy/light particles. For large particles ($St \simeq 4.1$) we find $\sqrt{a_0} \simeq \beta\sqrt{a_{0,T}}$. (For interpretation of the references to colour in this figure legend, the reader is referred to the web version of this article.)

conclusive, as a better resolution and statistics of both the experiments and the numerics would be important for firmer conclusions. Nevertheless, in this section we shall have a closer look at the differences and propose some explanations.

First of all, there is only qualitative agreement on the ratio $a_{0,H}/a_{0,T}$. It is larger for the experiment than for the numerics. Moreover, the tails of the numerical PDF of the bubble acceleration seem to be enhanced as compared to those for tracer acceleration. Vice versa, the tails of the numerical PDF of the particle acceleration seem to be reduced as compared to those for tracer acceleration.

What is the origin of the difference between the experiments and the numerics? First of all the Taylor–Reynolds numbers are different, but Ref. [16] suggests an at most weak dependence of the acceleration PDFs on the Reynolds number; a finding that is supported by a comparison of our numerical simulations at $Re_\lambda = 185$ and $Re_\lambda = 75$.

Next, in the numerical simulations we disregarded the lift and the gravitational force. While this presumably has little effect on heavy particles and tracer, it does modify the dynamics of the bubbles. In Refs. [7,8] we had shown by comparison of numerical simulations for point bubbles with and without lift, that without lift the bubble accumulation inside the vortices is more pronounced, i.e. bubbles without lift are more exposed to the small-scale fluctuations, which clearly will contribute to the pronounced tails of the numerically found acceleration PDF, see Fig. 3, bottom.

Next, also the two-way coupling of the particles (i.e., the back-reaction of the particles on the flow due to their buoyancy difference) has been neglected in the simulations of this paper. As e.g. shown in Refs. [7,8] for bubbles and in Ref. [27] for particles, it has an effect on the turbulent energy spectrum and thus also on the acceleration statistics. However, as in the present experiments the particle and bubble concentrations are

very low, the two-way coupling effect on the spectra should hardly be detectable.

The final difference between numerics and experiments we will discuss here – and presumably the most relevant one – is the finite size of the particles in the experiments as compared to the numerics which is based on effective forces on a point particle. Although the heavy particles are not large as compared to η, this clearly holds for the bubbles and the 250 μm diameter neutral particles. Indeed, Fig. 3 shows how the finite size of these particles smears out the acceleration autocorrelation, as compared to the tracer case. Also the ratio $a_{0,N}/a_{0,T}$ for large neutral particles is only 0.34, which demonstrates that the size of large particles has a large effect on their acceleration variance. This type of spatial filtering, which also lowers the PDF of large neutral particles in the experiment, is not related to a temporal filtering of the particle based on its response time. This is clearly visible in Fig. 2 (middle) where one can see that two neutral particles ($\beta = 1$) with different response times (different St or τ_p) have the same acceleration PDF, with same a_0, and same autocorrelation function. Thus this size effect, which is not taken into account in the point-particle-based numerical simulations, presumably is responsible for both the relatively small value of $a_{0,B}/a_{0,T}$ measured for bubbles, and the change in the shape of the PDF.

To conclude, we have reported acceleration measurements of inertial particles using extended Laser Doppler velocimetry and have compared the experimental data to DNS simulations of the motion of pointwise particles with finite density. We have observed a qualitative agreement between experiments and numerics in the shape of the PDF and of the autocorrelation function. We have given arguments for the small discrepancies. An experimental study of the motion of bubbles with smaller sizes is needed for a better comparison with the numerical simulations. Also numerical simulations keeping into account the finite size of particles would presumably improve the agreement between experiments and numerical data and detailed comparisons as the one presented in this paper help to reveal the limitations of point-particle models. Obviously, going beyond point-particles is extremely challenging in numerical simulations. A first step in this direction has e.g. been taken by Prosperetti and coworkers with their *Physalis* method [28] which presently is extended towards turbulent flows [29].

Acknowledgements

RV, GV, NM and JFP are indebted to Artem Petrosian for his help in setting-up up the optics of the experiment, and to Mickael Bourgoin for many fruitful discussions. We are grateful to Massimo Cencini, who contributed to the numerical study. This work was partially funded by the Region Rhône-Alpes, under Emergence Contract No. 0501551301, and by ANR contract #192604. We thank the CASPUR (Rome-ITALY), CINECA (Bologna-ITALY) and SARA (Amsterdam, The Netherlands) for computing time and technical support.

References

[1] S. Sundaram, L.R. Collins, J. Fluid Mech. 379 (1999) 105.
[2] J. Bec, M. Cencini, R. Hillerbrand, Physica D 226 (2007) 11;
J. Bec, L. Biferale, M. Cencini, A. Lanotte, S. Musacchio, F. Toschi, Phys. Rev. Lett. 98 (2007) 084502.
[3] M. Cencini, J. Bec, L. Biferale, G. Boffetta, A. Celani, A.S. Lanotte, S. Musacchio, F. Toschi, J. Turb. 7 (36) (2006) 1–17.
[4] J.R. Fessler, J.D. Kulick, J.K. Eaton, Phys. Fluids 6 (1994) 3742–3749.
[5] S. Ayyalasomayajula, A. Gylfason, L.R. Collins, E. Bodenschatz, Z. Warhaft, Phys. Rev. Let. 97 (2006) 144507.
[6] L. Wang, M.R. Maxey, Appl. Sci. Res. 51 (1993) 291–296.
[7] I. Mazzitelli, D. Lohse, F. Toschi, Phys. Fluids 15 (2003) L5–L8.
[8] I. Mazzitelli, D. Lohse, F. Toschi, J. Fluid Mech. 488 (2003) 283–313.
[9] J.M. Rensen, S. Luther, D. Lohse, J. Fluid Mech. 538 (2005) 153–187.
[10] T.H. van den Berg, S. Luther, I. Mazzitelli, J. Rensen, F. Toschi, D. Lohse, J. Turb. 7 (2006) 1–12.
[11] T.H. van den Berg, S. Luther, D. Lohse, Phys. Fluids 18 (2006) 038103.
[12] E. Calzavarini, T.H. van den Berg, S. Luther, F. Toschi, D. Lohse, Quantifying microbubble clustering in turbulent flow from single-point measurements, Phys. Fluids (2008) (in press). arXiv:0607255.
[13] G.A. Voth, A. La Porta, A.M. Crawford, J. Alexander, E. Bodenschatz, J. Fluid Mech 469 (2002) 121.
[14] N. Mordant, et al., Phys. Rev. Lett. 87 (21) (2001) 214501;
N. Mordant, P. Metz, O. Michel, J.-F. Pinton, Rev. Sci. Instr. 76 (2005) 025105.
[15] N. Mordant, E. Lévêque, J.-F. Pinton, New J. Phys. 6 (2004) 116.
[16] R. Volk, N. Mordant, G. Verhille, J.-F. Pinton, Laser Doppler measurement of inertial particle and bubble accelerations in turbulence, Eur. Phys. Lett. (2008) (in press). arXiv:0708.3350.
[17] N. Mordant, A.M. Crawford, E. Bodenschatz, Physica D 193 (2004) 245;
N. Mordant, A.M. Crawford, E. Bodenschatz, Phys. Rev. Lett. 94 (2004) 024501.
[18] E. Calzavarini, M. Kerscher, D. Lohse, F. Toschi, Dimensionality and morphology of particle and bubble clusters in turbulent flow, J. Fluid Mech. (2007) (submitted for publication). Arxiv:nlin.CD/0710.1705.
[19] E. Calzavarini, M. Cencini, D. Lohse, F. Toschi, Quantifying turbulence induced segregation of inertial particles, Phys. Rev. Lett. (2008) (submitted for publication). arXiv:0802.0607.
[20] C. Martinez-Bazá, J.-L. Montañés, J.C. Lasheras, J. Fluid Mech. 401 (1999) 183–207.
[21] N. Mordant, O. Michel, J.-F. Pinton, J. Acoust. Soc. Am. 112 (2002) 108–119.
[22] I.M. Mazzitelli, D. Lohse, New J. Phys. 6 (2004) 203.
[23] N. Qureshi, M. Bourgoin, C. Baudet, A. Cartellier, Y. Gagne, Phys. Rev. Lett. arXiv:0706.3042 (in press).
[24] M.R. Maxey, J. Riley, Phys. Fluids 26 (1983) 883.
[25] L. Biferale, G. Boffetta, A. Celani, B. Devenish, A. Lanotte, F. Toschi, Phys. Rev. Lett. 93 (2004) 064502.
[26] L. Biferale, E. Bodenschatz, M. Cencini, A.S. Lanotte, N.T. Ouellette, F. Toschi, H. Xu, arXiv:0708.0311, 2007.
[27] M. Boivin, O. Simonin, K.D. Squires, J. Fluid Mech. 375 (1998) 235–263.
[28] Z. Zhang, A. Prosperetti, J. Comput. Phys. 210 (2005) 292–324; J. Appl. Mech. - Transactions of the ASME 70 (2003) 64–74.
[29] A. Naso, A. Prosperetti, Proceedings of ICMF 2007, Leipzig (D) July 9-13, 2007.

A.2 Transport de particules de taille finie

[A 3] E. Calzavarini, R. Volk, M. Bourgoin, E. L'évêque, J.-F. Pinton, F. Toschi. Acceleration statistics of finite-sized particles in turbulent flows : the role of Faxen forces. *J. Fluid Mech.*, 630 , 179–189 (2009).

[A 5] R. Volk, E. Calzavarini, E. L'évêque, J.-F. Pinton. Dynamics of inertial particles in a von Karman turbulent flow. *J. Fluid Mech.*, 668 :223-235, (2011).

[A 8] E. Calzavarini, R. Volk, E. L'évêque, J.-F. Pinton, Federico Toschi. Impact of trailing wake drag on the statistical properties and dynamics of finite-sized particle in turbulence. *Physica D*, 241(3) :237-241 (2012).

J. Fluid Mech. (2009), *vol.* 630, *pp.* 179–189.
doi:10.1017/S0022112009006880 Printed in the United Kingdom

Acceleration statistics of finite-sized particles in turbulent flow: the role of Faxén forces

E. CALZAVARINI[1,4]†, R. VOLK[1,4], M. BOURGOIN[2,4], E. LÉVÊQUE[1,4], J.-F. PINTON[1,4] AND F. TOSCHI[3,4]

[1]Laboratoire de Physique de École Normale Supérieure de Lyon, CNRS et Université de Lyon, 46 Allée d'Italie, 69007 Lyon, France

[2]Laboratoire des Écoulements Géophysiques et Industriels, CNRS/UJF/INPG UMR5519, BP53, 38041 Grenoble, France

[3]Department of Physics and Department of Mathematics and Computer Science, Eindhoven University of Technology, PO Box 513, 5600 MB Eindhoven, The Netherlands

[4]International Collaboration for Turbulence Research

(Received 26 November 2008 and in revised form 9 March 2009)

The dynamics of particles in turbulence when the particle size is larger than the dissipative scale of the carrier flow are studied. Recent experiments have highlighted signatures of particles' finiteness on their statistical properties, namely a decrease of their acceleration variance, an increase of correlation times (at increasing the particles size) and an independence of the probability density function of the acceleration once normalized to their variance. These effects are not captured by point-particle models. By means of a detailed comparison between numerical simulations and experimental data, we show that a more accurate description is obtained once Faxén corrections are included.

1. Introduction

The study of Lagrangian turbulence and of turbulent transport of material particles has received growing interest in recent years (Toschi & Bodenschatz 2009). Modern experimental techniques (based on synchronization of multiple fast cameras or ultrasonic/laser Doppler velocimetry) allow nowadays to fully resolve particle tracks in turbulent flows (La Porta *et al.* 2001; Mordant *et al.* 2001; Berg 2006; Xu *et al.* 2006; Volk *et al.* 2008*b*). These techniques have opened the way towards a systematic study of the dynamics of material (or inertial) particles. When the particle density is different from the one of the carrier fluid, a rich phenomenology emerges, such as particle clustering and segregation (Squires & Eaton 1991; Calzavarini *et al.* 2008*a*,*b*). Numerical studies have proven to be essential tools in complementing and benchmarking experimental data of early days: investigations of fluid-tracer dynamics have shown remarkable agreement with experiments (Mordant, Lévêque & Pinton 2004; Arneodo *et al.* 2008; Biferale *et al.* 2008). Lagrangian numerical studies through direct numerical simulations (DNSs) of very small – computationally assumed to be pointwise – particles have also shown encouraging consistency with experimental measurements for inertial particles (Ayyalasomayajula *et al.* 2006; Bec *et al.* 2006; Salazar *et al.* 2008; Volk *et al.* 2008*a*). However, in many situations the size of the

† Email address for correspondence: enrico.calzavarini@ens-lyon.fr

particles is not small with respect to turbulence scales, in particular the dissipative scale η. One example is the plankton which, while neutrally buoyant, cannot be considered as a tracer because of its size in the order of few dissipative scales. Typical marine and atmospherical environmental flows have $\eta \sim O(10)$ μm.

The statistics of particle accelerations, which directly reflect the action of hydrodynamical forces, have been used to experimentally assess the statistical signature of 'large' spherical particles, i.e. whose diameter d is larger than the smallest turbulence scale η. Recent studies (Voth *et al.* 2002; Qureshi *et al.* 2007) and detailed comparison between experiments and numerical simulations (Volk *et al.* 2008*a*) have shown that finite-sized neutrally buoyant particles cannot be modelled as pointwise in numerical studies. Features which have been clearly associated with a finite particle size are as follows:

(i) For neutrally buoyant particles with $d > \eta$ the acceleration variance $\overline{a^2}$ decreases at increasing the particle size. A scaling law behaviour, $\overline{a^2} \sim \overline{\varepsilon}^{4/3} d^{-2/3}$ (with $\overline{\varepsilon}$ being the mean energy dissipation rate), has been suggested on the basis of Kolmogorov's (1941) turbulence phenomenology (Voth *et al.* 2002; Qureshi *et al.* 2007).

(ii) The normalized acceleration probability density function (p.d.f.) depends at best very weakly on the particle diameter. Its shape can be fitted with stretched exponential functions (see Voth *et al.* 2002; Qureshi *et al.* 2007).

(iii) The autocorrelation function of acceleration shows increased correlation time with increasing particle size (Volk *et al.* 2008*a*).

While experimentally it is easier to study large ($d > \eta$) particles, theoretically (and therefore computationally) this turns out to be a far more difficult task. Our aim in this paper is to study the novel features associated with finite particle size in developed turbulent flows while presenting an improved numerical model capable to solve most of the discrepancies between experiments and simulations noticed in Volk *et al.* (2008*a*). We show that qualitatively the new features are well captured by an equation of motion which takes into account the effect of the non-uniformity of the flow at the particle scale. To our knowledge the impact on acceleration statistics of such forces, known since a long time as Faxén corrections (Faxén 1922), has never been considered.

The paper is organized as follows: First we comment on the problems of obtaining an equation of motion for finite-sized particles. We examine the approximation on which point-particle (PP) equations rely and discuss two highly simplified models for the dynamics of small ($d < \eta$) and finite-sized ($d > \eta$) particles. Section 3 gives the numerical implementation of the proposed Faxén-corrected (FC) model. In §4 we show basic physical differences between the statistics of particle acceleration given by numerics with or without Faxén corrections. Section 5 contains the comparison of the model against experimental results, focusing on neutrally buoyant particles. Finally in §6 we summarize the results, critically review the model and discuss how it can be improved.

2. Equation of motion for finite-sized particle in turbulence

Many studies on fine-particulate flows have based particle's description on an equation – referred to as Maxey–Riley–Gatignol – which is an exact derivation of the forces on a particle in a non-uniform unsteady flow in the limit of vanishing Reynolds numbers $Re_p = dv_s/\nu$ and $Re_S = d^2\Gamma/\nu$, where v_s is the slip particle velocity with respect to the fluid and $\Gamma = |\nabla \boldsymbol{u}|$ the typical shear scale in the flow (Gatignol 1983; Maxey & Riley 1983). In the net hydrodynamical force acting on a particle given by

this equation one recognizes several contributions: the steady Stokes drag, the fluid acceleration force (sum of the pressure gradient and the dissipative forces on the fluid), the added mass, the buoyancy, the history Basset–Boussinesq force and Faxén corrections. When the control parameters Re_p and Re_S become finite, the nonlinearity of the flow dynamics in the vicinity of the particle must be taken into account (see the review by Michaelides 1997). An expression for the added mass term which is correct at any Re_p value has been derived by Auton, Hunt & Prud'homme (1988). But much more complicated is the situation for the other forces involved. The drag term becomes Re_p-dependent, and empirical expressions based on numerical computations have been proposed (see Clift, Grace & E. 1978). Furthermore, a lift force appears at finite values of Re_p and Re_S. This force is notably hard to model because of the nonlinear combination of shear and vorticity, and approximate expressions based on Saffman (small Re_p) and Lighthill–Auton (large Re_p) mechanisms are often used in studies (see e.g. discussion on lift on bubbles by Magnaudet & Legendre 1998).

Theoretical and numerical studies of fine disperse multi-phase flows, which aim at describing the behaviour of a large number of particles, have adopted simplified models in which the sub-dominant terms in Maxey–Riley–Gatignol equation are neglected (Balkovsky, Falkovich & Fouxon 2001; Bec 2005). A minimal model, used to address particle Lagrangian dynamics in highly turbulent suspensions, takes into account only a few ingredients: the Stokes drag, the Auton added mass and the fluid acceleration term (Babiano *et al.* 2000; Calzavarini *et al.* 2008 *b*). This leads to

$$\frac{\mathrm{d}\boldsymbol{v}}{\mathrm{d}t} = \frac{3\ \rho_f}{\rho_f + 2\ \rho_p}\ \left(\frac{\mathrm{D}\boldsymbol{u}}{\mathrm{D}t} + \frac{3\nu}{r^2}\,(\boldsymbol{u}-\boldsymbol{v})\right), \tag{2.1}$$

where ρ_f and ρ_p are respectively the fluid and the particle density, ν the fluid kinematic viscosity and $r = d/2$ the radius of the particle, which is considered spherical; $\boldsymbol{v}$ denotes the particle velocity, while $\boldsymbol{u}$ and $\mathrm{D}\boldsymbol{u}/\mathrm{D}t$ are the fluid velocity and acceleration evaluated in its centre of mass. A particle described by the above equation feels the fluid fluctuations only in one point and therefore has no real spatial extension; we may say its size r is essentially 'virtual'. Equation (2.1) indeed contains only a time scale, namely the particle relaxation time τ_p, which embodies the particle length scale merely in combination with the kinematic viscosity of the flow and with the densities coefficients, i.e. $\tau_p \equiv r^2(\rho_f + 2\ \rho_p)/(9\nu\rho_f)$. In practice, the drag term in (2.1) performs a purely temporal filtering of the flow velocity fluctuations.

It is the role of Faxén terms to account for the non-uniformity of the flow at the particle scale. Faxén forces represent necessary physical corrections when analysing the behaviour of $d > \eta$ particles in turbulence. The Faxén theorem for the drag force on a moving sphere states the relation

$$\boldsymbol{f}_D = 6\pi\nu\rho_f r\ \left(\frac{1}{4\pi r^2}\int_{S_p}\boldsymbol{u}(\boldsymbol{x})\ \mathrm{d}S - \boldsymbol{v}\right) = 6\pi\nu\rho_f r(\langle\boldsymbol{u}\rangle_{S_p} - \boldsymbol{v}), \tag{2.2}$$

where the integral is over surface of the sphere and $\boldsymbol{u}(\boldsymbol{x})$ the non-homogeneous steady motion of the fluid in the absence of the sphere. As later shown by Gatignol (1983), Faxén force corrections via sphere volume averages should also be included on the inertial hydrodynamic forces acting on the sphere. In particular the expression for the fluid acceleration and added mass force becomes

$$\boldsymbol{f}_A = \frac{4}{3}\pi r^3\rho_f\left(\left\langle\frac{\mathrm{D}\boldsymbol{u}}{\mathrm{D}t}\right\rangle_{V_p} + \frac{1}{2}\left(\left\langle\frac{\mathrm{d}\boldsymbol{u}}{\mathrm{d}t}\right\rangle_{V_p} - \frac{\mathrm{d}\boldsymbol{v}}{\mathrm{d}t}\right)\right), \tag{2.3}$$

where similarly as above $\langle \ldots \rangle_{V_p}$ denotes the volume average over the spherical particle. Putting together the two force contributions of (2.2) and (2.3) into an equation of motion for a sphere, $(4/3)\pi r^3 \rho_p \, \mathrm{d}\boldsymbol{v}/\mathrm{d}t = \boldsymbol{f}_D + \boldsymbol{f}_A$, and keeping into account the Auton added mass correction for finite Re_P, i.e. $\mathrm{d}\boldsymbol{u}/\mathrm{d}t \to \mathrm{D}\boldsymbol{u}/\mathrm{D}t$, we obtain the phenomenological FC equation of motion:

$$\frac{\mathrm{d}\boldsymbol{v}}{\mathrm{d}t} = \frac{3\ \rho_f}{\rho_f + 2\ \rho_p} \left(\left\langle \frac{\mathrm{D}\boldsymbol{u}}{\mathrm{d}t} \right\rangle_{V_p} + \frac{3\nu}{r^2} (\langle \boldsymbol{u} \rangle_{S_p} - \boldsymbol{v}) \right), \tag{2.4}$$

which we propose as a first-order implementation of finite-sized correction for particle dynamics. In the small particle limit, when $r \to 0$ and $\boldsymbol{u} \simeq \boldsymbol{v}$, corrections can be approximated by Taylor expansion $\langle \boldsymbol{u}(\boldsymbol{x}, t) \rangle_{S_p} \simeq \boldsymbol{u} + (r^2/6)\nabla^2 \boldsymbol{u} + O(r^4)$; $\langle \mathrm{D}\boldsymbol{u}(\boldsymbol{x}, t)/\mathrm{D}t \rangle_{V_p} \simeq (\mathrm{d}/\mathrm{d}t)(\boldsymbol{u} + (r^2/10)\nabla^2 \boldsymbol{u} + O(r^4))$; therefore the first-order Faxén correction accounts for the curvature of the unperturbed flow at the particle location. In a turbulent flow the correction term becomes important when $r > \eta$, with a weak Taylor–Reynolds number Re_λ dependence. An order of magnitude estimate is as follows: Recalling that the Taylor microscale is defined as the radius of curvature of the velocity spatial correlation function at the origin, $\lambda^2 \sim u^2/|u\nabla^2 u|$, one estimates $r^2|\nabla^2 u|/|u| \sim r^2/\lambda^2$. Now by using the relation for the dissipative scale $\eta \sim \lambda/\sqrt{Re_\lambda}$, we find $r^2|\nabla^2 u|/|u| \sim r^2/(\eta^2 Re_\lambda)$. Faxén corrections are relevant when $r \gtrsim \eta\sqrt{Re_\lambda}$, which corresponds to $r \gtrsim O(10)\ \eta$ in typical laboratory experiments ($Re_\lambda \sim O(100)$).

3. Numerical implementation of particle model and turbulence DNSs

We adopt here a further approximation which allows efficient numerical computations of (2.4). Volume averages at particles' positions are substituted by local interpolations after filtering by a Gaussian envelope with standard deviation, σ, proportional to the particle radius. Gaussian convolutions are then efficiently computed in spectral space, and the Gaussian volume averaged field reads

$$\langle u_i \rangle_{G,V_\sigma}(\boldsymbol{x}) = \mathscr{D}\mathscr{F}\mathscr{T}^{-1}_{(N^3)}[\tilde{G}_\sigma(\boldsymbol{k})\ \tilde{u_i}(\boldsymbol{k})], \tag{3.1}$$

where $\mathscr{D}\mathscr{F}\mathscr{T}^{-1}_{(N^3)}$ denotes a discrete inverse Fourier transform on a grid N^3; $\tilde{G}_\sigma(\boldsymbol{k}) = \exp(-\sigma^2\boldsymbol{k}^2/2)$ is the Fourier transform of a unit volume Gaussian function of variance σ; and $\tilde{u_i}(\boldsymbol{k})$ is the Fourier transform of a vector field (the material derivative of fluid velocity in (2.4)). The surface average is obtained using the exact relation

$$\langle u \rangle_{S_p} = \frac{1}{3r^2} \frac{\mathrm{d}}{\mathrm{d}r} (r^3 \langle \boldsymbol{u} \rangle_{V_p}), \tag{3.2}$$

which leads to

$$\langle u_i \rangle_{G,S_\sigma}(\boldsymbol{x}) = \mathscr{D}\mathscr{F}\mathscr{T}^{-1}_{(N^3)}[\tilde{S}_\sigma(\boldsymbol{k})\ \tilde{u_i}(\boldsymbol{k})], \tag{3.3}$$

where $\tilde{S}_\sigma(\boldsymbol{k}) = (1-(1/3)\sigma^2\boldsymbol{k}^2)\mathrm{e}^{-(1/2)\sigma^2\boldsymbol{k}^2}$. It can be shown that with the choice $\sigma = r/\sqrt{5}$, the Gaussian convolution gives the right prefactors for the Faxén corrections in the limit $r \to 0$. Our simplified approach for the integration of (2.4) (FC model) allows to track inertial particles in turbulent flows with minimal additional computational costs as compared to (2.1) (PP model): the fluid acceleration and velocity fields are filtered once for every particle radius size; then the averaged flow at the particle positions are obtained through a trilinear interpolation. We track particles via (2.4) in a stationary homogeneous isotropic flow, generated by large-scale volume forcing

on a cubic domain. The Navier–Stokes (NS) equation is discretized on a regular grid, integrated using a pseudo-spectral algorithm and advanced in time with a second-order Adams–Bashford integrator. The spatial and temporal accuracy of the integration and its validation have been carefully examined. To ensure a good spatial resolution of NS equation we set $\eta\ k_{max} \simeq 1.7$, where k_{max} is the largest represented wave vector. For the time accuracy, controlled by the marching step δt, the Courant number is chosen to be small, $Co \equiv \boldsymbol{u}_{rms}\ k_{max}\ \delta t \simeq 0.16$. With this choice $\tau_\eta \simeq O(10^2)\ \delta t$; therefore the Lagrangian equations for particles considered in this study (all with response time $\tau_p \gtrsim \tau_\eta$) can be safely integrated with the same time stepping of the Eulerian field. We have checked the integration in simple flows cases, e.g. a two-dimensional stationary cellular flow in which the filtered particle dynamics can be derived analytically. The turbulent case instead has been validated by a comparison with an independently developed code, implementing the same equations for particles but with different forcing scheme, temporal integration method (Verlet algorithm) and local interpolation procedure (tricubic algorithm).

We have explored in a systematic way the two-dimensional parameter space $[\rho_p/\rho_f, d/\eta]$ in the range $\rho_p/\rho_f \in [0.1, 10]$ and $d/\eta \in [2, 50]$ for a turbulent flow at $Re_\lambda = 180$ (512^3 collocation points). We tracked $\sim 2 \times 10^6$ particles for a total of ~ 4 large-eddy turnover times in statistically stationary conditions. Lower-resolution DNSs at $Re_\lambda = 75$ (128^3) have been used to explore a larger parameter space and to study the differences between the PP model (2.1) and the FC model (2.4) in the asymptote $d \to L$ (with L the turbulence integral scale).

4. Phenomenology of PP and FC models

We compare the statistics of acceleration of particles tracked via the PP and FC equations. In the small particle limit ($d/\eta \to 0$) the two model equations behave the same way, and the particle trajectory becomes the one of a fluid tracer. The ensemble-average acceleration variance reaches the value $\overline{a^2} \to \overline{a_f^2}$ with the subscript f labelling the fluid tracer acceleration. As the particle diameter is increased we notice important differences between the two models. In the PP model the drag term becomes negligible, and one gets $\overline{a^2} \simeq \beta^2 \overline{a_f^2}$, with $\beta = 3\rho_f/(\rho_f + 2\rho_p)$. In the FC model the volume average of the fluid acceleration $\mathrm{D}\boldsymbol{u}/\mathrm{D}t$ reduces progressively the particle acceleration. This is illustrated in figure 1(a), where the particle acceleration variance (normalized by $\beta^2\overline{a_f^2}$) is shown for three cases: neutral buoyant, heavy ($\rho_p/\rho_f = 10$) and light ($\rho_p/\rho_f = 0.1$) particles. (The effect of gravity is here assumed negligible compared to the one of turbulent fluctuations.) We note that the behaviour of $\overline{a^2}$ for particles whose diameter is roughly larger than 10η seems to be identical apart from the scaling factor β^2.

Differences are also present in higher-order moments: for this we focus on the flatness $F(a) \equiv \overline{a^4}/(\overline{a^2})^2$. In the large d limit PP model gives the rather unphysical behaviour $F(a) \simeq F(a_f)$; that is to say large particles, irrespectively of their density, show the same level of intermittency as a fluid tracer. On the other hand the FC equation gives asymptotically $F(a) \simeq 3$, i.e. the Gaussian flatness value, meaning that acceleration of large particles independent of their mass density value has lost its intermittent character (see figure 1b). Furthermore, it is noticeable that above a certain critical value of the diameter the flatness of heavy/neutral and light particles

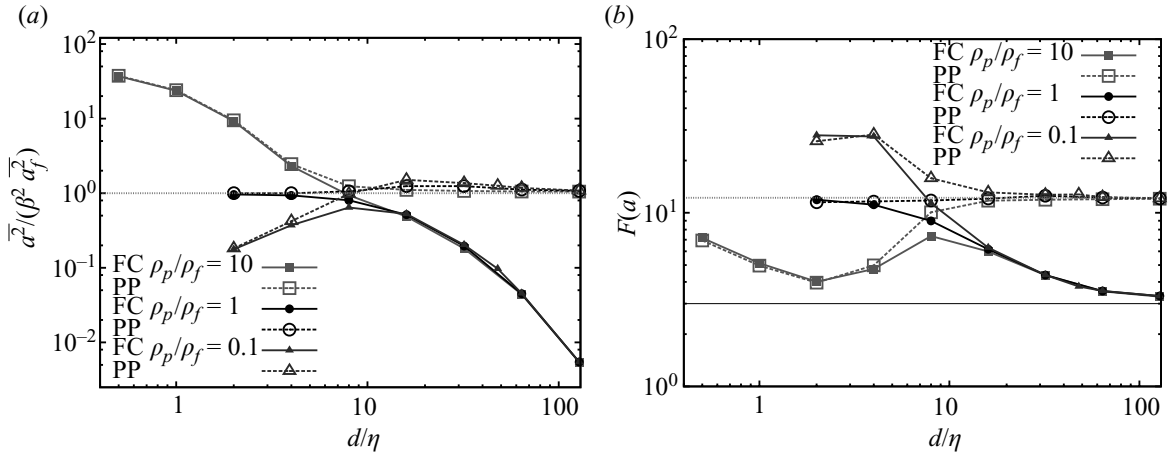

FIGURE 1. (*a*) The acceleration variance $\overline{a^2}$ normalized by $\beta^2\overline{a_f^2}$ versus the particle diameter as derived from the FC model (solid lines/symbols) and from PP the model system (dashed lines/empty symbols). Density ratios shown are $\rho_p/\rho_f = 0.1, 1, 10$, i.e. heavy (□), neutral (○) and light (△) particles. (*b*) Same as above for the acceleration flatness $F(a) = \overline{a^4}/(\overline{a^2})^2$. Horizontal lines shows the flatness of the fluid acceleration $F(a_f)$ and the flatness value for Gaussian distribution $F(a) = 3$. Data from simulations at $Re_\lambda = 75$.

reaches the same level: this suggests that also the p.d.f.s may have very similar shapes.

5. Comparison with experiments for neutrally buoyant particles

We study now how the FC model compares with the experimental observations listed in the introduction – recalling than none is captured by the PP model.

5.1. *Acceleration variance*

In figure 2 the behaviour of the one-component acceleration variance, normalized by the Heisenberg–Yaglom scaling, $a_0 = \overline{a_i^2}\,\overline{\varepsilon}^{-3/2}\nu^{1/2}$, is displayed. Although this way of normalizing the acceleration has a weak Reynolds number dependence (see Voth *et al.* 2002; Bec *et al.* 2006) we notice a very similar behaviour as compared to the experimental measurements at $Re_\lambda = 160$ by Qureshi *et al.* (2007) and the $Re_\lambda = 970$ experiments by Voth *et al.* (2002). In the inset of figure 2 the same quantity but with a different normalization is shown. The particle acceleration variance there is divided by the second moment of fluid tracer acceleration $\overline{a_f^2}$. The experimental data from Voth *et al.* (2002) can also be rescaled in the same way by dividing a_0 by the value for the smallest considered particle (which has size $d \simeq 1.44\eta$ and essentially behaves as a fluid tracer). This alternate way of looking at the data renormalizes the weak Re_λ dependence, providing a good agreement between the DNSs and experiments even when comparing results with one order of magnitude difference in Re_λ.

In a DNS one can estimate the relative weight of the terms contributing to the total acceleration: the drag and fluid acceleration terms, respectively, $a^D = (\langle \boldsymbol{u}\rangle_{S_p} - \boldsymbol{v})/\tau_p$ and $a^A = \beta\langle \mathrm{D}\boldsymbol{u}/\mathrm{D}t\rangle_{V_p}$. It is important to note that in the case of neutrally buoyant particles, one finds $\overline{a^2} \simeq \overline{(a^A)^2}$ with per cent accuracy. It indicates that the observed effect – decrease of particle acceleration variance for increasing particle diameter – comes uniquely from volume averaging of fluid acceleration at the particle position. The drag contribution is sub-leading at all d values (from few per cent up to 15 % of total acceleration variance); it just contributes to compensate the $a^D a^A$ correlations.

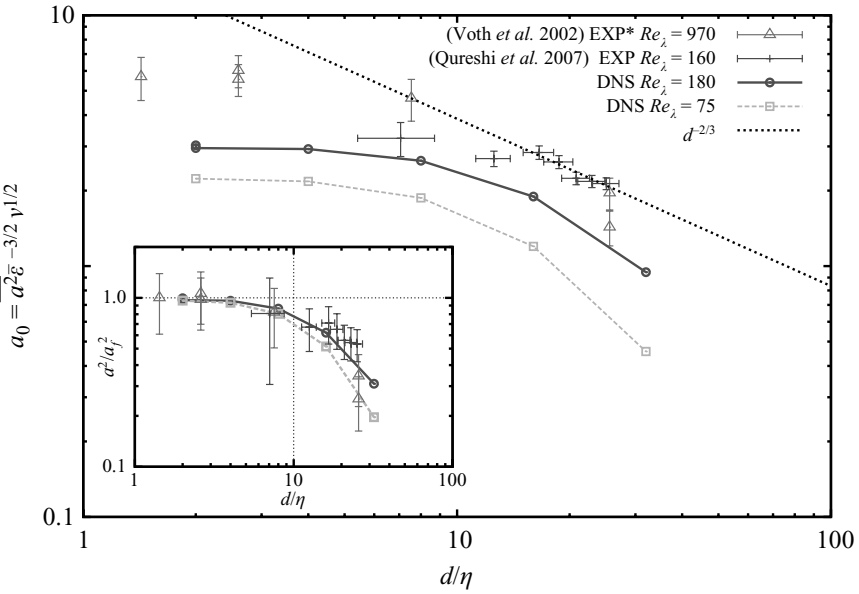

FIGURE 2. One-component acceleration variance versus particle size. Acceleration is normalized by the Heisenberg–Yaglom relation, while the particle size is normalized by the dissipative scale. DNS results have uncertainty of the order of the symbol size. Experimental data (EXP) are from Qureshi *et al.* (2007), with experimental measurement (EXP*) from (Voth *et al.* 2002, figure 32)–particles with density contrast $\rho_p/\rho_f = 1.06$. Inset: $\overline{a^2}/\overline{a_f^2}$ versus d/η from the same DNS and experimental (EXP*) measurements.

Stated differently, one can say that the acceleration of a finite-sized neutrally buoyant particle is essentially given by $\langle \mathrm{D}\boldsymbol{u}/\mathrm{D}t\rangle_{V_p} = \langle \nabla\cdot\boldsymbol{\tau} + \boldsymbol{f}_e\rangle_{V_p} \simeq (1/3r)\langle \boldsymbol{\tau}\cdot\boldsymbol{n}\rangle_{S_p}$, where $\boldsymbol{\tau}$ is the stress tensor, $\boldsymbol{n}$ a unit norm vector pointing outward the sphere and $\boldsymbol{f}_e$ the external large-scale forcing whose contribution $\langle \boldsymbol{f}_e\rangle_{V_p} \simeq 0$ is negligible at the particle scale. One expects the situation to be different for particles whose densities do not match that of the fluid.

Our simulations are consistent with the $a_0 \sim d^{-2/3}$ scaling which has been proposed on the basis of dimensional arguments rooted on K41 turbulence phenomenology without special assumptions of particle dynamics (Voth *et al.* 2002; Qureshi *et al.* 2007); however at $Re_\lambda = 180$ the scale separation is still too limited to observe a true scaling range.

5.2. *Acceleration p.d.f.*

The second quantity under study is the acceleration p.d.f. Here, to cope with Re_λ effects, one compares only the two most similar data sets: the DNS at $Re_\lambda = 180$ and the experiment at $Re_\lambda = 160$ (Qureshi *et al.* 2007). Experiments have revealed a universal behaviour for acceleration p.d.f. normalized by $(\overline{a_i^2})^{1/2}$ in the size range $d = 12$–25η. DNS instead shows a systematic difference in its trend: larger particles have less intermittent acceleration statistics (see figure 3*a*). However, the shape of the p.d.f. in the limit of large particles $d \simeq 30\eta$ shows a good similarity. To better visualize differences, in figure 3(*b*), we show the flatness $F(a)$ versus particle diameter for DNSs and experiments. As already observed, the FC model leads to decreasing intermittency for bigger neutral particles and in the asymptotic limit ($d \to L$) to Gaussian distribution; also acceleration flatness is an increasing function of Re_λ. The experiment of Qureshi and co-workers' (2007) on the other hand showed a d-independent behaviour around $F(a) = 8.5$. A further possible source of differences can be connected to the variations in the large-scale properties of turbulent flows:

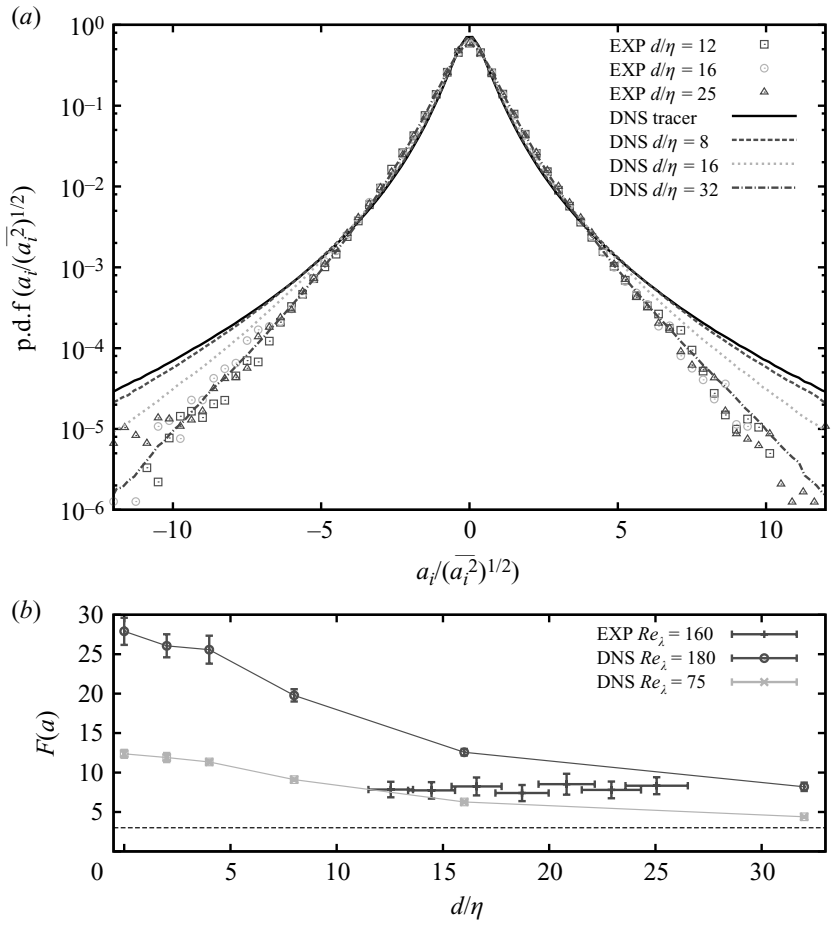

FIGURE 3. (*a*) Comparison of p.d.f.s of acceleration normalized by its r.m.s. value, from Qureshi *et al.* (2007), denoted by EXP, at $Re_\lambda = 160$ and DNS at $Re_\lambda = 180$. (*b*) One-component acceleration flatness $F(a) = \overline{a_i^4}/(\overline{a_i^2})^2$ versus the normalized particle diameter d/η from the same experiment and DNS at two different Reynolds numbers.

experimental tracks come from a decaying grid-generated turbulence; simulations instead uses volume large-scale forced flow in a cubic domain without mean flow.

5.3. *Acceleration time correlation*

Finally, we consider the dynamics of the neutral particles. We study the normalized one-component correlation function, $C_{aa}(\tau) \equiv \overline{a_i(t)a_i(t+\tau)}/\overline{a_i^2}$. In Volk *et al.* (2008*a*) it has been noted that PP model cannot account for the increasing autocorrelation for larger particles. This is understood from (2.1): In the large d/η limit the drag term is negligible, and the acceleration of a neutrally buoyant particle is dominated by the inertial term $\mathrm{D}\boldsymbol{u}/\mathrm{D}t$. Therefore the time correlation of acceleration, $C_{aa}(\tau)$, is related to the temporal correlation of $\mathrm{D}\boldsymbol{u}/\mathrm{D}t$ along the particle trajectory. Because in the large d limit $\boldsymbol{v} \neq \boldsymbol{u}$ (Babiano *et al.* 2000), one expects an acceleration correlation time which is equal to or even shorter than the one of a fluid tracer. This is confirmed by our numerics based on the PP equation (2.1). In the FC model instead, the averaged quantity $\langle \mathrm{D}\boldsymbol{u}/\mathrm{D}t \rangle_{V_p}$ dominates the particle's acceleration and also its time correlation $C_{aa}(\tau)$. In figure 4 we show that simulations based on (2.4) display increasing correlation time for bigger particles, as observed in experiment (Volk *et al.* (2008*a*) although at much larger Re_λ values. A detailed comparison of the $C_{aa}(\tau)$ curves coming from DNSs with experiments by Qureshi and co-workers (2007) is at present not possible, because of limited statistics. Therefore, we examine integral

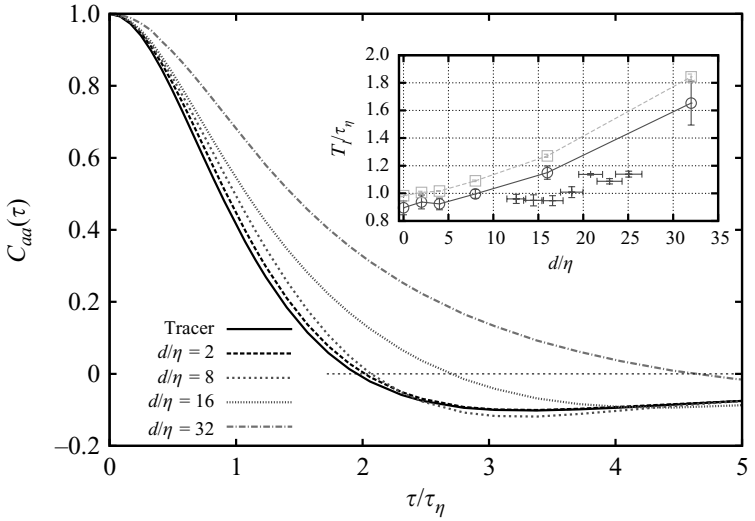

FIGURE 4. Autocorrelation function of acceleration $C_{aa}(\tau)$ for neutral particles ($\rho_p = \rho_f$), with different sizes $d = 2\eta, 8\eta, 16\eta, 32\eta$ and a tracer particle; zoom for $\tau/\tau_\eta < 5$; asymptotically all the curves go to zero. Inset: integral acceleration time $T_I = \int_0^{T_0} C_{aa}(\tau)\,\mathrm{d}\tau$, with T_0 the zero-crossing time, $C_{aa}(T_0) = 0$, versus particle diameter. Symbols: (□, ○) DNS at $Re_\lambda = (75, 180)$; (+) data from experiments at $Re_\lambda = 160$.

quantities such as an integral acceleration time T_I. Since by kinematic constraint the time integral of $C_{aa}(\tau)$ for a small tracer is zero, we define T_I as the integral over time of the positive part of $C_{aa}(\tau)$; this choice proves to be stable in the experiments and weakly dependent on the unavoidable (Gaussian) smoothing of noisy data sets (see Volk *et al.* 2008*b*). The result of this analysis is reported in figure 4 (inset). The order of magnitude of T_I/τ_η, which is very near unity, as well its increasing trend with d qualitatively confirm the prediction of the FC model at similar Reynolds number. Using DNS results, it is also interesting to note that this time decreases with increasing Reynolds number.

6. Discussion of results and conclusions

We have investigated the origin of several experimental observations concerning neutrally buoyant finite-sized particle acceleration in turbulent flows and shown the relevance of Faxén corrections. Faxén terms account for inhomogeneities in the fluid flow at the spatial extension of the particle. They act as spatial coarse graining of the surrounding turbulent flow, in contrast with the drag term which performs a temporal filtering. Numerically, the spatial average is efficiently implemented via Gaussian filtering in spectral space. Comparing with experimental measurements, the main achievements of the FC model are (i) prediction of the reduction of acceleration fluctuations at increasing the particle size and (ii) prediction of the increasing of acceleration time correlation at increasing the particle size. Both effects originate from the volume average of the fluid acceleration term or in other word from the surface average of the stress tensor of the unperturbed flow. While the FC model gives the correct trend, it does not solve the puzzling point of invariant p.d.f. with particle size, observed by Qureshi *et al.* (2007).

The FC model improves the statistical description of realistic turbulent particle suspensions. We emphasize that none of the observed trends in the acceleration of neutrally buoyant particles can be captured by previous purely local models, as e.g. the PP one in (2.1). Faxén corrections are of special relevance in the case of neutrally

buoyant particles, because it is the case for which the slip velocity ($v_s \equiv |\boldsymbol{v} - \langle \boldsymbol{u} \rangle_{S_p}|$) is the smallest (as compared to $\rho_p \neq \rho_f$ particles) and therefore in which drag, history and lift have the least impact on the net force. In our case we observe that when increasing the size of particles, the p.d.f.s of slip velocity normalized by the fluid velocity root mean square (r.m.s.) value ($v_s/\boldsymbol{u}_{rms}$) change from a sharp delta-like shape (for tracers) to larger distributions approaching a Gaussian (for large particles). A size-dependent slip velocity for neutrally buoyant particles in chaotic flows has been reported recently in Ouellette, O'Malley & Gollub (2008): Faxén corrections to the added mass should be significant in that case too. We also observe that the particle Reynolds number Re_p measured in our simulations reaches values $O(100)$; hence a more accurate description of the drag force on a sphere in a turbulent environment (see for instance Bagchi & Balachandar 2003) may be important particularly for a faithful reproduction of the far tails of the acceleration p.d.f.

The authors acknowledge the Grenoble team (N. M. Qureshi, C. Baudet, A. Cartellier and Y. Gagne) for generously sharing their experimental data measurements and J. Bec for useful discussions. Numerics have been performed at SARA (The Netherlands), CINECA (Italy) and PSMN at ENS-Lyon (France). Numerical raw data on FC particles are freely available on the iCFDdatabase (http://cfd.cineca.it) kindly hosted by CINECA (Italy).

REFERENCES

Arneodo, A., Benzi, R., Berg, J., Biferale, L., Bodenschatz, E., Busse, A., Calzavarini, E., Castaing, B., Cencini, M., Chevillard, L., Fisher, R., Grauer, R., Homann, H., Lamb, D., Lanotte, A. S., Leveque, E., Luthi, B., Mann, J., Mordant, N., Muller, W.-C., Ott, S., Ouellette, N. T., Pinton, J.-F., Pope, S. B., Roux, S. G., Toschi, F., Xu, H. & Yeung, P. K., ICTR Collaboration 2008 Universal intermittent properties of particle trajectories in highly turbulent flows. *Phys. Rev. Lett.* **100** (25), 254504–254505.

Auton, T., Hunt, J. & Prud'homme, M. 1988 The force exerted on a body in inviscid unsteady non-uniform rotational flow. *J. Fluid Mech.* **197**, 241–257.

Ayyalasomayajula, S., Gylfason, A., Collins, L. R., Bodenschatz, E. & Warhaft, Z. 2006 Lagrangian measurements of inertial particle accelerations in grid generated wind tunnel turbulence. *Phys. Rev. Lett.* **97**, 144507.

Babiano, A., Cartwright, J. H. E., Piro, O. & Provenzale, A. 2000 Dynamics of a small neutrally buoyant sphere in a fluid and targeting in Hamiltonian systems. *Phys. Rev. Lett.* **84** (25), 5764–5767.

Bagchi, P. & Balachandar, S. 2003 Effect of turbulence on the drag and lift of a particle. *Phys. Fluids.* **15** (11), 3496–3513.

Balkovsky, E., Falkovich, G. & Fouxon, A. 2001 Intermittent distribution of inertial particles in turbulent flows. *Phys. Rev. Lett.* **86** (13), 2790–2793.

Bec, J. 2005 Multifractal concentrations of inertial particles in smooth random flows. *J. Fluid Mech.* **528**, 255–277.

Bec, J., Biferale, L., Boffetta, G., Celani, A., Cencini, M., Lanotte, A., Musacchio, S. & Toschi, F. 2006 Acceleration statistics of heavy particles in turbulence. *J. Fluid Mech.* **550**, 349–358.

Berg, J. 2006 Lagrangian one-particle velocity statistics in a turbulent flow. *Phys. Rev.* E **74**, 016304.

Biferale, L., Bodenschatz, E., Cencini, M., Lanotte, A. S., Ouellette, N. T., Toschi, F. & Xu, H. 2008 Lagrangian structure functions in turbulence: a quantitative comparison between experiment and direct numerical simulation. *Phys. Fluids* **20** (6), 065103.

Calzavarini, E., Cencini, M., Lohse, D. & Toschi, F. 2008*a* Quantifying turbulence-induced segregation of inertial particles. *Phys. Rev. Lett.* **101**, 084504.

Calzavarini, E., Kerscher, M., Lohse, D. & Toschi, F. 2008*b* Dimensionality and morphology of particle and bubble clusters in turbulent flow. *J. Fluid Mech.* **607**, 13–24.

Clift, R., Grace, J. R. & Weber, M. E. 1978 *Bubbles, Drops and Particles*. Academic.

Faxén, H. 1922 Der Widerstand gegen die Bewegung einer starren Kugel in einer zähen Flüssigkeit, die zwischen zwei parallelen ebenen Wänden eingeschlossen ist, *Annalen der Physik* **373** (10), 89–119.

Gatignol, R. 1983 The Faxén formulae for a rigid particle in an unsteady non-uniform stokes flow. *J. Mec. Theor. Appl.* **1** (2), 143–160.

Kolmogorov, A. N. 1941 The local structure of turbulence in incompressible viscous fluid for very large Reynolds numbers. *Proc. USSR Acad. Sci.* **30**, 299–303.

La Porta, A., Voth, G. A., Crawford, A. M., Alexander, J. & Bodenschatz, E. 2001 Fluid particle accelerations in fully developed turbulence. *Nature* **409**, 1017.

Magnaudet, J. & Legendre, D. 1998 Some aspects of the lift force on a spherical bubble. *Appl. Sci. Res.* **58**, 441.

Maxey, M. R. & Riley, J. J. 1983 Equation of motion for a small rigid sphere in a non-uniform flow. *Phys. Fluids* **26** (4), 883–889.

Michaelides, E. E. 1997 Review – the transient equation of motion for particles, bubbles, and droplets. *J. Fluid Eng.* **119**, 233–247.

Mordant, N., Lévêque, E. & Pinton, J. F. 2004 Experimental and numerical study of the Lagrangian dynamics of high Reynolds turbulence. *New J. Phys.* **6**, 116.

Mordant, N., Metz, P., Michel, O. & Pinton, J.-F. 2001 Measurement of Lagrangian velocity in fully developed turbulence. *Phys. Rev. Lett.* **87** (21), 214501.

Ouellette, N. T., O'Malley, P. J. J. & Gollub, J. P. 2008 Transport of finite-sized particles in chaotic flow. *Phys. Rev. Lett.* **101**, 174504.

Qureshi, N. M., Bourgoin, M., Baudet, C., Cartellier, A. & Gagne, Y. 2007 Turbulent transport of material particles: an experimental study of finite size effects. *Phys. Rev. Lett.* **99** (18), 184502.

Salazar, J., de Jong, J., Cao, L., Woodward, S., Meng, H. & Collins, L. 2008 Experimental and numerical investigation of inertial particle clustering in isotropic turbulence. *J. Fluid Mech.* **600**, 245–256.

Squires, K. D. & Eaton, J. K. 1991 Preferential concentration of particles by turbulence. *Phys. Fluids* A **3** (5), 1169–1179.

Toschi, F. & Bodenschatz, E. 2009 Lagrangian properties of particles in turbulence. *Annu. Rev. Fluid Mech.* **41**, 375–404.

Volk, R., Calzavarini, E., Verhille, G., Lohse, D., Mordant, N., Pinton, J. F. & Toschi, F. 2008*a* Acceleration of heavy and light particles in turbulence: comparison between experiments and direct numerical simulations. *Physica* D **237** (14–17), 2084–2089.

Volk, R., Mordant, N., Verhille, G. & Pinton, J. F. 2008*b* Laser doppler measurement of inertial particle and bubble accelerations in turbulence. *Europhys. Lett.* **81** (3), 34002.

Voth, G. A., La Porta, A., Crawford, A. M., Alexander, J. & Bodenschatz, E. 2002 Measurement of particle accelerations in fully developed turbulence. *J. Fluid Mech.* **469**, 121–160.

Xu, H., Bourgoin, M., Ouellette, N. T. & Bodenschatz, E. 2006 High order Lagrangian velocity statistics in turbulence. *Phys. Rev. Lett.* **96** (2), 024503.

J. Fluid Mech. (2011), *vol.* 668, *pp.* 223–235.
doi:10.1017/S0022112010005690

Dynamics of inertial particles in a turbulent von Kármán flow

R. VOLK†, E. CALZAVARINI, E. LÉVÊQUE AND J.-F. PINTON

International Collaboration for Turbulence Research, Laboratoire de Physique de l'École Normale Supérieure de Lyon, UMR5672, CNRS et Université de Lyon, 46 Allée d'Italie, 69007 Lyon, France

(Received 27 January 2010; revised 27 October 2010; accepted 27 October 2010)

We study the dynamics of neutrally buoyant particles with diameters varying in the range $[1, 45]$ in Kolmogorov scale units (η) and Reynolds numbers based on Taylor scale (Re_λ) between 590 and 1050. One component of the particle velocity is measured using an extended laser Doppler velocimetry at the centre of a von Kármán flow, and acceleration is derived by differentiation. We find that the particle acceleration variance decreases with increasing diameter with scaling close to $(D/\eta)^{-2/3}$, in agreement with previous observations, and with a hint for an intermittent correction as suggested by arguments based on scaling of pressure spatial increments. The characteristic time of acceleration autocorrelation increases more strongly than previously reported in other experiments, and possibly varying linearly with D/η. Further analysis shows that the probability density functions of the acceleration have smaller wings for larger particles; their flatness decreases as well, as expected from the behaviour of pressure increments in turbulence when intermittency corrections are taken into account. We contrast our measurements with previous observations in wind-tunnel turbulent flows and numerical simulations.

Key words: homogeneous turbulence, isotropic turbulence, particle/fluid flows

1. Introduction

Research in dynamics and transport phenomena in turbulence has recently benefited from experimental tracking of flow tracers (see for instance Ott & Mann 2000; La Porta *et al.* 2001; Mordant *et al.* 2001; Arneodo *et al.* 2008; Toschi & Bodenschatz 2009). Ideally, these tracers should have a size much smaller than the Kolmogorov length (η) at which the velocity gradients are smooth and hence their motion follows fluid streamlines, but experimental constraints have often led to the use of larger particles – with some bias as discussed e.g. by Mei (1996) and Brown, Warhaft & Voth (2009). On the other hand, the question of the dynamics of objects with a finite size freely advected by turbulent motions remains. Indeed, while theories developed in the small particle limit and vanishing particle Reynolds numbers Re_p yield the widely used Maxey–Riley–Gatignol equation, the equation of motion of a large particle with high-Re_p is largely unknown (see, however, Auton, Hunt & Prud'homme 1988; Lovalenti & Brady 1993; Loth & Dorgan 2009). A recent systematic analysis has been made in a wind tunnel ($Re_\lambda = 160$) using helium-inflated soap bubbles (Qureshi

† Email address for correspondence: romain.volk@ens-lyon.fr

et al. 2007, 2008). Other studies were performed with neutrally buoyant polystyrene particles in water in a turbulent von Kármán (VK) flow ($Re_\lambda \in [400, 815]$)(Voth *et al.* 2002; Brown *et al.* 2009). These studies have obtained several noteworthy results. (i) The variance of acceleration decreases as $D^{-2/3}$, consistent with the scaling of pressure increments in Kolmogorov's phenomenology of turbulence. The influence of varying Reynolds numbers ($Re_\lambda \in [400, 815]$) has also been studied in Brown *et al.* (2009), showing that the variance of acceleration actually scales according to $\epsilon^{3/2}\nu^{-1/2}(D/\eta)^{-2/3}$. (ii) The probability distribution functions (PDFs) of acceleration components do not depend on particle sizes in the range explored, $D/\eta \in [12, 25]$ (Qureshi *et al.* 2007) and $D/\eta \in [0.4, 27]$ (Brown *et al.* 2009). Brown *et al.* (2009) note that PDFs for large particle sizes may have slightly reduced wings as compared to the fluid particle PDF. However, because of systematic uncertainties, they do not draw any firm conclusion. A numerical study based on the Faxén model (Calzavarini *et al.* 2009) suggests that the PDF flatness should decrease with increasing particle size for $Re_\lambda = 75, 180$. This finding is questioned by a more recent numerical study (Homann & Bec 2010) based on a direct simulation approach using penalty methods, which finds a collapse of the PDFs for $D/\eta \in [2, 14]$ at $Re_\lambda = 32$. Following these studies, we have collected new experimental data using an extended laser Doppler velocimetry (LDV) technique in a VK flow (improved experiment from Volk *et al.* 2008*b*). We observe as follows. (i) There may be intermittent corrections to the $(D/\eta)^{-2/3}$ scaling of acceleration variance. (ii) The acceleration PDFs normalized by their variance are not independent of the particle size. Our statistical analysis shows that the wings of the distributions become less extended as D/η increases. (iii) The response time of the particle, as computed from the acceleration autocorrelation function, increases more strongly than that computed from wind-tunnel or DNS data (reported by Calzavarini *et al.* 2009), and possibly linearly with D/η.

2. Description of the experiment

2.1. *Experimental set-up*

The flow is of the von Kármán type and uses the same set-up as described by Volk *et al.* (2008*a*). Water fills a cylindrical container of internal diameter 15 cm, height $H = 25$ cm. It is driven by two counter-rotating disks of diameter $2R = 14$ cm, fitted with eight straight blades of height 0.5 cm in order to impose inertial steering (figure 1*a*). The distance between the disks is 20 cm and the rotation rate Ω is fixed at values up to 10 Hz, with two calibrated DC motors driven with a constant voltage. The angular velocity of the disks, directly measured from the tachometers of the motors, is adjusted so that they rotate at the same velocity but in opposite directions. Their rotation rate remains constant in time with a precision of about 2 %. This inertial forcing generates a fully turbulent flow ($Re_\lambda > 400$) in a compact region of space. This is why the von Kármán counter-rotating flow has been used in many studies of very-high-Reynolds-number turbulence, both for studies focusing on Eulerian quantities (see, for example, Zocchi *et al.* 1994) and on Lagrangian statistics (La Porta *et al.* 2001; Mordant *et al.* 2001; Voth *et al.* 2002). As opposed to wind-tunnel (WT) flows, the von Kármán flow has a mean three-dimensional spatial structure (figure 1*b*). As the disks rotate in opposite directions, the flow has a large azimutal component with a strong gradient in the axial (z) direction. It is of the order of $2\pi R\Omega$ close to the disks, and zero in the midplane ($z = 0$) of the cylinder. Because we use blades to improve stirring, the disks also act as centrifugal pumps ejecting the fluid radially at the top and bottom of the set-up, resulting in a large scale poloidal

Ω (Hz)	u_{rms} ($m\,s^{-1}$)	a_{rms} ($m\,s^{-2}$)	τ_η (ms)	η (μm)	ϵ ($W\,kg^{-1}$)	Re_λ (–)	a_0 (–)
4.1	0.57	144	0.53	24.8	4	590	2.8
6.4	0.85	375	0.33	19.6	10.2	815	4.6
7.2	0.99	496	0.28	18.2	13.9	950	5.1
8.5	1.17	706	0.19	16.2	21.8	1050	5.2

TABLE 1. Parameters of the flow. Ω, rotation rate of the disks; ϵ, dissipation rate, from the power consumption of the motors. Note that u_{rms} and a_{rms} are computed using the x-component of the velocity, and the Taylor-based Reynolds number is estimated as $Re_\lambda = \sqrt{15u_{rms}^4/\epsilon\nu}$. a_0 is derived from the Heisenberg–Yaglom relation $a_0 \equiv a_{rms}^2 \nu^{1/2}\epsilon^{-3/2}$.

recirculation with a stagnation point in the geometrical centre of the cylinder. The flow proved to be locally homogeneous in the central region (Marié & Daviaud 2004), but non-isotropic at both large and small scales (Voth *et al.* 2002), the small scales approaching isotropy in the very-high-Re_λ limit.

The dissipation rate ϵ is computed from the global power consumption of the flow with the formula $\epsilon = 2(P_{water} - RI_{water}^2 - P_{air} + RI_{air}^2)/M$, where P is the power consumption of one motor, R is the electrical resistance of the rotor, I is the electrical current, M is the total mass of fluid, and the indices denote measurements with water or air filling the vessel. This procedure removes the Joule and mechanical friction contributions and yields an estimation of ϵ in agreement with Zocchi *et al.* (1994), who have measured the local dissipation ϵ from hot-wire anemometry in flows with the same geometry. For the measurements reported here, the flow temperature is regulated at 15° C for all rotation rates. The Taylor-based Reynolds number, computed with the formula $Re_\lambda = \sqrt{15u_{rms}^4/\epsilon\nu}$ using the x-component of the velocity to scale the velocity fluctuations, ranges from 590 to 1050, with a maximum dissipation rate ϵ equal to 22 $W\,kg^{-1}$ (table 1). The Eulerian measurement of pressure has been performed with a Kistler 7031 pressure sensor mounted flush with the lateral wall, in the midplane of the experiment (figure 1).

2.2. *Extended laser Doppler velocimetry*

The particles, which are tracked in a small volume located in the geometrical centre of the cylinder, have a density of 1.06, with diameters $D = 30, 150, 250, 430, 750$ μm. Further changing the flow stirring will correspond to $D/\eta \in [1, 45]$. In order to measure the velocity of the particles along their trajectories, we use the extended laser Doppler velocimetry (eLDV) introduced by Volk *et al.* (2008*a*,*b*). We use wide laser beams intersecting in the centre of the flow to illuminate particles on a significant fraction of their path (figure 1*c*). In the set-up, the axis of rotation is vertical and the laser beams are horizontal, resulting in fringes perpendicular to the x-axis. When a particle crosses the fringes, the scattered light is then modulated at a frequency directly proportional to the x-component of the velocity (denoted u_x). As the beams are not collimated, the inter-fringe remains constant across the measurement volume, whose size is about $5 \times 5 \times 10\,mm^3$. In practice, we use a 2W continuous Argon laser of wavelength 514 nm, with single longitudinal mode and stabilized power output, to impose a 41 μm inter-fringe. The measurement volume is imaged on a low noise Hamamatsu photomultiplier in the case of the smallest (fluorescent) particles, while for larger particles, the detection is made using a PDA-36A photodiode from Thorlab. In order to get the sign of the velocity, we use two acousto-optic modulators (AOM)

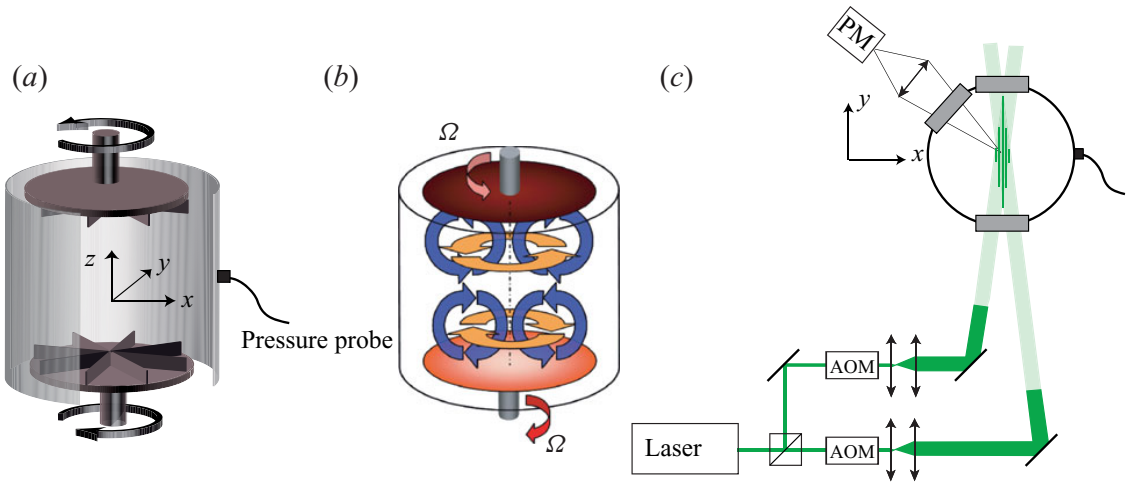

FIGURE 1. (Colour online) Experimental set-up. (*a*) Geometry of the turbulence generator. (*b*) Schematics of the von Kármán flow in water. (*c*) Principle of the LDV using wide beams (eLDV) – top view of the experiment. PM denotes location of the photomultiplier which detects scattering light modulation as a particle crosses the interference pattern created at the intersection of the laser beams. The eLDV measures, for one particle at a time, the evolution of its velocity component $u_x(t)$ along the particle trajectory.

to impose a 100 kHz frequency shift between the beams so that the fringes are actually travelling at a constant speed. The output is recorded using a National Instrument PXI-NI5621 16-bit digitizer at rate 1 MHz. The velocity is computed from the light-scattering signal using a demodulation algorithm described by Mordant, Michel & Pinton (2002), with a time resolution adjustable in the range [5–30] μs. We adjust the seeding density to be low enough so that we do not observe events with two particles at the same time in the measurement volume, but high enough to observe at least one trajectory per second. The output of the measurement is a collection of 15 000 trajectories $(u_x^n(t))_n$ of mean duration of 20 Kolmogorov times (τ_η), from which the acceleration $(a_x^n(t))_n$ is computed by differentiation. Because of measurement noise, the signal has to be filtered using a Gaussian smoothing kernel with window width w as proposed by Mordant, Crawford & Bodenschatz (2004*a*). Moments of the statistics of fluctuations of acceleration are computed for varying values of w and extrapolated to zero filter width as in Volk *et al.* (2008*a*). Note that the argon laser used in this study is stabilized both in power output and phase (with single longitudinal mode in the cavity). This improvement leads to a better estimation of the acceleration variance; therefore, the values of a_0 reported in table 1 are 20 % smaller than those in Volk *et al.* (2008*a*).

3. Results

3.1. *Particle velocitiy*

One expects that Eulerian and Lagrangian velocity statistics coincide under ergodicity approximation, so that the tracer-particle velocities are expected to have Gaussian statistics. Our observation is that the velocity distribution is markedly sub-Gaussian as seen in figure 2(*a*) – flatness values are (2.56, 2.58, 2.62, 2.46) for the four Reynolds number values explored in this work. Sub-Gaussian statistics for the velocity have been observed in many experimental set-ups, however usually less pronounced than in our case. Flatness values for velocities in WT flow are closer to three (M. Bourgoin

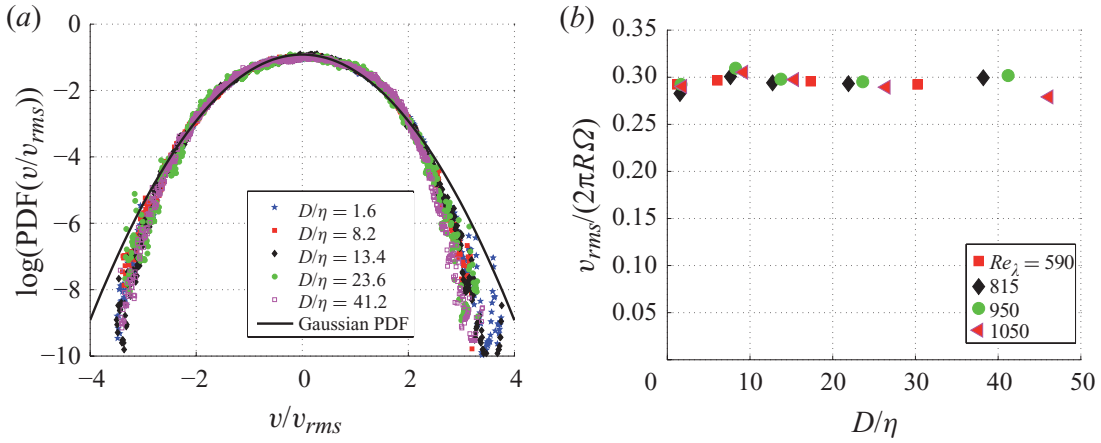

FIGURE 2. (Colour online) (*a*) PDF of particle velocities. (*b*) Evolution of the r.m.s. velocity of the particles normalized by the disk velocity $2\pi R\Omega$ as a function of particle size for the different Reynolds numbers studied.

private communication). Here the VK flow has a large-scale inhomogeneity and anistropy (cf. Voth *et al.* 2002; Marié & Daviaud 2004; Volk, Odier & Pinton 2006), which may enhance the sub-Gaussianity. In such a confined geometry, the VK flow is known to have several possible configurations of its large-scale velocity profile (Monchaux *et al.* 2006; de la Torre & Burguete 2007); each configuration may lead to Gaussian velocity fluctuations about a locally different mean value with an overall effect leading to a sub-Gaussian histogram. However, we have not observed any change in the velocity statistics when the Reynolds number is increased or when the size of the particle is changed by over an order of magnitude in D/η. In fact, for this fully turbulent regime, the velocity variance is equal to 30 % of the impeller tip speed, as can be seen in figure 2(*b*). As shown by Ravelet, Chiffaudel & Daviaud (2008), this is a characteristic of the von Kármán driving impellers, and not a characteristic of the inertial particle size. We note that this observation is in agreement with a prediction following Faxén argument at the leading order, $v^2/u^2_{fluid} = 1-(5/12)(D^2/\lambda^2)$ (Homann & Bec 2010) – where λ is Taylor's microscale, giving a correction smaller than 1 % for the Taylor-based-Reynolds-number range considered here.

3.2. *Particle acceleration variance*

With one component of velocity probed by the eLDV system and in a situation in which the direction of motion is not prescribed, the first moment of the distribution of acceleration is zero. One expects that the second moment (acceleration variance) reduces with increasing particle size, because the pressure forces which mainly cause the motion are averaged over a growing area. As shown in figure 3, this is indeed observed. The evolution of the acceleration variance measured here is in qualitative agreement with previous studies by Voth *et al.* (2002), Qureshi *et al.* (2007) and Brown *et al.* (2009): when normalized by the acceleration variance of the smallest particles (fluid tracers, denoted as $\langle a_T^2\rangle$), the quantity $\langle a_D^2\rangle/\langle a_T^2\rangle$ exhibits a decrease consistent with the power-law $(D/\eta)^{-2/3}$ for all Reynolds numbers and inertial range particle sizes. Recall that this power-law behaviour is obtained when one assumes that the particle acceleration scales like pressure increments over a length proportional to the particle's diameter. In the inertial range of scales, this argument yields the scaling $\langle a_D^2\rangle \propto \langle(\delta_D P/D)^2\rangle \sim D^{4/3-2} = D^{-2/3}$, where $\langle(\delta_D P)^n\rangle \equiv S_p^n(D)$ is the pressure nth-order spatial structure function. Later, we show that one may also include

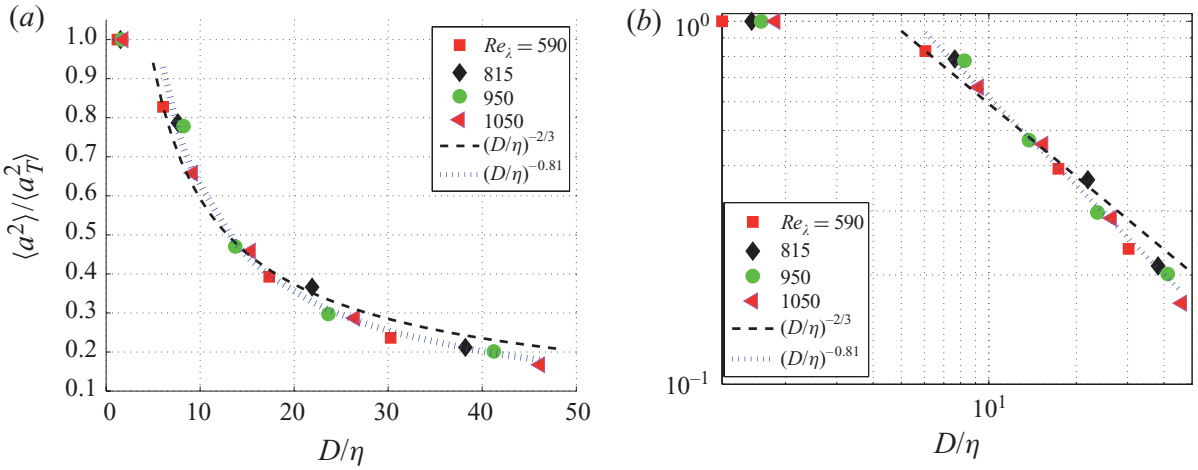

FIGURE 3. (Colour online) (*a*) Variance of one component of acceleration of the particles versus particle size. (*b*) The same figure in log-log representation. In order to be able to compare flows at varying Reynolds numbers Re_λ, the particle acceleration variance is normalized by the one measured with the smallest particles (tracers (T), for which $D/\eta \leqslant 2$ at all Re_λ), and diameters are normalized by the viscous dissipative scale η. Thick solid line denotes Kolmogorov scaling $\langle a_D^2\rangle \propto (D/\eta)^{-2/3}$. Thin dashed line denotes refinement including intermittency corrections (see details in § 3.4).

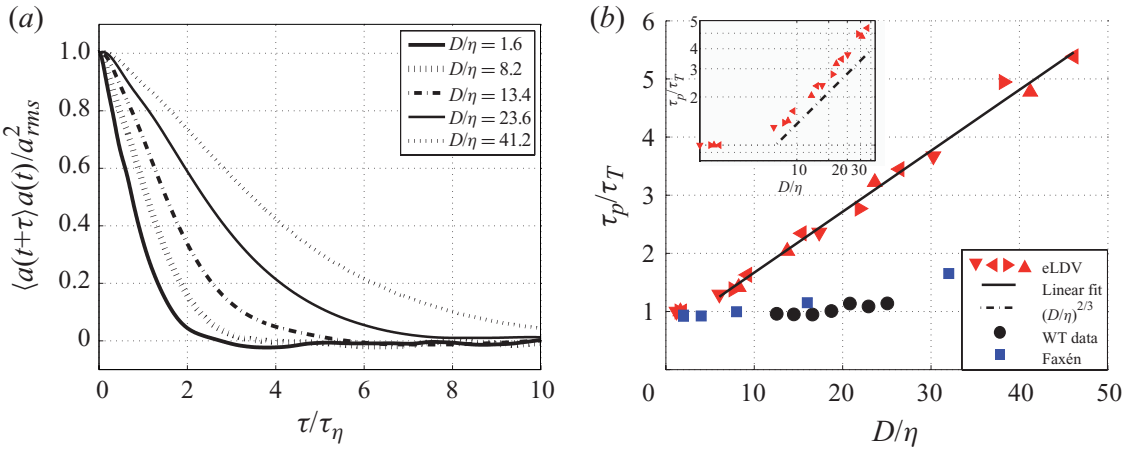

FIGURE 4. (Colour online) (*a*) Particle acceleration autocorrelation functions for $Re_\lambda = 950$; (*b*) evolution of particle response times. The wind-tunnel and Faxén data are extracted from Calzavarini *et al.* (2009) ($Re_\lambda = 160$ for wind-tunnel data and $Re_\lambda = 180$ for Faxén model data). For the eLDV data, the symbols correspond to increasing Reynolds numbers: ▼, $Re_\lambda = 590$; ◀, $Re_\lambda = 815$; ▶, $Re_\lambda = 850$; ▲, $Re_\lambda = 1050$. (inset) Log–log of the particle response times (triangles) together with a $(D/\eta)^{2/3}$ power law (dashed line).

intermittency corrections to obtain the dashed line in figure 3, which yields an improved fit of our experimental data.

3.3. *Particle response time*

A characteristic time for the evolution of a particle response to flow changes is obtained from the acceleration autocorrelation functions. Their shape and evolution with particle size are shown in figure 4(*a*), for $Re_\lambda = 950$. In agreement with previous observations for tracers, the autocorrelation for small particles vanishes in times of the order of a few Kolmogorov times $\tau_\eta = \sqrt{\nu/\epsilon}$. As expected, the response time τ_p, defined as the integral over time of the positive part of $C_{aa}(\tau)$, increases with size, at

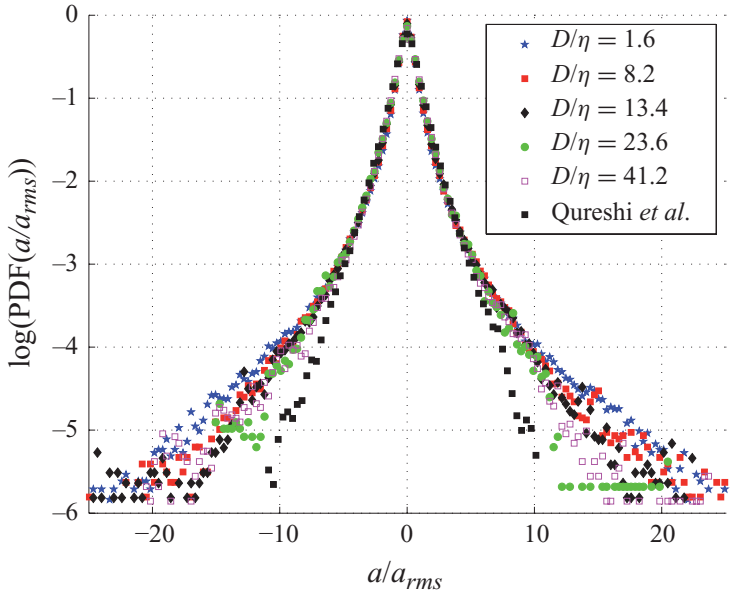

FIGURE 5. (Colour online) PDFs of particle acceleration at $Re_\lambda = 950$, normalized by their variance. The wind-tunnel data of Qureshi *et al.* (2007, 2008) correspond to $Re_\lambda = 160$.

any given Reynolds number. Our observation is that for a given Reynolds number, τ_p increases *linearly* with the particle diameter D for sizes larger than about 10η. In addition, as shown in figure 4(*b*)(red/triangle symbols), measurements performed at various Re_λ all line-up on the same curve when τ_p is normalized by the response time of the smallest particles (tracers, T) for which $\tau_T = (1.07 \pm 0.16)\tau_\eta$. This confirms that the evolution is indeed given by the relevant dimensionless variables, $\tau_p/\tau_\eta = f(D/\eta)$, i.e. when the response time is counted in units of the Kolmogorov time $\tau_\eta = \sqrt{\nu/\epsilon}$ and the particle size is counted in units of the dissipative scale $\eta = (\nu^3/\epsilon)^{1/4}$.

The behaviour observed is quite different from the prediction of point-particle (PP) models, for which the Stokes drag term becomes rapidly negligible when the particle size increases, so that the response time remains that of fluid tracers (Volk *et al.* 2008*a*). A first refinement of the PP model is to account for size effects by averaging the flow fields over the area of the particle (for the estimation of drag) and over its volume (for added mass effects); this is the essence of the Faxén-corrected model introduced by Calzavarini *et al.* (2009). Using this model, the authors have observed a variation of the particle response time with size: it increases by almost a factor of 2 when the size of the particle increases from $D = 2\eta$ to up to $D = 32\eta$. This finding was in general agreement with experimental measurement in a wind tunnel by Qureshi *et al.* (2008). As shown in figure 4(*a*), our measurements in a von Kármán flow show a much steeper increase: the response time of the particles is about four times that of the tracers when the diameter has grown to 32η, and the variation is roughly linear when plotted in linear coordinates. However, as shown in figure 4(*b*), the scaling $\tau_p/\tau_\eta = (D/\eta)^{2/3}$ cannot be excluded; it is obtained by assuming that the response time of the particle scales as the eddy turnover time of flow motions at a scale equal to the particle diameter.

3.4. *Particle acceleration probability density function*

The estimation of higher even moments of particle accelerations requires specific data processing, as we show in the following. We first discuss the raw distributions of the accelerations. In figure 5, they are shown for $Re_\lambda = 950$; the particle accelerations have been normalized by their variance (whose behaviour has been discussed in § 3.2).

To leading order, the distribution functions are very similar, as observed in the wind-tunnel measurements by Qureshi *et al.* (2007, 2008). There is no reduction to Gaussian statistics as the particle size grows well into the inertial range (see also Gasteuil 2009 for measurements with particles with integral range sizes). In figure 5, the PDF for the smallest particles is identical to that measured for tracers by Voth *et al.* (2002) in another VK flow, and in numerical simulations by Yeung (2002) and Mordant, Lévêque & Pinton (2004*b*). It is different from the PDFs reported by Qureshi *et al.* (2007, 2008) from wind-tunnel measurements at $Re_\lambda = 160$. These differences are more pronounced than what could be expected from Reynolds-number variations alone between the experiments. The first explanation could be that the acceleration PDFs are not universal but flow-dependent. This hypothesis is supported by the results of Voth *et al.* (2002), who showed that the Lagrangian small-scale dynamics still reflects the anisotropy of the large scales. The second possibility is that the acceleration PDFs measured by Qureshi *et al.* are not the PDFs one would measure for tracers in a WT flow. This explanation is supported by the work of Ayyalasomayajula, Warhaft & Collins (2008), who showed that water droplets (which behave as tracers in wind-tunnel turbulence at $Re_\lambda = 180$) have an acceleration PDF with more extended tails than those reported by Qureshi *et al.* (2007). This would mean that the acceleration PDFs of material particles do change significantly with increasing size.

Investigating the possibility of changes in the statistics of acceleration with size or Reynolds number can be done by studying higher-order moments, starting with the distribution flatness. It requires a converged measurement of the PDFs and, as shown for tracer particles by Mordant *et al.* (2004*a*), this implies extremely large data sets. As a first attempt, we fit the acceleration PDF with a model functional form which we then use to *estimate* the flatness of the distribution. The procedure is as follows. We assume that the statistics is described by a functional form $\mathscr{F}_\theta(x = a/a_{rms})$; $\{\theta\}$ is a set of adjustable parameters which are determined by minimizing the distance $x^2\mathrm{PDF}(x) - x^2\mathscr{F}_\theta(x)$, where $\mathrm{PDF}(x)$ is the measured distribution. Two trial distributions have been tested:

$$\mathscr{F}_s^{LN}(x) = \frac{\mathrm{e}^{3s^2/2}}{4\sqrt{3}}\left(1 - \mathrm{erf}\left(\frac{\ln|x/\sqrt{3}| + 2s^2}{s\sqrt{2}}\right)\right), \tag{3.1}$$

which stems from the assumption that the acceleration amplitude has a lognormal distribution (s being the only adjustable parameter), and a stretched exponential functional form

$$\mathscr{F}_s^{SE}(x) = A\,\exp\left(\frac{-x^2}{2\sigma^2\left(1 + \left|\dfrac{x\beta}{\sigma}\right|^\gamma\right)}\right), \tag{3.2}$$

(A being a normalization constant) which has three adjustable parameters (σ, β, γ), and allows us for a finer adjustment of the distribution in the tails. Note that with distributions having such extended wings, a 'brute force' measurement of the flatness factor within a 5 % accuracy would mean a resolution of the distribution up to about 100 standard deviations, and events with probability below 10^{-11} – clearly outside of direct experimental reach.

Figure 6 shows a comparison of the acceleration PDF for the smallest particles at $Re_\lambda = 815$ and the corresponding fits that minimize the distance to the quantity $x^2\mathrm{PDF}(x)$ in the range $x = a/a_{rms} \in [-25, 25]$. As one can see, both functional forms fit correctly the experimental data up to $a/a_{rms} \sim 20$, the stretched exponential form

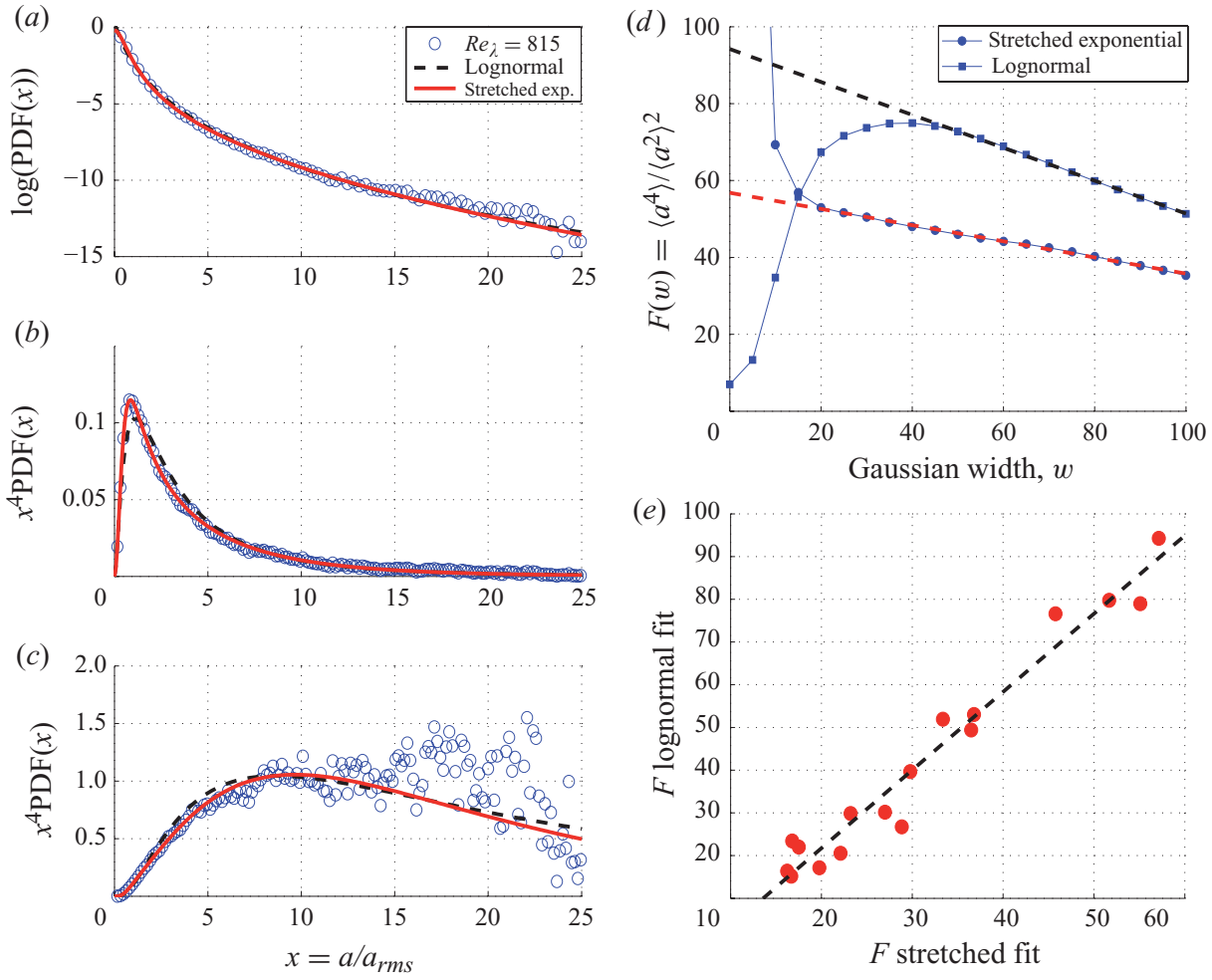

FIGURE 6. (Colour online) (*a*): PDF of particle acceleration with $D/\eta = 1.5$ at $Re_\lambda = 815$ and the corresponding lognormal (dashed line) and stretched exponential (exp., solid line) fits. The data have been processed using a Gaussian smoothing with width $w = 20$. (*b*) Linear plot of the second-order moment $x^2\mathrm{PDF}(x)$ with corresponding fits. (*c*) Linear plot of $x^4\mathrm{PDF}(x)$ with the lognormal and stretched exponential fits. (*d*) Evolution of the flatness $F(w) = \langle a^4\rangle/\langle a^2\rangle^2$ as a function of the width of the Gaussian window (w) for the lognormal estimator (■) and the stretched exponential estimator (●). For both curves, the dashed line is the linear fit of $F(w)$ in the region $w \in [50, 100]$, leading to an extrapolated flatness $F_L = 94$ for the lognormal estimator and $F_S = 57$ for the stretched exponential estimator. (*e*) Relative evolution of the flatness F estimated with the two estimators. (●), experimental data; dashed line, linear fit $F_D = 1.83\, F_S - 14.8$.

showing a better agreement with the second-order moment. As reported in previous studies, the moments of the acceleration PDFs strongly depend on the width w of the smoothing kernel used to extract the velocity data from the modulated optical signal (cf. § 2). We thus estimate the flatness by fitting the different PDFs for decreasing w and then by interpolating to zero width. The result of this procedure is shown in figure 6(*d*) for the two trial functional forms. As can be seen, the flatness derived from the lognormal estimator is roughly 1.6 higher than that computed from the stretched exponential estimator. As the two trial distributions model the wings of the PDFs in a different way, we find that the flatness estimated from the two functions is not strictly proportional to each other, but is related by a linear relationship as shown in figure 6(*e*). The values of the flatness reported have to be taken as estimates, the true values strongly depending on the real shape of the acceleration PDF in the far tails.

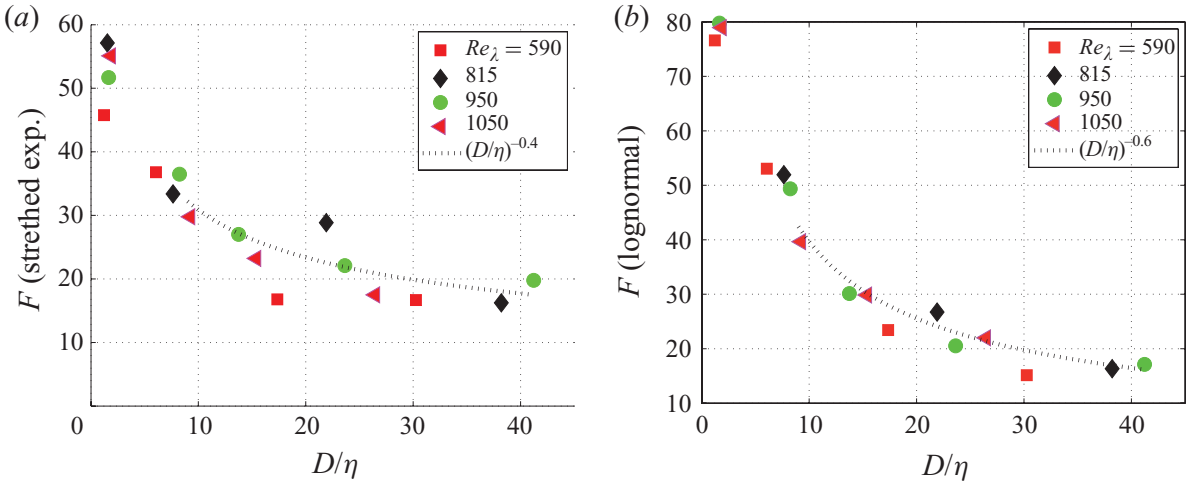

FIGURE 7. (Colour online) Variation of the estimated flatness as a function of D/η for different sizes and different Reynolds numbers. (a) Stretched exponential (exp.) estimator and (b) lognormal estimator.

We propose however that the *variations* detected here yield a first-order estimation of the evolution of acceleration statistics with particle size.

The results are shown in figure 7(a,b). For both estimators, one observes a reduction in the flatness with increasing particle sizes. This can be understood if one takes into account the intermittency of the pressure increments for inertial range separations. Following the approach developed by Voth *et al.* (2002), Qureshi *et al.* (2007) and Brown *et al.* (2009), one estimates the acceleration flatness $F(D)$ by assuming that the force acting on the particles is dominated by the pressure gradient over a length scale proportional to D. All moments of the acceleration ($\langle a_D^n \rangle$) should then scale as $S_P^n(D)/D^n$, with a behaviour dictated by pressure structure functions. Now, in order to estimate the pressure structure functions, one can either use the ansatz that pressure increments scale as the square of velocity increments, $\langle \delta_D P \rangle \propto \langle (\delta_D v)^2 \rangle$, or one can measure directly the scaling of pressure in the experiment. In the first case, one obtains $S_P^n(D) \propto D^{2\zeta_n}$, ζ_n being the structure function exponents of the Eulerian velocity increments. One then obtains $F(D) \propto D^{\zeta_8 - 2\zeta_4} \sim D^{-0.42}$, if one assumes a lognormal scaling for the Eulerian velocity structure functions as in Chevillard *et al.* (2006), independent of the Reynolds number.

In order to have an experimental measurement of pressure structure functions, we have recorded the pressure using a transducer mounted flush in the lateral wall, in the midplane of the flow. This measurement, although not performed in the bulk of the flow, yields $S_P^2 \propto D^{1.2\pm0.1}$ and $S_P^4/(S_P^2)^2 \propto D^{-0.38\pm0.03}$, power laws which are both in agreement with wind-tunnel data of Pearson & Antonia (2001) and Eulerian DNS data at $Re_\lambda = 180$ (from the same DNS described by Calzavarini *et al.* 2009). In the case of the stretched exponential estimator, these predictions for the scaling exponent are consistent with the value $\alpha \sim -0.4$ obtained by fitting the data with a power-law $F_s(D) = A(D/\eta)^\alpha$, with D/η in the range $[10, 40]$. In the case of the lognormal estimator, one finds a scaling law $F_l(D) \propto (D/\eta)^{-0.6}$. Here we stress that $\mathscr{F}_s^{LN}(a)$ and $\mathscr{F}_s^{SE}(a)$ are intrinsically different distributions; therefore, it is in principle impossible to fit both curves with the same scaling exponent. The true value of the exponent (if it exists) should depend on the real shape of the PDFs. However, the consistency between the estimation using the stretched exponential estimator and the Eulerian measurements of pressure suggests that this functional form is a good estimation of

the acceleration PDFs in the case of large acceleration flatness ($F > 20$). This was confirmed by comparing the quality of the two different estimators with numerical data obtained at $Re_\lambda = 180$ ($F \simeq 27.5$, Calzavarini *et al.* 2009). Using a truncated data set as a test, the stretched exponential estimator proved to yield a better fit than the lognormal estimator, and was able to give an estimate of the flatness only 15 % lower than the converged value computed using the whole data set.

Finally, we note that following the same approach, one can use the second-order pressure structure function to get a new estimation of the decrease of the acceleration variance $\langle a_D^2 \rangle$. Assuming a lognormal scaling for the velocity increments, one then finds $\langle a_D^2 \rangle \propto \langle (\delta_D P/D)^2 \rangle \sim D^{\zeta_4 - 2} = D^{-0.78 \pm 0.02}$ very close to the experimental measurements, which yields $\langle a_D^2 \rangle \sim D^{-0.8 \pm 0.1}$. These two values are in a very good agreement with the best fit shown by a dashed line in figure 3, which yields $\langle a_D^2 \rangle / \langle a_T^2 \rangle \propto (D/\eta)^{-0.81}$. In our opinion, this is an indirect proof that intermittency plays a role and that our results concerning the acceleration flatness, although preliminary, are consistent.

4. Concluding remarks

We have described here new eLDV measurements in an extended range of particle sizes. With an improved set-up and analysis techniques, we have obtained the evolution of the statistics of one component of the acceleration of the particles, and a measurement of a characteristic time of their response to flow changes. The response time is found to increase more steeply in our von Kármán flow than previously reported for wind-tunnel or DNS data. Concerning the statistics of acceleration fluctuations, we have investigated the behaviour of the second and fourth moments. The variance is well converged, and we have observed that in the study of its evolution with particle size, two normalization factors are important in order to collapse our observation on a single curve: the diameter should be scaled by the Kolmogorov dissipation length and the acceleration should be compared to that of tracer particles, which are more efficient at removing bias and Reynolds number effects than the Heisenberg–Yaglom scaling because $a_0 = \langle a^2 \rangle \epsilon^{-3/2} \nu^{1/2}$ is a function of Re_λ. The change of the flatness is *estimated* using model distributions. We have observed a steep evolution with particle size, particularly for $D < 10\eta$. Together with Reynolds number evolutions, this observation is consistent with the values reported for wind-tunnel turbulence (from $F \sim 25$–30, as measured for tracers by Ayyalasomayajula *et al.* 2008, to $F \sim 8$, as measured by Qureshi *et al.* 2007 for slightly larger particles). When looking for scaling properties of the variance or flatness of the acceleration, we have found that the variations are in agreement with the behaviour of pressure fluctuations; i.e. their evolution with scale is well predicted by the scaling of pressure increments over a separation proportional to the particle diameter. In fact, the best agreement between pressure increments and fluctuations of acceleration is obtained when intermittency corrections are added to mean field Kolmogorov arguments. Intermittency is natural in turbulence and well documented in VK flows. It may not be so surprising that it influences the statistics of motion of neutrally buoyant particles. Several points, however, deserve further studies in the future: the influence of the flow anisotropy must be quantified. To this end, we have recently devised a more symmetric version of VK flows driven by the rotation of 12 propellers, which has adjustable isotropy in the large scales (Zimmermann *et al.* 2010). Another point is the evolution when $D \sim L$, i.e. for particles approaching the integral scale. Power-law scaling may not be extended to this limit, and preliminary studies (Gasteuil 2009) in VK flows with comparable Reynolds numbers have

shown that the PDF of the accelerations of large particles ($D \sim L/5$) still has wide wings.

The authors thank Mickael Bourgoin for many useful discussions. This work was supported by grant ANR-BLAN-07-1-192604.

REFERENCES

Arneodo, A., Benzi, R., Berg, J., Biferale, L., Bodenschatz, E., Busse, A., Calzavarini, E., Castaing, B., Cencini, M., Chevillard, L., Fisher, R. T., Grauer, R., Homann, H., Lamb, D., Lanotte, A. S., Leveque, E., Luthi, B., Mann, J., Mordant, N., Muller, W. C., Ott, S., Ouellette, N. T., Pinton, J. F., Pope, S. B., Roux, S. G., Toschi, F., Xu, H. & Yeung, P. K. 2008 Universal intermittent properties of particle trajectories in highly turbulent flows. *Phys. Rev. Lett.* **100** (25), 254504-5.

Auton, T., Hunt, J. & Prud'homme, M. 1988 The force exerted on a body in inviscid unsteady non-uniform rotational flow. *J. Fluid Mech.* **197**, 241–257.

Ayyalasomayajula, S., Warhaft, Z. & Collins, L. R. 2008 Modeling inertial particle acceleration statistics in isotropic turbulence. *Phys. Fluids* **50**, 095104.

Brown, R., Warhaft, Z. & Voth, G. 2009 Acceleration statistics of neutrally buoyant spherical particles in intense turbulence. *Phys. Rev. Lett.* **103**, 194501.

Calzavarini, E., Volk, R., Lévêque, E., Bourgoin, B., Toschi, F. & Pinton, J.-F. 2009 Acceleration statistics of finite-size particles in turbulent flow: the role of Faxén corrections. *J. Fluid Mech.* **630**, 179–189.

Chevillard, L., Castaing, B., Lévêque, E. & Arneodo, A. 2006 Unified multifractal description of velocity increments statistics in turbulence: intermittency and skewness. *Physica* D **218**, 77–82.

Gasteuil, Y. 2009 Instrumentation Lagrangienne en turbulence: mise en oeuvre et analyse. PhD thesis, Ecole Normale Supérieure de Lyon.

Homann, H. & Bec, J. 2010 Finite-size effects in the dynamics of neutrally buoyant particles in turbulent flow. *J. Fluid Mech.* **651**, 81–91.

La Porta, A., Voth, G. A., Crawford, A. M., Alexander, J. & Bodenschatz, E. 2001 Fluid particle accelerations in fully developed turbulence. *Nature* **409**, 1017–1019.

Loth, E. & Dorgan, A. 2009 An equation of motion for particles of finite Reynolds number and size. *Environ. Fluid Mech.* **9**, 187–206.

Lovalenti, P. & Brady, J. 1993 The hydrodynamic force on a rigid particle undergoing arbitrary time-dependent motion at small Reynolds number. *J. Fluid Mech.* **256**, 561–605.

Marié, L. & Daviaud, F. 2004 Experimental measurement of the scale-by-scale momentum transport budget in a turbulent shear flow. *Phys. Fluids* **16**, 457–461.

Mei, R. 1996 Velocity fidelity of flow tracer particles. *Exp. Fluids* **22**, 1–13.

Monchaux, R., Ravelet, F., Dubrulle, B. & Daviaud, F. 2006 Properties of steady states in turbulent axisymmetric flows. *Phys. Rev. Lett.* **96**, 124502.

Mordant, N., Crawford, A. & Bodenschatz, E. 2004*a* Experimental Lagrangian acceleration probability density function measurement. *Physica* D **193**, 245–251.

Mordant, N., Lévêque, E. & Pinton, J. F. 2004*b* Experimental and numerical study of the Lagrangian dynamics of high Reynolds turbulence. *New J. Phys.* **6**, 116.

Mordant, N., Metz, P., Michel, O. & Pinton, J.-F. 2001 Measurement of Lagrangian velocity in fully developed turbulence. *Phys. Rev. Lett.* **87** (21), 214501.

Mordant, N., Michel, O. & Pinton, J.-F. 2002 Time-resolved tracking of a sound scatterer in a complex flow: non-stationary signal analysis and applications. *J. Acoust. Soc. Am.* **112**, 108–119.

Ott, S. & Mann, J. 2000 An experimental investigation of the relative diffusion of particle pairs in three-dimensional turbulent flow. *J. Fluid Mech.* **422**, 207–223.

Pearson, B. & Antonia, R. 2001 Reynolds-number dependence of turbulent velocity and pressure increments. *J. Fluid Mech.* **444**, 343–382.

Qureshi, N. M., Bourgoin, M., Baudet, C., Cartellier, A. & Gagne, Y. 2007 Turbulent transport of material particles: an experimental study of finite size effects. *Phys. Rev. Lett.* **99** (18), 184502.

Qureshi, N. M., Bourgoin, M., Baudet, C., Cartellier, A. & Gagne, Y. 2008 Turbulent transport of material particles: an experimental study of density effects. *Eur. Phys. J.* B **66**, 531–536.

Ravelet, F., Chiffaudel, A. & Daviaud, F. 2008 Supercritical transition to turbulence in an inertially driven von Kármán closed flow. *J. Fluid Mech.* **601**, 339–364.

de la Torre, A. & Burguete, J. 2007 Slow dynamics in a turbulent von Kármán swirling flow. *Phys. Rev. Lett.* **99**, 054101.

Toschi, F. & Bodenschatz, E. 2009 Lagrangian properties of particles in turbulence. *Annu. Rev. Fluid Mech.* **41**, 375–404.

Volk, R., Calzavarini, E., Verhille, G., Lohse, D., Mordant, N., Pinton, J. F. & Toschi, F. 2008*a* Acceleration of heavy and light particles in turbulence: comparison between experiments and direct numerical simulations. *Physica* D **237** (14–17), 2084–2089.

Volk, R., Mordant, N., Verhille, G. & Pinton, J. F. 2008*b* Laser Doppler measurement of inertial particle and bubble accelerations in turbulence. *Europhys. Lett.* **81** (3), 34002.

Volk, R., Odier, P. & Pinton, J.-F. 2006 Fluctuation of magnetic induction in von Kármán swirling flows. *Phys. Fluids* **18**, 085105.

Voth, G. A., La Porta, A., Crawford, A. M., Alexander, J. & Bodenschatz, E. 2002 Measurement of particle accelerations in fully developed turbulence. *J. Fluid Mech.* **469**, 121–160.

Yeung, P. K. 2002 Lagrangian investigations of turbulence. *Annu. Rev. Fluid Mech.* **34**, 115–142.

Zimmermann, R., Xu, H., Gasteuil, Y., Bourgoin, M., Volk, R., Pinton, J.-F. & Bodenschatz, E. 2010 The Lagrangian exploration module: an apparatus for the study of statistically homogeneous and isotropic turbulence. *Rev. Sci. Instrum.* **81** (5), 055112.

Zocchi, G., Tabeling, P., Maurer, J. & Willaime, H. 1994 Measurement of the scaling of dissipation at high Reynolds numbers. *Phys. Rev.* E **50** (5), 3693–3700.

Physica D 241 (2012) 237–244

Contents lists available at SciVerse ScienceDirect

Physica D

journal homepage: www.elsevier.com/locate/physd

Impact of trailing wake drag on the statistical properties and dynamics of finite-sized particle in turbulence

Enrico Calzavarini [a,b,*,1], Romain Volk [a,1], Emmanuel Lévêque [a,1], Jean-François Pinton [a,1], Federico Toschi [c,d,1]

[a] Laboratoire de Physique, Ecole Normale Supérieure de Lyon, CNRS and Université de Lyon, 46 Allée d'Italie, 69007 Lyon, France

[b] Laboratoire de Mécanique de Lille (LML) CNRS/UMR 8107, Université Lille 1 et École Polytechnique Universitaire de Lille, Cité Scientifique Avenue Paul Langevin, 59650 Villeneuve d'Ascq, France

[c] Department of Physics and Department of Mathematics & Computer Science and J. M. Burgers Centre for Fluid Dynamics, Eindhoven University of Technology, 5600 MB Eindhoven, The Netherlands

[d] CNR-IAC, Via dei Taurini 19, 00185 Rome, Italy

ARTICLE INFO

Article history:
Available online 26 July 2011

Keywords:
Disperse multiphase flows
Turbulence
Faxén
Drag
History force

ABSTRACT

We study by means of an Eulerian–Lagrangian model the statistical properties of velocity and acceleration of a neutrally-buoyant finite-sized particle in a turbulent flow statistically homogeneous and isotropic. The particle equation of motion, besides added mass and steady Stokes drag, keeps into account the unsteady Stokes drag force – known as Basset–Boussinesq history force – and the non-Stokesian drag based on Schiller–Naumann parametrization, together with the finite-size Faxén corrections. We focus on the case of flow at low Taylor–Reynolds number, $Re_\lambda \simeq 31$, for which fully resolved numerical data which can be taken as a reference are available [Homann H., Bec J. Finite-size effects in the dynamics of neutrally buoyant particles in turbulent flow. J Fluid Mech 651 (2010) 81–91]. Remarkably, we show that while drag forces have always minor effects on the acceleration statistics, their role is important on the velocity behavior. We propose also that the scaling relations for the particle velocity variance as a function of its size, which have been first detected in fully resolved simulations, does not originate from inertial-scale properties of the background turbulent flow but it is likely to arise from the non-Stokesian component of the drag produced by the wake behind the particle. Furthermore, by means of comparison with fully resolved simulations, we show that the Faxén correction to the added mass has a dominant role in the particle acceleration statistics even for particles whose size attains the integral scale.

1. Introduction

The exact dynamics of a material particle in an inhomogeneous unsteady flow involves nonlinear equations that can be treated analytically only in approximate form [1–4]. For this reason, several simplified models for the hydrodynamic forces acting on a particle have been proposed in the literature [5,6]. It is still unclear however to what extent these models provide an accurate description in turbulent flow conditions, even in an averaged or statistical sense. A proper statistical description of particle dynamics would be a first important step toward building constitutive equations for the particulate phase carried by turbulent fluids. It would also be of practical importance for the many environmental phenomena and industrial applications in which particle suspensions in turbulence are involved. We intend here to contribute to this goal by carrying out refined simulations of particles in turbulent flow, and discriminate whether the particle model employed leads to physically sound results, in agreement with recent experiments and with fully resolved direct numerical simulations.

In previous studies, we have addressed the dynamics of small material particles with a description based on a minimal Lagrangian model accounting for pressure gradient, added mass term, and steady Stokes drag force [7,8]. While this system produces several features of particle dynamics, like clustering and segregation as well as single-/multi-time statistics of acceleration and velocity, it fails to predict some statistical properties, particularly when the size of the particle is progressively increased above the dissipative scale of turbulence [9]. In order to better understand these discrepancies we have focused on the case of finite-sized and neutrally buoyant particles. We have proposed that Faxén corrections are the essential ingredients to account for the statistical properties of finite-sized particle acceleration in

* Corresponding author at: LML, University of Lille 1, France.
E-mail addresses: enrico.calzavarini@polytech-lille.fr (E. Calzavarini), romain.volk@ens-lyon.fr (R. Volk).

[1] International Collaboration for Turbulence Research.

0167-2789/$ – see front matter © 2011 Elsevier B.V. All rights reserved.
doi:10.1016/j.physd.2011.06.004

turbulence [10]. Numerical predictions of the particle acceleration variance (and of its probability density function) based on the Faxén argument were compared with experiments made in wind-tunnel [11] and resulted in agreement with Von Karman flow measurements [12]. In a more recent work, experimental measurements support also other trends highlighted by the Faxén model: the effect of decrease of acceleration flatness as a function of the particle-size and the corresponding growth of the correlation time of the acceleration [13].

Another series of numerical studies were recently conducted by Homann and Bec [14] (HB in the following). These authors employed a direct numerical approach. They tracked the motion of a neutrally buoyant finite-sized particle in a turbulent flow by enforcing the no-slip velocity at the particle surface via a penalty method on the discretized Navier–Stokes equation. In such a way they have been able to access the dynamics of a single finite-size particle in the diameter range $[2, 16]\eta$ in a moderately turbulent flow at $Re_\lambda = 32$. Both velocity and acceleration statistics were investigated. Therefore, HB measurements provide a set of reference data against which one can test particle Lagrangian models, as attempted here. The scope of this work however goes beyond the validation of a model equation. We also aim at having a physical picture of the statistical dynamics of particles. We have specific questions in mind: What is the statistical effect of the drag, particularly the trailing wake drag, on the dynamics of a neutrally-buoyant finite-size particle in turbulent flow? Does it modify the acceleration statistics or rather the velocity one? Is the role of Faxén correction still relevant for particles with size in the inertial range? We will see how our study provides an answer to these questions and a possible interpretation of the phenomenological picture.

The paper is organized as follow. In Section 2 we describe the approach adopted in this study, we introduce the Lagrangian modeling of the particle dynamics, its numerical implementation, and some expected trends for the particle velocity and acceleration in the vanishing-size limit. In Section 3 we present the results of the numerical study, starting from the particle Reynolds number behavior, and addressing then acceleration and velocity statistics as a function of the particle size. Comparison with direct numerical simulation data is discussed in detail in Section 4. In the conclusions we summarize the main results and give suggestions for possible future experimental/numerical investigations.

2. Methods

2.1. Particle equation of motion

We consider a Lagrangian equation of motion one-way coupled to a continuum flow $\mathbf{u} \equiv \mathbf{u}(\mathbf{x}, t)$. Such an equation takes into account the pressure gradient and added mass term ($\sim D\mathbf{u}/Dt$), the drag force and the volume and surface Faxén corrections. The drag force is divided into three parts: the steady Stokes drag, the unsteady Stokes drag force or History force, and the non-Stokesian drag force. All together it reads as follow:

$$\frac{\mathrm{d}\mathbf{v}}{\mathrm{d}t} = \beta \left[\frac{D\mathbf{u}}{Dt}\right]_V + \frac{3\nu\beta}{r_p^2}\left([\mathbf{u}]_S - \mathbf{v}\right) \tag{1}$$

$$+ \frac{3\beta}{r_p}\int_{t-t_h}^{t} \left(\frac{\nu}{\pi(t-\tau)}\right)^{\frac{1}{2}} \frac{\mathrm{d}}{\mathrm{d}\tau}\left([\mathbf{u}]_S - \mathbf{v}\right)\mathrm{d}\tau \tag{2}$$

$$+ c_{Re_p}\frac{3\nu\beta}{r_p^2}\left([\mathbf{u}]_S - \mathbf{v}\right) \tag{3}$$

where r_p is the particle radius, ν the kinematic viscosity, β the density coefficient $\beta \equiv 3\,\rho_f/(\rho_f + 2\,\rho_p)$. Following [2] the Faxén corrections are expressed as volume and surface average of the continuum fields $D\mathbf{u}/Dt$ and $\mathbf{u}$ over a sphere of radius r_p centered at the particle position, respectively:

$$\left[\frac{D\mathbf{u}}{Dt}\right]_V = (4/3\,\pi r_p^3)^{-1}\int_V \frac{D\mathbf{u}}{Dt}(\mathbf{x}, t)\,\mathrm{d}^3x \tag{4}$$

$$[\mathbf{u}]_S = (4\pi r_p^2)^{-1}\int_S \mathbf{u}(\mathbf{x}, t)\,\mathrm{d}^2x. \tag{5}$$

The history force is based here on the Basset–Boussinesq diffusive kernel, $\sim(t-\tau)^{-1/2}$, while t_h is the time over which the memory effect is significant. The non-Stokesian drag coefficient c_{Re_p} models the effect of the drag induced by the presence of a wake behind the particle. Of course in a Lagrangian model of particle dynamics, which is only one-way coupled to the fluid flow, no wake can be produced. Therefore, we resort to a model: the well known Schiller–Naumann (SN) parametrization [15]. The c_{Re_p} coefficient, which is a function of the particle-Reynolds number based on the diameter size $d_p \equiv 2r_p$ and on an estimator of the slip velocity, $Re_p \equiv |[\mathbf{u}]_S - \mathbf{v}|\,d_p/\nu$, is chosen to have the form $c_{Re_p} = 0.15 \cdot Re_p^{0.687}$ considered to be a good approximation whenever $Re_p < 1000$ [16]. We note also that direct numerical simulations of the flow around a solid particle maintained fixed in a turbulent flow shows a good agreement between the real force acting on the particle (as computed from strain tensor at the surface of the particle) and the drag computed from the slip velocity with Schiller–Naumann parametrization [17,18].

For simplicity in this study the lift force is neglected. This may be regarded at first as a strong approximation, however for the case of neutrally buoyant particles the lift has indeed only a minor statistical effect. This is confirmed also by our numerical simulations based on equations (1), (2) and (3) plus the lift force [6] $\frac{\beta}{3}\left([\mathbf{u}]_S - \mathbf{v}\right) \times [\nabla \times \mathbf{u}]_S$ (not reported in the present article).

2.2. Numerical implementation

We aim at studying the statistical signature of the different forces acting on the particle. For this reason in our numerical simulations we follow the trajectories of four species (or families) of particles with slightly different evolution equations. The first family is described by (1), it includes only the added-mass term and the steady Stokes drag and their Faxén corrections. It will be called Faxén model with Stokes drag. The second family is defined by (1) + (2), hence it includes also the history force. The third is based on (1) + (3), therefore the Schiller–Naumann correction is here included but not the history force. Finally the fourth family (1) + (2) + (3) keeps into account all the effects. See Table 1 for a summary of the four particle families.

2.2.1. Faxén forces

The implementation of Faxén averages in our simulation is based on the Gaussian approximation proposed in a previous study [10]. The volume average of fluid acceleration at particle position is replaced by a local interpolation at the particle position of the continuum field after convolution by a three-dimensional Gaussian envelope $G(\mathbf{x})$, with unit volume and standard deviation σ. Convolutions are efficiently computed in spectral space, the volume averaged field hence reads:

$$\left[\frac{D\mathbf{u}}{Dt}(\mathbf{x}, t)\right]_V \simeq \int_{L^3} G(\mathbf{x}')\frac{D\mathbf{u}}{Dt}(\mathbf{x} - \mathbf{x}', t)\,\mathrm{d}^3x' \tag{6}$$

$$= \mathcal{D}\mathcal{F}\mathcal{T}^{-1}\left[\tilde{G}(\mathbf{k})\frac{\tilde{D\mathbf{u}}}{Dt}(\mathbf{k}, t)\right] \tag{7}$$

Table 1
The four particle families considered in the present study and their respective equations of motion.

Particle type	Eq.
Faxén model with Stokes drag	(1)
+History force	(1), (2)
+Non-Stokesian drag	(1), (3)
+Non-Stokesiandrag + Historyforce	(1), (2), (3)

In total we integrate simultaneously the dynamics of $N_p = 1.28 \cdot 10^6$ particles. This ensemble is divided into 4 families, each family having 8 different sizes, in the diameter range $d_p \in [0, 32]\eta$. This amount to $3.2 \cdot 10^4$ particles per type.

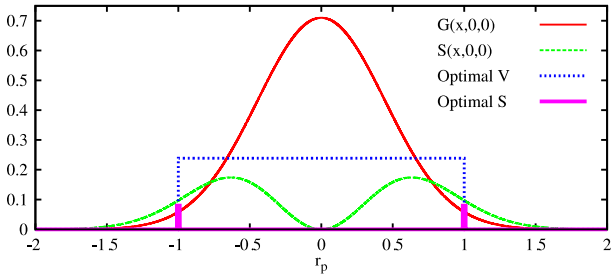

Fig. 1. Real space one-dimensional projection, on the direction $(x, 0, 0)$, of filter functions. The volume Gaussian filter is $G(\mathbf{x}) = (1/(\sqrt{2\pi}\sigma))^3 \exp(-\mathbf{x}^2/(2\sigma^2))$, while the surface convolution kernel turns out to be $S(\mathbf{x}) = (\mathbf{x}^2/(2\sigma^2))G(\mathbf{x})$. The optimal shape of volume and surface filter functions are also shown. The volume filter function is a three dimensional spherical gate function with total volume $4/3, \pi r_p^3$, while the surface one is a delta function over the surface of the sphere but normalized in such a way that its volume integral is $4\pi r_p^2$.

where $\mathcal{DFT}^{-1}$ denotes a discrete inverse Fourier transform on a cubic grid with N^3 nodes, while the over script $\sim$ indicates a direct Fourier transform, $\tilde{G}(\mathbf{k}) = \exp(-\sigma^2\mathbf{k}^2/2)$ being the Fourier transform of $G(\mathbf{x})$. We note that by setting the standard deviation $\sigma \equiv r_p/\sqrt{5}$, in the limit of small radii one gets $\tilde{G}(\mathbf{k}) \simeq 1 - (r_p^2/10)\mathbf{k}^2 + \mathcal{O}(r_p^4)$ which leads to the correct first order Faxén correction in real space, i.e., $\mathbf{u} + (r_p^2/10)\Delta\mathbf{u} + \mathcal{O}(r_p^4)$. Analogously the surface average reads:

$$[\mathbf{u}(\mathbf{x}, t)]_S = \frac{1}{3r_p^2}\frac{\mathrm{d}}{\mathrm{d}r_p}\left(r_p^3\,[\mathbf{u}(\mathbf{x}, t)]_V\right) \tag{8}$$

$$= \mathcal{DFT}^{-1}\left[\left(1 - \sigma^2\mathbf{k}^2/3\right)\tilde{G}(\mathbf{k})\tilde{\mathbf{u}}(\mathbf{k}, t)\right]. \tag{9}$$

For clarity in Fig. 1 the shape of the two convolution kernels (volume and surface) in real space are shown. The figure also shows for comparison the so called *optimal* convolution kernels, corresponding respectively to a three dimensional spherical gate function of volume $4/3\,\pi r_p^3$ for volume average and to a delta function over a spherical shell for surface average. Of course the implementation of such *optimal* averages in real space would be computationally more expensive. In Section 4 we will investigate in detail the bias induced on the particle dynamics by the use of such a Gaussian approximation for Faxén corrections instead of the rigorous definition.

2.2.2. History force

The Basset–Boussinesq history force can be computationally very expensive. This is due to the fact that the integral which is involved should be performed at each time-step on the full particle history. Furthermore the diffusive kernel, $\sim (t - \tau)^{-1/2}$ has a very slow decay and require a long memory time – virtually $t_h = \infty$ – to reach convergence. It is known however that the diffusive kernel overestimates the history force for particles characterized by finite Reynolds numbers Re_p [19]. The formation of a trailing wake either stationary, nonstationary or even turbulent is always associated to history kernel which decay faster than the Basset–Boussinesq [20]. Equivalently we can say that in $Re_p \gg 1$ conditions the Basset–Boussinesq history force should have a shorter memory time window t_h. This latter idea has been exploited in the computational approach called window method [21]. Recently a more accurate method based on the fit of the diffusive kernel tail via a series of exponential functions has also been proposed [22]. In this study we adopt a simple window approximation: instead of setting $t_h = \infty$ we chose $t_h \simeq 10\tau_\eta$ but keep the diffusive kernel functional form. This choice is based on the observation that in the turbulent conditions considered in our study after a time $10\tau_\eta$ the Lagrangian signal $\mathrm{d}([\mathbf{u}]_S - \mathbf{v})/\mathrm{d}t$ is already completely uncorrelated. The short memory on the history force is therefore not given by the specific kernel form (which is indeed almost flat in our case) but from the relatively short correlation time of the turbulent flow. With this choice, t_h corresponds approximately to 10^3 time-steps of our simulations, which are stored and used for the discrete estimation of the history integral at each time-step. We note that our t_h satisfies the criterion given in Ref. [21,6] for the window method and it has a double extension in time steps respect to the time window considered in the numerical validations considered in Ref. [22]. We have also performed *a posteriori* check in which the pre-recorded $\mathrm{d}([\mathbf{u}]_S - \mathbf{v})/\mathrm{d}t$ signal has been used to compute the history force with different values of the window's length. This test has further confirmed the convergence and reliability of the adopted implementation.

2.2.3. Eulerian dynamics

A suitable turbulent flow is generated by integrating the Navier–Stokes equation in a cubic box of size $L = 2\pi$ with periodic boundary conditions. The flow is forced on the largest shells in spectral space, on the wave-vectors for which the condition $\mathbf{k}^2 \leq 2^2(2\pi/L)^2$ is satisfied. The force we adopt in this study keeps fixed the amplitude of kinetic energy of the large scales. More details concerning the values of relevant input and output quantities of the numerical simulation of this turbulent flow are provided in Table 2.

2.3. Faxén corrections and small particle limit predictions

In the study of Homann and Bec [14] a derivation of the functional behavior of the variance of particle velocity and acceleration in the limit of vanishing particle diameters d_p has been proposed. The argument is based on a perturbative expansion of the Faxén correction for the velocity. This reads as[2]:

$$\mathbf{v} \simeq [\mathbf{u}]_S \simeq \mathbf{u} + \frac{d_p^2}{24}\Delta\mathbf{u} + \mathcal{O}(d_p^4). \tag{10}$$

Furthermore, the hypothesis of a spatially homogeneous particle distribution in the limit $d_p \to 0$ is made. By squaring Eq. (10), retaining only quadratic terms in d_p, and averaging over the particle ensemble and in time, $\langle \ldots \rangle$, one gets:

$$\langle \mathbf{v}^2 \rangle \simeq \langle \mathbf{u}^2 \rangle - \frac{d_p^2}{12}\langle \mathbf{u}\Delta\mathbf{u} \rangle = \langle \mathbf{u}^2 \rangle - \frac{d_p^2}{12}\frac{\varepsilon}{\nu} = \langle \mathbf{u}^2 \rangle - \frac{5}{3}\left(\frac{d_p}{2\lambda}\right)^2, \tag{11}$$

where $\varepsilon \equiv (\nu/2)\langle(\nabla\mathbf{u} + (\nabla\mathbf{u})^T)^2\rangle = \nu L^{-3}\int_{L^3}\mathbf{u}\Delta\mathbf{u}\,d^3x$ is the mean energy dissipation rate and $\lambda \equiv (5\nu\langle\mathbf{u}^2\rangle/\varepsilon)^{1/2}$ is the Taylor micro-scale. If we instead (i) differentiate with respect to time Eq. (10), (ii) make the assumption $D/Dt \simeq \mathrm{d}/\mathrm{d}t$, and then (iii) square and

[2] Note that (10) corrects a typo contained in Ref. [14] on the numerical coefficient in front of $d_p^2\Delta\mathbf{u}$, which had affected all the predictions proposed in that study. Our calculations for Eq. (11) provides a coefficient 5/3, instead of 1/100 given in [14]. Furthermore in Eq. (12) we find the coefficient 1/12, and not 1/20.

Table 2
Parameters of the numerical simulation: N number of grid points per spatial direction; $\delta x = 2\pi/N$ and δt are the spatial and temporal discretization; ν is the value of kinematic viscosity; ε the mean value of the energy dissipation rate. $\eta = (\nu^3/\varepsilon)^{1/4}$ and $\tau_\eta = (\nu/\varepsilon)^{1/2}$ are the Kolmogorov dissipative spatial and temporal scales, $u_{\rm rms} = \left(\overline{\langle u_i u_i\rangle_V}/3\right)^{1/2}$ the single-component root-mean-square velocity, $\lambda = (15\,\nu\,u_{\rm rms}^2/\varepsilon)^{1/2}$ the Taylor micro-scale, $T_E = (3/2)u_{\rm rms}^2/\varepsilon$ and $L_E = u_{\rm rms}\,T_E$ are the Eulerian large-eddy-turnover temporal and spatial scales; $Re_\lambda = u_{\rm rms}\,\lambda/\nu$ the Taylor scale based Reynolds number. $t_{\rm tot}$ is the total simulation time in statistically stationary conditions and the total time-span of particle trajectories.

N^3	δx	δt	ν	ε	η	τ_η	$u_{\rm rms}$	λ	T_E	L_E	Re_λ	$t_{\rm tot}$
128^3	$4.9\cdot10^{-2}$	$3.2\cdot10^{-3}$	$4.4\cdot10^{-2}$	$7.5\cdot10^{-1}$	$1.0\cdot10^{-1}$	$2.4\cdot10^{-1}$	1.2	1.1	2.9	3.5	31	192

average the result, we obtain an approximate prediction for the acceleration variance

$$\langle \mathbf{a}^2\rangle \simeq \left\langle \frac{D\mathbf{u}}{Dt}^2 \right\rangle - \frac{d_p^2}{12}\left\langle \left|\left| \frac{D(\nabla\mathbf{u})}{Dt} \right|\right|^2 \right\rangle. \tag{12}$$

We will see in the following to which extent these approximations can be considered appropriate to describe the particle behavior. We note that in the simulations we have direct access to the values $\langle([\mathbf{u}]_S)^2\rangle$ and $\langle([D\mathbf{u}/Dt]_V)^2\rangle$ which can be used for comparison. Finally, it is also worth noting that the particle Reynolds number Re_p is proportional to $|\mathbf{v} - [\mathbf{u}]_S|$, this means that in the small-particle limit the leading order is $\mathcal{O}(d_p^4)$, hence one expects $Re_p \sim d_p^5$.

3. Results

3.1. Particle Reynolds number

We begin investigating the particle Reynolds number Re_p as a function of the particle diameter, with measurements reported in Fig. 2. First we note that in the range $d_p \in [3.2, 32]\eta$ the mean Reynolds number varies considerably, three order of magnitudes from 10^{-1} to about 10^2. We can immediately observe that the particle models which are making use only of Stokes drag forces – that is to say based on the assumption $Re_p < 1$ – cannot be considered entirely consistent. Such models underestimate the actual drag on the particle. This is clearly noticeable for the Faxén model with Stokes drag in the large-d_p range, when Re_p attains the maximal value $\mathbf{u}_{\rm rms}d_p/\nu$, corresponding to a ballistic particle velocity $\mathbf{v}$ not varying in time and not correlated to the local fluid velocity $[\mathbf{u}]_S$. We note instead that for all the models in the small particle limit we have a steeper scaling (slope 4.50 ± 0.05), close to the expected d_p^5. Hence, in the small particle regime $\mathbf{v}$ and $[\mathbf{u}]_S$ are highly correlated, differing only by $\mathcal{O}(d_p^4)$ terms. We also notice that, while the history force produces just a shift, the non-Stokesian drag term changes the slope in the large particle regime. This apparently minimal variations have, as we will see later on, important consequences on the statistics of the particle velocity variance.

3.2. Acceleration statistics

We examine now some statistical properties of the acceleration. In Fig. 3 we show the behavior of the single-component particle acceleration variance $\langle a_i^2\rangle$ normalized by the fluid acceleration variance $\langle(D_t u_i)^2\rangle$ as a function of the particle size in d_p/η units. It is remarkable to note that all the particle models leads to very similar results. The History force or the Non-Stokesian drag have no effect, at least for this observable. The overall trend of the acceleration variance is dominated by the Faxén Volume correction, $\langle a_i^2\rangle \simeq \langle[D\mathbf{u}_i/Dt]_V^2\rangle$ with $[D\mathbf{u}_i/Dt]_V$ sampled homogeneously in space over the field (see Fig. 3). Eq. (12) based on the first order approximation, although qualitatively correct, fails to predict quantitatively the measurements for $d_p > 4\eta$. In Fig. 3 we have plotted the data points from HB [14]. The agreement with our data is excellent up to $d_p \simeq 4\eta$, while the Lagrangian model shows a less pronounced

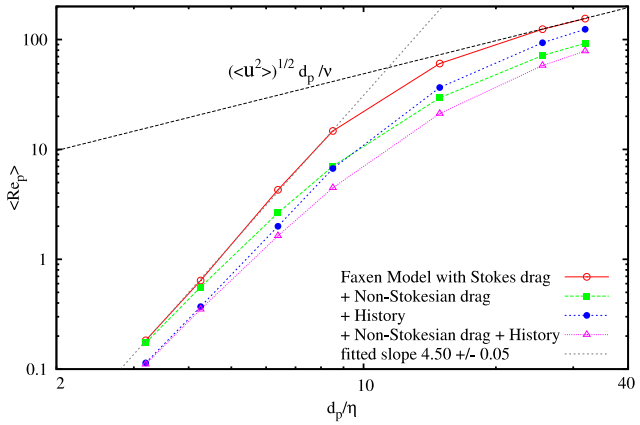

Fig. 2. Mean particle Reynolds number, $\langle Re_p\rangle$, versus the diameter in Kolmogorov scale units, d_p/η, form the four different models. A power-law fit to the Faxén model with Stokes drag on the smallest particle sizes is shown, we get a 4.5 slope. For the same model, the maximal Reynolds number $\mathbf{u}_{\rm rms}d_p/\nu$ is reached by the largest particles.

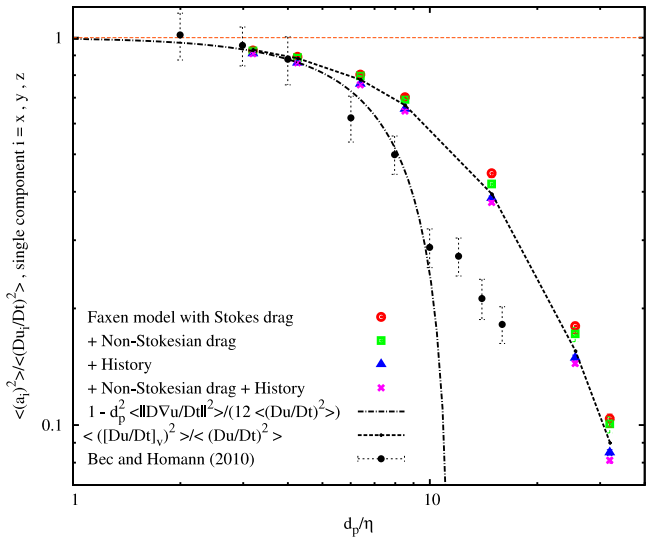

Fig. 3. Normalized single-component particle acceleration variance for particles of different sizes: $\langle(a_i)^2\rangle/\langle(D_t u_i)^2\rangle$ vs. d_p/η. Here $\langle(D_t u_i)^2\rangle$ is the fluid tracer acceleration variance or equivalently the Eulerian acceleration averaged over time and space. The behavior of the four different models adopted is reported. The dash-dotted line represent the behavior of particle acceleration variance expected to originate from Faxén corrections in the small particle limit (see Eq. (12)). The dotted line represents the ratio of the variance of the volume filtered Eulerian field $[D\mathbf{u}/Dt]_V$ to the fluid acceleration variance.

decrease (approximately by a factor of two) for larger diameters. We will analyze the possible origin of these difference in Section 4.

In Fig. 4 we show the measurements of the acceleration flatness $F(a_i) = \langle a_i^4\rangle/(\langle a_i^2\rangle)^2$ normalized by the fluid acceleration flatness $F(D\mathbf{u}_i/Dt)$ versus particle size. As already noticed in [10], and experimentally verified in [13] the flatness decreases with increasing the particle size. Here the different Lagrangian models

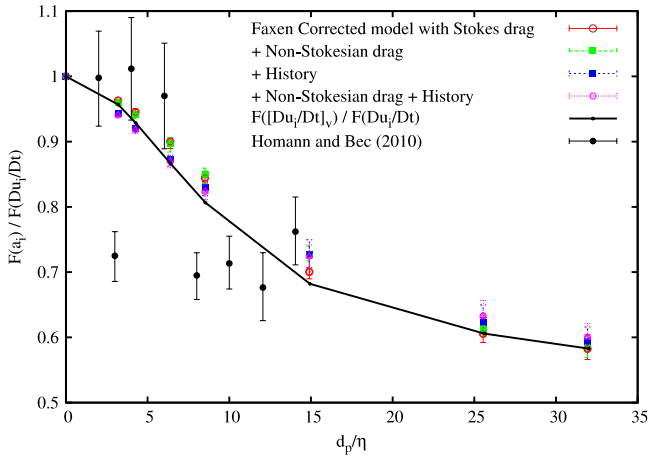

Fig. 4. Single-component particle acceleration flatness, $F(a_i)$, normalized by the fluid tracer acceleration flatness, $F(D_t u_i)$, as a function of the particle diameter in η units. The dotted line represents the ratio of the flatness of the volume filtered Eulerian field $[D\mathbf{u}/Dt]_V$ to the fluid acceleration flatness.

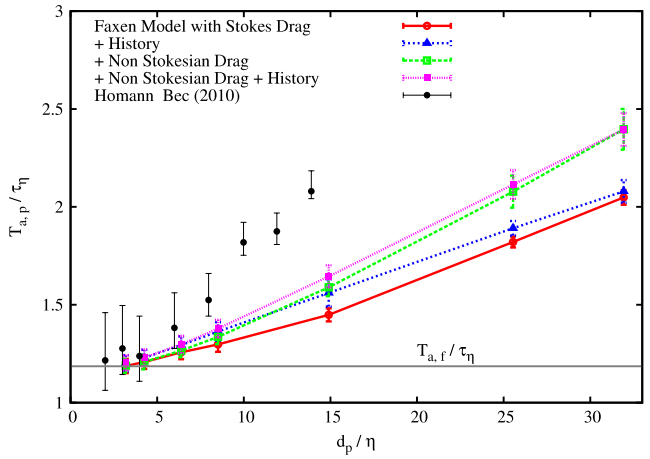

Fig. 5. Correlation time of acceleration $T_{a,p}$, in τ_η units, as a function of the normalized particle diameter d_p/η.

lead only to small shifts in the flatness value, hence the picture remains the same as for the variance. Although, HB direct numerical simulations may suffers of lack convergence the case of flatness, the measurements are in qualitative agreement with our simulations. Finally we look at the correlation time of the particle acceleration. As done before [10], we define the acceleration correlation time as the integral of the correlation function from time zero till its first change of sign:

$$T_{a,p} = \int_0^{\tau_0} C_{\mathrm{a}_i}(\tau)\,\mathrm{d}\tau; \quad C_{\mathrm{a}_i}(\tau) \equiv \frac{\langle \mathrm{a}_i(t+\tau)\mathrm{a}_i(t)\rangle}{\langle(\mathrm{a}_i(t))^2\rangle} \tag{13}$$

where $C_{\mathrm{a}_i}(\tau_0) = 0$. We observe that, as soon as the particle size grows, the acceleration correlation time $T_{a,p}$ deviates from the tracer value $T_{a,f}$ ($\simeq 1.2\,\tau_\eta$), Fig. 5. This growth, is a result of the Faxén averaging (in fact it is absent when averaging is not included, see the discussion in [10]) and comes from the fact that in finite-sized particles Stokes drag becomes negligible, leading to $\mathrm{d}\mathbf{v}/\mathrm{d}t \simeq [D\mathbf{u}/Dt]_V$. We note however that there is also a significant difference between the basic Faxén Stokes drag model, for which the mechanism explained before is at work, and the model with non-Stokesian drag, the latter one producing more correlation. This feature is rather surprising and has a different origin. One may think that including non-Stokesian drag, the effective response time of the particle, i.e., $1/\tau_{eff} = (1 + C_{Re_p})3\nu\beta/r_p^2$ is reduced, therefore the acceleration should be correlated on a shorter time scale $\sim\tau_{eff}$. As we will see later in Section 3.3 when non-Stokesian drag is active, the drag is never negligible and $\mathbf{v} \simeq [\mathbf{u}]_S$, hence for the acceleration $\mathrm{d}\mathbf{v}/\mathrm{d}t \simeq \mathrm{d}\,[\mathbf{u}]_S\,/\mathrm{d}t$. It is clear that $\mathrm{d}\,[\mathbf{u}]_S\,/\mathrm{d}t = \partial_t\,[\mathbf{u}]_S + [\mathbf{u}]_S \cdot \partial\,[\mathbf{u}]_S$ does not have the sub-grid (sub particle-size) correlations included in $[D\mathbf{u}/Dt]_V = \partial_t\,[\mathbf{u}]_v + [\mathbf{u}\cdot\boldsymbol{\partial}\,\mathbf{u}]_V$, which are correlated on shorter timescales.

Any Lagrangian model equation seems however to underestimate the real $T_{a,p}$ resulting form the HB direct numerical simulations. This fact has been also noticed, in a comparison of Faxén Lagrangian model with experimental data [13].

3.3. Velocity statistics

Contrary to the acceleration's case the velocity particle statistics is deeply affected by the form of the particle dynamical equation. In Fig. 6 we show as a function of the particle size the measurements of the deviation of normalized single-component particle velocity variance with respect to the velocity variance of the turbulent flow: $(\langle \mathbf{u}_i^2\rangle - \langle \mathbf{v}_i^2\rangle)/\langle \mathbf{u}_i^2\rangle$. The first model – based simply on Faxén terms and Stokes drag – predicts for this quantity a non-monotonous behavior, leading for the bigger particle sizes to a velocity

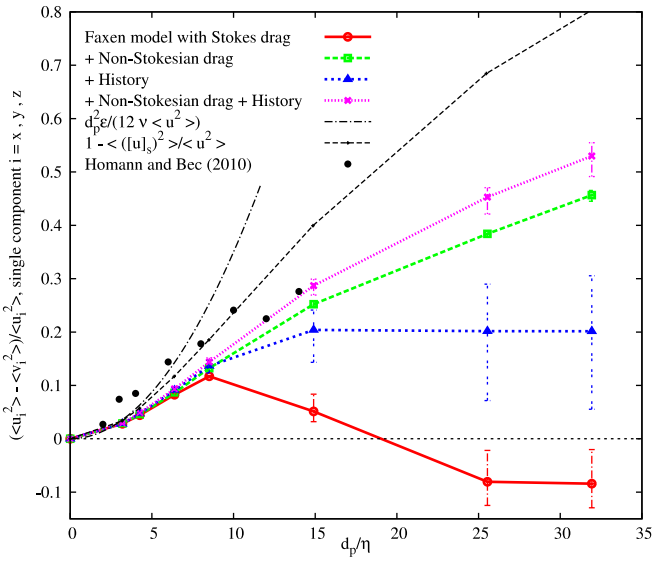

Fig. 6. Deviation of the particle velocity variance from the fluid value, as a function of the dimensionless particle diameter d_p/η. The behavior of the four different models adopted is reported. The dash-dotted line represent the deviation from the fluid root-mean-square (r.m.s.) velocity that is expected to originate from Faxén corrections in the small particle limit (see Eq. (11)). The dashed line represents the deviation of the variance of the surface filtered Eulerian field $[\mathbf{u}]_S$ from the unfiltered velocity variance.

variance even larger than the fluid one. This results is rather unphysical (as it is not possible for a particle to be on average more energetic then the flow by which it is driven and transported) and clearly it represents a limitation of the basic Faxén model with Stokes drag. This limitation is readily cured whenever an extra drag force is added. Among History and non-Stokesian drag it is definitely the latter one bringing the most significant changes. The non-Stokesian drag reduces the kinetic energy of the particle as compared to the one of a fluid tracer, this energy decreases monotonically with the particle size. For comparison, in Fig. 6 we have also reported the prediction in the limit of small-particles, Eq. (11). As for the acceleration, this analytical prediction seems to be a good approximation to the measurements up to $d_p \simeq 4\eta$. We also report in Fig. 6 the value of the variance of the Eulerian filtered field $[\mathbf{u}]_S$. One can note that by adding more drag to the basic Stokes term, the particle velocity approaches the filtered fluid velocity variance, i.e. $\mathbf{v} \to [\mathbf{u}]_S$. We note that the prediction of the Lagrangian models keeping into account all the considered effects Eqs. (1)–(3), agree well with the HB data. Apart from

the parabolic ($\sim d_p^2$) behavior for vanishing particle sizes no clear scaling of the normalized velocity variance can be detected form our measurement. In HB it was proposed that a scaling regime with slope $d_p^{2/3}$ would appear out of the Faxén dominated regime. This was attributed to the effect of the background turbulent flow, via the assumption $\langle v_i^2 \rangle \sim \langle (\delta u_{d_p})^2 \rangle \sim d_p^{2/3}$ where the Kolmogorov scaling relation for the second order Eulerian structure function $\langle (\delta u_r)^2 \rangle \equiv \langle (\mathbf{u}(\mathbf{x}+\mathbf{r}) - \mathbf{u}(\mathbf{x})) \cdot \hat{\mathbf{r}}^2 \rangle \sim r^{2/3}$ is implied. Here we would like to advance another explanation, the different scaling in that intermediate regime seems to be an effect of the drag term and in particular of the non-Stokesian drag (see again Fig. 6). We note that non-Stokesian drag term included in our model equations based on SN parametrization accounts rather for the effect of a stationary wake behind the particle than for wake generated turbulent fluctuations. Given the good agreement of our data with HB measurements, our guess is that the background turbulent fluctuations plays only a minor role in determining the particle velocity statistics.

The non-Stokesian term has also important consequences on the velocity correlation time. Such a time can be defined as the time integral of the correlation function:

$$T_p = \int_0^{+\infty} C_{\mathrm{v}_i}(\tau)\, \mathrm{d}\tau; \quad C_{\mathrm{v}_i}(\tau) \equiv \frac{\langle \mathrm{v}_i(t+\tau)\mathrm{v}_i(t) \rangle}{\langle (\mathrm{v}_i(t))^2 \rangle}. \tag{14}$$

As we have already mentioned, the Stokes drag force alone is not effective in slowing down the velocity especially for large particles. This produces quasi-ballistic trajectories, governed by $\mathbf{v}(t) \simeq \int_0^t \left[D_t \mathbf{u}(t')\right]_V \mathrm{d}t'$, that tend to have very large correlation time. The non-Stokesian (or wake) drag provides instead a way to reduce particle speed, $\mathbf{v}(t) \simeq [\mathbf{u}]_S$ and its correlation time. This is evident from Fig. 7 where the correlation functions for different terms for a large Stokesian and a large non-Stokesian particle are compared.

On Fig. 8 the trend of the velocity correlation time as a function of the particle size is shown. Non-Stokesian drag produces a reduction of T_p of more than 100% as compared to the purely Stokesian case.

4. Discussion

In previous sections we have shown that the agreement of the Lagrangian model, even in its complete form Eqs. (1), (2), (3), with the measurements from HB direct numerical simulations is rather satisfactory for the variance of the velocity as a function of the particle size. However, we observe systematic deviations when acceleration is concerned. Here we would like to discuss the causes of these discrepancies more in detail. We can advance the following hypothesis:

(i) The differences originate from a limitation of the model which takes into account volume and surface averages only in the approximate form of a Gaussian convolution. Although this approximation is well tuned for the first order Faxén correction, it might be less accurate for larger particles, when roughly $d_p > 4\eta$.

(ii) The model neglects the effect of particle interaction with its own wake. This effect, while negligible in a flow with a large mean component, might become relevant in the isotropic flow conditions considered here (and in HB work) where a particle can cross a region previously perturbed by its own wake.

(iii) The observed discrepancies may come from differences in the simulated turbulent flows—in fact differences in the forcing at such small Reynolds number $Re_\lambda \sim 32$ may have consequences even on the small scale statistics. The point (i) can be investigated carefully. In order to see if there is any bias induced by Gaussian averaging as compared to the mean over a sphere, we have averaged the field $D\mathbf{u}(\mathbf{x}, t)/Dt$ over a large number of spheres of diameters

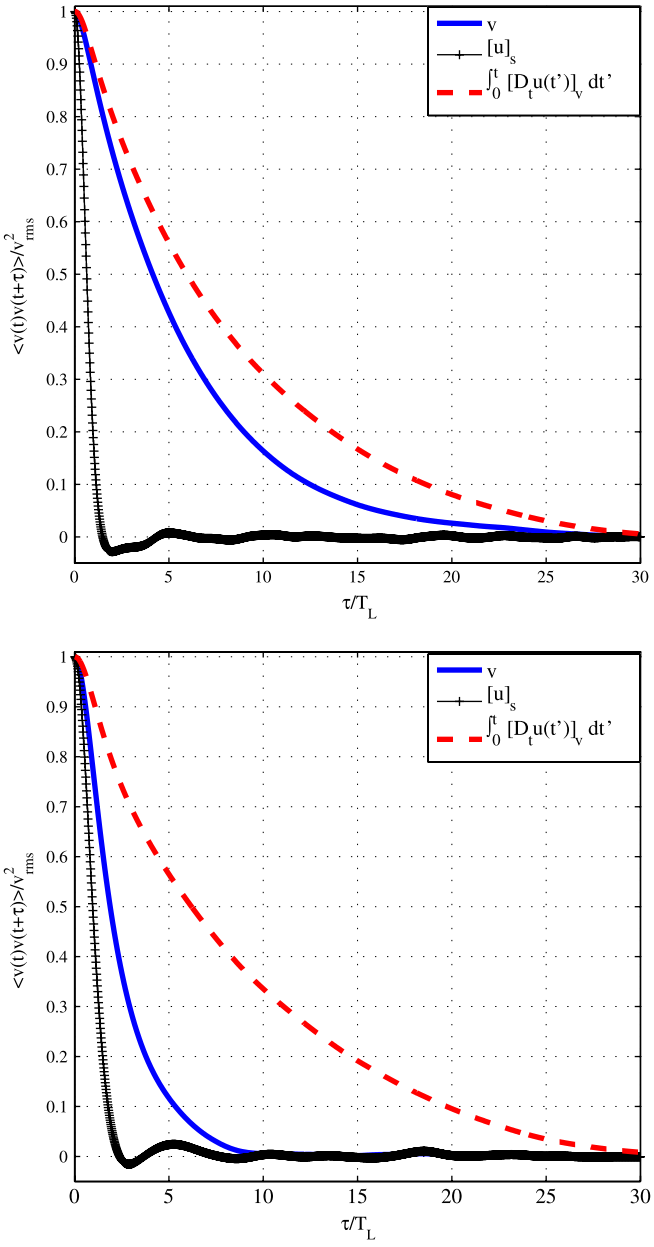

Fig. 7. Correlation function of particle velocity $\mathbf{v}$, of the filtered fluid velocity along the particle trajectory $[\mathbf{u}]_S$, and of the time integral of fluid acceleration $\int_0^t \left[D_t \mathbf{u}(t')\right]_V \mathrm{d}t'$ for particle size $d_p = 32\eta$. Faxén model with Stokes drag (top), with non-Stokesian drag (bottom).

d_p, uniformly distributed over random locations in space. This procedure is repeated over 250 Eulerian $D\mathbf{u}/Dt$ snapshots, equally spaced in time over an interval of $20\,T_E$. Although this method is not precise for small sphere diameters when only few points of the discretized $D\mathbf{u}/Dt$ field enter into the average, for large diameters the average converges rapidly to the correct (continuum-limit) values. In Fig. 9 we report the results of these measurements for the variance and the flatness of $[D\mathbf{u}/Dt]_V$ (sphere), as a function of d_p and we compare it with the Gaussian averages $[D\mathbf{u}/Dt]_V$ (Gauss), and with the measurements on the Lagrangian models and DNS data. The result shows that the sphere average is sensibly different from the Gaussian convolution. For small particles the discretization bias fails to match the analytical prediction (11), which is instead well captured by the Gaussian distribution. For larger particle sizes the sphere average shows a stronger decrease of the variance as compared to the Gaussian case. Remarkably in

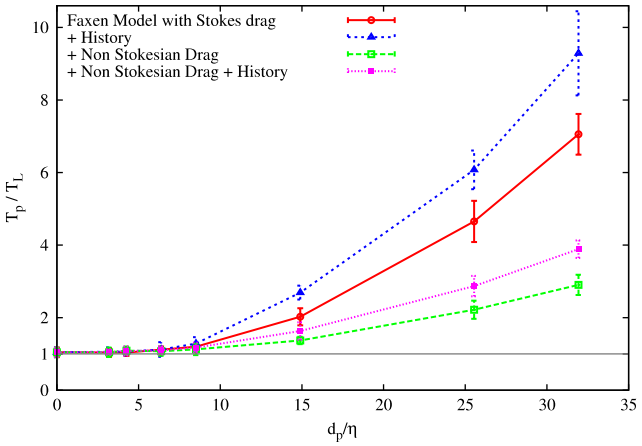

Fig. 8. Integral correlation time of particle velocity T_p as a function of the diameter d_p. T_p is made dimensionless by the integral velocity correlation time of a Lagrangian tracer T_L, while the diameter is normalized by the dissipative scale η.

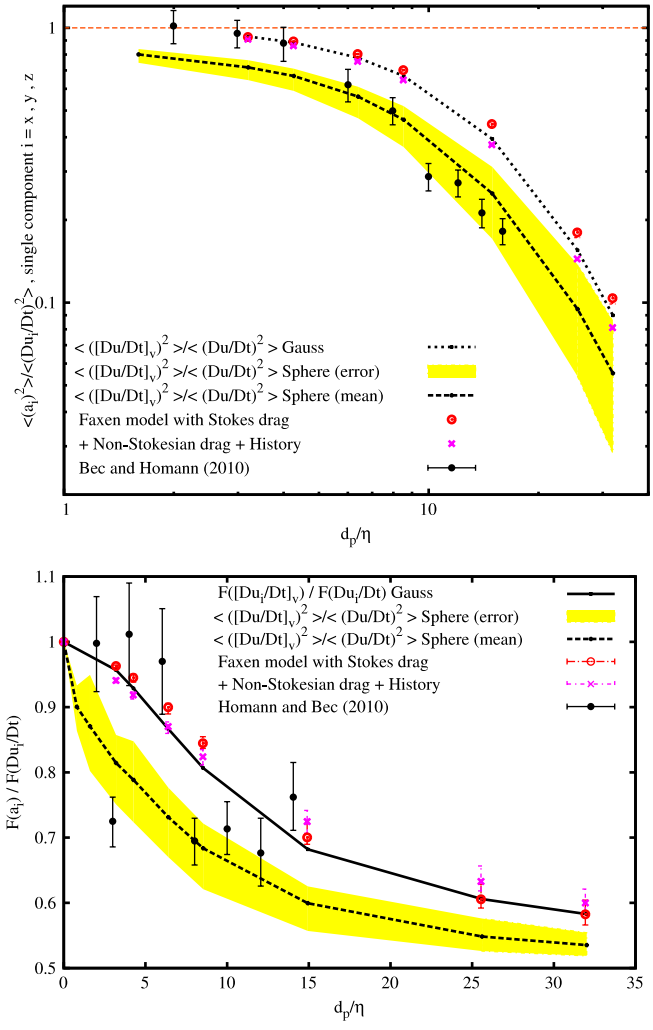

Fig. 9. Comparison between acceleration variance (top panel) and flatness (bottom panel) We show data coming from Gaussian convolutions, same as in Fig. 3, of the fluid acceleration field $D\mathbf{u}/Dt$ (dotted line), the quantity has been computed runtime therefore statistical errors are in this case of the order of the line thickness. Averages over spherical volumes (dashed line) are affected by a larger statistical uncertainty (yellow shaded region) which comes from the differences in the measurements between the three cartesian components. Measurements from the Lagrangian model based on Eq. (1) and Eqs. (1)–(3) are reported, together with HB data. (For interpretation of the references to colour in this figure legend, the reader is referred to the web version of this article.)

this region the average over spheres agrees with the HB results. A similar scenario appears for the flatness Fig. 9 (bottom). This finding is important at least for two reasons. First it shows that the Faxén correction to the fluid acceleration plays a central role in the particle acceleration statistics not only for a particle in the upper dissipative range $d_p < 4\eta$ but also for a particle with a much larger size, $d_p \leq 32\eta$. Second, it shows that, although the Gaussian convolution approximation is an efficient method to solve particle dynamics, it has limitations which becomes important approximately when $d_p > 4\eta$. The above observations have also an impact on the time-statistics: since a reduction of the variance of the filtered acceleration is associated to a slower fluctuations in time, we expect the correlation time of acceleration to increase for finite-sized particles. Hence the picture in Fig. 5 would change, solving the observed mismatch toward HB simulations and experiments [13]. However, this latter point may find a confirmations only in further studies.

Evaluating the impact of point (ii) is unfortunately not possible in the framework of the present model. One would need to introduce a coupling (so called two-way coupling) between the particle and the fluid enforcing conservation of the total momentum.

Finally on point (iii), for completeness we shall note that there are some differences between the turbulent flows simulated by Homann & Bec and the one used here. While we adopt a forcing which keeps constant the energy on the largest Fourier modes (amplitude-driving), HB also uses a random forcing of the phase in Fourier space (phase-driving). While these differences have no effect in fully developed turbulent flows, at the small Reynolds number considered here, $Re_\lambda \simeq 32$, they might have an impact. We see indeed that, already for the case of fluid tracers, while we find $\langle a_i^2 \rangle \varepsilon^{-3/2} \nu^{1/2} = 1.1$ and $F(a_i) = 5.7$, Homann & Bec report $\langle a_i^2 \rangle \varepsilon^{-3/2} \nu^{1/2} = 1.3$ and $F(a_i) = 8.4$, hence a flow slightly more intermittent at small-scales. This prevents us – for instance – from a direct comparison on the shape of the probability density functions of acceleration and velocity. Furthermore, since the wave-length of the forcing in our simulation measures about 63η, the statistical properties observed for the acceleration of the largest particle size ($d_p = 32\eta$) might be affected by sub-leading non-universal contributions coming from this large-scale force. This is a point which certainly deserve further studies.

5. Conclusions

In this study we have focused on the statistical properties of acceleration and velocity of finite-sized neutrally-buoyant particles driven in a moderately turbulent homogeneous and isotropic flow. We have adopted a Lagrangian model particle equation which keeps into account inertia effect, size effects, and the drag forces resulting both from a Stokes flow around the particle and form an asymmetric trailing wake state via Schiller–Naumann modeling. We have studied the contribution of these forces separately, in particular the drag force has been divided into three components: Stokes, History, and non-Stokesian force.

We find that the drag forces have minor effect on the statistical properties of acceleration. Acceleration statistics seems to be dominated by inertia effect and by the Faxén corrections, whose influences extends also over particles with sizes attaining the integral scale of turbulence.

On the contrary drag forces have important effects on the time integral of the acceleration, that is to say on the velocity statistics. This is particularly evident when considering the trend of the second order statistical moment (the variance) as a function of the particle size. For the case of neutrally buoyant particle analyzed here, the variance of the particle velocity from the different Lagrangian models start to separate at $d_p > 8\eta$, corresponding to

a particle Reynolds number $Re_p \sim \mathcal{O}(10)$. Above this threshold History and non-Stokesian drag have a dominant role. This lead us to propose that the trend observed for the particle velocity variance as a function of its size does not originate from inertial-scale properties of the background turbulent flow but arise from the non-Stokesian component of the drag produced by the wake behind the particle.

The effects detected in the velocity statistics are relevant for studies of particle dispersion in turbulence. For instance a simple finite-size particle model based on Stokes drag or history force only, would overestimate the average particle dispersion from a fixed source in space, and similarly for pair separation. Therefore, this study suggests that in order to validate Lagrangian models one should look not only into the small scale acceleration statistics – as done up to now in many studies – but also into velocity and possibly dispersion and pair separation statistics.

On the numerical side, we have shown that the Gaussian convolution approximation, despite its computational efficiency is not accurate when particles much larger than 4η are involved. On the other hand spherical averages in real space, as the one performed in our test, would be computationally very expensive and not enough accurate for small size particles (in particular it is not possible to capture the Laplacian correction (10) when only few grid points are used). Future numerical studies should find a trade off between efficient computations and accuracy. A possible way, which however needs careful scrutiny and tuning, is to consider the implementation of convolution kernel functions with sharper boundaries. Furthermore, the effect of two-way coupling in this type of homogeneous and isotropic turbulent flow deserve to be studied.

Acknowledgments

The authors are thankful to A. Naso and M. Bourgoin for useful discussions. Support from COST Action MP0806 "Particles in turbulence", from ANR-BLAN-07-1-192604 is acknowledged. E.C. was also supported by the HPC-EUROPA2 project (project number 228398) with the support of the European Commission - Capacities Area - Research Infrastructures. Numerics for this study have been performed at SARA (The Netherlands), CINECA (Bologna, Italy) and CASPUR (Roma, Italy). Numerical data of particle trajectories are available on iCFDdatabase (http://mp0806.cineca.it/icfd.php) kindly hosted by CINECA (Italy). More information available upon request to the authors.

References

[1] M.R. Maxey, J.J. Riley, Equation of motion for a small rigid sphere in a nonuniform flow, Phys. Fluids 26 (4) (1983) 883–889.
[2] R. Gatignol, The Faxén formulae for a rigid particle in an unsteady non-uniform stokes flow, J. Mécanique Théorique Appliquée 1 (2) (1983) 143–160.
[3] T. Auton, J. Hunt, M. Prud'homme, The force exerted on a body in inviscid unsteady non-uniform rotational flow, J. Fluid Mech. 197 (1988) 241–257.
[4] P.M. Lovalenti, J.F. Brady, The hydrodynamic force on a rigid particle undergoing arbitrary time-dependent motion at small Reynolds number, J. Fluid Mech. 545 (1993) 561–605.
[5] E.E. Michaelides, Review—the transient equation of motion for particles, bubbles, and droplets, J. Fluid Eng. 119 (1997) 233–247.
[6] E. Loth, A. Dorgan, An equation of motion for particles of finite Reynolds number and size, Environ. Fluid Mech. 9 (2009) 187–206.
[7] E. Calzavarini, M. Kerscher, D. Lohse, F. Toschi, Dimensionality and morphology of particle and bubble clusters in turbulent flow, J. Fluid Mech. 607 (2008) 13–24.
[8] E. Calzavarini, M. Cencini, D. Lohse, F. Toschi, Quantifying turbulence-induced segregation of inertial particles, Phys. Rev. Lett. 101 (2008) 084504.
[9] R. Volk, E. Calzavarini, G. Verhille, D. Lohse, N. Mordant, J.F. Pinton, et al., Acceleration of heavy and light particles in turbulence: comparison between experiments and direct numerical simulations, Physica D 237 (14–17) (2008) 2084–2089.
[10] E. Calzavarini, R. Volk, M. Bourgoin, E. Lévêque, J.F. Pinton, F. Toschi, Acceleration statistics of finite-sized particles in turbulent flow: the role of Faxén forces, J. Fluid Mech. (2009).
[11] N.M. Qureshi, M. Bourgoin, C. Baudet, A. Cartellier, Y. Gagne, Turbulent transport of material particles: an experimental study of finite size effects, Phys. Rev. Lett. 99 (18) (2007) 184502.
[12] R.D. Brown, Z. Warhaft, G.A. Voth, Acceleration statistics of neutrally buoyant spherical particles in intense turbulence, Phys. Rev. Lett. 103 (19) (2009) 194501.
[13] R. Volk, E. Calzavarini, E. Lévêque, J.-F. Pinton, Dynamics of inertial particles in a turbulent von karman flow, J. Fluid Mech. 668 (2011) 223–235.
[14] H. Homann, J. Bec, Finite-size effects in the dynamics of neutrally buoyant particles in turbulent flow, J. Fluid Mech. 651 (2010) 81–91.
[15] L. Schiller, A. Naumann, ber die grundlegenden berechungen bei der schwerkraftaufbereitung, Ver. Dtsch. Ing. 77 (1933) 318–320.
[16] R. Clift, J.R. Grace, M.E. Weber, Bubbles, Drops and Particles, Academic Press, Dover, 2005, 1978.
[17] T.M. Burton, J.K. Eaton, Fully resolved simulations of particle-turbulence interaction, J. Fluid Mech. 545 (2005) 67–111.
[18] S. Elghobashi, G.C. Truesdell, Direct simulation of particle dispersion in a decaying isotropic turbulence, J. Fluid Mech. 242 (1992) 655–700.
[19] R. Mei, R. Adrian, Flow past a sphere with an oscillation in the free-stream and unsteady drag at finite Reynolds number, J. Fluid Mech. 237 (1992) 323–341.
[20] N. Mordant, J.F. Pinton, Velocity measurements of a sphere settling in a fluid at rest, Eur. Phys. J. B 18 (2000) 343–352.
[21] A.J. Dorgan, E. Loth, Efficient calculation of the history force at finite Reynolds numbers, Int. J. Multiph. Flow 33 (2007) 833–848.
[22] M. van Hinsberg, J. ten Thije Boonkkamp, H. Clercx, An efficient, second order method for the approximation of the basset history force, J. Comput. Phys. 230 (2011) 1465–1478.

A.3 Dynamique d'une particule de taille intégrale

[A 6] R. Zimmermann, Y. Gasteuil, M. Bourgoin, R. Volk, A. Pumir, J.-F. Pinton. Tracking the dynamics of translation and absolute orientation of a sphere in a turbulent flow. *Review of Scientific Instruments*, 82 :033906, (2011).

[A 7] R. Zimmermann, Y. Gasteuil, M. Bourgoin, R. Volk, A. Pumir, and J.-F. Pinton. Rotational Intermittency and Turbulence Induced Lift Experienced by Large Particles in a Turbulent Flow. *Physical Review Letters*, 106(15) :154501, (2011).

Tracking the dynamics of translation and absolute orientation of a sphere in a turbulent flow

Robert Zimmermann,[1] Yoann Gasteuil,[1] Mickael Bourgoin,[1,2] Romain Volk,[1]
Alain Pumir,[1] and Jean-François Pinton[1]
(International Collaboration for Turbulence)
[1]*Laboratoire de Physique, CNR, UMR 5672, Ecole Normale Supérieure de Lyon, Lyon F-69007, France*
[2]*Laboratoire des Ecoulements Géophysiques et Industriels, CNRS, UJF INPG, Grenoble, F-38041, France*

(Received 17 October 2010; accepted 18 January 2011; published online 17 March 2011)

We study the six-dimensional dynamics—position and orientation—of a large sphere advected by a turbulent flow. The movement of the sphere is recorded with two high-speed cameras. Its orientation is tracked using a novel, efficient algorithm; it is based on the identification of possible orientation "candidates" at each time step, with the dynamics later obtained from maximization of a likelihood function. Analysis of the resulting linear and angular velocities and accelerations reveal a surprising intermittency for an object whose size lies in the inertial range, close to the integral scale of the underlying turbulent flow. © *2011 American Institute of Physics*. [doi:10.1063/1.3554304]

I. INTRODUCTION

The advent of resolved Lagrangian measurements has helped understand the dynamics of turbulence from the point of view of fluid particles.[1] In the experiments, solid *tracers* are followed in lieu of fluid particles, which naturally raises the question of the understanding of the dynamics of *finite size* objects in turbulent flows. It is a subclass of the issue of the dynamics of *inertial particles*, *i.e.*, particles which have inertia with respect to the fluid motions, either because their density differs from that of the fluid or because their spatial extent cannot be ignored. If the particles are quite small compared to the smallest fluid motion (the Kolmogorov dissipative length scale η), arguments show that they behave as tracers of fluid motions. Observations have revealed a very intense intermittency in the motion of fluid tracers.[2,3] They experience very strong accelerations, with a probability distribution which displays stretched exponential tails.[4]

When the diameter D of the advected particles is of the order of, or larger than η, their equation of motion is not known (see, however Refs. 5–7). We restrict our discussion to neutrally buoyant spheres. Several recent studies[8–11] have shown that the acceleration statistics of such inertial particles does not gently reduce to a Gaussian behavior as their diameter increases. It is an important feature because the characterization of forces acting on an object advected by a turbulent flow has many applications in engineering (from mixing issues in industrial processes to dispersion in the oceans or in the atmosphere).

The study reported here takes a leap forward in size and considers the motion of a neutrally buoyant sphere with diameter D of the order of the integral scale L_{int} (the scale at which energy is fed into the flow). In addition, we aim at resolving the 6 degrees of freedom of the particle dynamics, *i.e.,* the goal is to obtain a simultaneous tracking in time of the particle's position and its absolute orientation with respect to a reference frame. This enables the study of the forces and torques acting on a large inertial particle, thus permitting to ask yet fundamental questions about their dynamics.[12] Furthermore, the absolute orientation is important for future work using instrumented particles and for problems where there is a preferential direction—such as when there is a global rotation, a temperature gradient, or an imposed magnetic field.

The tracking of the particle position in space can be carried out by using methods already developed and successfully tested for small particles.[13] In comparison, following the *absolute* orientation of the particle is much more challenging, both because of the specifics of angular variables, and of specific algorithmic requirements.

Previous studies focused on directly measuring the angular velocity without resolving the absolute orientation as a function of time. Ye and Roco[14] tracked dots painted on a particle with high-speed cameras and computed the angular velocity from their displacement between two consecutive frames. Frish and Webb[15] created an Eulerian technique measuring one component of the angular velocity using specially engineered, transparent particles which contain an embedded mirror. The reported particle diameter is less than 50 μm, which is of the order of the Kolmogorov length scale, η.

The principle used here is completely different: it consists simply in painting the particle with a suitable layout, and in retrieving its orientation. For algorithmic efficiency (and robustness) this is not done step by step but for the entire trajectory using a global path extraction.

The text below is organized as follows: we first present the experimental setup and recall some important features of the orientation algebra in 3D. We then describe how the particle images are extracted from the movie images, and compared to synthetic images with arbitrary orientations. Possible candidates are identified and then assembled into an orientation time series using a global maximization of a likelihood function. Finally, we present some results concerning the particle dynamics.

II. BASICS

A. Experimental setup

A turbulent flow is generated in the gap between two counter-rotating impellers of radius $R = 10$ cm fitted with straight blades 1 cm in height. The flow domain in between the impeller has characteristic lengths $H = 2R = 20$ cm and the working fluid is a water–glycerol mixture, whose density can be finely tuned. In order to be able to perform direct optical measurements, the container is build with flat Plexiglas (Poly[methyl methacrylate]) side walls, so that the cross section of the vessel is square. This type of von Kármán swirling flow has been used extensively in the past for the study of fully developed turbulence;[1] its local characteristics approximate homogeneous turbulence in its center, although it is known to have a large scale anisotropy.[16,17] A sketch of the setup is provided in Fig. 1—further details about the flow turbulence are given later in Sec. IV.

A white, PolyAmid sphere with diameter $D = 18$ mm (accuracy 0.01 mm, Marteau & Lemarié, France) moves and rotates in the turbulent flow. It is neutrally buoyant in the fluid—whose density is adjusted to that of the particle $\rho_p = 1.14\ \mathrm{g\,cm^{-3}}$ by addition of glycerol to water. The density mismatch, measured from sedimentation speeds, is found to be less than $\Delta\rho/\rho = 10^{-4}$. The particle is textured black and white by hand using either black nail polish or a black-ink permanent marker. Its motion is tracked using two high-speed video cameras (Phantom V12, Vision Research) which record synchronously two views at $\sim 90^\circ$. The flow is illuminated by high power light-emitting diodes (LEDs) and sequences of 8 bit gray scale images are recorded at a rate of 600 frames per second.

Both cameras observe the measurement region with a resolution of 650×650 pixels, covering a volume of $15 \times 15 \times 15\ \mathrm{cm^3}$. Hence, the particle diameter is 70–90 pixels. In the choice of the particle texture, several features have to be considered:

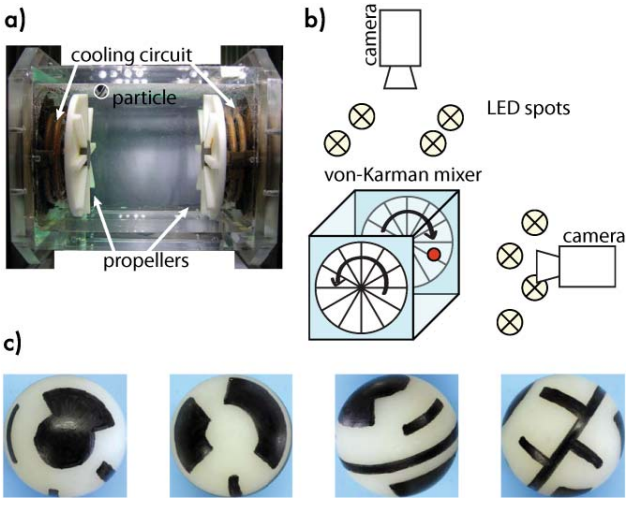

FIG. 1. (Color online) Sketch of the experimental setup: (a) image of the von Kármán mixer, (b) sketch of the camera arrangement, and (c) textured sphere for different orientations.

- A single view should correspond to a unique orientation.
- Illumination inhomogeneities may cause regions to look similar in the camera images. Optically resembling views should correspond to clearly distinct orientations.
- The cameras are gray scale so the texture has to be black and white.
- The number of black and white pixel should be approximately the same in every possible view.

In our configuration, the camera can store on the order of 15 000 frames in on-board memory, thus limiting the duration of continuous tracks. The movies are downloaded to a personal computer (PC), waiting to be processed. The processing is done on a gaming PC with a state of the art graphics card. Algorithm development and code testing is done on an Apple Macbook Pro. The code is written in MATLAB 2009a using the image and signal processing toolboxes as well as the PSYCHTOOLBOX extensions[18,19] which provide OPENGL wrappers for MATLAB.

B. Angular variables

The parametrization of an angular position in 3D space causes a number of difficulties which are briefly addressed in this section (see, e.g., Refs. 20–22 for a more complete presentation). One of them is caused by the degeneracy of the axes of rotation for certain orientations (the "gimbal lock" problem). Another is the choice of a suitable measure of distance between two orientations.

1. Describing orientations

As stated by the Euler rotation theorem, three parameters are needed to describe any rotation in 3D. We use here Euler angles with the Tait–Bryan convention as shown in Fig. 2. In the transformation from lab to particle coordinate system, we first apply a rotation around the z axis of angle θ_z, followed by a rotation around the intermediate y axis of angle θ_y and last a rotation of angle θ_x around the new x axis. The rotations work on the object using a right handed coordinate system and right handed direction of rotation. We will denote an orientation triplet by an underscore, *e.g.*, $\underline{\theta}$, in order to distinguish them from vectors (which are typeset in bold font, *e.g.*, $\boldsymbol{\omega}$).

The orientation of the object is fully described by an orthogonal 3×3 matrix $\underline{\underline{\mathbf{R}}}$, obtained from the composition of

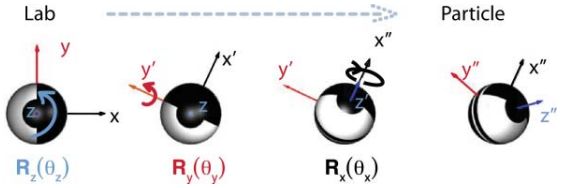

FIG. 2. (Color online) Tait–Bryan rotation sequence describing the sphere's orientation.

the three elementary rotations

$$\underline{\underline{\mathbf{R}}}(\theta_x,\theta_y,\theta_z)=\underline{\underline{\mathbf{R}}}_x(\theta_x)\underline{\underline{\mathbf{R}}}_y(\theta_y)\underline{\underline{\mathbf{R}}}_z(\theta_z)$$
$$=\begin{bmatrix} c\theta_y\,c\theta_z & -c\theta_y\,s\theta_z & s\theta_y \\ s\theta_x\,s\theta_y\,c\theta_z+c\theta_x\,s\theta_z & -s\theta_x\,s\theta_y\,s\theta_z+c\theta_x\,c\theta_z & -s\theta_x\,c\theta_y \\ -c\theta_x\,s\theta_y\,c\theta_z+s\theta_x\,s\theta_z & c\theta_x\,s\theta_y\,s\theta_z+s\theta_x\,c\theta_z & c\theta_x\,c\theta_y \end{bmatrix} \tag{1}$$

with $c\cdot=\cos(\cdot)$ and $s\cdot=\sin(\cdot)$. Consequently, from any rotation matrix the three Euler angles can be extracted using

$$\underline{\theta}=\{\theta_x,\theta_y,\theta_z\}=\begin{pmatrix}\mathrm{atan2}(-\underline{\underline{\mathbf{R}}}_{23},\underline{\underline{\mathbf{R}}}_{33})\\ \mathrm{asin}(\underline{\underline{\mathbf{R}}}_{13})\\ \mathrm{atan2}(-\underline{\underline{\mathbf{R}}}_{12},\underline{\underline{\mathbf{R}}}_{11})\end{pmatrix} \tag{2}$$

enforcing $\theta_x,\theta_z\in[0,2\pi[$ and $\theta_y\in[-\pi/2,\pi/2]$. However this choice is not unique because there is a second triplet with $\underline{\underline{\mathbf{R}}}\left(\theta_x+\pi,\mathrm{sign}(\theta_y)\cdot\pi-\theta_y,\theta_z+\pi\right)=\underline{\underline{\mathbf{R}}}\left(\theta_x,\theta_y,\theta_z\right)$. Needless to say, multiples of 2π can be added to each angle. An important practical consequence is that even for small changes in orientation the difference between two Euler angle triplets, $\underline{\theta}_1$ and $\underline{\theta}_2$, has formally four possible results.

The curvilinear coordinate $\underline{\theta}$ is related to the angular velocity, $\boldsymbol{\omega}^{\mathbb{P}}$, (in the particle frame) by

$$\boldsymbol{\omega}^{\mathbb{P}}\left(\underline{\theta}(t)\right)=\begin{bmatrix}1&0&s\theta_y\\0&c\theta_x&-s\theta_x\,c\theta_y\\0&s\theta_x&c\theta_x\,c\theta_y\end{bmatrix}\cdot\frac{d}{dt}\begin{pmatrix}\theta_x\\\theta_y\\\theta_z\end{pmatrix}$$
$$=\underline{\underline{\mathbf{H}}}(\theta_x,\theta_y)\cdot\frac{d}{dt}\begin{pmatrix}\theta_x\\\theta_y\\\theta_z\end{pmatrix}. \tag{3}$$

For $\cos\left(\theta_y\right)\approx 0$, the determinant of the matrix $\underline{\underline{\mathbf{H}}}$, $\det(\underline{\underline{\mathbf{H}}})$, vanishes and its inverse is not defined. In other words, finite body rotations need infinite change in the Euler angles. This singularity is called a *gimbal lock* and is a well-known problem in robotics and aerospace engineering. Geometrically, the second rotation turns the first axis parallel to the third axis of rotation, and the rotation loses 2 degrees of freedom. Unfortunately gimbal locks cannot be avoided by a wise choice of representation.

One then needs to define a distance between two arbitrary orientations, immune to this type of singularity. A natural distance between two arbitrary orientation matrixes, $\underline{\underline{\mathbf{A}}}$ and $\underline{\underline{\mathbf{B}}}$, is

$$\mathrm{Tr}\left((\underline{\underline{\mathbf{A}}}-\underline{\underline{\mathbf{B}}})(\underline{\underline{\mathbf{A}}}-\underline{\underline{\mathbf{B}}})^T\right)=6-2\mathrm{Tr}\left(\underline{\underline{\mathbf{A}}}\underline{\underline{\mathbf{B}}}^T\right)$$
$$=4(1-\cos(\phi)) \tag{4}$$

using $\underline{\underline{\mathbf{A}}}\,\underline{\underline{\mathbf{A}}}^T=\underline{\underline{\mathbf{B}}}\,\underline{\underline{\mathbf{B}}}^T=1$ and that $\underline{\underline{\mathbf{A}}}\underline{\underline{\mathbf{B}}}^T$ is a rotation matrix with the eigenvalues $1, e^{i\phi}, e^{-i\phi}$. The distance is thus a growing function of ϕ. We measure here the distance between two rotation matrices by

$$d(\underline{\underline{\mathbf{A}}},\underline{\underline{\mathbf{B}}})\equiv\mathrm{acos}\left(\frac{1}{2}\left[\mathrm{Tr}\left(\underline{\underline{\mathbf{A}}}\,\underline{\underline{\mathbf{B}}}^T\right)-1\right]\right). \tag{5}$$

Because it works directly on the orientation matrices it is neither sensitive to gimbal locks nor to the choice of the representation and thus an important tool in our algorithm. It should be noted that $d(\underline{\underline{\mathbf{A}}},\underline{\underline{\mathbf{B}}})$ is the angle of the rotation which turned the orientation from $\underline{\underline{\mathbf{A}}}$ to $\underline{\underline{\mathbf{B}}}$.

In the search of the particle orientation, one last inconvenience of Euler angles is that they are not locally orthogonal, in the sense that

$$d(\{\theta_x,\theta_y,\theta_z\},\{\theta_x+\Delta\theta_x,\theta_y+\Delta\theta_y,\theta_z+\Delta\theta_z\})^2$$
$$\approx\Delta\theta_x^2+\Delta\theta_y^2+\Delta\theta_z^2+2\Delta\theta_x\cdot\Delta\theta_z\cdot\sin(\theta_y) \tag{6}$$

for Δ small. As a consequence, a uniform spacing of the Euler angles in $\theta_x,\theta_y,\theta_z$ does not sample the space of possible orientations in an optimal way. In particular near gimbal locks, the sampling rate would be higher at no higher accuracy. The so called Lattman angles[23]

$$\{\theta_+,\theta,\theta_-\}\equiv\{\theta_x+\theta_z,\theta_y,\theta_x-\theta_z\} \tag{7}$$

fulfill local orthogonality since they verify

$$d(\{\theta_+,\theta,\theta_-\},\{\theta_++\Delta\theta_+,\theta+\Delta\theta,\theta_-+\Delta\theta_-\})^2$$
$$\approx\frac{\Delta\theta_+^2(1+\sin\theta)}{2}+\Delta\theta^2+\frac{\Delta\theta_-^2(1-\sin\theta)}{2}. \tag{8}$$

As they are locally orthogonal, it is sufficient for sampling purposes to keep $\Delta\theta_+^2(1+\sin\theta)/2$, $\Delta\theta^2$ and $\Delta\theta_-^2(1-\sin\theta)/2$ constant. After a constant sampling of N values of θ with $\Delta_{\mathrm{Latt}}\equiv\Delta\theta=\pi/(N-1)$, the stepping in θ_+ and θ_- can be computed with $\Delta\theta_+(\theta)=\Delta_{\mathrm{Latt}}/\sin(\theta/2+\pi/2)$ and $\Delta\theta_-(\theta)=\Delta_{\mathrm{Latt}}/\sin(\pi/2-\theta/2)$. It should be emphasized, that $\theta_-\in[0,2\pi[$ whereas $\theta_+\in[0,4\pi[$. The Lattmann angles allow us to sample the set of orientations in an optimal way, in terms of achieving the best resolution from the point of view of the metric given by Eq. (8), and also from an algorithmic point of view.

Finally, in several instances it is convenient to describe a rotation by the direction of an axis $\hat{\boldsymbol{n}}$ about which the systems is rotated by an amount ϕ. The corresponding rotation matrix can be computed using the Rodrigues formula[20,22]

$$\underline{\underline{\mathbf{R}}}(\hat{\boldsymbol{n}},\phi)$$
$$=\begin{bmatrix}c\phi+n_x^2A & -n_zs\phi+n_xn_yA & n_ys\phi+n_xn_zA\\ n_zs\phi+n_xn_yA & c\phi+n_y^2A & -n_xs\phi+n_yn_zA\\ -n_ys\phi+n_xn_zA & n_xs\phi+n_yn_zA & c\phi+n_z^2A\end{bmatrix}$$
with $A=(1-c\phi)$. (9)

Equation (9) also allows us to extract the axis, $\hat{\boldsymbol{n}}$, and the angle, ϕ from any arbitrary rotation matrix. As a result, changing the coordinate system or changing the representation of rotation can be done by expressing the orientation in its matrix form, applying the transformation which changes the coordinate system and extracting the desired representation.

2. Angular velocity and acceleration

Angular velocity and acceleration are often obtained by direct differentiation of a time series of Euler angles, *e.g.*, using Eq. (3). However, it is possible to obtain the angular

velocity in the particle frame directly from the matrices. This technique is not sensitive to Gimbal locks because of the uniqueness of the orientation matrices.

Let $\boldsymbol{e}^{\mathbb{P},k}_{x,y,z}$ be the particle coordinate system at time step k, whereas the fixed lab coordinate system is $\boldsymbol{e}^{\mathbb{L}}_{x,y,z}$. For two time steps, k and $k+m$, we know the corresponding orientation matrices which rotate the particle

$$\begin{array}{lcll} \underline{\underline{\mathbf{R}}}(\underline{\theta}_k) & : & \boldsymbol{e}^{\mathbb{L}}_{x,y,z} & \xrightarrow{\underline{\underline{\mathbf{R}}}(\underline{\theta}_k)} \quad \boldsymbol{e}^{\mathbb{P},k}_{x,y,z} \\ \underline{\underline{\mathbf{R}}}(\underline{\theta}_{k+m}) & : & \boldsymbol{e}^{\mathbb{L}}_{x,y,z} & \xrightarrow{\underline{\underline{\mathbf{R}}}(\underline{\theta}_{k+m})} \quad \boldsymbol{e}^{\mathbb{P},k+m}_{x,y,z} \\ \underline{\underline{\mathbf{T}}} & : & \boldsymbol{e}^{\mathbb{P},k}_{x,y,z} & \xrightarrow{\underline{\underline{\mathbf{R}}}(\underline{\theta}_{k+m})\underline{\underline{\mathbf{R}}}(\underline{\theta}_k)^T} \quad \boldsymbol{e}^{\mathbb{P},k+m}_{x,y,z} \end{array}$$

in which the matrix $\underline{\underline{\mathbf{T}}}$ is the change in orientation, in other words the matrix representation of the discrete angular velocity (for a given time difference). The change is with respect to the particle coordinate system at time k: $\boldsymbol{e}^{\mathbb{P},k}_{x,y,z}$. $\underline{\underline{\mathbf{T}}}$ expressed in the axis–angle convention [see Eq. (9)] returns a direction vector, $\hat{\boldsymbol{n}}$, of length unity and an angle, $\Delta\phi$ (meaning that between times k and $k+m$ the particles has rotated an angle $\Delta\phi$ around the vector $\hat{\boldsymbol{n}}$). The time difference, Δt, between the steps is a function of m. Therefore an estimator of angular velocity is

$$\boldsymbol{\omega}^{\mathbb{P}}(t(k)) = \frac{\Delta\phi}{\Delta t(m)}\left(n_x \cdot \boldsymbol{e}_x^{\mathbb{P},k} + n_y \cdot \boldsymbol{e}_y^{\mathbb{P},k} + n_z \cdot \boldsymbol{e}_z^{\mathbb{P},k}\right). \tag{10}$$

Averaging $\hat{\boldsymbol{n}}\frac{\Delta\phi}{\Delta t}$ over several separations, m, returns the angular velocity in the particle frame without a prior unwrapping nor problems near gimbal locks. The angular velocity with respect to the lab coordinate system is defined as

$$\boldsymbol{\omega}^{\mathbb{L}}(t(k)) = \underline{\underline{\mathbf{R}}}\left(\underline{\theta}_k\right)^T \boldsymbol{\omega}^{\mathbb{P}}(t(k)). \tag{11}$$

The angular acceleration in either particle or lab frame is defined as

$$\boldsymbol{\alpha}^{\mathbb{L}/\mathbb{P}} = \frac{d}{dt}\boldsymbol{\omega}^{\mathbb{L}/\mathbb{P}}. \tag{12}$$

In practice, it is obtained from a convolution of the angular velocity time series with the derivative of a Gaussian kernel. This technique has proved to be efficient in removing noise.[4]

III. TRACKING

A. Position

Although the identification of a large sphere from the camera images causes no particular conceptual difficulty, the fact that the sphere is *textured* raises some practical issues. A simple thresholding returns only either the white or the black part of the particle. Reflections from the impellers continuously change the background, and small impurities in the flow and possible bubbles add sharp gradient noise to the images. Furthermore, the illumination of the flow is not perfectly uniform, and thus, shadows as well as reflections occur.

For each movie and for each camera, we compute the background view as the average of an equally distributed subset of its images. For each frame we then subtract the background and perform a *difference of Gaussians* blob detection. The threshold is adjusted by hand for each camera and light arrangement. MATLAB's image-processing toolbox is used to identify blobs with a round shape and a diameter close to that of the particle. Shadows, bubbles, and reflections might be found during blob detection because of their sharp separation from the background, but they are of uniform texture and hence characterized by a small value of the variance of light intensity across the blob. The blob with highest variance and closest resemblance to a sphere is considered to be the particle. The precise position of the particle is refined using a *Canny edge* detection in a tight region around the blob. For each time step we record the position, (x, y), of the particle on the image in pixels plus its diameter, $2r$, and the deviation from the spherical shape as an error estimator. Since only one particle is placed into the flow, the track assembly is straightforward. The algorithm may temporarily loose the particle for short times (because of bad light reflection, blurs, ...); this is compensated by the large oversampling and gaps of less than five frames are interpolated to obtain longer tracks. Outliers are identified using a least square spline and replaced by an interpolation.

Tsai's camera model and calibration technique[24] is used to project the 2D positions into 3D. The calibration of the cameras contains the position of the camera plus its rotation with respect to the lab coordinate system, which is needed later for the orientation processing.

B. Orientation

The algorithm used to process the camera images and obtain a time series of orientations (and angular velocities) can be split into three parts: (i) by comparison of the sphere's picture with synthetic images, the algorithm identifies a set of possible orientations; (ii) from the set of possible candidates at successive instants, a *flow* algorithm identifies a likely time series; (iii) a post-treatment adjusts remaining ambiguities. These steps are described in details in this section.

1. Candidate finding

a. Synthetic images. The first step is to obtain a 2D projection, $\underline{\underline{\mathbf{S}}}(\underline{\theta})$, of a sphere with known texture and size at an arbitrary orientation, $\underline{\theta}$. This rendering is achieved using OPENGL, *via* the PSYCHTOOLBOX extensions for MATLAB—for a disk image of about 60 pixels, the algorithm can render several thousand orientations per second (see Fig. 3 for an illustration).

b. Texture extraction. Once the particle position and diameter are known, one extracts a disk subset of the image, centered on the particle, $\underline{\underline{\mathbf{G}}}$. In the first step the contrast is adjusted such that the global histogram of intensity contains at least b percent of black and w percent of white pixels (the algorithm only takes into account the disk/particle region in $\underline{\underline{\mathbf{G}}}$). The adjustable parameters b, w are fixed to $b = w \sim 30\%$ which is the minimum amount of black/white pixel in an arbitrary orientation. In a second step, the image is thresholded using Otsu's method[25] for the global histogram as well as for two moving regions. The thresholded image, $\underline{\underline{\mathbf{I}}}$, is adjusted such

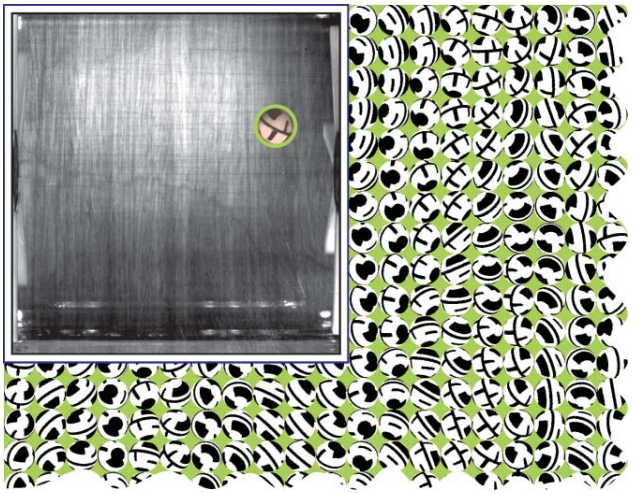

FIG. 3. (Color online) Synthetic 2D projections of the particle for a range of orientations, using OPENGL. A camera image of the moving particle is shown in the upper left corner (contrast enhanced; note the driving disks on either side).

that pixels outside the particle/disk are set to 0 whereas black is −1 and white +1. These steps are shown in Fig. 4.

c. Comparison, possible orientations. The image $\underline{\underline{\mathbf{I}}}$ (with diameter $2r$) obtained as above is ready for comparison with synthetic images. The resemblance to a rendered image $\underline{\underline{\mathbf{S}}}(\underline{\theta})$ with orientation $\underline{\theta}$ is estimated by

$$T(\underline{\underline{\mathbf{I}}}, \underline{\theta}) = \frac{1}{2} + \frac{1}{2\pi r^2} \sum_i \sum_j \underline{\underline{\mathbf{I}}}_{i,j} \cdot \underline{\underline{\mathbf{S}}}_{i,j}(\underline{\theta}), \tag{13}$$

which is ratio of the number of correct pixels to the total number of pixels.

At this point we note that the computational cost of directly comparing an image $\underline{\underline{\mathbf{I}}}$ to synthetic ones $\underline{\underline{\mathbf{S}}}(\underline{\theta})$ covering the set of possible orientation $\{\underline{\theta}\}$ scales roughly as $\Delta_{\text{Latt}}^{-3}$, where Δ_{Latt} is the grid spacing in the orientation space. There is also the additional difficulty that the particle apparent diameter changes slightly as the sphere moves in the flows. For efficiency and physical correctness, we use the following strategy: instead of finding at any time step the best images, we identify a set of possible candidates for all time steps and then extract globally the time series of orientations.

First we render images, $\underline{\underline{\mathbf{S}}}(\{\underline{\theta}_{\text{coarse}}\})$, covering *all* possible orientations with a coarse grid—in practice $\Delta_{\text{Latt}} \approx 12^\circ$.

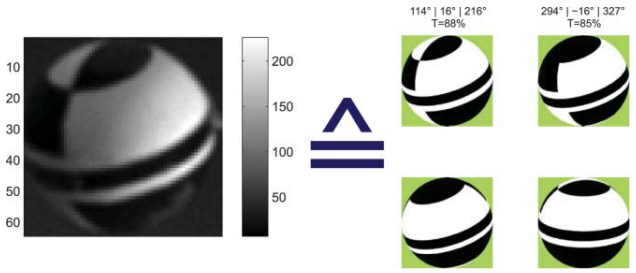

FIG. 5. (Color online) Particle camera image (left) and corresponding candidates, after analysis of the possible orientations (steps *1a–1c* described in the text).

Lattman angles are locally orthogonal and thus more efficient in creating such grids. The size of the rendered images is fixed to approximately one half of the particle's real diameter. Since their size does not change, these images are kept in the computer memory and do not need to be recomputed for every new image.

The thresholded particle image, $\underline{\underline{\mathbf{I}}}$, is then resized to the size of the renderings, $\underline{\underline{\mathbf{I}}}_{\text{coarse}}$, and compared to all synthetic images, $\underline{\underline{\mathbf{S}}}(\{\underline{\theta}_{\text{coarse}}\})$ as shown in Fig. 3 using Eq. (13). All angles $\underline{\theta}$ satisfying $T(\underline{\underline{\mathbf{I}}}_{\text{coarse}}, \underline{\theta}) > \max(T(\underline{\underline{\mathbf{I}}}_{\text{coarse}}, \{\underline{\theta}_{\text{coarse}}\})) - \delta_{\text{coarse}}$ are considered to be possible orientations. Here δ_{coarse} is an arbitrary thresholding value, with inspection showing that a value equal to 0.1 gives good results.

Experience shows that the identified possible orientations usually cover several broad classes. They are thus separated into groups of images whose orientations differ by less than a rough threshold, ∼30–45°. For each group, synthetic images are further added using a fine grid spacing, $\Delta_{\text{fine}} = 3^\circ$ (at this point "bad" images may cause the code to runaway; they are dropped and the code advances to the next time step). The possible orientations are then rendered in real size and compared [using Eq. (13)] to the image $\underline{\underline{\mathbf{I}}}$. For each group, the code returns the final best guess, i.e., the orientation with the maximum resemblance, thus drawing a list of *candidates*, see Fig. 5 for an example of a particle with its corresponding candidates.

2. Track assembly

After identifying the candidates for each time step, the most likely orientation for each time step has to be determined. However, the candidate with the highest count of correct pixels is not necessarily the best choice. Although

FIG. 4. (Color online) Texture extraction and comparison with a synthetic image. The resemblance between the image $\underline{\underline{\mathbf{I}}}$ and the synthetic projection $\underline{\underline{\mathbf{S}}}$ at angle $\underline{\theta}$ is estimated using Eq. (13).

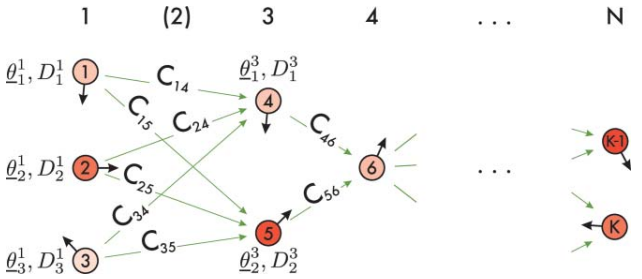

FIG. 6. (Color online) Sketch of a graph connecting the possible candidates using the cost function C [cf. Eq. (15)]. For each time step t, we have $b(t)$ candidates with an orientation $\underline{\theta}_b^t$ and a resemblance D_b^t. In the time series $t = 1 \ldots N$, the candidates are labeled $k \in 1 \ldots K$. The directed graph C connects all candidates at t to all their next valid time step $t + \Delta t$; gaps are skipped as indicated for time step **2**.

counterintuitive, the direct use of two cameras seeing the particle at different angles does not simplify the problem, because in the case of a bad image, one camera falsifies the choice of the candidates found by the other camera. Moreover, gimbal locks prevent the use of a predictor–corrector scheme for the prediction of the orientation. However, the norm of angular velocity is assumed to be smooth and we search the time series which globally minimizes the sum $\sum_t \xi(t)$ along the time series of the so called direct neighbor distance function

$$\xi(t) \equiv \left|\boldsymbol{\omega}(\underline{\theta}(t), \underline{\theta}(t+\Delta t))\right| = \frac{d(\underline{\theta}(t), \underline{\theta}(t+\Delta t))}{\Delta t}. \quad (14)$$

A direct neighbor is the next valid time step at $t + \Delta t$. The distance between two orientations does not depend on the representation, ensuring the robustness of the algorithm even at gimbal locks. Minimizing $\sum_t \xi(t)$ is only meaningful for small changes in orientation between two time steps, another requirement for high (over)sampling rates.

Flow algorithms are highly efficient in finding a global optimum for a discrete set of candidates. The following is done for each camera without considering the extra information from the second camera. In a first step we remove all candidates with a resemblance $T < s_{\text{quality}}$—in practice $s_{\text{quality}} = 0.5$. Then a directed graph is built which connects all candidates at time step t with all their direct neighbors at the nonempty time step $t + \Delta t$. The cost function is chosen such that it takes into account both the change in orientation and the quality of the matching

$$C(\{\underline{\theta}_A, T_A\}, \{\underline{\theta}_B, T_B\}) = d(\underline{\theta}_A, \underline{\theta}_B)\frac{2 - T_A - T_B}{\Delta t} \quad (15)$$

with $\{\underline{\theta}_A, T_A\}$ a candidate at time t and $\{\underline{\theta}_B, T_B\}$ a directly neighboring candidate at $t + \Delta t$.

A Dijkstra path finding algorithm returns the sequence of candidates having a global minimum of the total cost, i.e., the global minimum of change of orientation (weighted by the image quality) (cf. Fig. 6). In most cases this algorithm returns directly the time series of absolute orientation. Nevertheless, bad images introduce false candidates forcing the path finding algorithm to take a different, nonphysical path. These points manifest as spikes in the direct neighbor distance function, $\xi(t)$. After a spike, there is no guarantee that the path is still physical. Therefore, we segment the time series based on the spikes. The second view (from the second camera) treated with the same algorithm contains the information to correct such wrong segments. From the camera calibration the rotation matrix which transforms the orientations seen by one camera into the coordinate system of the other one, is known. Therefore, both views are expressed in an intermediate, common coordinate system where the segments with $d(\underline{\theta}_{\text{cam1}}, \underline{\theta}_{\text{cam2}}) \gtrsim 30^\circ$ can be corrected.

The algorithm presented so far assumes an orthographic view. This condition holds only true if the particle center is on the optical axis of the camera or in the case one uses telecentric lenses. In the present experiment we do not, and the perspective effect alters the measured orientation (note that the parallax displacement corresponds to a change in the 2D projection, and hence to a rotation). The distortion induced by the perspective is characterized by the position of the particle center in the camera image, $\boldsymbol{X}$, and the focal length, f. Common camera objectives allow only small angles, $\gamma_{\text{persp}} \equiv \text{atan}(\|\boldsymbol{X}\|/f) \lesssim 15^\circ$. As a consequence we assume that the shape of the particle does not change and we introduce an orientation matrix $R_{\text{persp.}}$ [taking advantage of the Rodrigues formula Eq. (9)]

$$\underline{\underline{\mathbf{R}}}_{\text{persp.}}(\boldsymbol{X} = (x, y), f) = \underline{\underline{\mathbf{R}}}\left(\frac{(-y, x, 0)}{\sqrt{x^2 + y^2}}, \text{atan}\left(\frac{\|\boldsymbol{X}\|}{f}\right)\right) \quad (16)$$

such that the measured orientation is related to the absolute orientation $\underline{\theta}_{\text{abs}}$ by $\underline{\underline{\mathbf{R}}} \cong \underline{\underline{\mathbf{R}}}_{\text{persp.}}\underline{\underline{\mathbf{R}}}(\underline{\theta}_{\text{abs}})$. The perspective distortion can then be removed from the orientation time series.

Finally, after correcting for perspective distortion, a combined time series of orientation can be built using the information from both views, if they are expressed in the same coordinate system. Euler angles are not locally orthogonal, hence, we use the weighted mean of the orientation expressed in the axis–angle representation. The variance within a moving window of the direct neighbor distance function, $\xi(t)$, proves to be a good error estimator of the noise, since for short times the particle is assumed to rotate smoothly. A sample orientation track is shown in the upper panel of Fig. 7.

C. Robustness

A full study of the accuracy and robustness considering all possible distortions is beyond the scope of this article. In practice, the problems with real images are mainly caused by reflections, bad illumination, and objects (such as bubbles or dirt particles) between the particle and the camera. The setup, light conditions, and particle texture must be first tuned in order to optimize these parameters—by trial and error methods. For the orientation algorithm *per se*, we have used a series of synthetic images of known orientation. We found that the measurement error is 2°, which is

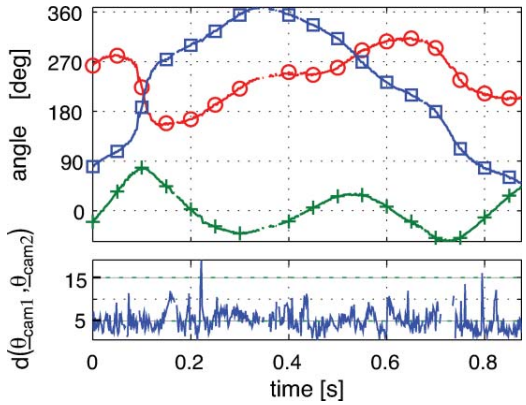

FIG. 7. (Color online) A sample orientation track; it is $\theta_x = \bigcirc$, $\theta_y = +$, $\theta_z = \square$, the bottom plot shows the distance (in degrees) between the independent orientation measurements from the two cameras.

smaller than the size, $\Delta_{\text{fine}} = 3^\circ$ of the fine grid used in the image processing (cf. paragraph III B 1 c). A finer grid would improve the resolution for ideal images, but not for real images which, as stated above, always contain some amount of distortions or impurities. In addition, the fast dynamics of the particle and high frame rate ensure that wrong detection do not persist for longer than a few frames. As a result, most defects are detected and skipped or interpolated or handled as part of postprocessing (wrong orientations correspond to jumps in the direct neighbor distance function).

We illustrate the accuracy of the detection on two examples. The first one concerns the agreement between the orientation as estimated from each camera measurement. In the upper panel of Fig. 7, the combined three angles with respect to the lab coordinate system are plotted. The lower panel shows the distance (in degrees of angle) between the two estimations, $d\left(\underline{\theta}_{\text{cam1}}, \underline{\theta}_{\text{cam2}}\right)$. The probability density function (PDF) of these distances, computed with and without processing for perspective corrections are shown in Fig. 8. Correcting the systematic error induced by the perspective distortion reduces the mean value and width of the distribution. The remaining error is of random nature. Combining the two independent views as described early leads to a weighted error of $\sim 3^\circ$.

IV. RESULTS

The results in this section correspond to the flow created by counter-rotation of the driving disks at a rate of 3 Hz. In this case the net power injection is of the order of $\epsilon \sim 1.7$ W/kg, a value in agreement with bulk scalings and measurements, as reported in Ref. 26. The integral time scale T_L is about 0.3 s, so that the dissipative time and space scales are $\eta \sim 30\,\mu$m and $\tau_\eta \sim 1$ ms. As a result, the particle tracked has a size corresponding to $D/\eta \sim 600$ and $D/L_{\text{int}} \sim 0.6$ (L_{int} is the scale at which energy is fed into the flow). The flow Reynolds number based on the Taylor microscale is $R_\lambda \sim 300$. The camera frame-rate is 600 Hz, and the trajectories analyzed have been selected so that their duration is longer than $0.25T_L$ and most range between 0.5 and $3T_L$.

Figure 9 shows a histogram of the duration of recorded tracks for which the 6D coordinates of the particle are recorded. It has an exponential tail (as it was also the case when using acoustic tracking[27]). For very small times the histogram is biased by the fact that tracks shorter than 50 contiguous frames are discarded. Note also that long tracks are likely to correspond to trajectories spanning the flow volume, i.e., a spatial extend over which the large scale (anisotropic) circulation cannot be ignored.

However, one first result is that the particle explores uniformly the orientation space. This is seen in Fig. 10 showing the probability distribution functions of the Euler angles: as expected from a random distribution of orientations, the θ_x and θ_z components have a flat distributions spanning a $[-\pi, +\pi[$ interval, with the inner angle θ_y having a $cos(\theta_y)$ distribution over $[-\pi/2, \pi/2]$.

Interesting features are observed for the rotation dynamics. The statistics of angular velocity fluctuations are shown in Fig. 11. The distributions are symmetric. The three components, with respect to the lab coordinate system, follow the same statistics. This reflects the spherical symmetry of the particle; furthermore, it also shows that the turbulent swirls at the scale of the particle have no preferred orientation. The

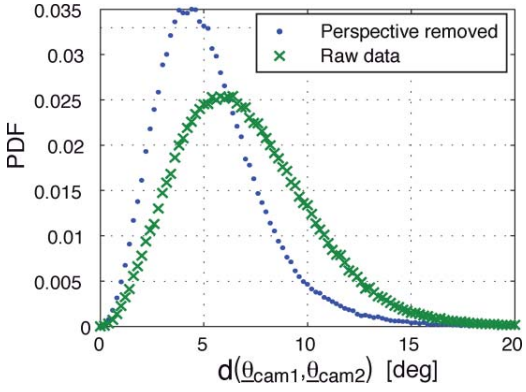

FIG. 8. (Color online) Probability density function (PDF) of the distance between the orientations measured from cameras 1 and 2, without correction for perspective distortion (×) and with it (○).

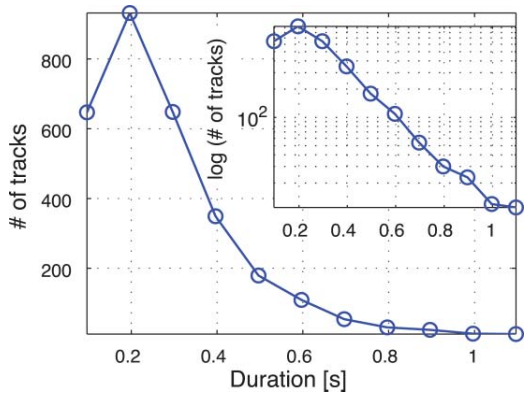

FIG. 9. (Color online) Histogram of track segments. The exponential decay rate is of the order of the integral time T_L of the flow.

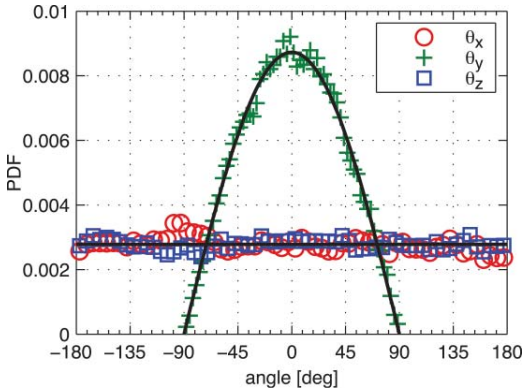

FIG. 10. (Color online) PDF of the orientation $\underline{\theta} = \{\theta_x, \theta_y, \theta_z\}$, the solid lines correspond to a uniform sampling of the orientation space.

mean of the angular velocity components (with respect to the lab reference frame) is essentially zero, up to statistical error. The *rms* amplitude of angular velocity fluctuation is of the order of 12 rad/s, see Table I, which is of the order of $u_{\rm rms}/D = 30$ rad/s. That is, it corresponds to the rotation that would result from imposing a velocity difference equal to almost $u_{\rm rms}$ across the diameter D of the sphere. Note that it is also of the order of the rotation rate of the driving disks. The PDF themselves displays weakly stretched-exponential tails; for a quantitative estimation we use the fitting function

$$\Pi_a(x) = \frac{e^{3a^2/2}}{4\sqrt{3}}\left(1 - \mathrm{erf}\left(\frac{\ln\left|x/\sqrt{3}\right| + 2a^2}{a\sqrt{2}}\right)\right), \qquad (17)$$

which has been used extensively in the analysis of the intermittency of the translational motion of Lagrangian tracers[4] —it stems from the approximation that the norm of the vector has a lognormal distribution. For the angular velocity, one finds a fitting parameter $a = 0.45$, which corresponds to a flatness factor $F = 4$. It would be $F = 3$ for Gaussian statistics, so that our measurements show only a slightly non-Gaussian behavior for the angular velocity. This differs

TABLE I. Characteristic values (mean ± rms) for the particle motion. The angular variables are given for the lab and particle coordinate systems.

		x	y	z	Norm
$\boldsymbol{v}$	(m/s)	0 ± 0.28	0 ± 0.40	0 ± 0.37	0.6 ± 0.2
$\boldsymbol{a}$	(m/s^2)	-0.2 ± 5.6	-0.3 ± 5.8	0.2 ± 6.3	8.5 ± 5.6
$\boldsymbol{\omega}^{\mathbb{L}}$	(rad/s)	0 ± 7.7	0.1 ± 7.3	0.1 ± 7.2	11.6 ± 5.5
$\boldsymbol{\omega}^{\mathbb{P}}$	(rad/s)	0 ± 6.5	-0.2 ± 7.8	-0.1 ± 7.8	
$\boldsymbol{\alpha}^{\mathbb{L}}$	(rad/s^2)	0 ± 540	0 ± 480	0 ± 420	670 ± 580
$\boldsymbol{\alpha}^{\mathbb{P}}$	(rad/s^2)	0 ± 510	0 ± 440	0 ± 460	

from the translational velocity, which is found to be slightly sub-Gaussian.

The angular acceleration has a strong non-Gaussian behavior, as seen in Fig. 12. Again, the three components follow identical statistics: there is no preferred direction for the torques acting on the moving sphere (with respect to the lab reference frame only—the issue of lift forces is addressed elsewhere[12]). The *rms* amplitude of angular acceleration is about 700 rad/s^2, see Table I, again of the order of $(u_{\rm rms}/D)^2$. The statistics is strongly non-Gaussian, a fit using the same stretched exponential distribution yields $a = 0.6$, i.e., a flatness factor $F \sim 7.6$. The angular acceleration can be viewed as an angular velocity increment over a very short time lag. Hence, the PDFs of angular velocity increments change shape with the length of the time lag—from the one in Fig. 11 for small time increments to the one in Fig. 12 for integral times.

For comparison, we recall some features of the translational dynamics of the particle. It has statistical characteristics which are very close to the one reported for neutrally buoyant inertial particles with a size much closer to the dissipation scales of turbulence.[3,9–11] The translational velocity follows a Gaussian distribution, its acceleration is strongly non-Gaussian, with stretched exponential tails. Using the stretched exponential distribution leads to $a = 0.6$. One thus observes that the angular variables have intermittent dynamics, just as the translational motion. The fact that it is quite

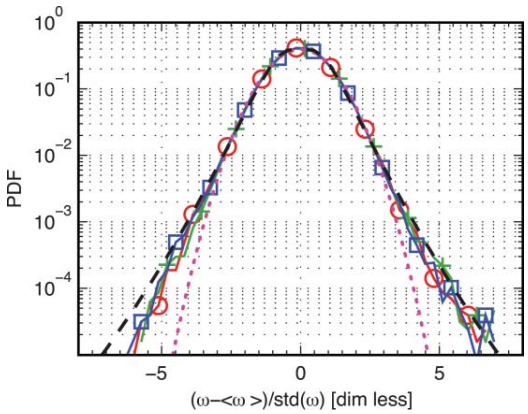

FIG. 11. (Color online) PDF of the (normalized) components of the angular velocity, $\omega_x = \bigcirc$, $\omega_y = +$, $\omega_z = \square$, the dotted curve is a Gaussian and the dashed one shows a stretched exponential with $a = 0.45 (F = 4)$.

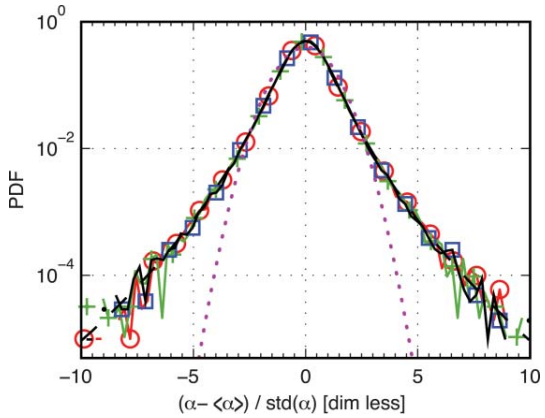

FIG. 12. (Color online) PDF of angular acceleration; it is $\boldsymbol{\alpha}_x = \bigcirc$, $\boldsymbol{\alpha}_y = +$, $\boldsymbol{\alpha}_z = \square$, the dotted curve is a Gaussian and the dashed one shows a stretched exponential with $a = 0.6 (F = 7.6)$.

pronounced, even for an object of size close to the integral scale of motions came as a surprise and deserves further investigations.

V. CONCLUDING REMARKS

The focus of the work reported here has been to establish a technique for the study of angular and translational motion of a particle freely advected by a turbulent flow. We have shown that the measurement technique is robust, efficient, and accurate. As an application, we report here the first observation of intermittency for the rotational dynamics of an inertial particle. It should be pointed out, that the technique can be easily extended to track multiple spheres in a flow. Suitable algorithms for the tracking of multiple particle are presented in, e.g., Ref. 13. Smaller particle sizes are possible, if the particle texture is sufficiently well resolved and accurately painted.

We note that the algorithm used to compute the angular velocity can be applied to a set of particle attached to a rigid body which are tracked using standard particle tracking algorithms. If one records the positions in space of three or more points, $\boldsymbol{P}_1 \ldots \boldsymbol{P}_N$ at time t and $t + \Delta t$, their motion can be split up into a translation of their center of mass plus a rotation. Once the translation part is subtracted, the rotation, $\underline{\underline{\mathbf{R}}}_{\text{kabsch}}$, of the points $\boldsymbol{P}_1 \ldots \boldsymbol{P}_N$ around their center of mass can be computed efficiently using Kabsch's[28,29] algorithm. $\underline{\underline{\mathbf{R}}}_{\text{kabsch}}$ is then the matrix representation of the change in orientation, and the angular velocity, $\boldsymbol{\omega}^{\mathbb{P}}$, (in the particle reference frame) at time t can be extracted as done here. It should be pointed out that, one does not gain access to neither the angular velocity in the lab reference frame, $\boldsymbol{\omega}^{\mathbb{L}}$, nor to the absolute orientation, $\underline{\theta}$.

The strong intermittency in the particle's rotation may eventually be traced back to the complex interaction between the particle and its wake. One notes that this is inherently a finite size effect; for particles with very small diameters (compared to the Kolmogorov length) the translational and rotational dynamics are note coupled. For larger particles, as in our case, the influence of rotation on the motion of the particle is of interest, and will be the object of further analysis. One may also note that the influence of the inhomogeneity at large scale must be clarified. Further measurements in a more isotropic turbulent flow (such as the Lagrangian Exploration Module[30]) are underway.

ACKNOWLEDGMENTS

We thank Aurore Naso for many fruitful discussions during the development and testing of the presented technique. This work was supported by ANR-07-BLAN-0155, and by PPF "Particules en Turbulence" from the Université de Lyon.

[1] F. Toschi and E. Bodenschatz, Annu. Rev. Fluid Mech. **41**, 375 (2009).
[2] A. La Porta, G. A.Voth, A. M. Crawford, J. Alexander, and E. Bodenschatz, Nature (London) **409**, 1017 (2001).
[3] N. Mordant, P. Metz, O. Michel, and J. Pinton, Phys. Rev. Lett. **87**, 214501 (2001).
[4] N. Mordant, A. Crawford, and E. Bodenschatz, Physica D **193**, 245 (2004).
[5] T. R. Auton, J. Hunt, and M. Prud'homme, J. Fluid Mech. **197**, 241 (1988).
[6] P. Lovalenti and J. Brady, J. Fluid Mech. **256**, 561 (1993).
[7] E. Loth and A. Dorgan, Environ. Fluid Mech. **9**, 187 (2009).
[8] N. Qureshi, M. Bourgoin, C. Baudet, A. Cartellier, and Y. Gagne, Phys. Rev. Lett. **99**, 184502 (2007).
[9] N. Qureshi, U. Arrieta, C. Baudet, A. Cartellier, Y. Gagne, and M. Bourgoin, Eur. Phys. J. B **66**, 531 (2008).
[10] R. Brown, Z. Warhaft, and G. A. Voth, Phys. Rev. Lett. **103**, 194501 (2009).
[11] R. Volk, E. Calzavarini, E. Lévêque, and J. F. Pinton, J. Fluid Mech. **668**, 223 (2011).
[12] Robert Zimmermann, Yoann Gasteuil, Mickaël Bourgoin, Romain Volk, Alain Pumir, and Jean-François Pinton, arXiv:1012.4381v1, submitted.
[13] *Springer Handbook of Experimental Fluid Dynamics*, edited by C. Tropea, A. Yarin, and J. F. Foss (Springer-Verlag, Berlin, 2007).
[14] J. Ye and M. C. Roco, Phys. Fluids A **4**, 220 (1992).
[15] M. B. Frish and W. W. Webb, J. Fluid Mech. **107**, 173 (1981).
[16] N. Ouellette, H. Xu, M. Bourgoin, and E. Bodenschatz, New J. Phys. **8**, 102 (2006).
[17] R. Monchaux, F. Ravelet, B. Dubrulle, A. Chiffaudel, and F. Daviaud, Phys. Rev. Lett. **96**, 124502 (2006).
[18] D. H. Brainard, Spatial Vis. **10**, 433 (1997).
[19] D. G. Pelli, Spatial Vis. **10**, 437 (1997).
[20] H. Goldstein, C. Poole, and J. Safko, Classical Mechanics [3rd ed.], Addison Wesley, New-York, 2002.
[21] B. L. Stevens and F. L. Lewis, *Aircraft Control and Simulation* (Wiley, New York, 2003).
[22] E. W. Weisstein (1999). MathWorld—A Wolfram Web Resource. http://mathworld.wolfram.com/
[23] E. Lattman, Acta Crystallogr. **28**, 1065 (1972).
[24] R. Tsai, IEEE J. Rob. Autom. **3**, 323 (1987).
[25] N. Otsu, IEEE Trans. Syst. Man Cybern. **9**, 62 (1979).
[26] G. Zocchi, P. Tabeling, J. Maurer, and H. Willaime, Phys. Rev. E **50**, 3693 (1994).
[27] N. Mordant, Ph.D. dissertation, École Normale Supérieure de Lyon, 2001.
[28] W. Kabsch, Acta Crystallogr. **32**, 922 (1976).
[29] W. Kabsch, Acta Crystallogr. **32**, 827 (1976).
[30] R. Zimmermann, H. Xu, Y. Gasteuil, M. Bourgoin, R. Volk, J.-F. Pinton, and E. Bodenschatz, Rev. Sci. Instrum. **81**, 055112 (2010).

Rotational Intermittency and Turbulence Induced Lift Experienced by Large Particles in a Turbulent Flow

Robert Zimmermann, Yoann Gasteuil, Mickael Bourgoin, Romain Volk, Alain Pumir, and Jean-François Pinton

Laboratoire de Physique de l'École Normale Supérieure de Lyon, UMR5672, CNRS and Université de Lyon, 46 Allée d'Italie, 69007 Lyon, France

(Received 17 December 2010; published 11 April 2011)

The motion of a large, neutrally buoyant, particle freely advected by a turbulent flow is determined experimentally. We demonstrate that both the translational and angular accelerations exhibit very wide probability distributions, a manifestation of intermittency. The orientation of the angular velocity with respect to the trajectory, as well as the translational acceleration conditioned on the spinning velocity, provides evidence of a lift force acting on the particle.

DOI: 10.1103/PhysRevLett.106.154501 PACS numbers: 47.27.T−, 05.60.Cd, 47.27.Ak, 47.55.Kf

The description of a solid object freely advected in a fluid requires, in addition to its translational degrees of freedom characterizing its position, 3 rotational degrees of freedom, specifying its orientation with respect to a reference frame. The evolution of its position and of its orientation depends, according to Newton's laws, on the forces and torques acting on the particle, which result from its interaction with the turbulent flow. Their determination raises challenging issues. The problem has been solved to a large extent for spherical particles of size D much smaller than the smallest length scale of the flow, the Kolmogorov scale η [1,2]. Because of the small size of the particle, the flow around it is locally laminar (see Fig. 1), so the equation governing the particle velocity $\boldsymbol{v}$ can be determined by solving the fluid (Stokes) equations once the fluid velocity $\boldsymbol{u}$ is known. In the simplest case, the particles are subject to the Stokes drag and the added mass term [3], so the velocity $\boldsymbol{v}$ can be determined by solving a simple differential equation. For $D \to 0$, the velocity of a neutrally buoyant particle reduces to the fluid velocity $\boldsymbol{u}$, so the particle behaves as a fluid tracer. This property is crucial for several experimental techniques [4]. In the limit $D \to 0$ [1,2], the translational and rotational degrees of freedom completely decouple.

Figure 1 suggests that the case of particles of radius larger than η is conceptually much more difficult. Experiments have shown that, upon increasing the ratio D/η from 1 to 40, the variance of the particle acceleration (i.e., of the forces) decreases as $(D/\eta)^{-2/3}$ [5,6]. The fluctuations of force remain non-Gaussian up to $D/\eta \lesssim 40$ [7–9], and a full derivation of the equation of motion of a large particle is still not available. The hydrodynamics forces can be decomposed parallel and perpendicular to the relative velocity $\mathbf{v}_{\mathrm{rel}}$ of the particle with respect to the flow. A generalization of the Magnus force, as derived in an inviscid, laminar flow: $\boldsymbol{F}_{\mathrm{lift}} = C_{\mathrm{lift}} \boldsymbol{v}_{\mathrm{rel}} \times \boldsymbol{\omega}^{\mathbb{P}}$, where $\boldsymbol{\omega}^{\mathbb{P}}$ is the rotation of the particle in the flow, appears as a natural possibility of a force acting perpendicular to $\boldsymbol{v}_{\mathrm{rel}}$ [10,11]. A lift has indeed been measured in laboratory experiments, when the flow is steady and laminar [12–14]. The flow conditions in these experiments are very different from the case of a particle in turbulence, schematically represented in Fig. 1. In such a flow field, the very definition of the fluid velocity around the particle is in fact very ambiguous. We therefore reduce the expression for the lift (Magnus) force to $\propto \boldsymbol{v} \times \boldsymbol{\omega}^{\mathbb{P}}$, where $\boldsymbol{v}$ is the particle velocity. The very existence of any lift force in these conditions, leading to a coupling between the translational and rotational degrees of freedom, is thus not obvious.

Here, we measure simultaneously the translational and rotational motion of a neutrally buoyant spherical particle, whose diameter is a fraction of the integral scale of the turbulence, and report the evidence of a lift force. We first briefly describe our six-dimensional tracking technique [15,16] and then present our results concerning the intermittency of the translational *and* rotational velocity and acceleration. Last, we discuss how the translational and rotational degrees of freedom of the particle couple, resulting in a lift force.

The flow and the tracking technique are described in detail in Ref. [16]. A von Kármán flow, as widely used for turbulence studies [6,17,18], is generated in the gap

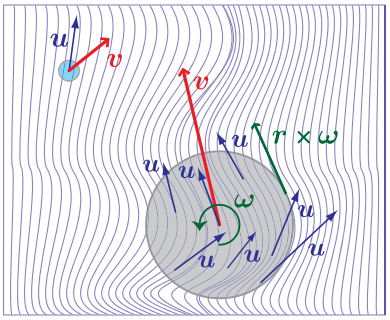

FIG. 1 (color online). Sketch of particles of increasing sizes superimposed on local velocity gradients. Whereas the flow around the small particle is smooth, it exhibits significant spatial variations around the large particle.

between two counterrotating impellers; see Fig. 2(a). In order to be able to perform direct optical measurements, the container is built with flat Plexiglas side walls, so that the cross section of the vessel has a square shape.

The driving disks are rotated here at 3 Hz, corresponding to an energy injection rate of $\varepsilon \sim 1.7$ W/kg. The integral time and length scales are $L_{\rm int} = 3$ cm and $T_L = 0.3$ s, respectively, so that the dissipative length and time scales are, respectively, $\eta \sim 30$ μm and $\tau_\eta \sim 1$ ms. The flow Reynolds number based on the Taylor microscale is $R_\lambda \sim 300$.

A polyamide sphere with density $\rho_p = 1.14$ g $\cdot$ cm^{-3} and diameter $D = 18$ mm is made neutrally buoyant by adjusting the density of the fluid by addition of glycerol to water (the final density mismatch is less than $\Delta\rho/\rho = 10^{-4}$). The spheres are homogeneous; i.e., the particle center of mass coincides with its geometrical center. Their size is comparable to the integral length of the flow, corresponding to $D/\eta \sim 600$ and $D/L_{\rm int} \sim 0.6$. Its motion is recorded at 600 Hz, by using 2 high-speed video cameras (Phantom V12, Vision Research Inc.) positioned at 90°. The measurement volume lies within 75% of the radial and axial distances on either side of the flow center, i.e., extends to regions where anisotropy and inhomogeneity are known to play a role. Restricting the measurement volume closer to the center does not affect significantly our results, thus strongly suggesting that the effects discussed in this Letter are not artifacts of the experimental setup. The position of the sphere is determined by using a position tracking algorithm, as in Ref. [6]. The time-resolved determination of the rotational degrees of freedom [15,16] is carried out by painting a pattern that enables a determination of the particle's orientation from the camera images; cf. Fig. 2(c). The orientation tracking algorithm then (i) compares the sphere's picture with synthetic images and identifies a set of possible orientations; (ii) from the set of possible candidates at successive instants, a *flow* algorithm identifies a likely time series; and (iii) a posttreatment adjusts remaining ambiguities, by using the independent views from the 2 cameras. After processing, all trajectories with a duration longer than $0.25T_L$ are analyzed, leaving 3434 trajectories with duration ranging between 0.25 and $3T_L$. A few particular examples are shown in Fig. 2(d), showing the position, color coded for the amplitude of the acceleration, together with two unit vectors fixed in the reference frame of the particle. Velocity and acceleration are computed from convolution with Gaussian kernels, as described in Refs. [16,19].

We find that the behavior of the translational degrees of freedom is qualitatively very similar to the results obtained for much smaller particles [5,7–9]—the size of the particles studied so far did not exceed $D \lesssim 40\eta$, whereas ours has $D \approx 600\eta$. The particle velocity has a quasi-Gaussian distribution; each component has zero mean and an rms intensity of fluctuations of about 60 cm/s, for impellers rotating at 3 Hz. This is of the order of 30% of the impeller tip speed and also of the order of the rms velocity fluctuations of tracers in the same flow. This leads to the consistent notion that the velocities of the particle are of the order of the large scale swirls generated in the von Kármán setup. The particle Reynolds number $\mathrm{Re}_p \equiv u_{\rm rms} D/\nu$ is estimated to $\sim$1200; one expects that the Reynolds number *relative* to the local fluid motions is of the same order of magnitude.

The particle's acceleration, with zero mean, has an rms amplitude of fluctuations equal to 8.5 m/s^2. Its probability distribution function (PDF) has strongly non-Gaussian fluctuations; see Fig. 3. In terms of velocity increments, the acceleration can be viewed as a velocity change over the shortest time scale, while the velocity increments over long times scales have the same distribution as the velocity itself. We have checked that, as expected, the PDFs of velocity increments evolve smoothly from a shape with wide tails [19] for very small time lags to a Gaussian shape

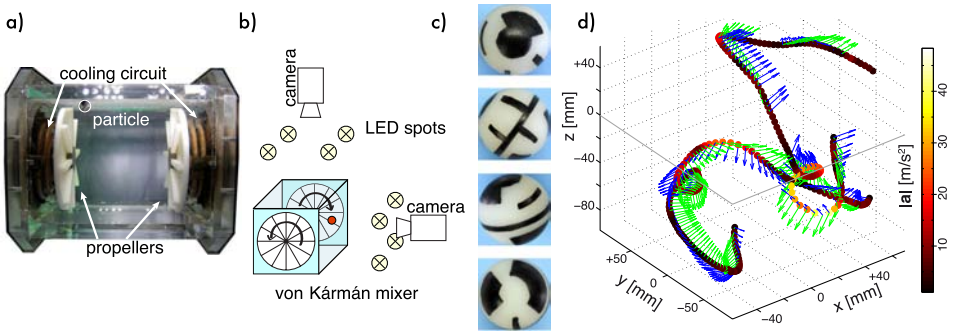

FIG. 2 (color online). (a) The flow domain in between the impeller has characteristic lengths $H = 2R = 20$ cm; the disks have radius $R = 10$ cm, fitted with straight blades 1 cm in height. (b) It is illuminated by high power light-emitting diodes, and sequences of 8-bit gray-scale images are recorded by using high-speed cameras; (c) an adequate texture painted on the particle allows the tracking of its orientation; (d) example of particle tracks and orientations (the green and blue arrows mark North-South and East-West directions, respectively).

at long time intervals, a phenomenon often called intermittency. This effect is observed here for a very large particle, compared to the Kolmogorov scale, η. The strong events in the acceleration PDF are, however, less intense than in the case of smaller particles. We estimate the normalized fourth moment, the flatness, to be $F = 7 \pm 1$ for our particle with $D/L_{\rm int} \sim 0.6$. Remarkably, this value is identical to the one found in Ref. [7], with a comparable ratio $D/L_{\rm int} \lesssim 1$, and generally with the very slow decay of the flatness with D observed in Refs. [9,20] for particles much smaller compared to $L_{\rm int}$ ($D/L_{\rm int} \sim 1/50$).

We now turn to the angular velocity of the sphere, $\boldsymbol{\omega}^{\mathbb{P}}$. The three components fluctuate around a zero mean value, with no preferred orientation, and their rms amplitude is 12 rad/s. This value is comparable to the rotation rate of the driving disks and also corresponds to the rotation that would result from imposing a velocity difference of the order of $u_{\rm rms}$ across the particle diameter D ($u_{\rm rms}/D \simeq 30$ rad/s). The PDFs of angular velocity components are shown in Fig. 3. The distributions are symmetric and slightly non-Gaussian (we estimate a flatness $F \sim 4$). The rms amplitude of the angular acceleration $\boldsymbol{\alpha}^{\mathbb{P}}$ is about 700 rad/s^2, again of the order of $(u_{\rm rms}/D)^2$. The PDF of $\boldsymbol{\alpha}^{\mathbb{P}}$ is strongly non-Gaussian (we estimate $F = 7 \pm 1$). Hence, the PDFs of the angular velocity increments become broader when the time lag τ decreases from $\tau \sim T_L$ to $\tau \sim \tau_\eta$: The angular dynamics is intermittent.

We now address the question of the coupling between the dynamics of rotation and translation. Figure 4(a) reveals a strong alignment between the direction of the angular velocity $\boldsymbol{\omega}^{\mathbb{P}}$ and the vectors defining the trajectory—the usual Frenet coordinate system ($\boldsymbol{T}$, $\boldsymbol{N}$, $\boldsymbol{B}$), denoting, respectively, the units vectors along the velocity, the curvature, and the direction perpendicular to the tangent plane of the trajectory. The fairly sharp distribution of the direction of $\boldsymbol{\omega}^{\mathbb{P}}$ on the sphere is quite surprising. In fact, Fig. 4(a) shows a maximum of probability at an angle of the order of 45° with respect to $\boldsymbol{T}$ in the ($\boldsymbol{T}$, $\boldsymbol{B}$) plane. This effective breaking of the rotational symmetry of $\boldsymbol{\omega}^{\mathbb{P}}$ strongly suggests a coupling between the translational and the rotational dynamics. We also note that $\boldsymbol{\omega}^{\mathbb{P}}$ is aligned perpendicular to $\boldsymbol{N}$, so both the acceleration $\boldsymbol{a}$ and $\boldsymbol{v} \times \boldsymbol{\omega}^{\mathbb{P}}$ lie in the ($\boldsymbol{T}$, $\boldsymbol{N}$) plane. Our measurements thus demonstrate that the expected expression of the lift (Magnus) force, $\approx \boldsymbol{v} \times \boldsymbol{\omega}^{\mathbb{P}}$, has a strong component in the $\boldsymbol{N}$ direction. This is consistent with a lift force acting on the particle. Further evidence for a lift force is provided by the observation that the amplitude of the normal acceleration, $a_N \equiv \boldsymbol{a} \cdot \boldsymbol{N}$, conditioned on the amplitude of $\omega_B \equiv \boldsymbol{\omega}^{\mathbb{P}} \cdot \boldsymbol{B}$ [Fig. 4(b)] increases from 6 to 9 m/s^2 (half a standard deviation) when the particle rotation varies in the range ± 12 rad/s (i.e., 1 standard deviation in rotation speed).

The main results of this work concern the strong intermittency for both the translational and the rotational accelerations and the coupling between the rotational and translational degrees of freedom.

The observed intermittency of the translational and rotational accelerations points to very intense fluctuations of the force and torque acting on the particle. The interaction between the sphere and the flow involves a pressure and a viscous term, resulting from the stress tensor:

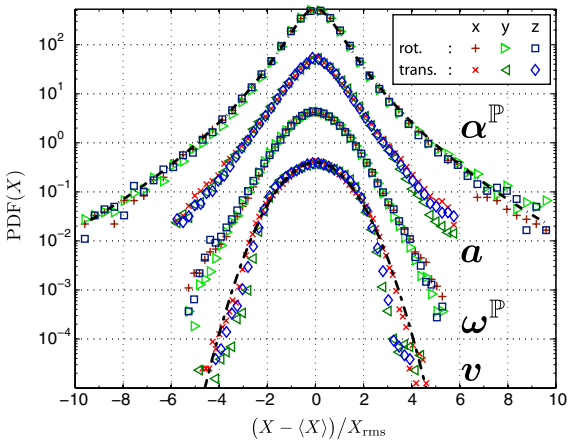

FIG. 3 (color online). PDFs of velocity and acceleration, for the linear and angular motions. The curves have been shifted vertically for clarity.

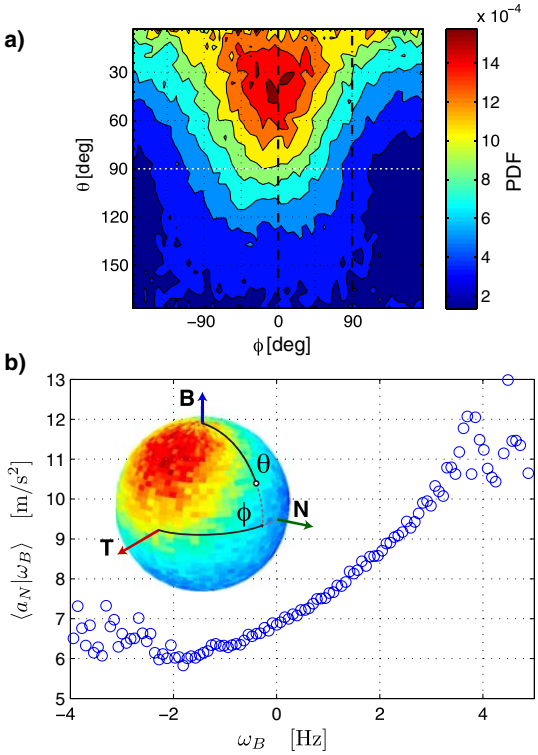

FIG. 4 (color online). (a) Alignment of the angular velocity $\boldsymbol{\omega}^{\mathbb{P}}$ with respect to the moving Frenet coordinate system; (b) normal acceleration conditioned to the component of angular velocity parallel to the binormal Frenet vector.

$\tau_{ij} = -p\delta_{ij} + \rho\nu(\partial_i u_j + \partial_j u_i)$. Measurements of the drag force acting on a particle of a large Reynolds numbers [21] demonstrate that pressure is the dominant effect in the force: At the particle Reynolds number in our experiment, $\mathrm{Re}_P \approx 10^3$, friction contributes to ~20% of the drag; this fraction diminishes at higher Reynolds numbers. Pressure is expected to be mostly coherent at the scale of our particle $D \sim L$, so the pressure effects act collectively on the object, resulting in a force of order $\rho D^2 u_{\mathrm{rms}}^2$, which yields the correct order of magnitude for the rms of the particle acceleration. The strongly non-Gaussian PDFs of $\boldsymbol{a}$ are more surprising, since the force acting on the particle results from an averaging over a size comparable to the correlation length of the flow.

The effect of friction, although weak compared to pressure, is essential to understand the torque. In fact, the pressure force, perpendicular to the surface of the sphere, does not contribute to the torque applied at the center of the particle. Thus, the rms of the angular acceleration is $\langle(\boldsymbol{\alpha}^{\mathbb{P}})^2\rangle^{1/2} \sim \langle\Gamma_v^2\rangle^{1/2}/I$, where Γ_v is the torque and I the moment of inertia of the particle. The torque results from an integral over the particle's surface, and Γ_v is proportional to $\nu\partial_x u$. This viscous term is quantified by the skin friction velocity $u_*^2 \equiv \nu\partial_x u$. Given the weak value of the moment of inertia $I = MD^2/10$, where M is the mass of the particle, one obtains $\langle(\boldsymbol{\alpha}^{\mathbb{P}})^2\rangle^{1/2} \sim 10(u_*/D)^2$. Previous measurements suggest a ratio u_*^2/u_{rms}^2 of the order of 0.2 at the particle Reynold's number $\mathrm{Re}_p \approx 1000$ [21]. This leads to $\langle(\boldsymbol{\alpha}^{\mathbb{P}})^2\rangle \sim (u_{\mathrm{rms}}^2/D^2)^2$, as observed in our experiment. Which properties of the turbulent flow control the rate of rotation of the particle also remains to be elucidated. In this respect, the naive vision of many small eddies, compared to the size of our big particle, implicit in Fig. 1, is likely to be an oversimplification. Small eddies acting on the particle in a spatially incoherent manner would result in a significantly reduced torque acting on the particle. This suggests a much more coherent flow pattern, at least at our particle Reynolds numbers, in fact consistent with the recent numerical results of Ref. [22]. We also note that, while the estimates above provide a qualitative explanation of the observed velocities and accelerations rms values, understanding the complete statistics of their fluctuations remains a challenge. Our evidence of a lift effect, i.e., a strong coupling between rotation and translation, rests on conditioning the acceleration (force) on the angular velocity of the particle, $\boldsymbol{\omega}^{\mathbb{P}}$. While this is a very sensible choice, the actual torque acting on the particle depends on the local structure of the flow, which remains to be determined, for instance, by local particle image (or tracking) velocimetry around the moving sphere [23] or numerically [20,22,24]. The sharply peaked distribution of $\boldsymbol{\omega}^{\mathbb{P}}$ in the Frenet basis [see Fig. 4(a)] is a very surprising result of this work. In this respect, determining experimentally the variation of the quantities studied here as a function of particle size and Reynolds number should provide important clues on the interaction between turbulent flow and the particle.

This work is part of the International Collaboration for Turbulence Research. We thank Aurore Naso for many fruitful discussions. This work was supported by ANR-07-BLAN-0155 and by PPF "Particules en Turbulence" from the Université de Lyon.

[1] R. Gatignol, J. Mec. Theor. Appl. **2**, 143 (1983).
[2] M. R. Maxey and J. J. Riley, Phys. Fluids **26**, 883 (1983).
[3] S. Elghobashi and G. C. Truesdell, J. Fluid Mech. **242**, 655 (1992).
[4] *Handbook of Experimental Fluid Dynamics* (Springer, New York, 2007).
[5] N. M. Qureshi *et al.*, Phys. Rev. Lett. **99**, 184502 (2007).
[6] G. A. Voth *et al.*, J. Fluid Mech. **469**, 121 (2002).
[7] N. M. Qureshi *et al.*, Eur. Phys. J. B **66**, 531 (2008).
[8] R. D. Brown, Z. Warhaft, and G. A. Voth, Phys. Rev. Lett. **103**, 194501 (2009).
[9] R. Volk *et al.*, J. Fluid Mech. **668**, 223 (2011).
[10] T. R. Auton, J. C. R. Hunt, and M. Prud'homme, J. Fluid Mech. **197**, 241 (1988).
[11] E. Loth and A. J. Dorgan, Environ. Fluid Mech. **9**, 187 (2009).
[12] J. Ye and M. Roco, Phys. Fluids A **4**, 220 (1992).
[13] E. A. van Nierop *et al.*, J. Fluid Mech. **571**, 439 (2007).
[14] M. Rastello *et al.*, J. Fluid Mech. **624**, 159 (2009).
[15] Y. Gasteuil, Ph.D. thesis, ENS Lyon, 2009.
[16] R. Zimmermann *et al.*, Rev. Sci. Instrum. **82**, 033906 (2011).
[17] R. Monchaux *et al.*, Phys. Rev. Lett. **96**, 124502 (2006).
[18] N. T. Ouellette *et al.*, New J. Phys. **8**, 109 (2006).
[19] N. Mordant, A. M. Crawford, and E. Bodenschatz, Physica (Amsterdam) **193D**, 245 (2004).
[20] H. Homann and J. Bec, J. Fluid Mech. **651**, 81 (2010).
[21] E. Achenbach, J. Fluid Mech. **54**, 565 (1972).
[22] A. Naso and A. Prosperetti, New J. Phys. **12**, 033040 (2010).
[23] M. Gibert and E. Bodenschatz (private communication).
[24] F. Lucci, A. Ferrante, and S. Elghobashi, J. Fluid Mech. **650**, 5 (2010).

A.4 Mesures de l'accélération lagrangienne par particules instrumentées

[A 10] Robert Zimmermann, Lionel Fiabane, Yoann Gasteuil, and Romain Volk. Characterizing flows with an instrumented particle measuring lagrangian accelerations. *arXiv : 1208.2809v1*, pages 1–13, (2012).

[A 11] R Zimmermann, L Fiabane, Y Gasteuil, and R Volk. Measuring Lagrangian accelerations using an instrumented particle. *arXiv :1206.1617v1*, pages 1–8, (2012).

Measuring Lagrangian accelerations using an instrumented particle

R. Zimmermann,[1] L. Fiabane,[1] Y. Gasteuil,[2] R. Volk,[1] and J.-F. Pinton[1]

[1] *Laboratoire de Physique, ENS de Lyon, UMR CNRS 5672, Université de Lyon, France*[*]
[2] *smartINST S.A.S., 46 allée d'Italie, 69007 Lyon, France*

(Dated: October 9, 2012)

Accessing and characterizing a flow impose a number of constraints on the employed measurement techniques; in particular optical methods require transparent fluids and windows in the vessel. Whereas one can adapt apparatus, fluid and methods in the lab to these constraints, this is hardly possible for industrial mixers. We present in this article a novel measurement technique which is suitable for opaque or granular flows: an instrumented particle, which continuously transmits the force/acceleration acting on it as it is advected in a flow. Its density is adjustable for a wide range of fluids and because of its small size and its wireless data transmission, the system can be used both in industrial and scientific mixers allowing a better understanding of the flow within. We demonstrate the capabilities and precision of the particle by comparing its transmitted acceleration to alternative measurements, in particular in the case of a turbulent von Kármán flow. Our technique shows to be an efficient and fast tool to characterize flows.

I. INTRODUCTION

Experimental fluid dynamics research in the lab consists of an interplay of suitable flow generation devices, working fluids, measurement techniques and analysis, with goals ranging from fundamental research in statistical / non-linear physics to the optimization of mixers in industrial R&D departments. In this endeavor, very significant progress has been achieved during the last decade with the advent of space and time resolved optical techniques based on high speed imaging [1]. However, direct imaging is not always possible especially in industry: opaque vessels, non-transparent fluids, environmental constraints among other things may be limiting factors. Even if the fluid is transparent, the injection of tracer particles might be still not allowed or unsuitable due to bio-medical or food regulations, or due to the chemical properties of the fluid. While techniques using other kinds of probing waves (*e.g.* acoustics [2]) have been developed, a direct resolution of the Eulerian flow pattern is not always possible. In this context, Lagrangian techniques provide an interesting alternative particularly for problems related to mixing [3, 4].

Lagrangian tracers with a temperature sensitive dependance have been used in the study of Rayleigh-Bénard convection [5], a problem for which our group has developed *instrumented particles* [6–9]. The approach was to instrument a neutrally buoyant particle in such a way that it measures the temperature fluctuations during its motion as it is entrained by the flow, while transmitting the data via radio frequency to a lab operator in real time. Meaningful information regarding the statistics of thermion plumes have been obtained, with excellent agreement with other techniques [5] and direct numerical simulations [10]. In the work reported here, we built upon this approach to instrument the particle such that one gets flow parameters directly from the measurements (in [6], one had to simultaneously film the particle motion). We equip the particle with a 3-axis accelerometer, whose measurements are sampled at a rate equal to 316 Hz and transmitted to the lab operator. This particle is intended for turbulent flows. Thanks to its radio transmission it is suitable for opaque fluids or apparatuses without access for optical measurement techniques. Its continuous operation is also advantageous over Particle Tracking Techniques which have to operate in chunks as the memory of the tracking cameras is necessarily limited. Moreover and in contrast to tracer particles this instrumented particle can be easily re-extracted from the apparatus after the experiment. However, as the particle is advected in a flow it rotates and consequently continuously changes its orientation with respect to the laboratory frame. Thereby the signals of the 3D accelerometer are altered in a non-trivial way, and detailed characterization and methods to extract meaningful information from the acceleration signals are needed. We present here the preliminary results of this characterization.

This article is organized as follows: first, we present the instrumented particle and additional techniques needed for its characterization (section II). In section III, we present an analysis of the results obtained in two different configurations: First, a simple pendulum with the particle attached at the end of a stiff arm, then the particle advected in a fully turbulent flow. In order to verify that the transmitted acceleration is well related

[*] Electronic address: robert.zimmermann@ens-lyon.org

to its motion, we compare the results to simultaneous alternative measurements. Finally, we discuss limitations and perspectives of this new measurement technique (section IV).

II. "SMART PARTICLES"

The apparatus described in the following is designed and built by smartINST S.A.S., a young startup situated on the ENS de Lyon campus. The device consists of a spherical particle (the so-called smartPART) which embarks an autonomous circuit with 3D-acceleration sensor, a coin cell and a wireless transmission system; and a data acquisition center (the so-called smartCENTER), which acquires, decodes, processes and stores the signal of the smartPART (see Fig. 1). The ensemble – smartPART and smartCENTER – measures, displays and stores the three dimensional acceleration vectors acting on the particle as it is advected in the flow. The accelerations are observed in a moving and rotating coordinate system and consist of four contributions: gravity, translation, noise and possibly a weak contribution of the rotation around the center of the particle itself.

A. Design & Technical Details

a. Sensor: The central component of the particle is the ADXL 330 (Analog Device) – a three axis accelerometer. This component belongs to the category of micro-electro-mechanical systems (MEMS). Each of the three axes returns a voltage proportional to the force acting on a small, movably mounted mass-load suspended by micro-fabricated springs. The three axes of the ADXL 330 are decoupled and form an orthogonal coordinate system attached to the chip package. From this construction arises a permanent measurement of the gravitational force/acceleration $\boldsymbol{g} \equiv 9.8\,\mathrm{m/s^2} \cdot \hat{\boldsymbol{e}}_g = g \cdot \hat{\boldsymbol{e}}_g$. Each axis has a guaranteed minimum full-scale range of $\pm 3\,g$; however, we observe a typical range of $\pm 3.6\,g = 35\,\mathrm{m/s^2}$ per axis. The sensor has to be calibrated to compute the physical accelerations from the voltages of the accelerometer.

b. smartPART: The signals from the ADXL 330 are first-order low-pass filtered at $f_c = 160\,\mathrm{Hz}$ and then digitized at 12 bits and 316 Hz sampling rate. A multiplexer prior the signal digitization induces a small time shift between the components of 0.64 ms. The output is then reshaped into small packets and send via radio frequency. The ensemble is powered by a coin cell. A voltage regulator ensures a stable supply voltage and thus a constant quality of the measurement. A Hall switch allows one to power-down most components; thereby, the battery is only used during experiments. Depending on the power needed to transmit the acceleration signals, a particle operates continuously for 6 to 36 hours. The ADXL 330 is soldered to the printed circuit board such that it is situated close to the geometrical center of the particle. The particle itself is spherical with a diameter of 25 mm. The capsule walls are made of Polyether-ether-ketone (PEEK) which is known for its excellent mechanical and chemical robustness. It is leak-proof and its density can be matched to fluids by adding extra weight (namely Tungsten paste) to the particle's interior; within the density range of $0.8 - 1.4\ \mathrm{g/cm^3}$ a relative density match of better than 10^{-4} is achievable. The particle is thus suited for most experiments in water and water-based solutions. It should be noted that the mass distribution inside the particle is neither homogeneous nor isotropic: in particular its center of mass does not coincide with the geometrical center, making it out-of-balance. In practice this results into a pendulum-like motion of the particle in the flow. Nevertheless, the imbalance can be adjusted to some extent by adding patches of Tungsten paste to its interior, and the particles we use are carefully prepared such that they are neutrally buoyant, avoid any pendulum-like behavior and rotate easily in the flow.

c. smartCENTER: The signals from the smartPART are received by an antenna connected to the smartCENTER, which contains radio reception, processing and display units. It demodulates and decodes in real-time the received raw signal into a time-series of raw voltages of the ADXL 330. The physical acceleration sensed by the smartPART $\boldsymbol{a}_{\mathrm{SP}}$ can then be computed:

$$\boldsymbol{a}_{\mathrm{SP}} = \begin{pmatrix} a_1 \\ a_2 \\ a_3 \end{pmatrix} = \begin{pmatrix} (A_1 - O_1)/S_1 \\ (A_2 - O_2)/S_2 \\ (A_3 - O_3)/S_3 \end{pmatrix}, \quad (1)$$

where A_i, O_i and S_i are the measured raw signal, the offset and the sensitivity of each axis, respectively. Offset and sensitivity have to be calibrated beforehand; the procedure is described in the following section. The resulting time-series are saved for further processing.

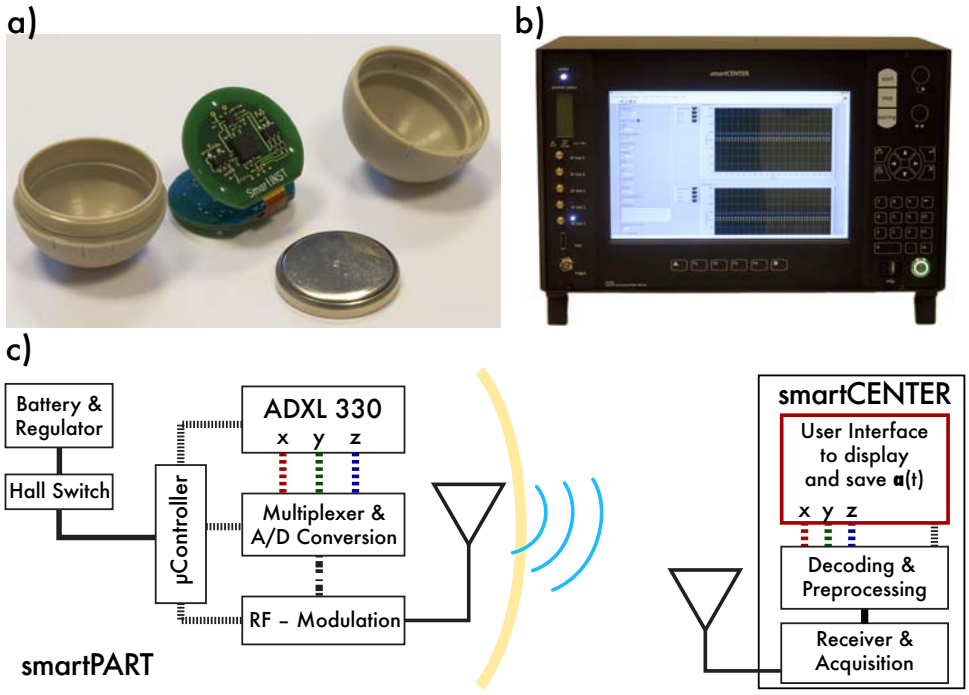

Figure 1: a) and b) : the instrumented particle (*smartPART*) and its data control & acquisition unit (*smartCENTER*). The coin cell is 20mm in diameter. c) The diagram sketches the measurement of the acceleration, its transmission to and the processing by the smartCenter.

B. Calibration and robustness

The offset and sensitivity of the ADXL 330 have to be calibrated to convert the measured voltages into a physical acceleration. The axes of the accelerometer form an orthogonal coordinate system according to Eq. (1). At rest one observes only gravity projected onto the sensor at an arbitrary orientation. The observed raw values define consequently a translated ellipsoid (for simplicity we set $|\boldsymbol{g}| \equiv 1$):

$$\boldsymbol{a}_{\mathrm{SP}} \cdot \boldsymbol{a}_{\mathrm{SP}} = \sum_i \frac{(A_i - O_i)^2}{S_i^2} = \boldsymbol{g}^2 = 1 \,. \qquad (2)$$

Eq. (2) can be arranged to:

$$1 = \sum_i \left(\xi_i \, A_i^2 - 2 \, \xi_{i+3} \, A_i \right) , \qquad (3)$$

with ξ_i six parameters containing offset and sensitivity. A sufficient number of measurements with different orientations define a set of equations which is solved using a linear least squares technique. Offset and sensitivity are then

$$O_i = \frac{\xi_{3+i}}{\xi_i} \quad \text{and} \quad S_i = \sqrt{\frac{1 + \sum_i \left(\xi_{3+i}^2 / \xi_i \right)}{\xi_i}} \,. \qquad (4)$$

We find that the particle at rest has an average noise of $\sigma_x = \sigma_y = 0.006\,g$ and $\sigma_z = 0.008\,g$, giving $|\boldsymbol{\sigma}| = \sqrt{\sum_i \sigma_i^2} = 0.012\,g$, where g is the magnitude of gravity. An analysis using the residuals showed a slightly higher resolution of $\sigma_x = \sigma_y = 0.005\,g$ and $\sigma_z = 0.003\,g$, and $|\boldsymbol{\sigma}| = 0.008\,g$. These values are thus the absolute errors of our measurement.

The ADXL 300 has among other things been chosen for its weak temperature dependance: its offset typically varies by $10^{-3}\,g/°\mathrm{C}$, and its sensitivity by $0.015\,\%/°\mathrm{C}$. Digitizing and transmission unit were verified to be temperature independent. Consequently, the total temperature dependence of the smartPART is given by its accelerometer. For high precision measurements, it is advised to calibrate the particle at experiment temperature shortly before the actual experiment.

We noticed a small drift of the order of $0.005\,g/\mathrm{h}$ for the $z-$axis. No drift was observed for the $x-$ and $y-$axes. Since a voltage regulator ensures a stable supply voltage of the circuit, this drift stems most likely from the internal construction of the accelerometer. Owing to the continuous data transmission of the instrumented particle, one flow configuration can be characterized in approximately 30 minutes. Hence, the little drift of the $z-$axis can be neglected.

Considering the mechanical robustness, the smartPART survived several days in a von Kár-

mán mixer and neither contacts with the wall nor with the sharp edged blades of the fast rotating propellers damaged its function or shell.

III. ACCELERATION SIGNALS

As mentioned previously, the smartPART transmits in real-time the accelerations acting on the particle as it is advected in the flow. The noise-to-signal ratio being small, we neglect the noise from here on. The contributions consist therefore of: gravity, translation, and rotation of the particle. We now test the accuracy of the particle signals in two different experimental configurations by comparison with alternative measurements.

A. 2D pendulum

A pendulum is a simple and well-known case, ideal to measure the resolution of the particle. A stiff pendulum with 60 cm long stiff arm is equipped with a position sensor returning the deflection angle φ of the arm. The particle is fixed at known length, l, with a known arbitrary orientation to the arm. The fact that a rotation of the particle around its center is restricted, implies that the contribution from the rotation of the particle around is center is known. Measuring $\boldsymbol{a}_{\mathrm{SP}}$ at rest ($\varphi = 0°$) and at several arbitrary positions one can determine the axis of rotation of the arm. Once this vector is known the measured acceleration signal is rotated/re-expressed such that a_y points with the arm, a_x with the movement, and a_z with the axis of rotation. Note that by definition the latter does not change when the pendulum moves. The signal seen by the particle is a two-dimensional problem and fully described as a function of the deflection angle φ:

$$\begin{aligned} a_x(\varphi) &= g\,\sin\varphi + l\,\ddot{\varphi}\,, \\ a_y(\varphi) &= g\,\cos\varphi + l\,\dot{\varphi}^2\,. \end{aligned} \tag{5}$$

In the limit of the small angle approximation, this simplifies to the well-known oscillations of frequency ω:

$$\begin{aligned} a_x(\varphi) &\approx -l\omega^2\,\sin\omega t\,, \\ a_y(\varphi) &\approx g + \frac{l\,\omega^2}{2}(1+\cos 2\omega t)\,. \end{aligned} \tag{6}$$

The simultaneous measurement of the angle, $\varphi(t)$, and the particle's signal, $\boldsymbol{a}_{\mathrm{SP}}(t)$, enables us to compare the two signals without any other approximation or fit than Eq. (5).

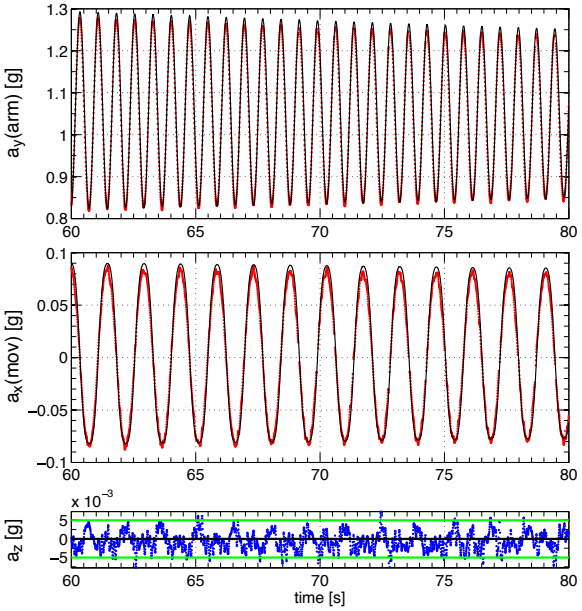

Figure 2: Comparison of the particle's signal $\boldsymbol{a}_{\mathrm{SP}}(t)$ (•) to the theoretical curves based on the position sensor (—). a_y points with the arm and a_x measures the force in direction of the movement. No force is exerted along the $z-$axis (the green lines represent the uncertainty of the calibration). Note, that acceleration is measured in $g = 9.8\,\mathrm{m/s^2}$.

Fig. 2 shows $\boldsymbol{a}_{\mathrm{SP}}(t)$ for several periods of the pendulum, measured by the smartPART and by the position sensor. The agreement between the two signals is very good, and in particular better than the uncertainty of the calibration. Hence, the Lagrangian acceleration of the smartPART corresponds well to its actual motion in this simple case. We now move on to more complicated motions.

B. Fully developed (3D) turbulence

The instrumented particle is intended for the characterization of complex/turbulent flows. Such flows exhibit strong, intermittent variations in the acceleration. To verify the suitability of the smartPART for these conditions, we now investigate its motion in a fully turbulent mixer while tracking it with an independent optical technique.

Namely, we use a von Kármán water flow: a swirling flow is created in a square tank by two opposing counter-rotating impellers of radius $R = 9.5\,\mathrm{cm}$ fitted with straight blades 1 cm in height. The flow domain in between the impellers has characteristic length $H = 20\,\mathrm{cm} \cong 2R$ (see Fig. 3) and the vessel is built with transparent flat side walls, allowing direct optical measurements over almost the whole flow domain. Blades on the impellers

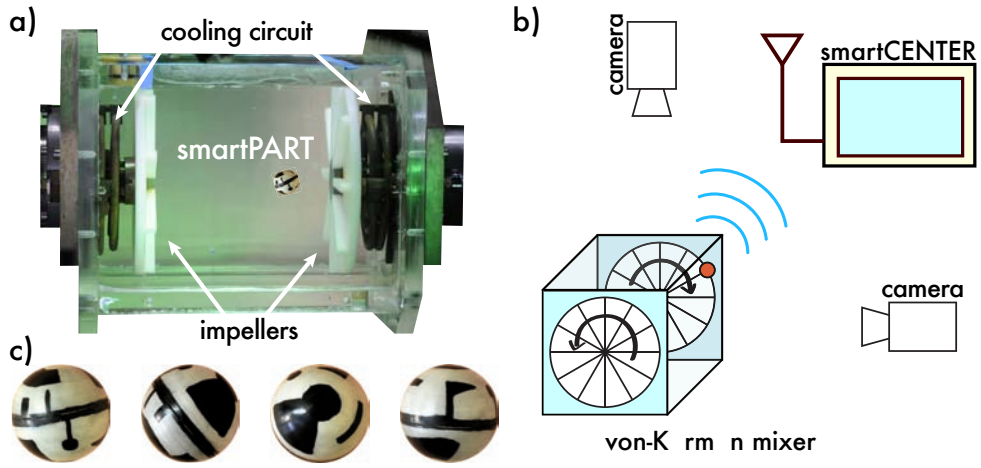

Figure 3: Experimental setup: a) picture of the apparatus; b) sketch of the arrangement; c) a textured instrumented particle at different orientations.

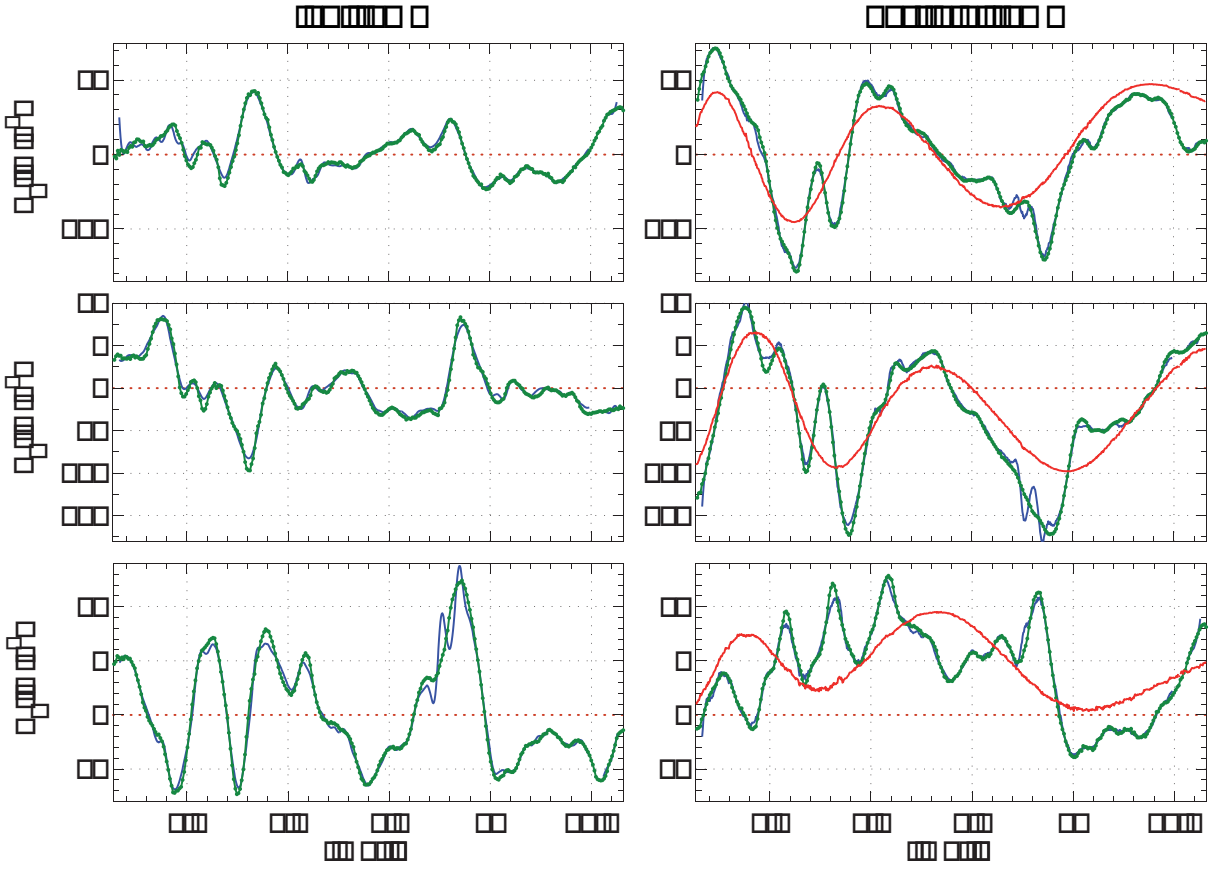

Figure 4: A sample trajectory of the instrumented particle seen by the camera (—) or smartPART (•), it is $f_{\text{prop}} = 3\,\text{Hz}$. The absolute orientation enables us to re-express the camera measurement of the particle (lab frame) in the moving frame of the particle and vice-versa. In the former gravity is subtracted and in the particle frame gravity is represented by the red line.

work similar to a centrifugal pump and add a poloidal circulation at each impeller. For counter-rotating impellers, this type of flow is known to exhibit fully developed turbulence [11]. Within a small region in the center the mean flow is little and the local characteristics approximate homogeneous turbulence. However, at a large scale it is known to have a large scale anisotropy [12, 13]. At a propeller frequency of 3 Hz we estimate a Reynolds number based on the Taylor micro-scale of $R_\lambda = 500 \pm 50$.

We optically track the translation and absolute orientation of the smartPART while simultaneously acquiring the transmitted acceleration time-series. These optical measurements are then used as a reference to compare with the instrumented particle's signals. The six-dimensional tracking technique (or 6D tracking, 3 components for the translation and 3 components for the rotation of the particle around its center) is explained in detail in [14, 15] and briefly sketched here (Fig. 3). In order to determine the absolute orientation the particle is textured by hand using black-ink permanent marker (see Fig. 3c). Acceleration sensor and texture are then calibrated/retrieved independently; nevertheless, the accelerometer is at a fixed but unknown orientation with respect to this texture, *i.e.* sensor and texture are related by a constant rotation matrix. We determine this matrix by acquiring the acceleration signals of the particle at arbitrary orientations while additionally determining its orientation and the location of gravity on the texture. The particle is then inserted into the apparatus, which is illuminated by high power LEDs. Its motion is tracked by two high-speed video cameras (Phantom V12, Vision Research) which record synchronously two views at approximately 90 degrees. The observation volume is $15 \times 15 \times 15$ [cm^3] in size and resolved at a resolution of 4.2 pixel/mm. In our configuration, a camera can store on the order of 14 000 frames in on-board memory, thus limiting the duration of continuous tracks. Therefore, a computer issues the recording of 8 bit gray-scale movies at a sufficiently high frame rate while controlling the smartCENTER such that acceleration signal and images are synchronized. After extracting the time-series of the particle's position and orientation, one can then compare the accelerometer's signal to the motion of the particle.

It should be stressed that the two measurement techniques observe the motion of the instrumented particle in two completely different reference frames. On the one hand, the 6D tracking uses a fixed, non-rotating coordinate system, and is referred to as the lab frame. On the other hand, as the particle is advected and turned in the flow, it and consequently the embarked accelerometer constantly rotate their coordinate system with respect to the lab frame; the acceleration signal is thus measured in a frame which is continuously rotating and not fixed. This frame is referred to as the particle frame. The acceleration sensor measures the forces acting on it as it moves in the flow. Knowing the absolute orientation of the particle at each instant we can express the signal of the smartPART in the lab frame by rotating it such that it corresponds to a non-rotating particle. Starting from the time-series of position and orientation, it is also possible to compute the linear, centrifugal and gravitational acceleration/force acting on a point inside the particle and then project these into the rotating particle frame. The different components are then expressed in the frame of the sensor.

Fig. 4 shows a sample trajectory in both coordinate systems. The agreement between the two techniques is remarkable. Furthermore, one observes that the projection of gravity is continuously changing: the particle is rotating in a non-trivial way. Deviations between the two techniques stem from several experimental errors. First, the position measurement: bubbles, reflections and other impurities alter the measured position of the particle. The acceleration is the second derivate and thus highly sensitive to such events. Second, the orientation measurement: the absolute orientation is needed to change between the reference frames. The uncertainty in the absolute orientation is typically 3°; that results in a wrong projection of gravity of $\pm 0.5\,\mathrm{m/s^2}$. It further biases the rotational forces, as they are derivatives of the orientation time-series. Finally, the matrix relating sensor and texture: this matrix is constant and thus a systematic contribution. The uncertainty is less than 2° – *i.e.* the error in projecting gravity is $< 0.3\,\mathrm{m/s^2}$. The observed agreement in the lab frame, $\Delta\boldsymbol{a} = \boldsymbol{a}_{\mathrm{SP}} - \boldsymbol{a}_{\mathrm{6D}}$, between the two techniques is as follows: all three components of $\Delta\boldsymbol{a}$ have the same PDF. Surprisingly, the (absolute) uncertainty almost doubles by increasing f_{prop} from 2 Hz to 3 Hz. Nevertheless, for 80% of the data the agreement is better than $0.8\,\mathrm{m/s^2}$ and $1.6\,\mathrm{m/s^2}$, respectively. For comparison, the absolute value $|\boldsymbol{a}_{\mathrm{6D}}|$ has a mean of $2.9\,\mathrm{m/s^2}$ and $6.6\,\mathrm{m/s^2}$ and a standard deviation of $1.8\,\mathrm{m/s^2}$ and $4.1\,\mathrm{m/s^2}$, respectively. The signal of the particle is thus corresponding to the flow, however, its interpretation is not simple. In particular, and after comparing many different trajectories, it becomes clear that no easy transformation is available to get rid of the rotation of the particle.

By construction the center of the accelerometer is placed at $\boldsymbol{r} = 3\,\mathrm{mm} \cdot \hat{\boldsymbol{e}}_z$. A rotation of the particle around its geometric center will thus add a

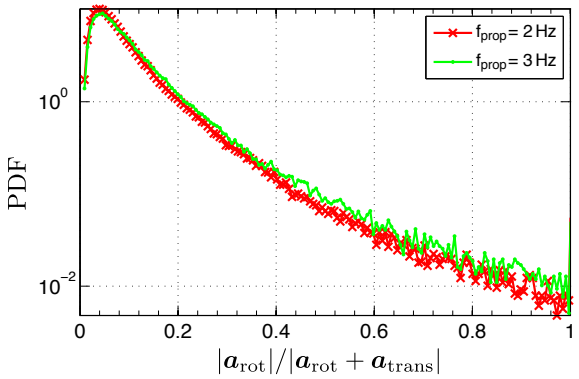

Figure 5: Ratio of the rotational forces to the total force acting on the particle. The 80% percentile is found at a ratio of 0.14 and 0.16, respectively.

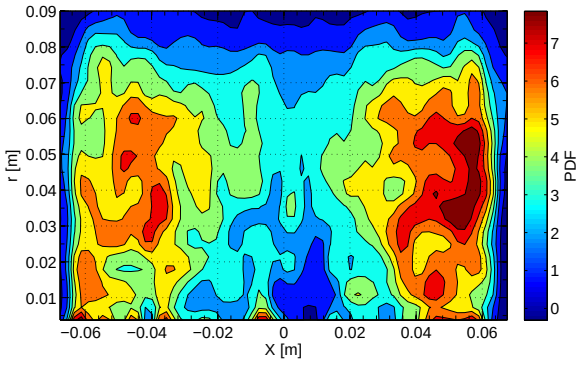

Figure 6: Preferred position of the instrumented particle: independent of the propeller speed it is mostly situated in a torus shape around the propeller.

centrifugal contribution to the measured acceleration. This rises the question which term – translation or rotation of the particle – dominates the acceleration signal. To address this question we take advantage of the 6D-tracking, which enables us to compute the different forces acting on a point at $\boldsymbol{r} = 3\,\mathrm{mm} \cdot \hat{\boldsymbol{e}}_z$ inside the sphere. We can thus compare the contribution of the translation and that of the rotation of the particle. Fig. 5 shows the ratio of the rotational (*i.e.* centrifugal) acceleration, $\boldsymbol{a}_{\mathrm{rot}} = \boldsymbol{\omega} \times \boldsymbol{\omega} \times \boldsymbol{r} + \frac{\mathrm{d}\boldsymbol{\omega}}{\mathrm{d}t} \times \boldsymbol{r}$ to the total acceleration, $\boldsymbol{a}_{\mathrm{trans}} + \boldsymbol{a}_{\mathrm{rot}}$, (without gravity). Dimensional arguments tell that $a_{\mathrm{trans}} \propto f_{\mathrm{prop}}^2$ and $a_{\mathrm{rot}} \propto f_{\mathrm{prop}}^2$. Consistently, the PDF of the ratio $|\boldsymbol{a}_{\mathrm{rot}}|/|\boldsymbol{a}_{\mathrm{trans}} + \boldsymbol{a}_{\mathrm{rot}}|$ differs only little for the two propeller frequencies. Moreover, it is peaked at 5% and the 80% percentile is at a ratio of 14% and 16%, respectively. Hence, it is legitimate to neglect the rotational forces if no 6D tracking is available.

IV. DISCUSSION

In the latter part of this article we studied the behavior of a large neutrally buoyant sphere in a turbulent flow. Comparing with solid spheres of the same size in the same mixer, we find that the particle in general behaves almost identically [16]. In particular (and despite the fact that the instrumented particle is neutrally buoyant) we observe that it generally stays in a region close to the impellers. Fig. 6 shows the PDF of position for the smartPART. Independent of the impeller speed it is mostly situated in a torus shape around the propeller, exhibiting a preferential sampling of the flow for these large neutrally buoyant spheres.

Moreover, since we investigate large particles with a size D_{part} comparable to the integral length scale, L_{int}, moving through the whole mixer, the Kolmogorov assumptions to characterize turbulence are no longer valid. For these reasons, the smartPART can be insufficient to access all details of a turbulent flow: some parts of the flow are little explored, and some scales of the turbulence might be filtered due to the size of the instrumented particle. However, one should bear in mind that these features of the flow are often accessed by means of optical methods whereas the instrumented particle operates also in environments and fluids which are unsuitable for optical measurement techniques.

Some other experimental constraints should be additionally stressed here. As previously said, the mass distribution inside the particle is neither homogeneous nor isotropic. It is therefore possible that the particle is out-of-balance, *i.e.* that the center of mass does not coincide with the geometrical center. Such a particle has a strong preferred orientation and wobbles similar to a kicked physical pendulum. The imbalance can be adjusted to some extent by adding weight to its interior, but the particle must be prepared very carefully and one must make sure that the particle used is well-balanced and rotates easily in the flow.

Also, the receiver/demodulation unit of the smartCENTER works best within a range of radio power, *i.e.* particles which are emitting either too strong or too weak are undesirable and one has to adjust the radio emission of the smartPART. A stronger radio emission power can be required, *e.g.* if the apparatus builds a Faraday cage (*i.e.* an electrically-connected metal structure surrounds the flow), or if the signal has to pass a longer distance in more water or in a bigger apparatus. Solutions with a high conductivity are also likely to damp the radio signal. Naturally, a stronger radio emission shortens the life time of the battery. Nevertheless, particles with stronger radio emission still

last 6 to 12 hours, which is sufficient in most cases.

To conclude, we presented the working principle of an instrumented particle giving a measure of the three components of the Lagrangian acceleration. We were able to show that the Lagrangian acceleration of the smartPART corresponds well to its actual translation and is not biased by a possible rotation of the particle around its center. Work on extracting detailed information on the flow from the acceleration time-series is ongoing. This instrumented particles can shed some light into mixers which were not or hardly accessible up to now. Due to its continuous transmission one flow configuration can be characterized within $\sim$ 30 min. Apart from its appeal for chemical and pharmaceutical industry, it might be an interesting tool to quantify flows in labs.

Acknowledgments

This work was partially supported by ANR-07-BLAN-0155. The authors want to acknowledge the technical help of Marius Tanase and Arnaud Rabilloud for the electronics, and of all the ENS machine shop. The authors also thank Michel Voßkuhle, Mickaël Bourgoin and Alain Pumir for fruitful discussions. Finally, R. Zimmermann warmly thanks the TMB-2011 committee for assigning the "Young Scientist Award" of the Turbulence Mixing & Beyond 2011 conference for the work he presented within this article.

[1] C. Tropea, A. Yarin, and J. F. Foss, eds., *Springer Handbook of Experimental Fluid Dynamics* (Springer-Verlag Berlin-Heidelberg, 2007).
[2] N. Mordant, P. Metz, O. Michel, and J.-F. Pinton, Physical Review Letters **87**, 214501 (2001).
[3] F. Toschi and E. Bodenschatz, Annual Review of Fluid Mechanics **41**, 375 (2009).
[4] B. Shraiman and E. Siggia, Nature **405**, 639 (2000).
[5] R. Ni, S.-D. Huang, and K.-Q. Xia, Journal of Fluid Mechanics **692**, 395 (2012).
[6] Y. Gasteuil, W. L. Shew, M. Gibert, F. Chillà, B. Castaing, and J.-F. Pinton, Physical Review Letters **99**, 234302 (2007).
[7] Y. Gasteuil, Ph.D. thesis, École Normale Supérieure de Lyon (2009).
[8] W. L. Shew, Y. Gasteuil, M. Gibert, P. Metz, and J.-F. Pinton, Review of Scientific Instruments **78**, 065105 (2007).
[9] J.-F. Pinton, P. Metz, Y. Gasteuil, and W. L. Shew, *Mixer, and device and method for monitoring or controlling said mixer*, Patent US 2011/0004344 A1 (2009).
[10] J. Schumacher, Physical Review E **79**, 056301 (2009).
[11] F. Ravelet, A. Chiffaudel, and F. Daviaud, Journal of Fluid Mechanics **601**, 339 (2008).
[12] N. T. Ouellette, H. Xu, M. Bourgoin, and E. Bodenschatz, New Journal of Physics **8**, 102 (2006).
[13] R. Monchaux, F. Ravelet, B. Dubrulle, A. Chiffaudel, and F. Daviaud, Physical Review Letters **96**, 124502 (2006).
[14] R. Zimmermann, Y. Gasteuil, M. Bourgoin, R. Volk, A. Pumir, and J.-F. Pinton, Review of Scientific Instruments **82**, 033906 (2011).
[15] R. Zimmermann, Y. Gasteuil, M. Bourgoin, R. Volk, A. Pumir, and J.-F. Pinton, Physical Review Letters **106**, 154501 (2011).
[16] R. Zimmermann, Ph.D. thesis, École Normale Supérieure de Lyon (2012).

Characterizing flows with an instrumented particle measuring Lagrangian accelerations

Robert Zimmermann,[1] Lionel Fiabane,[1] Yoann Gasteuil,[2] Romain Volk,[1] and Jean-François Pinton[1]

[1]*Laboratoire de Physique, CNRS UMR 5672, Ecole Normale Supérieure de Lyon, 46 allée d'Italie, F-69007 Lyon, France**

[2]*smartINST S.A.S., 46 allée d'Italie, F-69007 Lyon, France*

(Dated: August 15, 2012)

We present in this article a novel Lagrangian measurement technique: an instrumented particle which continuously transmits the force/acceleration acting on it as it is advected in a flow. We develop signal processing methods to extract information on the flow from the acceleration signal transmitted by the particle. Notably, we are able to characterize the force acting on the particle and to identify the presence of a permanent large-scale vortex structure. Our technique provides a fast, robust and efficient tool to characterize flows, and it is particularly suited to obtain Lagrangian statistics along long trajectories or in cases where optical measurement techniques are not or hardly applicable.

Turbulence is omnipresent in nature and in industry, and has received much attention for years. In the specific field of experimental fluid dynamics research, very significant progress has been achieved during the last decade with the advent of space and time resolved optical techniques based on high speed imaging [1]. However, a direct resolution of the Eulerian flow pattern is still not always possible nor simple to carry out. In this context, Lagrangian techniques, in which the fields are monitored along the trajectories of particles, provide an interesting alternative [2, 3] with information about the small scales of turbulence (especially isotropy) and a huge focus on the particle's Lagrangian acceleration that directly reflects the turbulent forces exerted on the particles [4–9].

From an experimental point of view several inconveniences arise. In the Lagrangian frame one would like to collect long trajectories. However, even in confined flows it is difficult to track even just a few particles over a long time using the existing methods. For instance to use optical methods, the flow must be entirely observed and continuously recorded, something which is not yet possible. Apart from its implication for computing converged statistical quantities, several theories such as the fluctuation theorem necessitate long trajectories instead of many short ones. Another issue is the possible rotation of large particles in a flow, and the influence of this possible rotation on the dynamics of the particle. An optical technique following simultaneously particle position and absolute orientation in time has been recently developed [10]. It shows in particular that for increasing turbulence, solid particles experience stronger rotation [11, 12]. The technique used in those experiments is not straightforward and needs careful calibration and synchronization, as well as an expensive set-up (high-speed cameras, strong illumination, etc) as well as time-consuming post-processing. Other common Lagrangian techniques, *e.g.* particle tracking velocimetry (PTV), generally do not allow a direct measurement of the possible rotation of the particle simultaneously with its translation.

The experimental technique presented here was designed to overcome these issues thanks to the design of *instrumented particles* [13–16]. This was initially developed by our group to study Lagrangian particles with a temperature sensitive dependance, there used in Rayleigh-Bénard convection [17]. The approach is to instrument a neutrally buoyant particle in such a way that it measures the temperature as it is entrained by the flow, and to transmit the data via a radio frequency link to the lab operator. This way, one gains access to trajectories for as long as the particle's battery lifetime. In the work reported here, we built upon this approach to instrument the particle with a 3D accelerometer such that one gets the accelerations – *i.e.* the forces – acting on a spherical particle in real time and for long trajectories. The instrumented particle has been previously tested, benchmarked and validated with the optical technique of Zimmermann *et al.* [18], showing a good agreement between the two different measurements of the acceleration. In the present work we establish methods to extract physical characteristics of the investigated flows from the particle's acceleration signal.

One further motivation is to gain insights into a flow when direct imaging is not possible, *e.g.* when dealing with opaque vessels, non-transparent fluids or granular media. These constraints occur especially in

*Electronic address: robert.zimmermann@ens-lyon.org

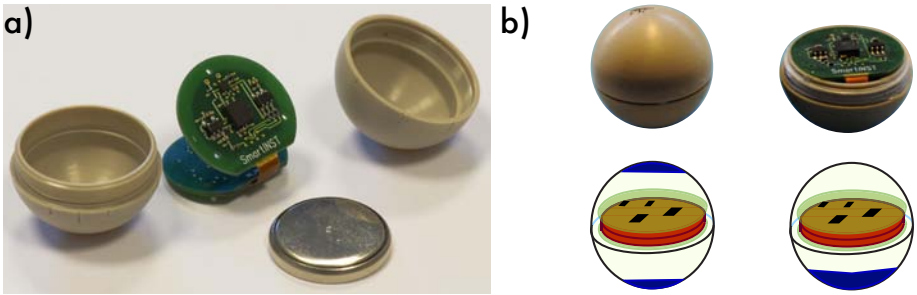

FIG. 1: a) Picture of the instrumented particle (so-called smartPART from smartINST S.A.S.); b) Possible mass distributions of the particle; its inertia consists mainly of a disk and a spherical shell, with different density adjustment and imbalance settings by adding Tungsten paste (in blue); experiments are best done with a symmetrical repartition of the masses.

industry where additional bio-medical or environmental constraints arise (the injection of tracer particles might be unsuitable and thus prevent any visualization technique). As mentioned above solid particles are found to rotate when advected in a highly turbulent flow [12]. We show here that it is possible to build quantities depending or not on the particle's rotation and we conclude about flow parameters that are directly accessible without any optical measurement.

The article is organized as follows: first, we present the experimental setup, as well as a brief reminder of the technical characteristics of the instrumented particle and the forces it measures (section I). Then, we present the new signal processing methods (section II). Finally, we discuss and conclude on this new measurement technique (section III).

I. EXPERIMENTAL SETUP

A. Instrumented particle

The device described in the following is designed and built by smartINST S.A.S., a spin-off from CNRS and the ENS de Lyon. It consists of an instrumented particle (the so-called smartPART ®), a spherical particle which embarks an autonomous circuit with 3D-acceleration sensor, a coin cell and a wireless transmission system, and a data acquisition center (the so-called smartCENTER ®) which receives, decodes, processes and stores the signals from the smartPART (see Fig. 1 and Fig. 2). The smartPART measures the three dimensional acceleration vector $\boldsymbol{a}_{\mathrm{SP}}$ acting on the particle in the flow. It is in good agreement with other techniques, details can be found in Ref. [18]. The accelerometer consists of a micro-electro-mechanical system giving the three components of the acceleration (each of the three decoupled axes returns a voltage proportional to the force acting on a small mass-load suspended by micro-fabricated springs). From this construction arises a permanent measurement of the gravitational force/acceleration $\boldsymbol{g} \equiv 9.8\,\mathrm{m/s^2} \cdot \hat{\boldsymbol{e}}_z = g \cdot \hat{\boldsymbol{e}}_z$. Each axis has a typical full-scale range of $\pm 3.6\,g = 35\,\mathrm{m/s^2}$. The sensor has to be calibrated in order to compute the physical accelerations from the voltages of the accelerometer. The detailed procedure is described in Ref. [18]. Concerning the resolution of the smartPART, the uncertainty on the acceleration norm is $|\boldsymbol{\sigma}| = \sqrt{\sum_i \sigma_i^2} = 0.008\,g$, with an average noise $\sigma_i \leq 0.005\,g$ on each axis.

The particle rotates freely and in an *a priori* unknown way as it is advected by the flow. The instantaneous orientation of the particle can be described by an absolute orientation with respect to a reference coordinate system, $\underline{\underline{\mathbf{R}}}(t)$ [19]. For readability we only write the time reference when necessary (*e.g.* when two different times are involved in an equation) and drop it otherwise. Using this rotation matrix, it is possible to express the contributions to the force acting on the particle and measured by the acceleration sensor in the lab frame or in the particle frame. The following contributions to the particle's acceleration signal $\boldsymbol{a}_{\mathrm{SP}}$ can be identified:

(i) Gravity: By construction, gravity $\boldsymbol{g}$ is always contributing to $\boldsymbol{a}_{\mathrm{SP}}$. Since the particle is *a priori* oriented arbitrarily in space, $\boldsymbol{g}$ is projected onto all 3 axes.

(ii) Translation: The forces acting on the particle are projected as the Lagrangian acceleration $\boldsymbol{a}_{\mathrm{trans}} = \dfrac{\mathrm{d}^2}{\mathrm{d}t^2}\boldsymbol{x}(t)$ onto the sensor.

(iii) Rotation: The particle rotates freely around its geometrical center with an angular velocity $\boldsymbol{\omega}$. If the sensor is placed by $\boldsymbol{r}$ outside the geometrical center of the sphere one observes the centrifugal force: $\boldsymbol{a}_{\mathrm{cf}} = \boldsymbol{\omega} \times (\boldsymbol{\omega} \times \boldsymbol{r}) + \left(\frac{\mathrm{d}}{\mathrm{d}t}\boldsymbol{\omega}\right) \times \boldsymbol{r}$. According to the technical drawings it is $\boldsymbol{r} \approx 3\ \mathrm{mm} \cdot \hat{e}_z$. Experiments on the rotation of the smartPART in a von Kármán flow created by two counter-rotating impellers show that the angular velocity ω of the particle is of the order of the impeller frequency f_{imp} [12, 18]. The rotational forces are of order $r\,\omega^2 \sim r \cdot (4\pi^2\, f_{\mathrm{imp}}^2) \lesssim 0.1\ |\boldsymbol{a}_{\mathrm{trans}}|$ and have consequently negligible effect. A more detailed analysis measured that the ratio between the contribution due to the rotation and the total acceleration is $|\boldsymbol{a}_{\mathrm{cf}}|/|\boldsymbol{a}_{\mathrm{trans}} + \boldsymbol{a}_{\mathrm{cf}}| < 0.1$ [18]. The contribution due to the rotation is thus neglected. It has to be noted that by construction of the accelerometer and because the circuit is fixed within the sphere, there is no contribution of the Coriolis force.

(iv) Noise & spikes: In ideal situations the smartPART has a noise of less than $0.005\,g$ for each axis, which can be handled by a moving average. Wrong detections appear as strong deviations from the signal and are hard to distinguish from high acceleration events due to the turbulent flow or contacts with *e.g.* the impellers. Experiments in different configurations prove the remaining noise to be negligible [18].

Combining the different terms, and neglecting possible noise and the rotational bias yields:

$$\boldsymbol{a}_{\mathrm{SP}} \approx \underline{\underline{\mathbf{R}}} \left[\boldsymbol{g} + \frac{\mathrm{d}^2}{\mathrm{d}t^2}\boldsymbol{x}\right] = \underline{\underline{\mathbf{R}}} \left[\boldsymbol{g} + \boldsymbol{a}_{\mathrm{trans}}\right]. \tag{1}$$

The contributions due to gravity and translation are thus entangled by the continuously changing orientation of the particle. Since gravity is of little interest here, one has to investigate how common quantities such as the mean and the variance (or **rms**) of the acceleration time series as well as auto correlation functions can give information about the particle motion.

Considering robustness, the smartPART is able to continuously transmit data for a few days. During various experiments in a von Kármán flow neither contacts with the wall nor with the sharp edged blades of the fast rotating impellers damaged its function or shell. Furthermore, the sensor has among other things been chosen for its weak temperature dependance; in order to achieve optimal precision of the measurements, we calibrate the particle at experiment temperature shortly before the actual experiment.

Finally, by adding Tungsten paste to the inside of the smartPART the weight of the particle can be adjusted such that the particle is neutrally buoyant in de-ionized water at 20 °C. It should be noted that the mass distribution inside the particle is neither homogeneous nor isotropic. The particle's inertia is best described by a heavy disk of 20 mm diameter (the battery), a spherical shell and patches of Tungsten paste. The paste must, therefore, be added carefully to minimize the imbalance of the particle (see Fig. 1b); otherwise the resulting out-of-balance particle (*i.e.* with the center of mass not coinciding with the geometrical center) induces a strong preferential orientation and wobbles similar to a kicked physical pendulum. For a well balanced particle, which rotates easily in the flow, one of the eigen-axes of inertia then coincides (approximately) with the $z-$axis of the accelerometer. The other two are within the $x - y$ plane due to rotational symmetry.

B. Von Kármán swirling flow

We investigate the motion of the instrumented particle in a fully turbulent flow. Namely, we use a von Kármán swirling flow; in contrast to Ref. [12] the apparatus is here filled with water and develops higher turbulence rates. A swirling flow is created in a square tank by two opposing counter-rotating impellers of radius $R = 9.5\,\mathrm{cm}$ fitted with straight blades 1 cm in height (see Fig. 2). The flow domain in between the impellers has characteristic length $H = 20\,\mathrm{cm} \cong 2R$. Blades on the impellers work similar to a centrifugal pump and add a poloidal circulation at each impeller. For counter-rotating impellers, this type of flow is known to exhibit fully developed turbulence [20]. Within a small region in the center the mean flow is little and the local characteristics approximate homogeneous turbulence. However, at large scales it is known to be anisotropic [21, 22]. Key parameters of the turbulence at different impeller speeds are given in Table I. The two impellers can also be driven co-rotating, creating a highly-turbulent

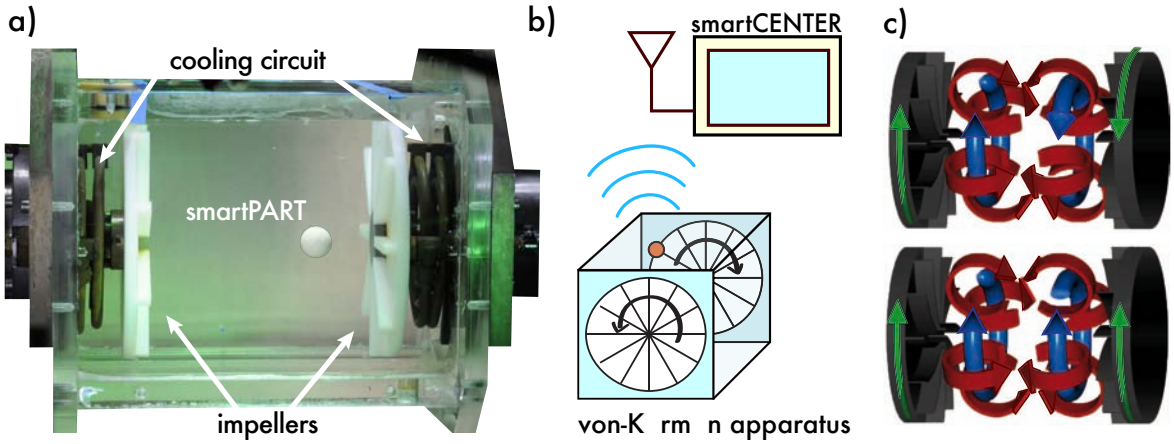

FIG. 2: a) Picture of the von Kármán swirling flow with the instrumented particle inside; b) Sketch of the experimental setup with the apparatus and the smartPART transmitting acceleration signals to the smartCENTER; c) Sketch of the global structures that can be found with the two co- and counter-rotating regimes.

f_{imp}[Hz]	Re	R_λ	ε[m^2/s^3]	η[µm]	τ_η[ms]	T_{int}[s]
1.0	62800	290	0.07	62	3.8	1.00
2.0	125700	410	0.48	38	1.4	0.50
3.0	188500	505	1.68	28	0.8	0.33
4.0	251300	580	4.03	22	0.5	0.25

TABLE I: Key-parameters of the counter-rotating flow configuration. The integral time scale is defined as $T_{\mathrm{int}} = 1/f_{\mathrm{imp}}$ and the integral length scale is estimated to be $L_{\mathrm{int}} = 3$ cm. We use the following definition for the Reynolds numbers: $Re = 2\pi R^2 f_{\mathrm{imp}}/\nu$ and $R_\lambda \approx \sqrt{\frac{15}{\nu} \cdot 2\pi L_{\mathrm{int}}^2 f_{\mathrm{imp}}}$. Note that the particle explores the whole apparatus, where the flow is known to be inhomogeneous and anisotropic. Thus, R_λ and the Kolmogorov scales are only rough estimates. For comparison: co-rotating impellers yield an energy injection rate which is half of the energy injection rate of counter-rotating impellers at the same impeller frequency.

flow inside the vessel with one pronounced persistent global vortex along the axis of rotation. Close to the axis of rotation the mean flow is weak, followed by a strong toroidal component and an additional poloidal circulation induced by blades on the impellers. The energy injection rate is a factor of 2 smaller than for counter-rotating impellers. This means that at the same impeller frequency, f_{imp}, co-rotating driving creates less turbulence than counter-rotation, but the flow is still highly turbulent [23]. Although the vortical structures near the disks are comparable (see Fig. 2c), the co- or counter-rotating regimes yield well distinct global structures in the center of the vessel. The two regimes are used to compare the signals obtained by the instrumented particle in two very different flow configurations. In addition, the co-rotating serves as a test case for persistent, large vortex structures as they are found in mixers with only one impeller.

II. ACCELERATION SIGNALS

Fig. 3 shows two sample time-series of the three components of the acceleration measured by the instrumented particle in the von Kármán flow, superimposed with the norm of the acceleration. Two different frequencies of the impellers are presented here: 1 Hz and 4 Hz. The mean value of the norm fluctuates around $g = 9.8\,\mathrm{m/s^2}$, indicating that gravity is always measured by the accelerometer. Furthermore, the fluctuations of the norm increase with the impeller frequency. It is, however, difficult to compare the three components of the acceleration, either between each other or for different impeller frequencies. This is mainly due to the measurement of the gravity that is randomly projected on the three axes of the accelerometer as the particle rotates in the flow. It results in signals containing both contributions from the gravity and the particle's translation, with no straight-

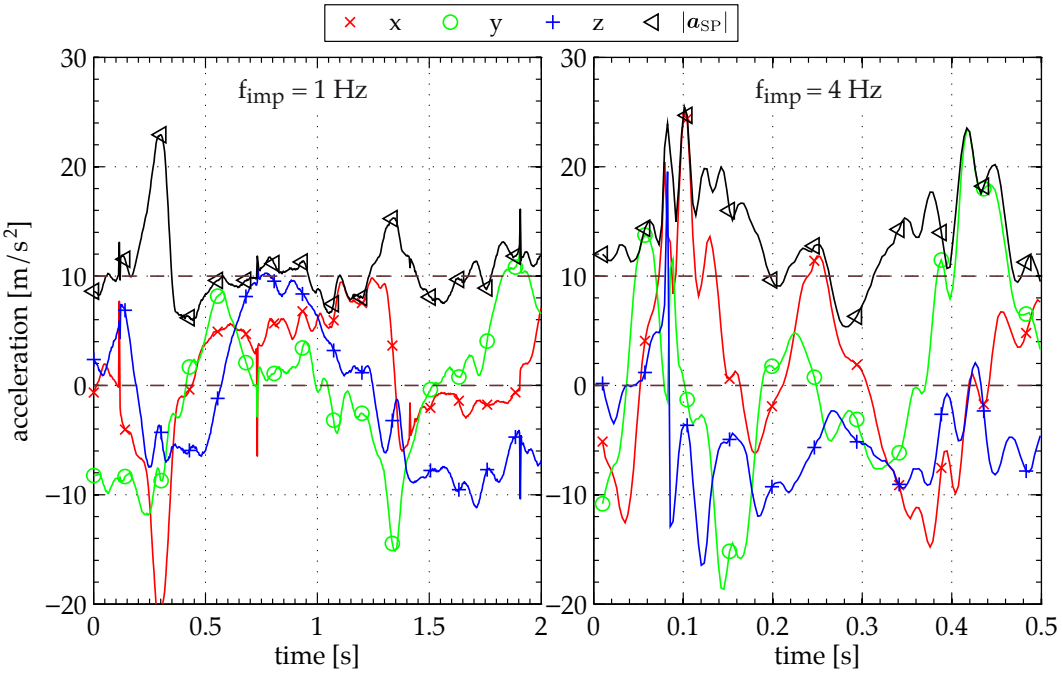

FIG. 3: Sample acceleration time-series, $\boldsymbol{a}_{\mathrm{SP}}(t)$, with the impellers counter-rotating at $f_{\mathrm{imp}} = 1$ Hz (left) and $f_{\mathrm{imp}} = 4$ Hz (right). Both samples last 2 integral times T_{int}.

forward method to separate them. In other words, contrary to other methods (*e.g.* particle tracking velocimetry) it is not possible to obtain directly the characteristics of the particle motion. Hence, one needs to post-process the data to derive information about the statistics and the dynamics of the particle.

A. Analysis of the raw signal a_{SP}

Fig. 4 shows different results of a basic statistical analysis of the acceleration signals, namely the PDFs of the three components and the norm of the acceleration for different impeller frequencies, and the fluctuating and mean values of the acceleration as a function of the impeller frequency. The accelerometer used in the smartPART saturates if one of the acceleration components exceeds $\pm 3.6g$, we exclude these points from the analysis. This removal diminishes the observed acceleration and the bias increases with the forcing. In the case of Fig. 4, almost 3% of all data points were removed at $f_{\mathrm{imp}} = 4$ Hz, which is two orders of magnitude higher than for $f_{\mathrm{imp}} = 1$ Hz. Looking at the PDFs of the acceleration for a given impeller frequency (Fig. 4a), one can see that the three components give similar results for a wide range of acceleration values. However, the PDFs are very different from one frequency to another. Whereas at low impeller frequencies the PDFs are skewed and shifted, they become centered and symmetric with increasing impeller frequency. This evolution in shape can be explained by the particle's mass distribution and imbalance. Although the particle is carefully prepared, its moment of inertia is not that of a solid sphere and the particle's center of mass does not perfectly coincide with its geometrical center. Consequently, the particle becomes slightly out-of-balance, with a preferred orientation at low impeller frequency: the peaks then correspond to the projection of $\boldsymbol{g}$ on the axes in this preferred orientation and fluctuations around it. When the impeller frequency (and consequently the turbulence level) increases, the particle is able to explore all the possible orientations, meaning $\boldsymbol{g}$ is randomly projected in all directions, and the asymmetry disappears. The PDFs of the norm $|\boldsymbol{a}_{\mathrm{SP}}|$ (Fig. 4b) also show this difference in shape, with a clear peak near the value g (again, gravity is always measured by the 3D accelerometer), but with a narrow strong peak at low impeller speed and a more stretched PDF at high impeller speed.

The evolution of the fluctuations of acceleration (**rms** $\boldsymbol{a}_{\mathrm{SP}}$) with the impeller frequency is given in Fig. 4c. Only one component of the acceleration is presented here for readability, since no preferred direction in any of the axes was found. This results in all three components **rms** values having the same

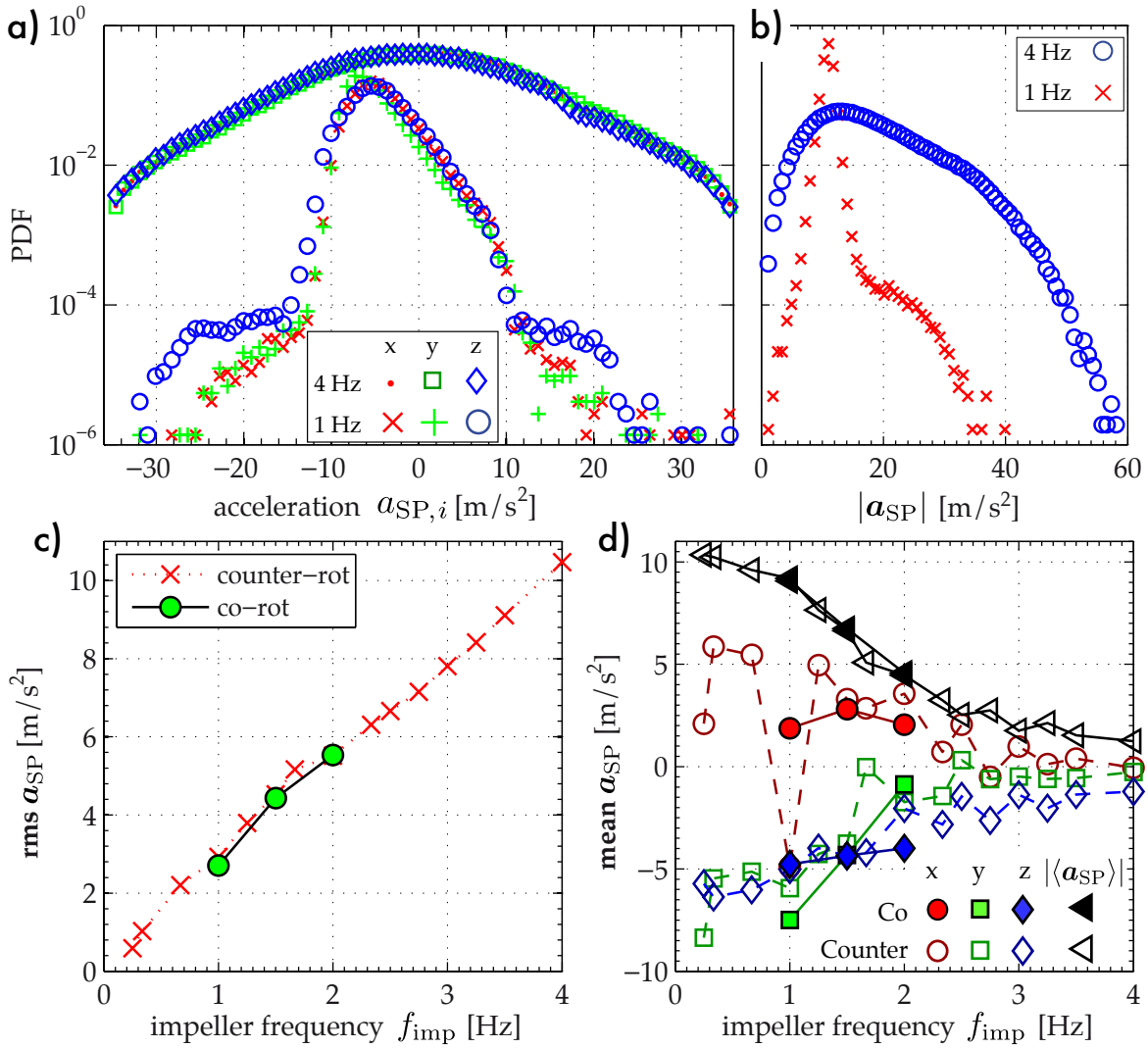

FIG. 4: Top: Probability density functions of a) the components and b) the norm of the acceleration $\boldsymbol{a}_{SP}$ for two different impeller frequencies. For readability, the PDFs of acceleration components at 4 Hz have been arbitrarily shifted. Bottom: Evolution of c) **rms** $\boldsymbol{a}_{SP}$ and d) $\langle\boldsymbol{a}_{SP}\rangle$ with the impeller frequency f_{imp}; filled symbols (○) indicate co-rotating impellers. In all cases the particle explored the flow for a sufficient amount of time for the statistics to converge. In good agreement with Eq. (2), $|\langle\boldsymbol{a}_{SP}\rangle|$ continuously decreases from $1g$ to $0g$ as the impeller frequency increases.

behavior and amplitudes. One can see that surprisingly, the fluctuations of acceleration increase linearly with the frequency. That is in contrast to dimensional arguments that tell $\boldsymbol{a}_{trans} \propto f_{imp}^2$. Moreover, it is not possible to distinguish between the co- and counter-rotating regimes of the impellers.

Fig. 4d shows $\langle\boldsymbol{a}_{SP}\rangle$ as a function of the impeller frequency, f_{imp}, and the forcing. As expected the mean accelerations are becoming smaller with increasing impeller frequency. Indeed taking the average of Eq. (1) yields:

$$\langle\boldsymbol{a}_{SP}\rangle = \langle\underline{\underline{\mathbf{R}}}\,\boldsymbol{g}\rangle + \langle\underline{\underline{\mathbf{R}}}\,\boldsymbol{a}_{trans}\rangle\,. \tag{2}$$

If the particle explores continuously all the possible orientations, the mean vanishes; whereas a fixed orientation (*i.e.* no rotation) yields $\langle\boldsymbol{a}_{SP}\rangle = \underline{\underline{\mathbf{R}}}\,(\boldsymbol{g} + \langle\boldsymbol{a}_{trans}\rangle)$. This is what is observed in Fig. 4. In the case of weak turbulence (*i.e.* for smaller values of f_{imp}), the mean acceleration gives an estimate of gravity: $\langle\boldsymbol{a}_{SP}\rangle \approx \langle\underline{\underline{\mathbf{R}}}\,\boldsymbol{g}\rangle$. However, for stronger turbulence and even if the mass distribution slightly induces a preferred direction, the particle can rotate freely around this axis, resulting in a vanishing mean

acceleration when the impeller frequency increases: $\langle \boldsymbol{a}_{\mathrm{SP}} \rangle \to 0$. In the latter case, contacts with impellers, walls, eddies, etc also help overpowering any preferred direction easily and force the particle to rotate. It can be noted that again, it is not possible to distinguish between the co- and counter-rotating regimes. Furthermore, the variance of a component $a_{\mathrm{SP,i}}$ of $\boldsymbol{a}_{\mathrm{SP}}$ depends strongly on its mean value, $\langle a_{\mathrm{SP,i}} \rangle$. As explained before, gravity renders $\langle a_{\mathrm{SP,i}} \rangle$ non-negligible. Additionally, we observe for weak turbulence levels ($f_{\mathrm{imp}} \lesssim 1$ Hz) that particles are able to stay in an orientation for several seconds. Hence, a global mean of the complete time-series is not a meaningful quantity.

The direct study of the raw acceleration signal, $\boldsymbol{a}_{\mathrm{SP}}$, only allows to conclude whether the particle rotates or not. It does not permit to disentangle the contributions of the gravity and the particle translation, and subsequently to have any precise insight on the flow. Other methods adapted to this problem are thus needed to extract informations from the instrumented particle related to its motion.

B. Moments of the acceleration due to the particle's translation

In confined flows and provided the statistics are converged, it is $\langle \boldsymbol{a}_{\mathrm{trans}} \rangle = 0$. One is, therefore, interested in the PDF of $\boldsymbol{a}_{\mathrm{trans}}$. Although, we mentioned we don't have direct access to $\boldsymbol{a}_{\mathrm{trans}}$ and its PDF, we can compute the even (central) moments of its PDF.

The variance of $\boldsymbol{a}_{\mathrm{SP}}$ is

$$\begin{aligned} \langle \boldsymbol{a}_{\mathrm{SP}}^2 \rangle &= \left\langle |\underline{\underline{\mathbf{R}}}\, \boldsymbol{g}|^2 \right\rangle + \left\langle |\underline{\underline{\mathbf{R}}}\, \boldsymbol{a}_{\mathrm{trans}}|^2 \right\rangle + 2 \langle \underline{\underline{\mathbf{R}}}\, \boldsymbol{g} \cdot \underline{\underline{\mathbf{R}}}\, \boldsymbol{a}_{\mathrm{trans}} \rangle \\ &= g^2 + \langle \boldsymbol{a}_{\mathrm{trans}}^2 \rangle + 2\, g\, \langle a_z \rangle \,, \end{aligned} \tag{3}$$

where $a_z \equiv \hat{\boldsymbol{e}}_z \cdot \boldsymbol{a}_{\mathrm{trans}}$. It should be kept in mind, that each axis of the smartPART's accelerometer is limited to $\pm 3.6\, g$, and possible events of higher acceleration are therefore not included in the analysis. The PDF of $|\boldsymbol{a}_{\mathrm{SP}}|^2$ for different impeller frequencies is shown in Fig. 5a. As expected, a peak is clearly observed at g^2. One can also see that there are breaks in the slope at $|\boldsymbol{a}_{\mathrm{SP}}|^2 \approx (3.6\, g)^2$ and $|\boldsymbol{a}_{\mathrm{SP}}|^2 \approx 2\,(3.6\, g)^2$, corresponding to cases where one or two axes would saturate. Some information is inevitably lost, and to investigate the behavior at large f_{imp}, the sensor would have to be replaced with a different model supporting higher accelerations.

If the particle is neutrally buoyant and the flow is confined, one expects $\langle a_z \rangle = 0$. We therefore obtain an estimate of the standard deviation (**rms**) of $\boldsymbol{a}_{\mathrm{trans}}$:

$$a_{\mathrm{rms}} \equiv \sqrt{\langle \boldsymbol{a}_{\mathrm{trans}}^2 \rangle} = \sqrt{\langle \boldsymbol{a}_{\mathrm{SP}}^2 \rangle - g^2}. \tag{4}$$

a_{rms} is independent of how gravity is projected on the axes of the accelerometer (in other words it is insensitive to the particle's absolute orientation). Nevertheless, a bad calibration (*e.g.* caused by longterm drift or strong temperature change) can introduce a systematic offset to a_{rms}. Nevertheless, this bias can be minimized by calibrating the thermalized smartPART before the actual experiment. Fig. 5b depicts the evolution of a_{rms} with the impeller frequency. In agreement with dimensional analysis, $a_{\mathrm{rms}}\,(f_{\mathrm{imp}})$ describes a parabola, although one could also argue that a_{rms} seems linear with f_{imp} for $f_{\mathrm{imp}} \geq 3\,\mathrm{Hz}$. As illustrated in Fig. 5a, this is caused by saturation of the accelerometer, which cuts off/underestimates high acceleration events present at these high turbulence level.

Similarly to the variance, one can estimate the fourth central moment of $\boldsymbol{a}_{\mathrm{trans}}$. It is

$$\begin{aligned} \left\langle\, |\boldsymbol{a}_{\mathrm{SP}}|^4 \,\right\rangle &= \left\langle \left[g^2 + \boldsymbol{a}_{\mathrm{trans}}^2 + 2\, g\, a_z \right] \left[g^2 + \boldsymbol{a}_{\mathrm{trans}}^2 + 2\, g\, a_z \right] \right\rangle \\ &= g^4 + \left\langle\, |\boldsymbol{a}_{\mathrm{trans}}|^4 \,\right\rangle + 2\, g^2 \left\langle \boldsymbol{a}_{\mathrm{trans}}^2 \right\rangle + 4\, g^2 \left\langle a_z^2 \right\rangle + 4\, g^3 \langle a_z \rangle + 4\, g \left\langle |\boldsymbol{a}_{\mathrm{trans}}|^2\, a_z \right\rangle . \end{aligned} \tag{5}$$

Assuming no preferred direction in $\boldsymbol{a}_{\mathrm{trans}}$, as found for small particles in a windtunnel [4] and verified for solid particles of size comparable to the integral length scale in the same apparatus [11], one has $4g^2 \left\langle a_z^2 \right\rangle \approx 4/3\, g^2\, \boldsymbol{a}_{\mathrm{trans}}^2$. Again, the terms $\langle a_z \rangle$, $4\, g^3 \langle a_z \rangle$ and $4g \left\langle\, |\boldsymbol{a}_{\mathrm{trans}}|^2\, a_z \right\rangle$ are expected to vanish in the case of confined flows. Eq. (5) then simplifies to

$$\left\langle\, |\boldsymbol{a}_{\mathrm{SP}}|^4 \,\right\rangle \approx g^4 + \left\langle\, |\boldsymbol{a}_{\mathrm{trans}}|^4 \,\right\rangle + \frac{10}{3} g^2 a_{\mathrm{rms}}^2. \tag{6}$$

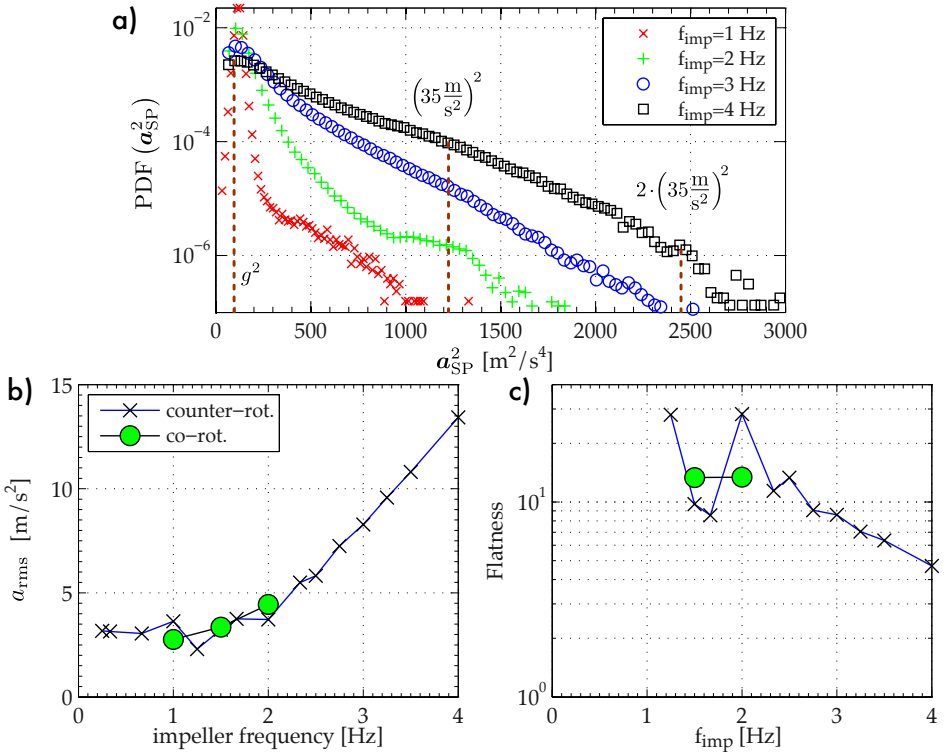

FIG. 5: Moments of $\boldsymbol{a}_{\mathrm{trans}}$. a) PDF $\left(\boldsymbol{a}_{\mathrm{SP}}^2\right)$ at different impeller frequencies. The 3 vertical lines mark gravity and the saturation of one or two accelerometer axes. b) and c) : RMS and fourth moment of $\boldsymbol{a}_{\mathrm{trans}}$ as a function of the impeller frequency. $a_{\mathrm{rms}}(f_{\mathrm{imp}}) = \sqrt{\langle |\boldsymbol{a}_{\mathrm{SP}}(f_{\mathrm{imp}})|^2 \rangle - g^2}$.

The flatness, $F(\boldsymbol{a}_{\mathrm{trans}})$, is defined as:

$$F\left(\boldsymbol{a}_{\mathrm{trans}}\right) = \frac{\left\langle \left|\boldsymbol{a}_{\mathrm{trans}}\right|^4 \right\rangle}{\left\langle \boldsymbol{a}_{\mathrm{trans}}^2 \right\rangle^2} = \frac{\left\langle \left|\boldsymbol{a}_{\mathrm{SP}}\right|^4 \right\rangle - g^4 - \frac{10}{3} g^2 a_{\mathrm{rms}}^2}{a_{\mathrm{rms}}^4}. \tag{7}$$

As shown in Fig. 5c we observe a flatness of the order of 10 in our von Kármán flow, which is close to the flatness obtained in the case of much smaller particles [6] and to our finding for solid particles of similar size [11]. The uncertainty in the flatness can partially be attributed to an uncertainty in g and stems from the resolution, noise and measurement range of the smartPART, but also from the particle's weak drift. It is furthermore biased by contacts with impellers and walls. More surprisingly, the flatness decreases with the forcing. This decline is again due to the limited measurement range of the accelerometer used: at high accelerations the sensor saturates and thereby sets PDF $\left(\boldsymbol{a}_{\mathrm{trans}} \,\middle|\, |a_{\mathrm{SP},i}| > 3.6g\right) = 0$. Since the flatness is the fourth moment of the PDF and as such highly sensitive to strong accelerations, we find a decrease whereas solid large spheres in the same flow have an increasing flatness [11]. We also conclude that calculating moments of higher order is out of reach.

It is remarkable, that based only on the second and fourth moment of $\boldsymbol{a}_{\mathrm{trans}}$ one cannot clearly distinguish between a counter-rotating and a co-rotating flow although these two forcings induce two clearly different large scale flow structures. Similar behavior has been found for solid spheres of comparable size in the same flow [11], too. It should be noted that the energy injection rates for the two ways of driving the flow differ by only a factor of 2: the co-rotating forcing is highly turbulent, too. In addition, in vicinity of the disks the flow has a strong contribution of the centrifugal pumping of the blades on the impellers and the flow configurations are comparable in that region.

C. Auto-correlation functions

In order to distinguish between the two regimes, we now turn to the auto-correlation of the acceleration time-series to estimate correlation time scales of the flow. Ideally, one would want to compute the auto-correlation of the translational force, *e.g.* $\langle \boldsymbol{a}_{\mathrm{trans}}(t) \cdot \boldsymbol{a}_{\mathrm{trans}}(t+\tau)\rangle$, but again the constantly changing orientation of the smartPART blocks any direct access to $\boldsymbol{a}_{\mathrm{trans}}(t)$ and quantities derived thereof. We therefore need to find quantities, which are either not altered by the orientation of the smartPART or extract information on its rotation.

1. *An Auto-correlation invariant to the rotation of the sensor*

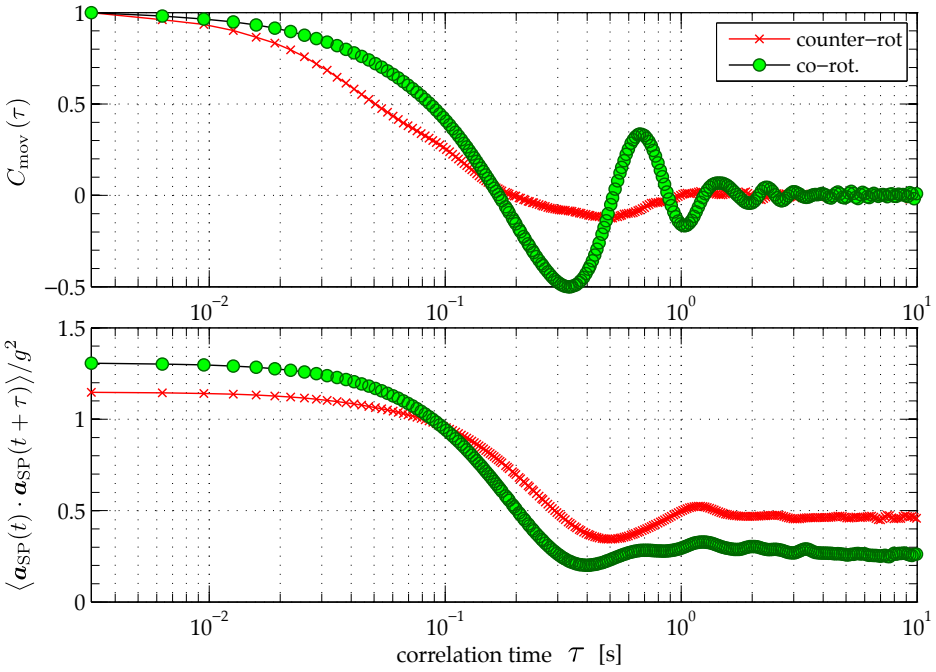

FIG. 6: Top: Rotation-invariant auto-correlation function $C_{\mathrm{mov}}(\tau)$ (Eq. (8) after rescaling); the auto-correlation significantly differs between counter- and co-rotating impellers. Bottom: Rotation-sensitive auto-correlation function $\langle \boldsymbol{a}_{\mathrm{SP}}(t)\cdot\boldsymbol{a}_{\mathrm{SP}}(t+\tau)\rangle/g^2$. In all cases the impeller frequency is 1.5 Hz. A logarithmic scale is chosen for the abscissae to display both short and long time contributions to the correlations.

In the spirit of Eq. (3) and Eq. (5) one can construct the auto-correlation function of the magnitude of $\boldsymbol{a}_{\mathrm{SP}}$. It is:

$$
\begin{aligned}
&\left\langle |\boldsymbol{a}_{\mathrm{SP}}(t)|^2\,|\boldsymbol{a}_{\mathrm{SP}}(t+\tau)|^2\right\rangle \\
&\quad= \left\langle \left[g^2+\boldsymbol{a}^2_{\mathrm{trans}}(t)+2\,\boldsymbol{g}\cdot\boldsymbol{a}_{\mathrm{trans}}(t)\right]\left[g^2+\boldsymbol{a}^2_{\mathrm{trans}}(t+\tau)+2\,\boldsymbol{g}\cdot\boldsymbol{a}_{\mathrm{trans}}(t+\tau)\right]\right\rangle \\
&\quad= \left\langle |\boldsymbol{a}_{\mathrm{trans}}(t)|^2\,|\boldsymbol{a}_{\mathrm{trans}}(t+\tau)|^2\right\rangle + g^4 + 2g^2\,\left\langle \boldsymbol{a}^2_{\mathrm{trans}}\right\rangle + 4g^2\,\langle a_z(t)\,a_z(t+\tau)\rangle \\
&\qquad + 4\,g^3\,\langle a_z\rangle + 2g\left\langle |\boldsymbol{a}_{\mathrm{trans}}(t+\tau)|^2\,a_z(t)\right\rangle + 2g\left\langle |\boldsymbol{a}_{\mathrm{trans}}(t)|^2\,a_z(t+\tau)\right\rangle \\
&\quad\approx \left\langle |\boldsymbol{a}_{\mathrm{trans}}(t)|^2\,|\boldsymbol{a}_{\mathrm{trans}}(t+\tau)|^2\right\rangle + g^4 + 2\,g^2 a^2_{\mathrm{rms}} + 4g^2\,\langle a_z(t)\,a_z(t+\tau)\rangle\,.
\end{aligned}
\tag{8}
$$

Again, the terms containing $a_z \equiv \hat{\boldsymbol{e}}_z\cdot\boldsymbol{a}_{\mathrm{trans}}$ are expected to have zero mean. However, the last term on the right-hand side of Eq. (8) does not vanish for $\tau\approx 0$, becoming $4g^2\,\langle a_z(t)\,a_z(t+\tau)\rangle = 4g^2\left\langle |a_z|^2\right\rangle$. Assuming no preferred direction in $\boldsymbol{a}_{\mathrm{trans}}$ this can be approximated as $4/3\,g^2\,a^2_{\mathrm{rms}}$. In contrast to Eq. (8), we preferably compute the autocorrelation of the fluctuations around the mean $\left\langle \boldsymbol{a}^2_{SP}\right\rangle$. Hence, the

autocorrelation of the norm can be negative. We further normalize the auto-correlation such that it is 1 at $\tau = 0$. After rescaling, we refer to this rotation-invariant quantity as $C_{\mathrm{mov}}(\tau)$.

Fig. 6 displays $C_{\mathrm{mov}}(\tau)$ for the co- and counter-rotating regime at an impeller frequency of 1.5 Hz. The auto-correlation of the counter-rotating forcing is well approximated by a sum of exponential decays. In contrast thereto, we observe that co-rotating impellers correspond to an auto-correlation function showing a damped oscillation, *i.e.* the smartPART observes the longer coherence in the large scale motion of the flow. This is in agreement with Eulerian measurements, where pressure probes were mounted in a von Kármán flow: whereas the counter-rotating flow produces typical pressure spectra, the same probe in the co-rotating case yields a spectrum which peaks at multiples of the impeller frequency. Similar behavior has been reported for the magnetic field in a von Kármán flow [24] filled with liquid Gallium (in that particular case the co-rotating regime was created by rotating only one impeller).

Summing up, $\left\langle \left|\boldsymbol{a}_{\mathrm{SP}}(t)\right|^2 \left|\boldsymbol{a}_{\mathrm{SP}}(t+\tau)\right|^2 \right\rangle$ is insensitive to the particular tumbling/rotational dynamics of the particle and it gives necessary information to determine the type of flow. We also checked that this result is not altered by a possible imbalance of the particle.

2. *An Auto-correlation related to the tumbling of the particle*

One can further focus on the rotation of the particle by considering the product:

$$
\begin{aligned}
&\langle \boldsymbol{a}_{\mathrm{SP}}(t)\cdot\boldsymbol{a}_{\mathrm{SP}}(t+\tau)\rangle \\
&= \langle [\underline{\underline{\mathbf{R}}}(t)\ (\boldsymbol{g}+\boldsymbol{a}_{\mathrm{trans}}(t))]\cdot[\underline{\underline{\mathbf{R}}}(t+\tau)\ (\boldsymbol{g}+\boldsymbol{a}_{\mathrm{trans}}(t+\tau))]\rangle \\
&= \left\langle \left[\underline{\underline{\mathbf{R}}}^T(t+\tau)\cdot\underline{\underline{\mathbf{R}}}(t)\ (\boldsymbol{g}+\boldsymbol{a}_{\mathrm{trans}}(t))\right]\cdot[(\boldsymbol{g}+\boldsymbol{a}_{\mathrm{trans}}(t+\tau))]\right\rangle \\
&= \langle \boldsymbol{g}\cdot[\underline{\underline{\mathbf{T}}}(t,\tau)\boldsymbol{g}]\rangle + \langle [\underline{\underline{\mathbf{T}}}(t,\tau)\boldsymbol{a}_{\mathrm{trans}}(t)]\cdot\boldsymbol{a}_{\mathrm{trans}}(t+\tau)\rangle + \langle [\underline{\underline{\mathbf{T}}}(t,\tau)\boldsymbol{g}]\cdot\boldsymbol{a}_{\mathrm{trans}}(t+\tau)\rangle + \langle [\underline{\underline{\mathbf{T}}}(t,\tau)\boldsymbol{a}_{\mathrm{trans}}(t)]\,\boldsymbol{g}\rangle \\
&\approx g^2\,\langle \hat{\boldsymbol{e}}_z\cdot[\underline{\underline{\mathbf{T}}}(t,\tau)\hat{\boldsymbol{e}}_z]\rangle + \langle [\underline{\underline{\mathbf{T}}}(t,\tau)\cdot\boldsymbol{a}_{\mathrm{trans}}(t)]\,\boldsymbol{a}_{\mathrm{trans}}(t+\tau)\rangle\,,
\end{aligned}
\tag{9}
$$

where the term $\underline{\underline{\mathbf{T}}}(t,\tau) \equiv \underline{\underline{\mathbf{R}}}^T(t+\tau)\underline{\underline{\mathbf{R}}}(t)$ is a rotation matrix related to the instantaneous angular velocity $\boldsymbol{\omega}$ of the particle as explained in Ref. [10]. Again, the two terms containing products of $\boldsymbol{g}$ and $\boldsymbol{a}$ vanish if the particle is neutrally buoyant. The term $g^2\,\langle \hat{\boldsymbol{e}}_z\cdot[\underline{\underline{\mathbf{T}}}(t,\tau)\hat{\boldsymbol{e}}_z]\rangle$ is related to the tumbling of a spherical particle [25]. In contrast to the other auto-correlation Eq. (8), one cannot subtract a mean value prior to computing $\langle \boldsymbol{a}_{\mathrm{SP}}(t)\cdot\boldsymbol{a}_{\mathrm{SP}}(t+\tau)\rangle$. To estimate the ratio between $g^2\,\langle \hat{e}_z\cdot[\underline{\underline{\mathbf{T}}}(t,\tau)\hat{e}_z]\rangle$ and $\langle [\underline{\underline{\mathbf{T}}}(t,\tau)\boldsymbol{a}_{\mathrm{trans}}(t)]\cdot\boldsymbol{a}_{\mathrm{trans}}(t+\tau)\rangle$ it is helpful to normalize by g^2.

If $\langle [\underline{\underline{\mathbf{T}}}(t,\tau)\cdot\boldsymbol{a}_{\mathrm{trans}}(t)]\,\boldsymbol{a}_{\mathrm{trans}}(t+\tau)\rangle$ becomes uncorrelated, $\langle \boldsymbol{a}_{\mathrm{SP}}(t)\cdot\boldsymbol{a}_{\mathrm{SP}}(t+\tau)\rangle$ does not necessarily vanish. If uncorrelated ($\tau \gg T_{\mathrm{int}}$):

$$
\begin{aligned}
\langle \boldsymbol{a}_{\mathrm{SP}}(t)\cdot\boldsymbol{a}_{\mathrm{SP}}(t+\tau)\rangle &\cong g^2\,\langle \underline{\underline{\mathbf{R}}}(t)\,\hat{\boldsymbol{e}}_z\cdot\underline{\underline{\mathbf{R}}}(t+\tau)\,\hat{\boldsymbol{e}}_z\rangle \\
&= g^2\,\langle \underline{\underline{\mathbf{R}}}\hat{\boldsymbol{e}}_z\rangle^2 \geqslant 0
\end{aligned}
\tag{10}
$$

That means $\langle \boldsymbol{a}_{\mathrm{SP}}(t)\cdot\boldsymbol{a}_{\mathrm{SP}}(t+\tau)\rangle$ approaches a plateau whose height is determined by the average orientation of the particle. In analogy to C_{mov}, one can then subtract $g^2\,\langle \underline{\underline{\mathbf{R}}}\hat{\boldsymbol{e}}_z\rangle^2$ and rescale $\langle \boldsymbol{a}_{\mathrm{SP}}(t)\cdot\boldsymbol{a}_{\mathrm{SP}}(t+\tau)\rangle$, which is termed $C_{\mathrm{tumb}}(\tau)$ in the following.

The lower plot in Fig. 6 depicts $\langle \boldsymbol{a}_{\mathrm{SP}}(t)\cdot\boldsymbol{a}_{\mathrm{SP}}(t+\tau)\rangle / g^2$ for the two forcing regimes at an impeller frequency of 1.5 Hz. In agreement with Eq. (10), a plateau is reached for both forcings. To investigate the role of the plateau we plot the auto-correlation of the particle for increasing f_{imp} in Fig. 7. For $f_{\mathrm{imp}} \lesssim 1$ Hz one finds little change with the plateau at almost 1. For $f_{\mathrm{imp}} \approx 2$ Hz the plateau drops but is still non-zero. The value of the plateau diminishes with further increase in f_{imp}. At the same frequency range we observe that the PDFs of the components of $\boldsymbol{a}_{\mathrm{SP}}$ become centered and symmetric (cf. Fig. 4). $C_{\mathrm{tumb}}(\tau)$ – *i.e.* Eq. (9) after subtracting the plateau and rescaling – accesses the fluctuations around a mean value and is shown in the bottom plot of Fig. 7. We find that $C_{\mathrm{tumb}}(\tau)$ evolves from a long-time correlated oscillatory shape at low impeller speeds to an exponential decay at high f_{imp}.

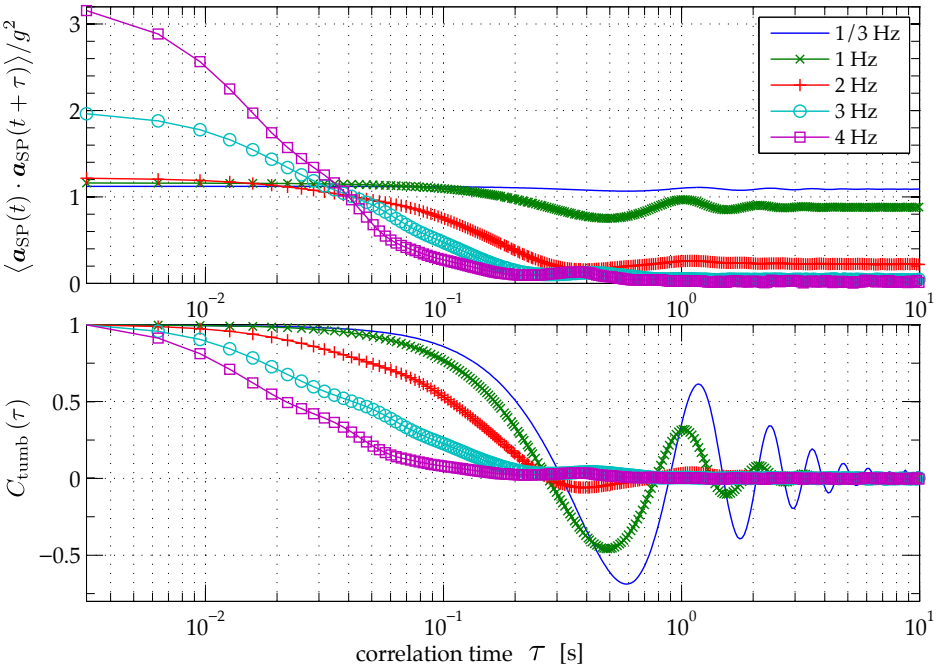

FIG. 7: Top: Dependence of $\langle \boldsymbol{a}_{\rm SP}(t) \cdot \boldsymbol{a}_{\rm SP}(t+\tau) \rangle / g^2$ on the impeller frequency for counter-rotating impellers; Bottom: Same data after subtracting the plateau and rescaling.

3. *Time scales*

The autocorrelation functions contain time-scales which are related to the movement of the particle in the flow. We identify two scenarios for the autocorrelations ($C_{\rm mov}(\tau)$ and $C_{\rm tumb}(\tau)$): as illustrated in Fig. 6, they are either conducting a weakly- or a critically-damped oscillation. With increasing turbulence level the oscillation is gradually changing towards the critically damped case and for high propeller speeds ($f_{\rm imp} > 2.5\,{\rm Hz}$) no damped oscillation is observed (cf. Fig. 7). In order to extract meaningful time-scales we, therefore, fit two test-functions to each autocorrelation function. The functions are the transient solution of a weakly damped harmonic oscillator:

$$f_w(\tau) = a_0 \, \exp\left(-\tau/\tau_{\rm corr}\right) \cdot \sin\left(2\pi f_{\rm osc} + \phi_0\right), \tag{11}$$

and of a critically damped one:

$$f_d(\tau) = \exp\left(-\tau/\tau_{\rm corr}\right) \cdot \left(a_0 + a_1\,\tau\right). \tag{12}$$

$\tau_{\rm corr}, f_{\rm osc}$ and a_0, a_1, ϕ_0 are fit-parameters. We return $\tau_{\rm corr}$ and (if available) $f_{\rm osc}$ from the test-function which performs better in approximating the autocorrelation. $C_{\rm mov}(\tau)$ and $C_{\rm tumb}(\tau)$ access motion and tumbling of the particle, respectively, and yield thus different time scales. For the oscillatory case, $f_{\rm osc}$ contributes additional details on the particle's motion.

Fig. 8 shows $\tau_{\rm corr}$ as a function of the impeller frequency and driving. We find that both rotation-invariant (Eq. (8)) and rotating-sensitive (Eq. (9)) function find very similar correlation times in the counter-rotating configuration. Moreover, $\tau_{\rm corr}$ of the particle follows roughly a $f_{\rm imp}^{-3/2}$ power-law as suggested by the scaling of the Kolmogorov time scale (it is $\tau_\eta \propto \varepsilon^{-1/2}$ and $\varepsilon \propto f_{\rm imp}^3$). Furthermore, $\tau_{\rm corr}$ obtained from the rotation-sensitive function is independent of the way we drive the flow. In contrast thereto, the rotation-invariant function gives correlation times, $\tau_{\rm corr}$, which are larger and only little dependent on the impeller frequency if the impellers are co-rotating. That means one can distinguish co- from counter-rotating forcing by comparing the timescales of the two auto-correlation functions.

Concerning the oscillation frequency $f_{\rm osc}$ (not shown in figure), we find that the rotation-sensitive autocorrelation senses the tumbling/wobbling of the particle, which is directly related to the particle's imbalance and independent of the flow. The rotation-invariant autocorrelation on the other hand shows an oscillation frequency following the impeller frequency with $f_{\rm osc} \sim \frac{2}{3} f_{\rm imp}$.

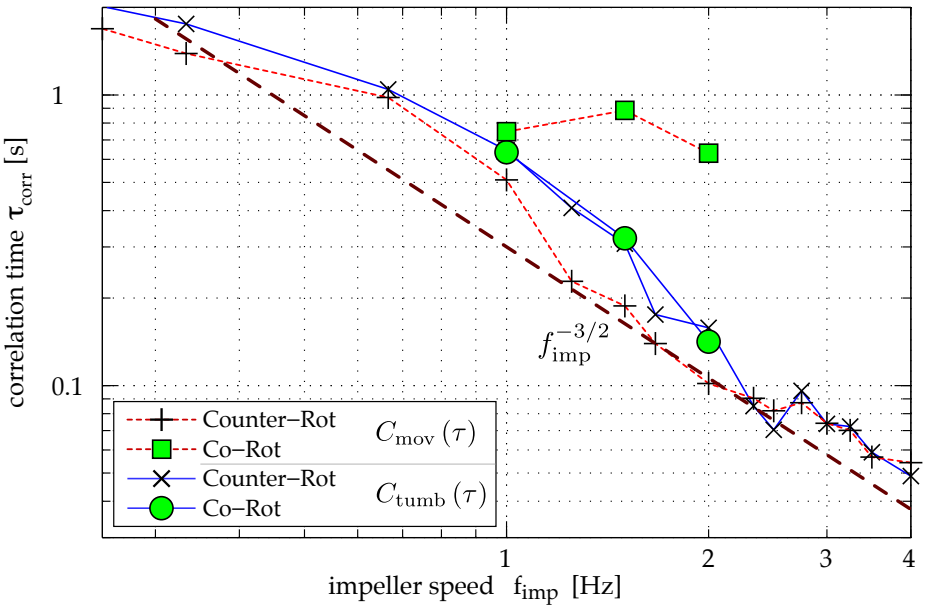

FIG. 8: Characteristic flow time scale τ_{corr} determined from rotation-invariant, $C_{mov}(\tau)$, and rotation-sensitive, $C_{tumb}(\tau)$, auto-correlation function. Whereas both autocorrelation functions yield comparable τ_{corr} for counter-rotating driving, we find that their results are well distinct in the case of co-rotating impellers. The dashed line indicates a $f_{imp}^{-3/2}$ power-law, as suggested by the scaling of the Kolmogorov time scale ($\tau_\eta \propto \varepsilon^{-1/2}$ and $\varepsilon \propto f_{imp}^3$).

III. DISCUSSION

After briefly presenting the working principle of an instrumented particle measuring Lagrangian accelerations, we established a mathematical framework based on statistical moments and auto-correlation functions to analyze turbulent flows from the particle's signals. In particular, we developed methods which are either invariant or sensitive to the rotation of the particle and its sensor in the flow. These methods perform well within the wide range of tested turbulence levels. With a smartPART one gets access to correlation time scales of the flow, as well as the variance and flatness of the (translational) acceleration. Comparing the rotation-sensitive and the rotation-invariant autocorrelation allows distinguishing between different flow regimes, notably detecting long-time correlated large vortex structures as shown here with the co-rotating forcing of a von Kármán flow. In contrast to particle tracking methods the instrument particle returns one long trajectory instead of many short realizations. To that extent, it has to be noted that we limited our analysis to the extraction of global flow features. In order to follow the evolution of a slowly changing flow in time, these methods can, however, be extended to sliding windows. Work on adaptive filtering techniques is ongoing, in particular we are testing the *Empirical Mode Decomposition*, which might be able to separate the different contributions of the signal and thereby get even deeper insight into the flow.

We emphasize that after usage the particle can be easily extracted from the flow and then be reused and that by virtue of the developed mathematical framework no optical access is needed. The instrumented particle can therefore shed some light into flows that are not or hardly accessible up to now. Due to its continuous transmission one flow configuration can be characterized within ~ 30 min. This technique is an interesting tool for a fast quantification of a wide range of flows as they are found both in research labs and industry.

Acknowledgments

This work was supported by ANR-07-BLAN-0155. The authors want to acknowledge the technical help of Marius Tanase and Arnaud Rabilloud for the electronics, and of all the ENS machine shop staff. The

authors also thank Michel Voßkuhle, Mickaël Bourgoin and Alain Pumir for many fruitful discussions.

---

[1] C. Tropea, A. Yarin, and J. F. Foss, eds., *Springer Handbook of Experimental Fluid Dynamics* (Springer-Verlag Berlin-Heidelberg, 2007).
[2] F. Toschi and E. Bodenschatz, Annual Review of Fluid Mechanics **41**, 375 (2009).
[3] B. Shraiman and E. Siggia, Nature **405**, 639 (2000).
[4] G. A. Voth, A. L. Porta, A. Crawford, J. Alexander, and E. Bodenschatz, Journal of Fluid Mechanics **469**, 121 (2002).
[5] N. Mordant, J. Delour, E. Léveque, O. Michel, A. Arnéodo, and J.-F. Pinton, Journal of Statistical Physics **113**, 701 (2003).
[6] N. Qureshi, M. Bourgoin, C. Baudet, A. Cartellier, and Y. Gagne, Physical Review Letters **99**, 184502 (2007).
[7] N. Qureshi, U. Arrieta, C. Baudet, A. Cartellier, Y. Gagne, and M. Bourgoin, The European Physical Journal B **66**, 531 (2008).
[8] R. Volk, E. Calzavarini, G. Verhille, D. Lohse, N. Mordant, J.-F. Pinton, and F. Toschi, Physica D: Nonlinear Phenomena **237**, 2084 (2008).
[9] H. Xu and E. Bodenschatz, Physica D **237**, 2095 (2008).
[10] R. Zimmermann, Y. Gasteuil, M. Bourgoin, R. Volk, A. Pumir, and J.-F. Pinton, Review of Scientific Instruments **82**, 033906 (2011).
[11] R. Zimmermann, Ph.D. thesis, École Normale Supérieure de Lyon - Université de Lyon (2012).
[12] R. Zimmermann, Y. Gasteuil, M. Bourgoin, R. Volk, A. Pumir, and J.-F. Pinton, Physical Review Letters **106**, 154501 (2011).
[13] Y. Gasteuil, W. L. Shew, M. Gibert, F. Chillà, B. Castaing, and J.-F. Pinton, Physical Review Letters **99**, 234302 (2007).
[14] Y. Gasteuil, Ph.D. thesis, École Normale Supérieure de Lyon (2009).
[15] W. L. Shew, Y. Gasteuil, M. Gibert, P. Metz, and J.-F. Pinton, Review of Scientific Instruments **78**, 065105 (2007).
[16] J.-F. Pinton, P. Metz, Y. Gasteuil, and W. L. Shew, *Mixer, and device and method for monitoring or controlling said mixer*, Patent US 2011/0004344 A1 (2009).
[17] R. Ni, S.-D. Huang, and K.-Q. Xia, Journal of Fluid Mechanics **692**, 395 (2012).
[18] R. Zimmermann, L. Fiabane, Y. Gasteuil, R. Volk, and J. Pinton, Arxiv preprint arXiv:1206.1617 (2012).
[19] H. Goldstein, *Classical Mechanics* (Pearson, 2002).
[20] F. Ravelet, A. Chiffaudel, and F. Daviaud, Journal of Fluid Mechanics **601**, 339 (2008).
[21] N. T. Ouellette, H. Xu, M. Bourgoin, and E. Bodenschatz, New Journal of Physics **8**, 102 (2006).
[22] R. Monchaux, F. Ravelet, B. Dubrulle, A. Chiffaudel, and F. Daviaud, Physical Review Letters **96**, 124502 (2006).
[23] C. Simand, Ph.D. thesis, École Normale Supérieure de Lyon (2002).
[24] R. Volk, P. Odier, and J.-F. Pinton, Physics of Fluids **18**, 085105 (2006).
[25] M. Wilkinson and A. Pumir, Journal of Statistical Physics **145**, 113 (2011).

A.5 Concentration préférentielle des particules matérielles

[A 4] R. Zimmermann, H. Xu, Y. Gasteuil, M. Bourgoin, R. Volk, J.-F. Pinton, E. Bodenschatz. The lagrangian exploration module : an apparatus for the study of homogeneous and isotropic turbulence. *Review Of Scientific Instrument*, 81(5), (2010).

[A 9] L Fiabane, R Zimmermann, R Volk, J.-F Pinton, and M Bourgoin. Clustering of finite-size particles in turbulence. *Physical Review E*, 035301 :1–4, (2012).

The Lagrangian exploration module: An apparatus for the study of statistically homogeneous and isotropic turbulence

Robert Zimmermann,[1,a)] Haitao Xu,[1,b)] Yoann Gasteuil,[2] Mickaël Bourgoin,[3] Romain Volk,[2] Jean-François Pinton,[2] and Eberhard Bodenschatz[1]
(International Collaboration for Turbulence Research)
[1]*Max Planck Institute for Dynamics and Self-Organization, Göttingen D-37077, Germany*
[2]*Laboratoire de Physique, CNRS and Ecole Normale Supérieure de Lyon, UMR 5672, Lyon F-69007, France*
[3]*Laboratoire des Ecoulements Geophysiques et Industriels, CNRS UJF INPG, UMR5519, Grenoble F-38041, France*

(Received 31 December 2009; accepted 21 April 2010; published online 28 May 2010)

We present an apparatus that generates statistically homogeneous and isotropic turbulence with a mean flow that is less than 10% of the fluctuating velocity in a volume of the size of the integral length scale. The apparatus is shaped as an icosahedron where at each of the 12 vertices the flow is driven by independently controlled propellers. By adjusting the driving of the different propellers the isotropy and homogeneity of the flow can be tuned, while keeping the mean flow weak.
 [doi:10.1063/1.3428738]

I. INTRODUCTION

Fully developed fluid turbulence is most easily studied under the assumption of statistical homogeneity and isotropy.[1] This is hard to realize in laboratory flows and basically never found in naturally occurring flows. In experiments it would be desirable to implement a situation, in which the conditions such as the homogeneity or the isotropy of the flow can be tuned. Additionally, such experiments should allow simultaneous Eulerian and Lagrangian measurements. The latter have captured renewed interest in the community[2–6] as they provide new insights into turbulent mixing and transport. Lagrangian studies require the measurement volume to follow the mean flow, while local measurements, such as hot wire or laser Doppler velocimetry, are sufficient to measure Eulerian statistics under the assumption of Taylor's frozen flow hypothesis.

Traditionally, grid generated turbulence in wind tunnels has been the first choice for experiments. There the statistics of the decaying turbulence have been observed to be close to homogeneous and isotropic. Recently active grids have provided an increased Reynolds number and some control on the flow properties.[7,8] Although wind tunnel flows are ideally suited for Eulerian measurements with local probes, the typically fast mean flow velocities make Lagrangian measurements difficult. Additionally, in conventional wind tunnels the maximum available observation time, given by the length of the tunnel divided by the mean velocity of the flow, is short. Thus, even if the measurement volume would move with the mean flow, it is rarely possible to follow Lagrangian tracers over inertial time scales. Seminal work was conducted by Snyder and Lumley,[9] where multiple cameras were used to follow the flow. Only few experiments have been conducted in wind or water tunnels since, with most of them moving the measurement system with the mean flow,[10–12] or with a measurement volume elongated in the flow direction.[13] Most recent measurements have been limited to observation times sufficient to measure velocity and acceleration, but not the transport properties of the flow.

In order to allow easier measurements of the Lagrangian properties of turbulent flows, several other types of experimental apparatuses with small mean flow velocities have been devised. The best known example is the von Kármán flow, i.e., the high Reynolds number turbulent water flow between two counter-rotating disks. For the past ten years, it has been the "workhorse" for Lagrangian measurements.[2–4,14,15] Although, near the center of the apparatus, the mean velocities are much weaker than the fluctuations, the inhomogeneity and anisotropy make the interpretation of the results difficult. In fluids, oscillating grids[16,17] are able to generate nearly homogeneous and isotropic turbulence with a small mean flow. The achievable Reynolds numbers, however, are small compared to that of turbulent von Kármán flows in laboratory scale devices. Variano *et al.*[18] used an array of random jets to create an approximately homogeneous and isotropic turbulent water flow in an open tank, again the Reynolds numbers were quite small. Hwang *et al.*[19] used eight speakers at the corners of a cube to drive turbulence in air. Results from two-dimensional particle image velocimetry (PIV) showed that the apparatus generated turbulence with very small mean flow and with a high degree of homogeneity and isotropy at Reynolds numbers comparable to those of oscillating grids. Similar devices utilizing

[a)]Present address: Laboratoire de Physique, Ecole Normale Supérieure de Lyon, Lyon, F-69007 France.
[b)]Author to whom correspondence should be addressed. Electronic mail: haitao.xu@ds.mpg.de.

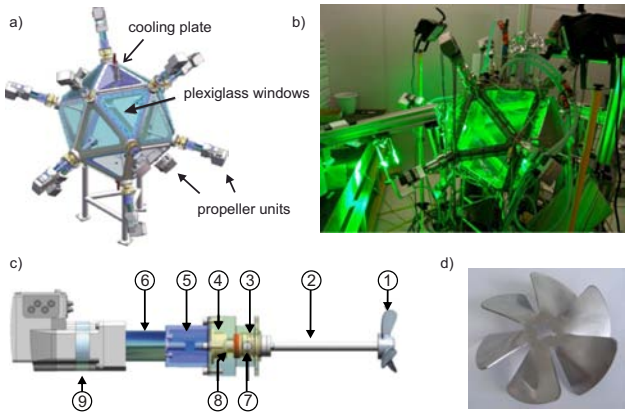

FIG. 1. (Color online) (a) A CAD drawing of the LEM. (b) A photograph of the LEM in operation. An expanded frequency-double Nd:YAG laser beam illuminates the measurement volume. Three high-speed CMOS cameras record the motion of tracer particles from different viewing angles. (c) A CAD drawing of the propeller unit. 1: propeller, 2: exchangeable propeller shaft, 3: rotating seal, 4: bearing, 5: shaft coupling, 6: gearbox, 7: air passage to the bubble trap, 8: ventilation hole for water vapor to escape, 9: brushless dc motor. (d) Stainless steel propeller with a diameter of 10 cm.

multiple jets to drive turbulence in both air and water have been developed later.[20–22] In a more recent development, 32 spherically arranged speakers are used to generate a turbulent gas flow that has tunable isotropy and homogeneity.[23]

Here we present a novel apparatus, the Lagrangian exploration module (LEM). By comparing Eulerian statistics obtained from three-dimensional Lagrangian particle tracking (LPT) measurements with theoretical relationships derived for homogeneous and isotropic turbulence, we show that the LEM can generate statistically highly homogeneous and isotropic turbulence, as well as turbulence with tunable isotropy and homogeneity.

II. DESCRIPTION OF THE APPARATUS

The Max Planck Institute of Dynamics and Self-Organization in Göttingen designed and constructed the LEM in cooperation with the Laboratoire de Physique of the Ecole Normale Supérieure de Lyon. The apparatus is shaped as a regular icosahedron. Twelve independently controlled propellers, one at each vertex, are used to create turbulent flows with little mean velocity in the central region of the device. By independently controlling each propeller, different forcing schemes can be explored. For isotropic and constant forcing all propellers are rotating with constant rotation frequency; for isotropic and random forcing again all propellers are used, but the frequency and direction of each propeller is randomly changed after random time intervals. When only few propellers are used the flow is anisotropic and for two opposing propellers the von Kármán counter-rotating flow is realized. Here we report data on isotropically and constantly forced flows at Taylor microscale Reynolds number up to $R_\lambda \approx 350$. The flows were characterized by LPT. A photograph of the apparatus during LPT measurement is shown in Fig. 1(b). Currently a second device, which has the same icosahedral shape, but has motors installed on 12 of its 20 faces, is being put into operation at the ENS de Lyon.

The apparatus and the experimental setup are described in the following six subsections. First the technical details of the LEM are presented, followed by a detailed description of the LPT system.

A. Basic structure

The LEM has a stainless steel, skeletal structure in the shape of an icosahedron. A computer-aided design (CAD) drawing is provided in Fig. 1(a). The length of the edges of the icosahedron is 40 cm, which leads to a total volume of 140 l. An O-ring is placed on each face between the icosahedron skeleton and the confining plate. To avoid corrosion the material of all parts were made of plastics or stainless steel. The side plates were either made of Plexiglas [poly(methyl methacrylate)] for optical observation or stainless steel for cooling. The apparatus was mounted on three legs with the middle at a height of 80 cm.

B. Motor and propeller unit

The design of a propeller unit is shown schematically in Fig. 1(c). Both the propeller and the propeller shaft could be easily exchanged. This allowed maximum flexibility in testing different shaft lengths and propeller designs. The inner part of the shaft was held by a double-row ball bearing. A ceramic seal (Pac Seal, from Flowserve Cooperation, Irving, TX) was installed on each shaft. A threaded hole above the rotating seal on the water side was used for particle insertion or bubble removal (to be described in detail in the next section). Another hole on the dry side of the seal allowed possible water vapor to leave the housing of the propeller unit. The propeller shaft was driven by a brushless dc motor (IFE71, Berger-Lahr, Germany) through a planetary gear box that reduced the motor speed by a ratio of 5:1. The gearbox and the propeller shaft were connected by a stainless steel flexible coupler. For the experiments reported here, we used home-made six-blade round stainless steel disks of 10 cm in diameter, and a helix angle of approximately 60°. A photo of the propeller is shown in Fig. 1(d).

Each of the 12 motors was powered with a constant dc voltage of 36 V and controlled through a CAN-bus (controller area network). A laptop through a CAN-universal serial bus (USB) adapter (PCAN-USB, Peak Systems GmbH, Germany) controlled via CANopen commands the direction, the rotation frequency, and the angular acceleration of each motor. The CANopen protocol allows up to 127 devices at a data rate of 125 kbits/s, which was more than enough for this purpose. A user defined protocol adjusted the speed and the rotational direction of each motor at specified times. The rotation frequency of the propeller ranged from 1 to 16.67 Hz. As the maximum mechanical power of each motor was 120 W, the upper limit for the turbulent energy dissipation rate was 10 m^2/s^3. After filling with water, a small amount of air, as well as dust or lint, were always present inside the apparatus. As bubbles and dust interfere with particle tracking, they needed to be removed before measurements.

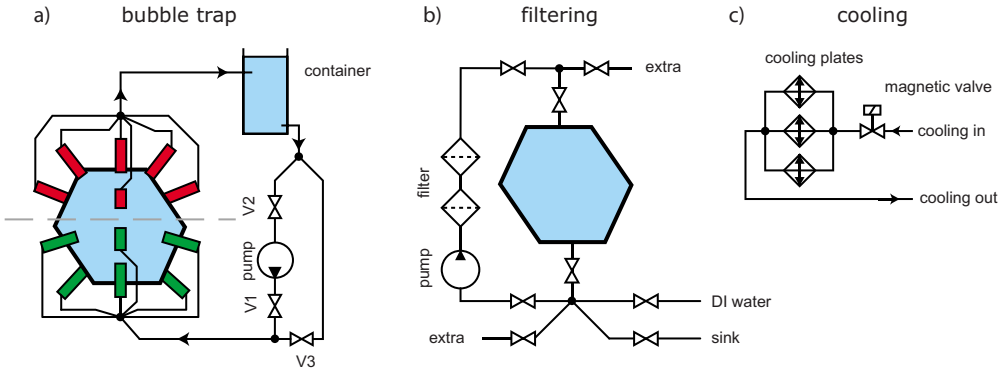

FIG. 2. (Color online) (a) Particle insertion and degassing: When the propellers were rotating, air bubbles accumulated in the low pressure region near the shaft of the six upper propeller units. By pumping water from the upper six propeller units to a gas/water exchange container and from there back to the lower six propeller units, gas bubbles could be removed or tracer particles could be inserted into the LEM. By switching a filter into the circulation circuit the water was filtered to 5 μm. The three valves (V1, V2, and V3) allowed pressurizing or depressurizing of the LEM. (b) Schematic of the plumbing system for filling, draining, and filteration of the water. (c) Schematic of the temperature control system: A microcontroller regulated the temperature to the set point by controlling the flow of building supplied cooling water with a solenoid valve.

C. Particle insertion, degassing, and filtration system

Figure 2 shows schematics of the degassing, particle insertion, and filtration system. Air was removed by pumping fluid from the six upper propeller units [see part 7 in Fig. 1(c)] through a gas/water exchange container and from there back to the lower six propeller units. Degassing was most efficient when at any given time only two opposing propellers were driven in the same direction. This created a vortex, in which air bubbles were trapped. When the propellers were stopped the air bubbles floated upwards and were removed by the circulation into the gas/water exchange container. By randomly switching on and off pairs of propellers air bubbles that adhered to the walls could be efficiently removed. For efficient degassing it was also advantageous to raise the temperature of the water to about 40 °C. Simultaneous with the air removal a secondary water circulation was used for filtration. A pump drew water from an outlet on the bottom plate, pushed it through two filters [the first 100 μm and the second 5 μm (both from ThermoFisher Scientific)], and then pumped it back to the LEM through the inlet on the top plate. This is shown schematically in Fig. 2(b). Experience showed that 24 h were sufficient to complete the filtration and degassing procedures. The air removal system could also be used to introduce particle and/or other additives (such as premixed polymer solutions) via the gas/water exchange container.

It was also possible to pressurize or depressurize the working fluid in the apparatus by connecting the gas/water exchange container to a vacuum pump or a high pressure bottle. Evacuation is useful to visualize vortex filaments and to study cavitation in turbulence.[24] Pressurization is useful to avoid cavitation. In both cases, the pumps had to be bypassed by the valves shown in Fig. 2(a).

D. Temperature control

As turbulence transforms all the kinetic energy delivered by the propellers to the flow into heat, it is necessary to temperature control the apparatus in order to avoid a drift in fluid properties. For particle tracking experiments at least four faces of the LEM needed to be covered with polyacrylamide windows (three for cameras and one for laser illumination), while the others could be covered with cooling plates for temperature control. For the power delivered by the motors three cooling plates were found to be sufficient for maintaining the temperature of the fluid: one on the top, one on the bottom, and one opposing the illuminating laser beam. In principle, it was easy to extend the cooling capacity by adding further cooling plates.

Each cooling plate consisted of a labyrinthian water channel machined into a stainless steel body through which building supplied cooling water was circulated. The cooling power of the plates was adjusted by regulating the flux of the cooling water with a microprocessor (C-Control 2, Conrad, Germany) controlled solenoid valve. Two PT100 resistance temperature detectors were mounted inside the LEM. Their resistances were converted to voltage signals, offset-subtracted, amplified, and then converted by a 10-bit analog-digital (AD) converter. The microcontroller then compared the temperature averaged over 2 s with the set point and either opened the solenoid valve or closed it. A sketch of the cooling circuit is shown in Fig. 2(c). The accuracy of the temperature control was 0.4 K mostly due to internal noise of the AD converter in the microcontroller. In all experiments presented here the water temperature was at (18.0 ± 0.4) °C.

E. LPT setup

The LPT system used was similar to that described in Refs. 14 and 15. It consisted of three cameras, a high-power pulsed neodymium-doped yttrium aluminum garnet (Nd:YAG) laser, a master personal computer (PC) for control, and a computer cluster for storing and processing the images. Figure 3 shows a sketch of the wiring diagram for the LPT system. Three Phantom V7.2 high-speed complementary metal oxide semiconductor (CMOS) cameras (Vision Research, Wayne, NJ) recorded 10-bit grayscale images at frame rates of up to 11 000 frames per second at a resolution of 512×512 pixels. Only the upper 8 bit of each image were read out via gigabit-ethernet into the computer cluster. The synchronization of the image capture from the three cameras were achieved by illuminating the measure-

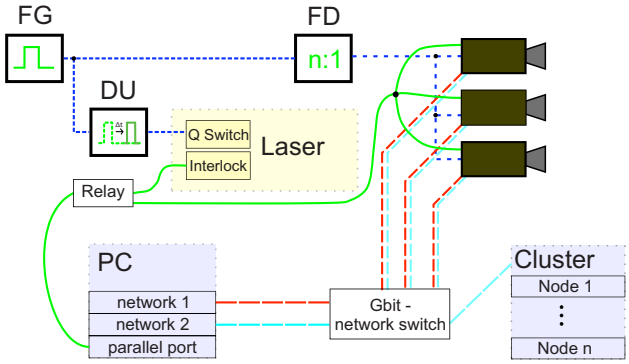

FIG. 3. (Color online) Schematic wiring of the LPT system: for details see text. FG generates a pulse train. FD is the frequency divider and DU is the delay unit. A master PC controlled the image capture and laser shutter through the parallel port. The images from the three cameras were downloaded via ethernet to the computer cluster for analysis.

ment volume with a pulsed laser, which in turn was triggered by a waveform generator (Agilent Technologies, Santa Clara, CA). The laser could only run at repetition rates higher than 20 kHz, and thus was faster than the camera frame rate used. Synchronization was achieved by triggering the laser at a frequency that was an integer times the camera frame rate and by triggering the cameras with the appropriate frequency divided signal. It was important that the laser trigger was delayed by a few microseconds in order to compensate for the internal response time of the cameras.

For each experiment, the frame rate of the cameras was selected based on the Kolmogorov time scale. Initially it was estimated and later extrapolated based on existing measurements. The frame rate was selected one or two orders of magnitude faster than the Kolmogorov time scale[3,25] since Lagrangian properties of turbulence are highly intermittent,[6] especially the acceleration.[3] Details on the frame rates in units of frames per Kolmogorov timescale are listed in Table I.

Sieved hollow glass spheres (MO-SCI cooperation), with diameters of 60–70 μm were used as tracer particles. These hollow spheres have a wide range of density, ranging between 0.8 and 2 g/cm^3, but the majority is within 1 and 1.2 g/cm^3, approximately the same as the water density. The inertial effect and the Stokes numbers, *St*, of these particles are discussed later.

The laser was a frequency-doubled, pulsed Nd:YAG laser (DDC Technologies, Oceanside, NY) with a wavelength of 532 nm and pulse width of 200 ns. The output power was approximately 30 W over a repetition rate range between 20 and 100 kHz. The laser beam was collimated and expanded to 15 cm in diameter. The whole system was aligned so that the beam entered the LEM perpendicular to the window surface and passed through the center of the apparatus. The scattering light can be seen in Fig. 1(b), a photograph taken while the LEM was in operation. The measurement volume was approximately $15\times10\times10$ cm^3 in size, as defined by the overlapping region among the observation volumes from all three cameras. The spatial resolution of the imaging system was 0.2 mm per pixel. The optical system was calibrated with an optical mask as described in Ref. 26.

The LPT system was controlled by a master PC (master), which set the parameters, such as the frame rate, frame format, exposure time, etc., as well as the operation sequence of the different components. In addition, five to ten nodes (slaves) in a computer cluster (Dell PowerVault) were used for image analysis. For each recording cycle the master first armed the laser by opening the shutter. After a few seconds, when the laser had stabilized, the master sent a "recording" command to the cameras. After acquiring images for the given recording time (typically less than a second due to the size of the onboard memory of the cameras), the master stopped the camera recording and closed the laser shutter. This "synchronous stop" allowed the master to instruct a slave to download the acquired images from the three cameras, counting backward, ensuring synchronization of the images. After downloading (typically 3–5 min) the slave issued an "end of downloading" (EoD) signal to the master, and started calculating the particle trajectories using the algorithm described in Ref. 26. After having received the EoD from the node the master started the next recording cycle and selected the next slave from a list for download. The process continued until all the slaves on the list had been called upon. The number of nodes was selected so that the first slave was finished with calculating trajectories by the time

TABLE I. Parameters of the experiments. f is the propeller frequency. $u' \equiv (u'_x+u'_y+u'_z)/3$ is the fluctuation velocity, averaged over the entire measurement volume. ε is the turbulence energy dissipation rate per unit mass, measured from the inertial range scaling of the Eulerian velocity structure functions. R_λ is the Taylor microscale Reynolds number, calculated from Eq. (4). $L \equiv u'^3/\varepsilon$ is the integral scale. η and τ_η are the Kolmogorov length and time scales of the flow, respectively. $St \equiv \tau_p/\tau_\eta$ is the Stokes number of tracer particles, where $\tau_p \equiv (2\rho_p+\rho_f)d_p^2/(36\mu_f)$ is the viscous relaxation time of the particles and ρ_p=1.1 g/cm^3 and d_p=65 μm are used. f_{cam} is the camera frame rate in units of frames per τ_η. $|u|$ is the average of the magnitude of the mean flow in the measurement volume.

f (Hz)	u' (cm/s)	ε (m^2/s^3)	R_λ	L (cm)	η (μm)	τ_η (ms)	St	f_{cam} (frame/τ_η)	$\lvert u\rvert$ (cm/s)
1	1.5	$(3.24\pm0.15)\times10^{-5}$	150 ± 10	10 ± 1	420 ± 5	175 ± 4	2.1×10^{-3}	175	0.1
1.67	2.7	$(2.14\pm0.03)\times10^{-4}$	195 ± 10	9.4 ± 0.6	261 ± 1	68 ± 0.5	5.5×10^{-3}	68	0.1
2.25	3.6	$(6.33\pm0.15)\times10^{-4}$	200 ± 8	7.3 ± 0.5	200 ± 1	40 ± 0.5	9.4×10^{-3}	40	0.3
5	6.2	$(5.2\pm0.8)\times10^{-3}$	210 ± 45	5 ± 1.6	118 ± 4	14 ± 1	2.7×10^{-2}	35	0.5
7.5	9.7	$(1.4\pm0.2)\times10^{-2}$	300 ± 60	6 ± 2	91 ± 4	8.4 ± 0.6	4.5×10^{-2}	42	1.2
9.33	12.6	$(3.6\pm0.5)\times10^{-2}$	330 ± 70	6 ± 2	73 ± 3	5.3 ± 0.3	7.1×10^{-2}	26.5	1.1

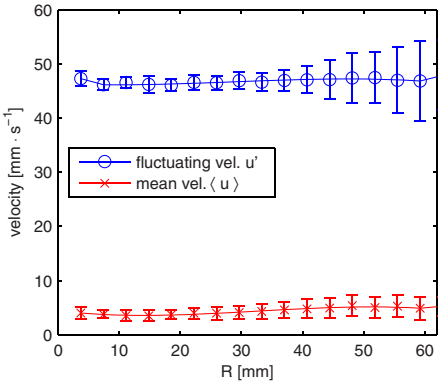

FIG. 4. (Color online) The magnitudes of the mean $|u|$ and the fluctuating velocities u' averaged in spherical shells around the center of the measurement volume, vs the radius measured from he center. The error bars indicate the standard deviation within each shell. $R_\lambda = 195$.

the master selected it for the next download. After the experimental run, which consisted of many recording cycles, all the trajectories were processed with the algorithm in Ref. 27 to connect interrupted segments resulted from fluctuation in illumination, particle shading, and pixel blinking.

III. RESULTS

In this section, we report the quantitative measurements in the LEM at different propeller speeds. The particle velocities were calculated with a smoothing and differentiating kernel.[28] Eulerian statistics were measured by simultaneously tracking several hundreds of particles.

The energy dissipation rate, ε, was determined from the well-known scalings of the velocity structure functions in the inertial range (see, e.g., Ref. 29)

$$\varepsilon = \frac{1}{r}\left[\frac{D_{LL}(r)}{C_2}\right]^{3/2}, \tag{1}$$

$$\varepsilon = \frac{1}{r}\left[\frac{3D_{NN}(r)}{4C_2}\right]^{3/2}, \tag{2}$$

and

$$\varepsilon = -\frac{5D_{LLL}(r)}{4r}, \tag{3}$$

where $D_{LL}(r)$ and $D_{NN}(r)$ are the second-order longitudinal and transverse structure functions, $D_{LLL}(r)$ is the third-order longitudinal structure function, and C_2 is an universal constant. The currently accepted value for $C_2 = 2.1$ was used.[30] Although these scaling relations are strictly applicable only to statistically homogeneous and isotropic turbulence, experience[31] shows that they work well even in other situation. As we will find, the LEM can produce statistically homogeneous and isotropic turbulence. Therefore, in this case the application of the scaling relations if fully justified. All three methods give similar values and here the average ε is reported.

The Taylor microscale Reynolds number of the flow, R_λ, was also calculated based on the assumption of statistically homogeneous and isotropic turbulence (see, e.g., Ref. 29)

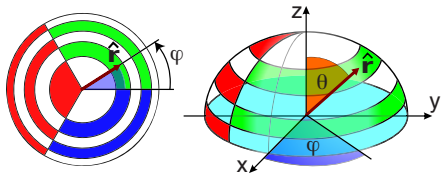

FIG. 5. (Color online) Grouping of the separation vectors on a unit hemisphere with 3×5 bins. Each bin covers the same solid angle.

$$R_\lambda = \frac{u'\lambda}{\nu} = \frac{\sqrt{15}\tau_\eta u'^2}{\nu} = \sqrt{\frac{15u'^4}{\nu\varepsilon}}, \tag{4}$$

where u' is the turbulence fluctuating velocity and τ_η denotes the Kolmogorov time scale.

The integral length scale, L, which characterizes the largest eddies of the turbulent flow, is estimated from the relationship

$$L = C_L u'^3/\varepsilon, \tag{5}$$

where u' is the turbulence fluctuating velocity and C_L is a dimensionless constant. For $R_\lambda \leq 400$, a collection of available experimental and numerical data suggests that $0.5 \lessapprox C_L \lessapprox 1.5$,[32,33] so here $C_L = 1$ in Eq. (5) was used for the estimation of the parameters reported in Table I. Please note that L can also be estimated from the decay of the longitudinal and transverse velocity correlations. This yielded for all R_λ an integral scale of ≈ 4.5 cm, in good agreement with the values given in Table I. Discrepancies could be attributed to the unknown Reynolds number dependence of C_L. In the following we present mostly results for $R_\lambda = 195$; other Reynolds numbers gave similar results.

A. Statistical homogeneity

The statistical homogeneity of the velocity field was quantified by dividing the observation volume into spherical, "onion" shells of radius R around the center of the measurement volume and by calculating the fluctuating and the mean velocities in each shell. Figure 4 shows the mean and the fluctuating velocities averaged over the spherical shells versus R. The error bars in Fig. 4 indicate the standard deviation within each shell. Both the fluctuating and the mean velocities were observed to be nearly constant up to $R \approx 4$ cm. Thus, the flow was observed to be statistically homogeneous up to the integral length scale L (see Table I) of the turbulence. The increasing uncertainties with increasing R was due to worsening counting statistics: The intensity of the laser illumination decreased at the outer shells and less particle trajectories were observed. Thus, it is likely that the homogeneous region was even larger. Figure 4 also indicates that the magnitude of the mean velocity is much smaller than the fluctuating velocity throughout the measurement volume.

B. Statistical isotropy

The statistical isotropy of the flow was quantified by the second order longitudinal and transverse velocity structure functions $D_{LL}(\mathbf{r})$ and $D_{NN}(\mathbf{r})$ conditioned on the direction of the separation vector $\mathbf{r}$. The separation vectors $\mathbf{r}$ were grouped into bins that each occupied the same solid angle. Figure 5 shows schematically this grouping. Then the struc-

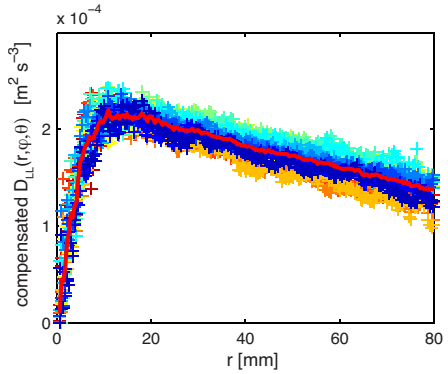

FIG. 6. (Color online) Independence of the longitudinal velocity structure function, $D_{LL}(\mathbf{r})$ on the direction of the separation vector $\mathbf{r}$. The structure functions were compensated as in Eq. (1) and the maximum value gives the energy dissipation rate ε. The symbols show the data for 15 bins of $\mathbf{r}$ in different directions, but spanning the same solid angle. The line is the average. $R_\lambda = 195$.

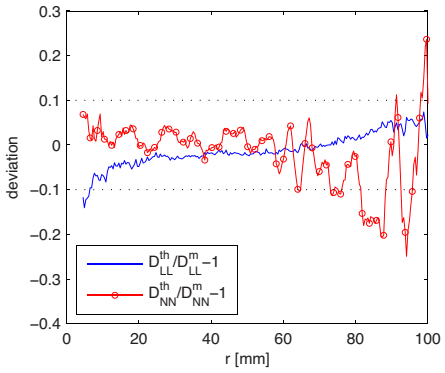

FIG. 7. (Color online) Relative deviations of the measured longitudinal and transverse velocity structure functions from the theoretical values that were calculated under the assumption of statistical homogeneity and isotropy. The horizontal dotted lines mark the ±10% deviations. $R_\lambda = 195$.

ture functions $D_{LL}(\mathbf{r})$ and $D_{NN}(\mathbf{r})$ for $\mathbf{r}$ were calculated in each bin. As shown in Fig. 6, the longitudinal structure function $D_{LL}(\mathbf{r})$ calculated from all 15 (φ, θ) bins collapsed well, i.e., it is indeed independent of the direction of $\mathbf{r}$ and thus isotropic. The same was true for $D_{NN}(\mathbf{r})$.

In statistically homogeneous and isotropic turbulence, the structure functions $D_{LL}(r)$ and $D_{NN}(r)$ are related by (see, e.g., Ref. 29)

$$D_{NN}(r) = D_{LL}(r) + \frac{r}{2}\left[\frac{\partial}{\partial r} D_{LL}(r)\right] \tag{6}$$

or equivalently

$$D_{LL}(r) = \frac{2}{r^2}\int_0^r x D_{NN}(x) dx. \tag{7}$$

If either $D_{LL}(r)$ or $D_{NN}(r)$ is known, the above equations can be used to calculate the other. By comparing the measured and calculated values, the degree of isotropy can be estimated. Figure 7 compares the measured structure functions (superscript ^{m}) with the calculated ones (superscript th). For both $D_{LL}(r)$ and $D_{NN}(r)$, the relative deviations were below 10% for separations smaller than 8 cm. The slightly larger relative deviations in $D_{NN}(r)$ can be attributed to the numerical differentiation when calculating D^{th}_{NN} from Eq. (6).

The statistical isotropy can also be quantified by a directional analysis of the coarse-grained velocity gradients at the integral scale. A method similar to that in Ref. 34 was used over the whole measurement volume. The coarse-grained velocity gradients can be decomposed into the "large-scale" vorticity and the rate-of-strain tensors. Figures 8(a) and 8(b) show the distribution of the direction of the coarse-grained vorticity vectors ω and the eigenvectors $\mathbf{e}_1$ corresponding to the largest eigenvalues of the coarse-grained rate-of-strain tensors, as measured by the cosines of the angles between the three axes of the laboratory coordinates and these two vectors. If the flow is isotropic, both vectors ω and $\mathbf{e}_1$ should orient randomly in space and the probability density functions (PDFs) of the angular cosines should be flat, i.e., a uniform distribution. Figures 8(a) and 8(b) show that this was the case for the turbulent flow in the LEM. As a comparison, the same PDFs were analyzed for a von Kármán flow using the experimental data from Refs. 14 and 15. The results are shown in Figs. 8(c) and 8(d), in which the coordinate system is chosen such that the axis of rotation of the propellers is the z-axis. The axial symmetry of the forcing can be seen in these PDFs. In comparison, the LEM successfully produced highly isotropic flows.

C. Reynolds number effects

The turbulence properties were also measured at different driving speeds of the propellers, ranging from 1 to 9.33 Hz, as shown in Table I. At constant observation volume the maximum achievable Reynolds number was limited by the laser illumination and not by the power of the motors. As the Reynolds number increases, the Kolmogorov time scale τ_η decreases. If one assumes that the integral length scale is constant, then τ_η decreases as $R_\lambda^{-3/2}$. Thus reliable measurement of the fastest motions of the flow requires the camera frame rate to increase with R_λ. On the other hand, the laser delivered constant average power and not a constant energy per pulse. In other words, the available number of photons per frame decreased with increasing frame rates and thus limited the maximal useable frame rate. At a motor frequency of 9.33 Hz and a camera frame rate of 5000 frames per second the image quality was already borderline.

For all Reynolds numbers, the tracer particles were smaller than the Kolmogorov scale of the turbulent flow. To characterize the effect of particle inertia, Table I lists the particle Stokes number, defined as the ratio of the particle relaxation time $\tau_p \equiv [(2\rho_p + \rho_f) d_p^2]/36\mu_f$ to the Kolmogorov time scale τ_η. The Stokes numbers are much smaller than one and hence the particles may be considered tracers.

At all the speeds, the flow was observed to be nearly statistically homogeneous and isotropic and the mean flow was small compared to the fluctuations. Figure 9 shows the mean and rms fluctuation of the three velocity components and the ratio of the mean to the fluctuation. In the range of Reynolds number explored that ratio was observed to be less than 15% and no systematic trend was observed.

One interesting observation is that the integral scale of the flow, as calculated from Eq. (5), decreased with propeller speed (or R_λ) at low speed ($R_\lambda \leq 200$) before reaching a con-

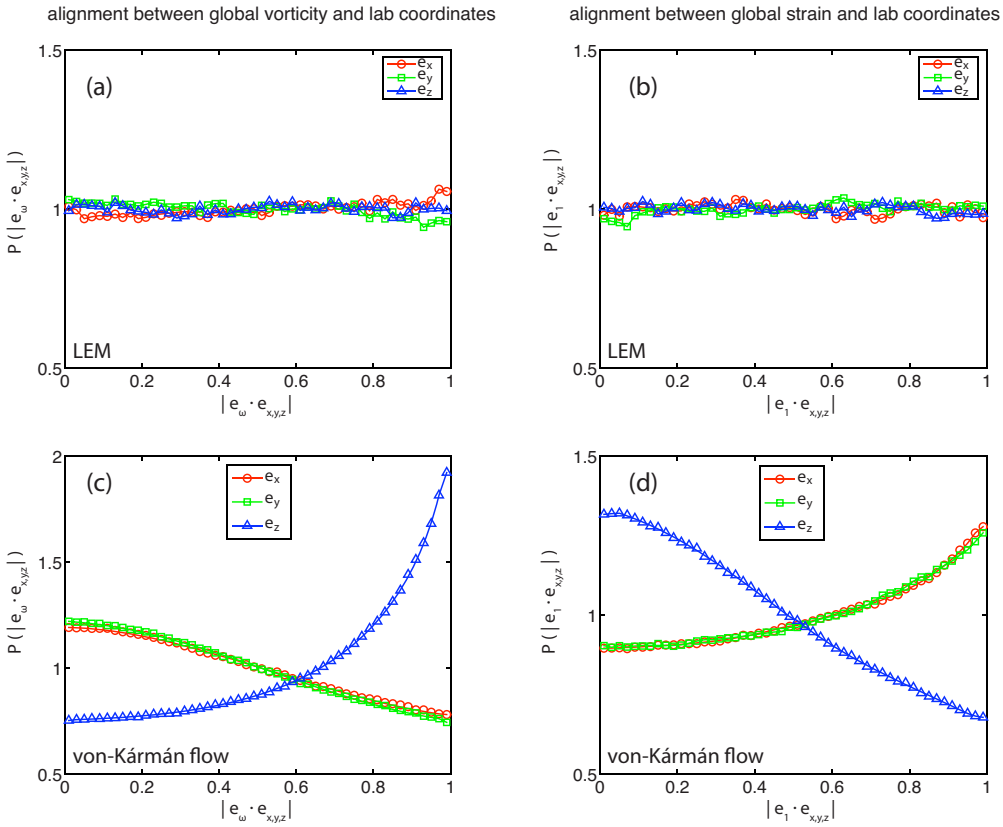

FIG. 8. (Color online) [(a) and (c)] PDFs of the alignment of the coarse-grained large scale vorticity vector $\omega(t)$ with the axes of laboratory coordinates. [(b) and (d)] PDFs of the alignment of the eigenvector $\mathbf{e}_1$, corresponding to the largest eigenvalue of the coarse-grained large scale rate of strain tensor. (a) and (b) are from the LEM at $R_\lambda = 195$. (c) and (d) are from the von Kármán device at $R_\lambda = 690$ (Refs. 14 and 15).

stant of approximately 6 cm. This is slightly different from the von Kármán flow reported in Ref. 25, where the integral scale was approximately independent of the propeller speed. It is possible that the particular shape of the propellers affects the turbulence at low Reynolds numbers through the mean flow field. This we also had observed in a von Kármán flow driven with a different propeller design.[35] It is also possible that the dimensionless constant C_L in Eq. (5) depends on Reynolds number and flow geometry.

IV. SUMMARY AND OUTLOOK

We constructed an apparatus, the LEM, that generated laboratory flows by 12 independently controlled propellers arranged symmetrically in three dimension (3D). Results from 3D LPT measurements demonstrated that at the center of the apparatus a region comparable in size to that of the integral length scale of the turbulence was statistically homogeneous and isotropic. Moreover, the mean flow was at least one order of magnitude smaller than the turbulent fluctuating velocities. These features make the LEM an attractive device for studying the Lagrangian properties of turbulence. The large number of flat windows on the LEM can be used to simultaneously carry out several measurements using different techniques, for example, Eulerian measurements using PIV and Lagrangian measurements using particle tracking.

Figure 10 shows that the turbulent fluctuating velocity in the LEM varied linearly with propeller speed, as in many other laboratory disk/propeller driven flows (see, e.g., Ref. 25). If the linear fit in Fig. 10 is extrapolated to the maximum motor speed and assuming that the integral scale remained at $L \approx 6$ cm, then the highest Reynolds number would be $R_\lambda \approx 450$. In that case, the maximum turbulent energy dissipation rate per unit mass is $\varepsilon \approx u'^3/L \approx 0.18$ W/kg, which means that the propellers very inefficiently converted mechanical power into turbulent kinetic energy. By changing the design of the propellers, e.g., by using propellers with larger blades it should be possible to

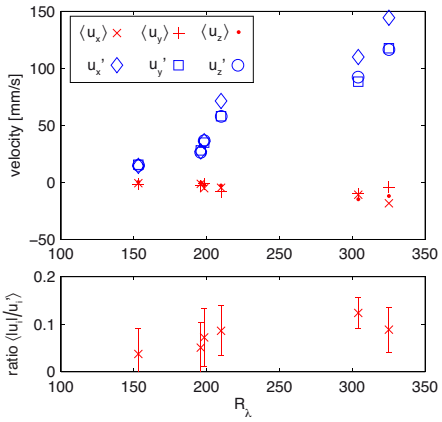

FIG. 9. (Color online) Top: components of the mean and fluctuating velocities, averaged over the entire measurement volume, at different Taylor scale Reynolds numbers. Bottom: ratio of the mean velocity to the fluctuating velocity, $[(|\langle u_x\rangle|/u_x') + (|\langle u_y\rangle|/u_y') + (|\langle u_z\rangle|/u_z')]/3$. The error bars in the bottom plot indicate the standard deviation within the three components.

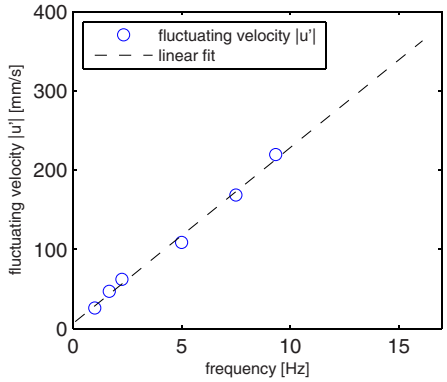

FIG. 10. (Color online) The change in fluctuating velocity with motor frequency.

increase the turbulence level of the flow. Theoretically, a Reynolds number of $R_\lambda \approx 900$ could be achieved in the LEM, if it is possible to convert all the mechanical power of the motors into kinetic energy of the flow while keeping the integral length scale at $L \approx 6$ cm. This would be comparable with active grids driven turbulence in a moderate size wind tunnel.[7] This optimistic estimate remains to be examined in the future.

Here we reported only results from driving the propellers at constant speeds and in one rotating direction. More driving patterns were tested, such as randomly modulating the speeds of individual propellers while keeping the energy injection rate constant.[36] In addition, the LEM allows to gradually change the flow from anisotropic forcing, such as using only a pair of propellers, to the more isotropic forcing as done in an air flow in Ref. 23. It is clear that many more tests and diagnostics must be performed in order to fully quantify the achievable degree of resemblance of such a laboratory flow with ideal homogenous isotropic turbulence. Flows forced in confined geometries are indeed bound to inject energy at many scales, possibly mixing several kinds of dynamics in a way different from the statistical equilibrium assumed theoretically or achieved in direct numerical simulations using volume forcing in a 3D-periodic space. These issues are currently under investigation.

ACKNOWLEDGMENTS

We are grateful to the machine shop at MPIDS, especially U. Schminke and J. Hesse; and P. Metz and D. Le Tourneau at ENS-Lyon for technical assistances during the construction of the apparatus. This work was supported by the Max Planck Society and by French ANR BLAN 07 1 192604. We also acknowledge PROCOPE support that initiated this project. This work is based primarily on the Diploma thesis "The Lagrangian Exploration Module" by Robert Zimmermann.

[1] A. N. Kolmogorov, Dokl. Akad. Nauk SSSR **30**, 301 (1941).
[2] G. A. Voth, K. Satyanarayan, and E. Bodenschatz, Phys. Fluids **10**, 2268 (1998).
[3] A. La Porta, G. A. Voth, A. M. Crawford, J. Alexander, and E. Bodenschatz, Nature (London) **409**, 1017 (2001).
[4] N. Mordant, P. Metz, O. Michel, and J.-F. Pinton, Phys. Rev. Lett. **87**, 214501 (2001).
[5] G. Falkovich, K. Gawedzki, and M. Vergassola, Rev. Mod. Phys. **73**, 913 (2001).
[6] F. Toschi and E. Bodenschatz, Annu. Rev. Fluid Mech. **41**, 375 (2009).
[7] L. Mydlarski and Z. Warhaft, J. Fluid Mech. **320**, 331 (1996).
[8] A. K. Kuczaj, B. J. Geurts, D. Lohse, and W. van de Water, Comput. Fluids **37**, 816 (2008).
[9] W. H. Snyder and J. L. Lumley, J. Fluid Mech. **48**, 41 (1971).
[10] Y. Sato and K. Yamamoto, J. Fluid Mech. **175**, 183 (1987).
[11] S. Ayyalasomayajula, A. Gylfason, L. R. Collins, E. Bodenschatz, and Z. Warhaft, Phys. Rev. Lett. **97**, 144507 (2006).
[12] M. Virant and T. Dracos, Meas. Sci. Technol. **8**, 1539 (1997).
[13] N. M. Qureshi, M. Bourgoin, C. Baudet, A. Cartellier, and Y. Gagne, Phys. Rev. Lett. **99**, 184502 (2007).
[14] M. Bourgoin, N. T. Ouellette, H. Xu, J. Berg, and E. Bodenschatz, Science **311**, 835 (2006).
[15] H. Xu, N. T. Ouellette, and E. Bodenschatz, New J. Phys. **10**, 013012 (2008).
[16] I. P. D. De Silva and H. J. S. Fernando, Phys. Fluids **6**, 2455 (1994).
[17] S. Ott and J. Mann, J. Fluid Mech. **422**, 207 (2000).
[18] E. A. Variano, E. Bodenschatz, and E. A. Cowen, Exp. Fluids **37**, 613 (2004).
[19] W. Hwang and J. K. Eaton, Exp. Fluids **36**, 444 (2004).
[20] D. R. Webster, A. Brathwaite, and J. Yen, Limnol. Oceanogr. Methods **2**, 1 (2004).
[21] E. A. Variano and E. A. Cowen, J. Fluid Mech. **604**, 1 (2008).
[22] C. Goepfert, J.-L. Marie, D. Chareyron, and M. Lance, Exp. Fluids **48**, 809 (2010).
[23] K. Chang, G. Bewley, and E. Bodenschatz, "Manipulating the isotropy of turbulence," J. Fluid Mech. (submitted).
[24] A. La Porta, G. A. Voth, F. Moisy, and E. Bodenschatz, Phys. Fluids **12**, 1485 (2000).
[25] G. A. Voth, A. La Porta, A. M. Crawford, J. Alexander, and E. Bodenschatz, J. Fluid Mech. **469**, 121 (2002).
[26] N. T. Ouellette, H. Xu, and E. Bodenschatz, Exp. Fluids **40**, 301 (2006).
[27] H. Xu, Meas. Sci. Technol. **19**, 075105 (2008).
[28] N. Mordant, A. M. Crawford, and E. Bodenschatz, Physica D **193**, 245 (2004).
[29] S. B. Pope, *Turbulent Flows* (Cambridge University Press, Cambridge, England, 2000).
[30] K. R. Sreenivasan, Phys. Fluids **7**, 2778 (1995).
[31] M. A. Taylor, S. Kurien, and G. L. Eyink, Phys. Rev. E **68**, 026310 (2003).
[32] K. R. Sreenivasan, Phys. Fluids **10**, 528 (1998).
[33] B. R. Pearson, P.-Å. Krogstad, and W. van de Water, Phys. Fluids **14**, 1288 (2002).
[34] M. Chertkov, A. Pumir, and B. I. Shraiman, Phys. Fluids **11**, 2394 (1999).
[35] H. Xu and E. Bodenschatz (unpublished).
[36] R. Zimmermann, "The Lagrangian Exploration Module," Diploma thesis, University of Göttingen, 2008.

PHYSICAL REVIEW E **86**, 035301(R) (2012)

Clustering of finite-size particles in turbulence

L. Fiabane,[1,*] R. Zimmermann,[1] R. Volk,[1] J.-F. Pinton,[1] and M. Bourgoin[2]
[1]*Laboratoire de Physique, ENS de Lyon, UMR CNRS 5672, Université de Lyon, France*
[2]*LEGI, UMR CNRS 5519, Université Joseph Fourier, Grenoble, France*
(Received 24 May 2012; published 21 September 2012)

We investigate experimentally the spatial distributions of heavy and neutrally buoyant particles of finite size in a fully turbulent flow. Because their Stokes number (i.e., the ratio of the particle viscous relaxation time to a typical flow time scale) is close to unity, one may expect both classes of particles to aggregate in specific flow regions. This is not observed. Using a Voronoï analysis we show that neutrally buoyant particles sample turbulence homogeneously, whereas heavy particles do cluster. These results show that several dimensionless numbers are needed in the modeling (and understanding) of the behavior of particles entrained by turbulent motions.

DOI: 10.1103/PhysRevE.86.035301 PACS number(s): 47.27.Gs, 47.27.T−, 82.70.−y

Turbulent flows laden with particles are widely found in industry and nature; their study is therefore of great interest and holds many fundamental aspects, issues, and limits still to be explored. One striking feature of these flows is the trend for the particles to concentrate in specific regions of the carrier flow. This has been observed and investigated for a long time both in experiments and simulations, and it is still widely studied (see the review paper [1] and references therein). The focus is usually put on small (namely, much smaller than the dissipation scale η of the flow) and heavy particles (with a high density compared to that of the fluid), especially in numerical studies. Because of their high specific density, the dynamics of such small and heavy inertial particles deviates from that of the carrier flow. Clustering phenomena are then one of the many manifestations of these inertial effects, generally attributed to the centrifugal expulsion of heavy particles from turbulent vortices, and more recently to a sticking effect of zero-acceleration points of the carrier flow [2]. Other studies indicate that light particles exhibit the same trend to cluster but with different cluster geometries [3,4]. Finally, tracers (which ought to be neutrally buoyant and much smaller than η) are used as seeds to characterize the flow dynamics and should not cluster. As small and heavy particles, finite-size heavy particles have been found to cluster [5]. However, the case of finite-size neutrally buoyant particles (with a diameter significantly larger than η) has never been treated to our knowledge in the context of preferential concentration. Such particles are known experimentally [6–8] and numerically [9,10] to differ from tracers, with in particular different acceleration statistics. But existing studies have focused on the dynamics of isolated particles, not on the spatial structuration of laden flows. Whether they cluster or not remains an open question.

Particles interacting with a turbulent flow are commonly characterized by their Stokes number, that is, the ratio between the particle viscous relaxation time τ_p and a typical time scale of the flow. Dealing with finite-size particles, we use the same definition as in Refs. [11,12], using the eddy-turnover time at the scale of the particle, τ_d, as the time scale of the flow, and a corrective factor f_ϕ based on the Reynolds number at particle scale: $\mathrm{St} \equiv \tau_p/\tau_d = f_\phi \phi^{4/3}(1+2\Gamma)/36$, where $\Gamma = \rho_p/\rho_f$ is the particle to fluid density ratio and $\phi = d/\eta$ is the particle diameter normalized by the dissipation scale (note that our conclusions remain the same using a point-particle definition of the Stokes number). This dimensionless number is often used as the key parameter to characterizing particle dynamics in turbulence, using simple Stokesian models where the dominant force acting on the particle is taken as the drag due to the difference between the particle velocity and that of the fluid. These models predict preferential concentration of particles with nonvanishing Stokes number, with a maximal segregation for St around unity [13,14]. This behavior is confirmed, at least qualitatively, in experiments with small and heavy particles [15]. In the present study we address the case of finite-size particles (both neutrally buoyant and heavier than the fluid) and investigate the particle concentration field as a function of their Stokes number in a homogeneous and isotropic turbulent flow. First, we describe the experimental setup and the data processing used. Then, we describe the results on spatial structuration for finite-size particles. We finish with a brief discussion and conclusions.

To study the behaviors of both neutrally buoyant and heavy particles, we use water as the carrier fluid. The turbulence is generated in the Lagrangian Exploration Module (LEM, see Fig. 1), whose characteristics are described in detail in Ref. [16] and summed up in Table I. The LEM produces turbulence in a closed water flow forced by 12 impellers evenly distributed on the faces of an icosahedral vessel. Here, all impellers rotate simultaneously at the same constant frequency f_{imp} which can be varied from 2 Hz up to 12 Hz; opposing impellers form counterrotating pairs. This produces a very homogeneous and isotropic turbulence in a significant central region of the device of the order of $(15\,\mathrm{cm})^3$, with the integral length of the order of 5 cm [16]. It also permits us to obtain high Reynolds number turbulent flow with mean velocities much weaker than the fluctuations near the center of the apparatus. Acquisitions are performed using 8-bit digital imaging at a resolution corresponding to a visualization window of the order of 16×12 cm in the center of the LEM. The visualization zone is illuminated by a 100 W Nd:YAG pulsed laser synchronized with the camera, creating a green light sheet with millimetric thickness. The camera is equipped with a macro lens. A

*lionel.fiabane@ens-lyon.org

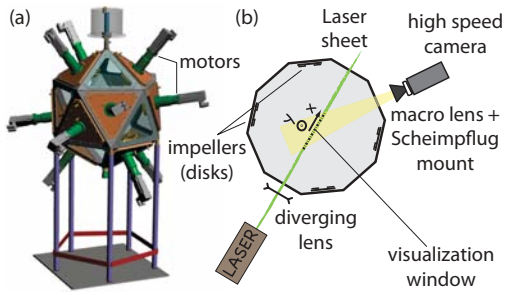

FIG. 1. (Color online) (a) CAD drawing of the LEM. (b) Schematic upper view of the setup.

Scheimpflüg mount compensates for the depth of field effects resulting from the angle between the camera and the laser sheet (see Fig. 1). Images are recorded at a low repetition rate of 2.5 Hz sufficient to address particle spatial distribution as we ensemble average over 2000 independent flow realizations for each experiment (particle dynamics is not addressed here).

We explore the behavior of two kinds of finite-size particles: neutrally buoyant and heavy ones. Regarding the neutrally buoyant particles, we use expanded polystyrene particles whose density has been irreversibly adjusted (prior to actual experiments) by moderate heating so that the density ratio to water is $1 \leqslant \Gamma_n \leqslant 1.015$. Depending on their size, the particles can be regarded as *tracers* following the carrier flow dynamics, or as *finite-size particles* whose dynamics departs from that of the flow. The limit for tracer behavior is known to be $d_n \simeq 5\eta$, whereas finite-size effects appear for $d_n > 5\eta$ [7,8,17]. In our case the particle diameter is $d_n = 700 \pm 20\ \mu$m and ranges from 4.5η to 17η (from the lowest to the highest investigated R_λ). Hence, our particles transit from tracers to finite-size particles as f_{imp} increases. As for heavy particles, we use slightly polydispersed sieved glass particles with diameters $225 \pm 25\ \mu$m and a density ratio $\Gamma_h = 2.5$, making them *inertial particles*. The neutrally buoyant particles cover a Stokes number from 0.38 to 1.23, while the heavy particles cover a Stokes number from 0.25 to 1.04 (see Table I). These two ranges overlap allowing some comparison. Since for each class of particles the diameter and density are kept constant, the Stokes number is varied by tuning the flow dissipation time scale. Therefore, it cannot be varied independently of the Reynolds number of the carrier flow.

We identify the particles on the images as local maxima with light intensity higher than a threshold, assuming in a first approximation that all the particles illuminated in the laser sheet belong to one plane. The center of the particles is determined as the center of mass of all the pixels surrounding one local maximum. Due to the high contrast between the light diffused by the particles and the background, changing slightly the threshold value does not significantly impact the number of detected particles, which is of order 100 (150) for the neutrally buoyant (heavy) particles (note that dealing with finite-size particles, the maximum authorized seeding density is drastically reduced by particles in the bulk blocking or eclipsing the image of particles in the laser sheet, compared to, e.g., experiments with small particles where thousands of particles per image are typically recorded [15]). The number of detected neutrally buoyant particles remains constant in time, indicating a good stationarity of seeding concentration as expected for nonsettling particles. However large heavy particles tend to settle for low impeller rotation rates f_{imp}. The heavy particles we consider here are sufficiently large to be considered as *finite size* and sufficiently small to prevent significant settling, since the entrainment by the flow is still capable of keeping them in suspension. Because of this limitation we did not consider bigger particles, and we did not investigate regimes where $f_{imp} < 2$ Hz (for which settling becomes important). Moreover, we make sure that the flow is already set in motion when the particles are inserted in the vessel to prevent them from settling immediately. Additionally, the number of particles per image is monitored, and experiments are repeated (after reloading particles) if too many are found to have settled (a typical experiment can run a few hours with relatively stationary seeding conditions).

The particle concentration field is investigated using Voronoï diagrams; this technique recently introduced for the investigation of preferential concentration of small water droplets in a turbulent airflow [15] was shown to be particularly efficient and robust to diagnose and quantify clustering phenomena. A given raw image, the detected particles, and the associated Voronoï diagram are provided for neutrally buoyant particles in Figs. 2(a) and 2(b); Fig. 2(c) shows a typical Voronoï diagram for the heavy particle case. The Voronoï diagrams give a tessellation of a two-dimensional space where each cell of the tessellation is linked to a detected particle, with all points of one cell closer to its associated particle than to any other particle. Thus, the area of each Voronoï cell is the inverse

TABLE I. Turbulence characteristics. f_{imp}: rotation frequency of the 12 impellers; u': fluctuation velocity of the flow; ε: energy dissipation rate; $\eta \equiv (\nu^3/\varepsilon)^{1/4}$ and $\tau_\eta \equiv (\nu/\varepsilon)^{1/2}$: Kolmogorov length and time scales of the flow; $R_\lambda \equiv (15u'^4/\nu\varepsilon)^{-1/2}$: Taylor microscale Reynolds number; St_n and St_h: Stokes numbers of neutrally buoyant and heavy particles, respectively.

f_{imp} (Hz)	u' (cm/s)	ε (m^2/s^3)	η (μm)	τ_η (ms)	R_λ	St_n	St_h
2	4	0.0016	159	24.9	160	0.38 ± 0.02	0.25 ± 0.04
4	8	0.0144	92	8.3	210	0.64 ± 0.03	0.46 ± 0.09
6	12	0.0611	64	4.0	260	0.87 ± 0.04	0.68 ± 0.11
8	17	0.1086	55	3.0	310	0.98 ± 0.04	0.78 ± 0.11
10	22	0.2087	47	2.2	360	1.11 ± 0.05	0.92 ± 0.11
12	26	0.3518	41	1.7	395	1.23 ± 0.05	1.04 ± 0.16

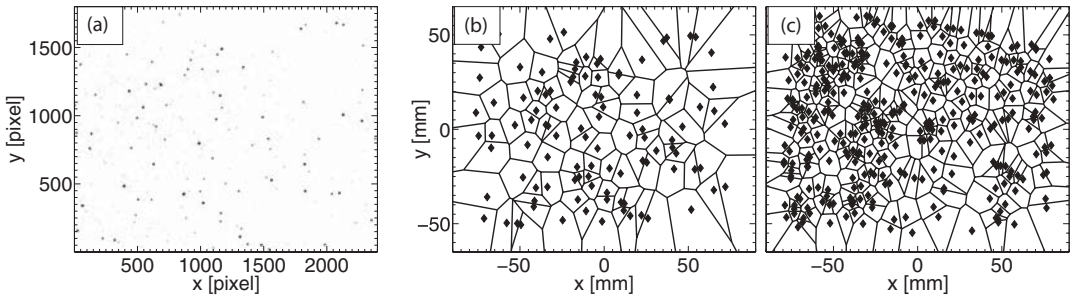

FIG. 2. (a) Typical raw acquired image of neutrally buoyant particles and (b) the detected particles located in real space with the associated Voronoï diagram. (c) Heavy particles located in real space with the associated Voronoï diagram (corresponding raw image not shown).

of the local concentration of particles, i.e., Voronoï area fields are a measure of the local concentration fields at interparticle length scale. To compare the results of experiments made with different amounts of detected particles per image, the Voronoï area is normalized using the average Voronoï area $\bar{A}$ defined as the mean particles concentration inverse, independent of the spatial organization of the particles. Therefore, we focus in the rest of this Rapid Communication on the distribution of the normalized Voronoï area $\mathcal{V} \equiv A/\bar{A}$. Clustering properties are quantified by comparing the probability density function (PDF) of Voronoï cell areas obtained from the experiments to that of a synthetic random Poisson process (RPP) whose shape is well approximated by a Gamma distribution [18].

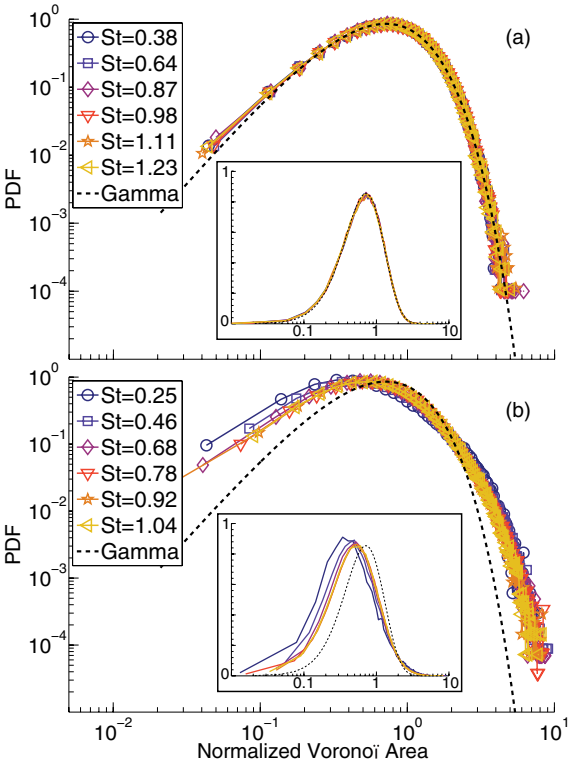

FIG. 3. (Color online) Superposition of the normalized Voronoï area PDFs for six experiments with varying Stokes number (plain lines) and a Gamma distribution (dashed line). Inserts represent the same results with linear ordinates. (a) Neutrally buoyant particles. (b) Heavy particles.

The PDFs of Voronoï cell areas for the different experiments described in Table I are plotted in Fig. 3, as well as the Gamma distribution approximation for a RPP. In the case of neutrally buoyant particles, all PDFs collapse and no Stokes number dependency is found. An important finding of the present work is that these PDFs are almost indistinguishable from the RPP distribution, meaning large neutrally buoyant particles do not exhibit any preferential concentration whatever their Stokes number. In the case of heavy particles, the PDFs clearly depart from the RPP distribution, with higher probability of finding depleted regions (large Voronoï areas) and concentrated regions (small Voronoï areas), which is the signature of preferential concentration. Furthermore, the shape of the PDF clearly depends on experimental parameters ($\mathrm{St_h}$ and/or R_λ). Interestingly, this dependence is stronger for the small Voronoï area tails, whereas the tail for large Voronoï areas (corresponding to depleted regions) appears to be more robust. This was also observed for small inertial particles [15,19]. The level of clustering can be further quantified using the standard deviation of the normalized Voronoï areas $\sigma_\mathcal{V} = \sqrt{\langle \mathcal{V}^2 \rangle - 1}$, plotted in Fig. 4. For neutrally buoyant particles we find a constant value $\sigma_\mathcal{V} \simeq 0.53$, which is the expected value for a RPP. For heavy particles we find $\sigma_\mathcal{V} > 0.53$ for all the experimental configurations investigated, revealing the presence of clustering. This result is in agreement with previous measurements [5] that find clustering for large ($\phi \simeq 4$) and heavy ($\Gamma = 1.4$) particles. We find the clustering level to globally decrease as $\mathrm{St_h}$ and/or R_λ increase, with no hint of

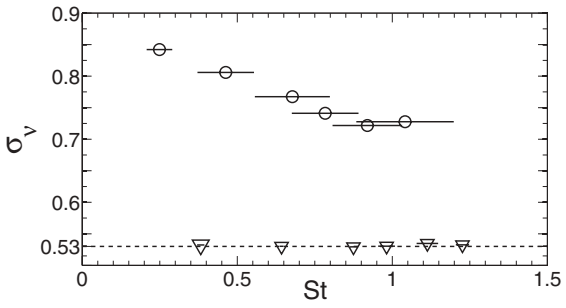

FIG. 4. Standard deviations of the normalized Voronoï areas vs the Stokes number with error bars (plain lines) for neutrally buoyant (▽) and heavy particles (○), to compare with $\sigma_\mathcal{V}^{\mathrm{RPP}} \simeq 0.53$ in the case of a RPP.

maximum clustering for $\mathrm{St_h}$ around unity. This is contrary to common observations: for numerical Stokesian models [13,14] a maximum is found for $\mathrm{St} \simeq 0.6$; for experiments with small particles [15,19], a peak is observed for $\mathrm{St} \gtrsim 1$ while Ref. [20] found a mild maximum for $\mathrm{St} \simeq 1$. If a maximum of clustering exists in our case (which is reasonable assuming that tracer behavior is to be recovered for $\mathrm{St_h} \to 0$), the peak would be at $\mathrm{St_h} < 0.25$. However, the limit $\mathrm{St_h} \to 0$ (i.e., $R_\lambda \to 0$) could not be explored here due to the settling effects at low R_λ. The clustering properties (Stokes number dependence and clusters geometry) for such finite-size and heavy particles go beyond the scope of the present research and will be investigated in future experiments.

Two important conclusions can be drawn from these results. (i) While inertial Stokesian models predict clustering within the explored range of St, this is not observed in the specific case of finite-size neutrally buoyant particles. Consequently, even though they do not behave as tracers, such particles are clearly not of the *inertial* class. The absence of clustering also supports experimental results on the dynamics of finite-size neutrally buoyant particles [7,8,17] suggesting that simple time-response effects are not sufficient to describe the particle-flow interaction and that other mechanisms (such as the role of pressure increments at the scale of the particle) are to be accounted for. (ii) Subsequently, the Stokes number by itself cannot be taken as sufficient to characterize clustering, because we have shown that particles with similar Stokes numbers may or not exhibit preferential concentration. Note that the limitation of the Stokes number has previously been shown for dynamical properties (rather than spatial distribution properties as illustrated here) of both isolated particles in turbulent flows [3,21] and two-way coupling effects [22]. These observations combined with ours stimulate the need for further investigations on the possible connection between dynamical features and preferential sampling of particles (including for instance turbophoresis and stick-sweep mechanisms [2], but also ergodic mechanisms [23]), by coupling Voronoï analysis of particles distribution to Lagrangian tracking [4,15].

We are currently investigating which set of parameters $f(\phi, \Gamma, R_\lambda, \ldots)$ drives the finite-size particle clustering, in particular by exploring how clustering is affected when Stokes number is varied (using particles with different sizes) at a fixed Reynolds number.

This work is partially supported by the ANR project TEC. We thank D. Le Tourneau for the manufacturing of the LEM.

[1] R. Monchaux, M. Bourgoin, and A. Cartellier, Int. J. Multiphase Flow **40**, 1 (2012).
[2] S. Goto and J. C. Vassilicos, Phys. Rev. Lett. **100**, 054503 (2008).
[3] E. Calzavarini, M. Kerscher, D. Lohse, and F. Toschi, J. Fluid Mech. **607**, 13 (2008).
[4] Y. Tagawa, J. M. Mercado, V. N. Prakash, E. Calzavarini, C. Sun, and D. Lohse, J. Fluid Mech. **693**, 201 (2012).
[5] M. Guala, A. Liberzon, K. Hoyer, A. Tsinober, and W. Kinzelbach, J. Turb. **9**, N34 (2008).
[6] G. A. Voth, A. La Porta, A. M. Crawford, J. Alexander, and E. Bodenschatz, J. Fluid Mech. **469**, 121 (2002).
[7] N. M. Qureshi, M. Bourgoin, C. Baudet, A. Cartellier, and Y. Gagne, Phys. Rev. Lett. **99**, 184502 (2007).
[8] R. D. Brown, Z. Warhaft, and G. A. Voth, Phys. Rev. Lett. **103**, 194501 (2009).
[9] E. Calzavarini, R. Volk, M. Bourgoin, E. Lévêque, J.-F. Pinton, and F. Toschi, J. Fluid Mech. **630**, 179 (2009).
[10] H. Homann and J. Bec, J. Fluid Mech. **651**, 81 (2010).
[11] F. G. Schmitt and L. Seuront, J. Marine Systems **70**, 263 (2008).
[12] H. Xu and E. Bodenschatz, Phys. D **237**, 2095 (2008).
[13] J. Bec, L. Biferale, M. Cencini, A. Lanotte, S. Musacchio, and F. Toschi, Phys. Rev. Lett. **98**, 084502 (2007).
[14] S. W. Coleman and J. C. Vassilicos, Phys. Fluids **21**, 113301 (2009).
[15] R. Monchaux, M. Bourgoin, and A. Cartellier, Phys. Fluids **22**, 103304 (2010).
[16] R. Zimmermann, H. Xu, Y. Gasteuil, M. Bourgoin, R. Volk, J.-F. Pinton, and E. Bodenschatz, Rev. Sci. Instrum. **81**, 055112 (2010).
[17] R. Volk, E. Calzavarini, E. Lévêque, and J.-F. Pinton, J. Fluid Mech. **668**, 223 (2011).
[18] J.-S. Ferenc and Z. Néda, Physica A **385**, 518 (2007).
[19] M. Obligado, M. Missaoui, R. Monchaux, A. Cartellier, and M. Bourgoin, J. Phys.: Conf. Ser. **318**, 052015 (2011).
[20] J. R. Fessler, J. D. Kulick, and J. K. Eaton, Phys. Fluids **6**, 3742 (1994).
[21] N. M. Qureshi, U. Arrieta, C. Baudet, A. Cartellier, Y. Gagne, and M. Bourgoin, Eur. Phys. J. B **66**, 531 (2008).
[22] F. Lucci, A. Ferrante, and S. Elghobashi, Phys. Fluids **23**, 025101 (2011).
[23] K. Gustavsson and B. Mehlig, Europhys. Lett. **96**, 60012 (2011).